1999

Magneto-optic Kerr effect of strongly correlated electron compounds

Rüdiger Johannes Lange
Iowa State University

INFORMATION TO USERS

This manuscript has been reproduced from the microfilm master. UMI films the text directly from the original or copy submitted. Thus, some thesis and dissertation copies are in typewriter face, while others may be from any type of computer printer.

The quality of this reproduction is dependent upon the quality of the copy submitted. Broken or indistinct print, colored or poor quality illustrations and photographs, print bleedthrough, substandard margins, and improper alignment can adversely affect reproduction.

In the unlikely event that the author did not send UMI a complete manuscript and there are missing pages, these will be noted. Also, if unauthorized copyright material had to be removed, a note will indicate the deletion.

Oversize materials (e.g., maps, drawings, charts) are reproduced by sectioning the original, beginning at the upper left-hand corner and continuing from left to right in equal sections with small overlaps. Each original is also photographed in one exposure and is included in reduced form at the back of the book.

Photographs included in the original manuscript have been reproduced xerographically in this copy. Higher quality 6" x 9" black and white photographic prints are available for any photographs or illustrations appearing in this copy for an additional charge. Contact UMI directly to order.

UMI

A Bell & Howell Information Company
300 North Zeeb Road, Ann Arbor MI 48106-1346 USA
313/761-4700 800/521-0600

Magneto-optic Kerr effect of strongly correlated electron compounds

by

Rüdiger Johannes Lange

A dissertation submitted to the graduate faculty

in partial fulfillment of the requirements for the degree of

DOCTOR OF PHILOSOPHY

Major: Condensed Matter Physics

Major Professor: David W. Lynch

Iowa State University

Ames, Iowa

1999

Graduate College
Iowa State University

This is to certify that the Doctoral dissertation of

Rüdiger Johannes Lange

has met the dissertation requirements of Iowa State University

Signature was redacted for privacy.

Committee Member

Signature was redacted for privacy.

Committee Member

Signature was redacted for privacy.

Committee Member

Signature was redacted for privacy.

Committee Member

Signature was redacted for privacy.

Major Professor

Signature was redacted for privacy.

For the Major Program

Signature was redacted for privacy.

For the Graduate College

Es gibt ja Leute, die gehen leichter durchs Leben, wenn sie ihre Erinnerungen über Bord werfen und ihren deutschen Rock an den Nagel hängen. Mir geht das nicht so. Vielen andern auch nicht. Wir tragen alle etwas Erde aus unserm Heimatdorf an den Stiefeln mit uns. Solange, bis wir sie ausziehen. Der eine Sand, der andre Lehm. Das macht unsern Gang hier nicht leichter; aber ich möchte die Heimaterde an meinen Stiefeln nicht missen.

Jürnjakob Swehn - der Amerikafahrer

Johannes Gillhoff

TABLE OF CONTENTS

1 INTRODUCTION

In 1846 Michael Faraday[1] observed a rotation of the plane of polarization of light transmitted through lead-borosilicate glass, magnetized along the direction of light propagation. This Faraday rotation, or magnetic circular birefringence (MCB), is accompanied by a second effect, called Faraday ellipticity or magnetic circular dichroism (MCD). If linearly polarized light is passed through a magnetized sample the transmitted light will have its plane of polarization rotated and also be slightly elliptical (see Chapter 2). A similar effect was observed by Kerr[2] some years later in a reflection experiment on magnetized samples. Linearly polarized light was found to be elliptically polarized with the major axis of the ellipse rotated by the Kerr rotation.

This magnetically induced change of polarization is called the magneto-optic Kerr effect (MOKE), as opposed to the electro-optic Kerr effect which Kerr discovered later. There are important differences in the MOKE depending on the direction of magnetization with respect to the direction of polarization of the incident light and the plane of incidence, which is the plane defined by the propagation vector of the light and the surface normal (for a vertically mounted sample this plane is parallel to the optical table). We distinguish three different MOKE geometries (shown in Fig. 1.1) the most common one being the polar Kerr effect, for which the sample is magnetized parallel (or antiparallel) to the surface normal. This effect is a *circular effect,* i.e. caused by different (complex) reflection coefficients for *right and left circularly* polarized light (see Section 2.3 for details). If the sample magnetization is parallel to the surface we distinguish between the longitudinal and transverse Kerr effect. For the longitudinal MOKE magnetization of the sample is in the plane of incidence whereas it is perpendicular to the plane of incidence in the transverse geometry. Both effects are *linear effects,* i.e. they result from different optical constants (refractive index n and absorption coefficient k) for light *linearly* polarized parallel and perpendicular to the direction of magnetization. Both effects are, to lowest order, quadratic in the magnetization. This means reversing the magnetization does not yield a different sense of rotation for the reflected light. The polar MOKE is linear in the magnetization and reversing the direction of magnetization results in a rotation in the opposite direction. This makes the polar MOKE suitable for

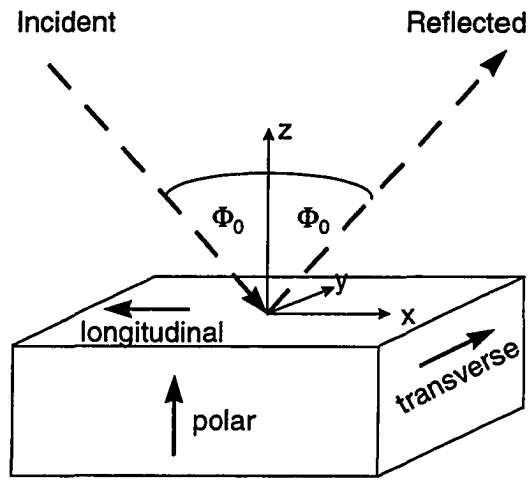

Figure 1.1 Three different geometries for the magneto-optic Kerr effect. Arrows indicate the direction of magnetization.

use in magneto-optic storage devices, where the direction of magnetization is utilized to encode binary information. In general, ferromagnets were considered the only candidates for high Kerr rotation since, in a simplified picture, the MOKE is proportional to the net spin polarization of the sample.

Early experiments concentrated on ferromagnetic 3d transition metal alloys and elemental lanthanides. Kerr rotations are typically of the order of several 0.1°. In the early 1980's van Engen *et al.*[3] discovered the highest room temperature Kerr rotation of 1.2° in PtMnSb. Feil and Haas[4] showed that the large room temperature Kerr effect is likely due to interference of a rather weak interband transition (which they assumed to be constant) and a plasma minimum in the optical reflectivity. Schoenes[5], on the other hand, argues that the assumptions they made about the dielectric function were oversimplified and that the sharp feature in the Kerr spectrum originates from a narrow interband transition. Although this dispute has never been settled, it is known that the Kerr effect is enhanced by a low reflectivity, as observed near the plasma resonance of free carriers, which would support Feil's and Haas' interpretation[4].

In 1996 Pittini *et al.*[6] reported the maximum Kerr rotation of 90° at 1.5 K and 60 kOe at a photon energy of 0.43 eV. A rotation, Θ_K, of the plane of polarization of more than 90° can experimentally not be distinguished from a negative Kerr rotation of $\Theta'_K = -180° + \Theta_K$. In general, it was observed that compounds of Ce and one of the pnictides (VA group: As, Sb, Bi) or chalcogenides (VIA group: S, Se, Te) show Kerr rotations which are one to two orders of magnitude larger than those found in $3d$-based materials[7, 8]. It is interesting to note that materials which show a large Kerr effect do not necessarily

order ferromagnetically. At low temperatures a high field can be applied to induce ferromagnetic order and large Kerr rotations can be observed even in antiferromagnets (like CeSb). In Table 1.1 we give an overview of the Kerr rotation of some representative materials. For a more thorough review of magneto-optic materials we would like to refer to articles by Schoenes[8, 9], Buschow[10], and Reim and Schoenes[7].

Table 1.1 Kerr rotation of some representative materials. Also shown is the photon energy where the maximum rotation was measured as well as the experimental parameters, i.e. temperature and applied magnetic field.

Sample	Kerr rotation	Energy (eV)	T (K)	H (kOe)
Ni	$-0.15°$	1.5	300	5
Co	$-0.38°$	1.4	300	5
PtMnSb	$-1.2°$	1.2	300	10
CeTe	$-3.3°$	2.0	2	50
CeSe	$-5.5°$	2.6	1.35	100
CeS	$-20°$	3.0	1.5	100
CeAs	$3.7°$	0.20	1.5	100
CeBi	$-8°$	0.50	1.5	60
CeSb	$90°$	0.46	1.5	50

Although attempts have been made to explain the Kerr effect on the basis of atomic level schemes (which is more appropriate for localized electronic states), as well as from first principles calculations, our understanding of the Kerr effect in strongly correlated electron systems is still not satisfactory. For compounds containing Ce both schemes fail. Local-density-type calculations cannot treat the electronic $4f$ state of Ce. The Ce-$4f$ bands are close to the Fermi energy and mix with conduction electron states. In addition, those materials can show strong electron-electron and electron-phonon interactions, which are neglected in band structure calculations. This often leads to unusual physical phenomena including heavy-Fermion behavior, the Kondo effect, or valence fluctuation, to name the most prominent effects.

An empirical approach to the problem of magneto-optics of strongly correlated electron systems was presented by Misemer[11]. It was pointed out that magneto-optic absorption, which gives rise to the Kerr effect, is proportional to the spin-obit interaction, $H_{SO} = -\xi \vec{L} \cdot \vec{S}$. Therefore, electronic states of heavier elements with large orbital and principal quantum number are more promising candidates for large magneto-optic signals. Figure 1.2(a) shows the spin-orbit splitting, ξ, of the highest occupied level as a function of atomic number[12]. It can be seen that ξ is fairly large for the lanthanide $5d$ state. Transitions involving $d \rightarrow f$ and $f \rightarrow d$ transitions can lead to large magneto-optic signals, whereas

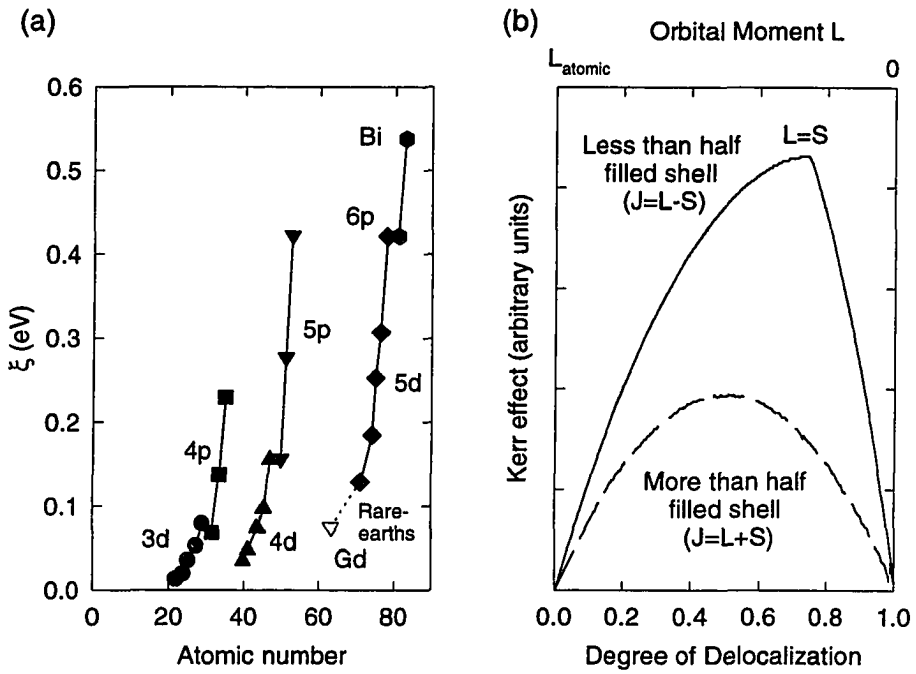

Figure 1.2 (a) Strength of the spin-orbit splitting for the highest occupied state as a function of atomic number. (b) Kerr effect as a function of the degree of delocalization.

their contribution to the optical constants of the material might be small.

Pittini and Wachter[13] used a simple calculation to investigate the size of the magneto-optic Kerr effect on the *degree of delocalization*, which is proportional to the overlap integral of wave functions originating from the *same* atomic state on neighboring lattice sites, i.e. they assume f-f-type hybridization, neglecting possible mixing with other atomic states. A large overlap leads to broadening of electronic states, i.e. band formation, which results in partial loss of the orbital magnetic moment. Figure 1.2(b) shows the size of the Kerr effect as a function of the degree of delocalization. From this plot it becomes clear that completely localized states do not contribute to the Kerr effect, as do fully delocalized states, since for $L = 0$ spin-orbit interaction vanishes and, according to Misemer[11], magneto-optic effects will be quenched. According to Pittini's and Wachter's model[13], the maximum Kerr effect occurs for materials in which the electronic $4f$-state is rather delocalized and the orbital moment is quenched to such an extend that $L = S$. However, this is only a crude approximation. In particular, the Ce-$4f$ states hybridize strongly with states in the vicinity of the Fermi level and this needs to be taken into account. A first principles calculation gives a better description of the electronic structure.

In the following chapter of this thesis we will introduce the macroscopic theory of magneto-optic

effects. Starting from Maxwell's equations, we will briefly review the reflection of light on a surface. We then derive expressions that relate the magneto-optic Kerr effect to the dielectric function or, in general, the dielectric tensor. In Chapter 3 the classical model for free-carrier contributions to the optical properties will be reviewed. We then present the quantum-mechanical derivation of the diagonal and off-diagonal elements of the optical conductivity tensor. The relationship between macroscopic phenomena (optical absorption) and microscopic theory (radiation interaction and matrix elements) will be established. In order to compare our experimental results with theoretical predictions we performed *ab initio* band structure calculations. The band structure program will be described briefly. Chapter 4 will give an overview of the experimental techniques, i.e. spectroscopic ellipsometry and Kerr spectroscopy. We will give the necessary background information to understand the principle of each experiment. Details on the experimental setup will be given for both experiments. Chapters 5 through 8 represent the main part of this thesis. We will discuss four different classes of materials and their optical properties. Chapter 5 deals with the magneto-optic properties of RAl_2 (R=La, Ce, Pr). $CeAl_2$ is a magnetic Kondo system. We will compare its electronic structure and optical properties to those of $LaAl_2$ and $PrAl_2$. In Chapter 6 we investigate $CeFe_2$, in which hybridization is stronger than in $CeAl_2$, leading to valence fluctuations and quenching of the orbital moment of Ce. Alloying of $CeFe_2$ with small amounts of Co leads to a magnetic instability, which is manifested in low-temperature antiferromagnetic ordering. We will investigate the antiferromagnetic to ferromagnetic phase transition using the Kerr effect. Motivated by the recent discovery of superconductivity and magnetism and RNi_2B_2C we will present magneto-optical spectra of RNi_2B_2C (R=Tm, Yb) in Capter 7. The magneto-optical properties of $TmNi_2B_2C$ will be investigated in the mixed and normal state. $YbNi_2B_2C$, which does not show magnetic order down to 0.4 K, is characterized by a large linear specific heat coefficient, placing this compound in the group of heavy Fermion compounds. We will compare its optical properties to those of $TmNi_2B_2C$, which represents the *common* borocarbide magnetic superconductors. Combining the ideas of Feil and Haas[4] and Pittini and Wachter[13], we were searching for materials that show 1) a low carrier concentration, which puts the plasma frequency in the spectral range covered by our instrument and 2) strong $4f$-hybridization. Two materials that meet these conditions are CeB_6 and YbBiPt. We present our investigation of these compounds in Chapter 8. Although conclusions will be given at the end of each individual chapter, we will summarize the results of this thesis in Chapter 9.

2 MACROSCOPIC THEORY

The optical properties of a solid can be described by its complex dielectric tensor or, equivalently, its optical conductivity tensor, $\tilde{\epsilon}_{ij}$ and $\tilde{\sigma}_{ij}$, respectively. The optical response can be measured using polarization modulation techniques, in particular we use ellipsometry and Kerr spectroscopy. We will first introduce the Jones calculus, which enables us to determine the transfer function of an optical system. We then derive the relationship between the components of the dielectric and conductivity tensors from Maxwell's equations. In the next section we will show how the Kerr effect can be expressed in terms of the optical conductivity and vice versa. We conclude this chapter on the macroscopic description of the electromagnetic response of a medium with the Kramers-Kronig relations for the dielectric function, the optical conductivity, and the Kerr effect.

2.1 Waves and polarization - the Jones calculus

Without loss of generality we will limit our discussion to monochromatic waves. Anharmonic waves can be decomposed into monochromatic components by Fourier analysis. Maxwell's equations (2.14)-(2.17) require electromagnetic waves to be transverse. Therefore, we will only consider the special case of a uniform transverse-electric plane wave. The electric vector of a linearly polarized wave of this type varies with position $\vec{r}$ and time t according to

$$\vec{E}(\vec{r},t) = E_0 \, \mathrm{e}^{i(\omega t - \vec{k}\cdot\vec{r})} \times \hat{e}, \tag{2.1}$$

where $\vec{k}$ is the wave vector along the direction of propagation and $\hat{e}$ is the unit polarization vector of the wave. For a wave propagating along the z-axis in a medium with refractive index $\tilde{n} = n - ik$, we may set

$$\vec{k}\cdot\vec{r} = k_z z = \frac{2\pi\tilde{n}}{\lambda_0} z, \tag{2.2}$$

where λ_0 is the vacuum wavelength. n is the index of refraction and k is the absorption coefficient. In the case of an arbitrary linearly polarized wave traveling along z the unit polarization vector may be

written as

$$\hat{e} = \begin{pmatrix} \cos\theta \\ \sin\theta \end{pmatrix}. \tag{2.3}$$

The electric vector oscillates along a general direction in the wave-front, inclined to the fixed x-axis by an azimuth angle θ. This notation is called the Jones vector of the wave. A sinusoidal time dependence is assumed. The wave is polarized in the x-y-plane and propagating along the z-axis. In this notation the time dependence and the phase information, i.e. the entire exponential term in Eq. (2.1), as well as the z-component (which is zero) are omitted. Figure 2.1 shows the electric field vectors of different states of polarization.

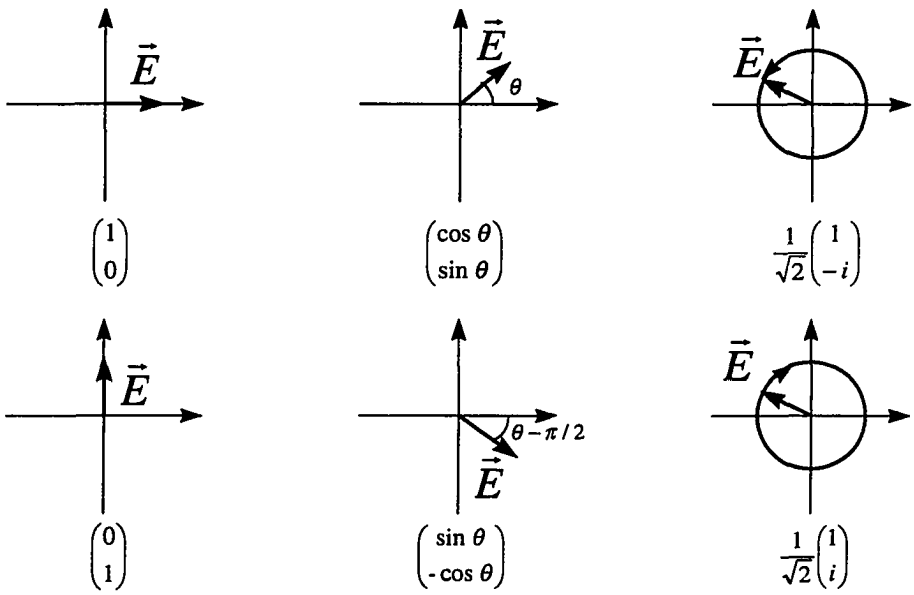

Figure 2.1 The most common states of polarization and their Jones vectors. The upper panel shows a wave linearly polarized along the x-axis, a linearly polarized wave inclined by an azimuth angle θ with respect to the x-axis, and a left-circularly polarized wave. The lower panel shows the states of polarization orthogonal to the ones above. Each pair of two forms a complete basis set.

Two special cases are waves polarized along the x-axis and y-axis, respectively:

$$\hat{e}_x = \begin{pmatrix} 1 \\ 0 \end{pmatrix}, \qquad \hat{e}_y = \begin{pmatrix} 0 \\ 1 \end{pmatrix}. \tag{2.4}$$

Equation (2.4) represents a pair of orthogonal linearly polarized waves, each of which is of unit amplitude. The two vectors form a basis and any arbitrary wave, which propagates along z, can be

decomposed into components along x and y. The Jones vector

$$\hat{e}' = \begin{pmatrix} \sin\theta \\ -\cos\theta \end{pmatrix} \tag{2.5}$$

is orthogonal to $\hat{e}$ in Eq. (2.3), and $\hat{e}$ and $\hat{e}'$ form another basis set. Yet another pair of orthogonal waves of interest are the left (LCP, $-$) and right-circularly (RCP, $+$) polarized waves, whose Jones vectors are given by

$$\hat{e}_- = \frac{1}{\sqrt{2}}\begin{pmatrix} 1 \\ -i \end{pmatrix}, \qquad \hat{e}_+ = \frac{1}{\sqrt{2}}\begin{pmatrix} 1 \\ i \end{pmatrix} \tag{2.6}$$

The linear oscillations along the x and y-axis, from which $\hat{e}_-$ and $\hat{e}_+$ are constructed, are of equal amplitude. In the case of LCP the y-component lags the x-component by a phase of $\pi/2$, whereas for RCP the y-component leads the x-component by $\pi/2$. LCP and RCP can be expressed by basis vectors along the two principal directions by

$$\hat{e}_- = \frac{1}{\sqrt{2}}(\hat{e}_x - i\hat{e}_y), \qquad \hat{e}_+ = \frac{1}{\sqrt{2}}(\hat{e}_x + i\hat{e}_y). \tag{2.7}$$

The states of linear and circular polarization are only limiting cases of the more general state of elliptical polarization (see Fig. 2.2). An elliptically polarized wave with ellipticity ϵ and the major axis of its polarization ellipse inclined by an azimuth angle θ is described by the unit vector

$$\hat{e}_{ell} = \begin{pmatrix} \cos\theta\cos\epsilon - i\sin\theta\sin\epsilon \\ \sin\theta\cos\epsilon + i\cos\theta\sin\theta \end{pmatrix}. \tag{2.8}$$

In the general case, the Jones vector of a wave is

$$\begin{pmatrix} E_x \\ E_y \end{pmatrix}, \tag{2.9}$$

with complex amplitudes E_x and E_y. The absolute intensity of a wave is the sum of the squared amplitudes of the component oscillations along two mutually orthogonal direction

$$I = |E_x|^2 + |E_y|^2 = E_x^* E_x + E_y^* E_y, \tag{2.10}$$

where E_i^* is the complex conjugate of E_i.

In our optical experiments we use systems consisting of a series of optical elements (e.g. polarizers, modulator, compensator, sample), each of which has its own transfer characteristics. The Jones calculus is a very powerful tool to determine the transfer function of an optical system. Assume we know the initial state of polarization or the incident electric wave $\vec{E}_{in}$. The wave enters the experiment consisting of a series of optical components $J_1, ..., J_n$. The Jones vector of the emerging light is then given by

$$\vec{E}_{out} = J_n \cdot J_{n-1} \cdot ... \cdot J_1 \cdot \vec{E}_{in} \tag{2.11}$$

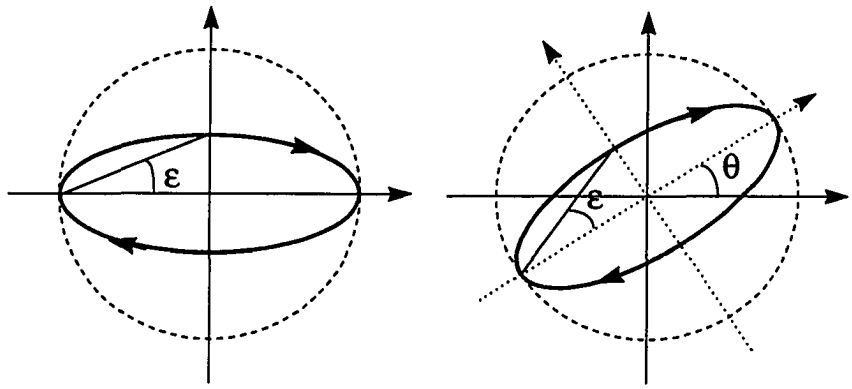

Figure 2.2 The most general polarization state is elliptical polarization. On the left an elliptically polarized wave is shown with its major and minor axis along the x and y direction, respectively, i.e. the ellipticity is ϵ and $\theta = 0$. On the right hand side the same ellipse is inclined at an angle θ with respect to the positive x-axis. Equation (2.8) is the Jones vector of this state.

It is now necessary to introduce the Jones matrices of the optical components used in our experiments. The Jones matrix of an ideal linear polarizer with its transmission axis subtending an angle θ from the x-axis is represented by

$$J_P = \begin{pmatrix} \cos^2\theta & \sin\theta\cos\theta \\ \sin\theta\cos\theta & \sin^2\theta \end{pmatrix} \tag{2.12}$$

A linear retarder introduces a phase shift δ between components of a wave polarized along its two mutually perpendicular optical axes. Its Jones matrix is given by

$$J_R = \begin{pmatrix} 1 & 0 \\ 0 & e^{i\delta} \end{pmatrix}. \tag{2.13}$$

In Chapter 4 we will use the Jones calculus to derive expressions for the intensity at the detector of an ellipsometer and Kerr spectrometer. We will also introduce the Jones matrices for a reflecting surface, i.e. the sample, which depends on the crystal structure and the state of magnetization of the sample.

2.2 Maxwell's equations

It was Maxwell's prediction that light is an electromagnetic wave phenomenon, and that electromagnetic waves of all frequencies could be produced. Therefore a complete description of electromagnetic waves and charges must invoke Maxwell's equations. We can write Maxwell's equations in differential form:

$$\nabla \cdot \vec{D} = 4\pi\rho \tag{2.14}$$

$$\nabla \cdot \vec{B} = 0 \tag{2.15}$$

$$\nabla \times \vec{E} = -\frac{1}{c}\frac{\partial \vec{B}}{\partial t} \tag{2.16}$$

$$\nabla \times \vec{H} = \frac{1}{c}\left(4\pi\vec{J} + \frac{\partial \vec{D}}{\partial t}\right) \tag{2.17}$$

where the electric field $\vec{E}$ and the magnetic induction $\vec{B}$ are the macroscopic field quantities, the electric displacement $\vec{D}$ and the magnetic field $\vec{H}$ are corresponding derived fields, related to $\vec{E}$ and $\vec{B}$ through the polarization $\vec{P}$ and magnetization $\vec{M}$ of the material by

$$\vec{D} = \vec{E} + 4\pi\vec{P} = (\mathbf{1} + \tilde{\alpha}_1)\vec{E} = \tilde{\epsilon}_1\vec{E} \tag{2.18}$$

$$\vec{B} = \vec{H} + 4\pi\vec{M} = (\mathbf{1} + \tilde{\chi}_1)\vec{H} = \tilde{\mu}_1\vec{H}, \tag{2.19}$$

neglecting non-linear effects. $\mathbf{1}$ denotes the unit matrix. $\tilde{\alpha}_1$ and $\tilde{\chi}_1$ are the real polarizability and magnetic susceptibility tensors, respectively. Equation (2.18) defines the real dielectric tensor $\tilde{\epsilon}_1$. Analogously, we can write Ohm's law with the real conductivity tensor $\tilde{\sigma}_1$:

$$\vec{J} = \tilde{\sigma}_1\vec{E}. \tag{2.20}$$

Using these definitions with Eqs. (2.16) and (2.17), and the time dependence defined in Eq. (2.1), we obtain

$$\nabla \times \vec{E} = -\frac{i\omega}{c}\tilde{\mu}_1\vec{H} \tag{2.21}$$

$$\nabla \times \vec{H} = \frac{1}{c}\left(\tilde{\epsilon}_1 - \frac{4\pi i}{\omega}\tilde{\sigma}_1\right)\frac{\partial \vec{E}}{\partial t}. \tag{2.22}$$

This leads to the definition of the complex dielectric function

$$\tilde{\epsilon} = \tilde{\epsilon}_1 - \frac{4\pi i}{\omega}\tilde{\sigma}_1, \tag{2.23}$$

which is equivalent to the definition of a complex conductivity

$$\tilde{\sigma} = \tilde{\sigma}_1 + \frac{i\omega(\tilde{\epsilon}_1 - \mathbf{1})}{4\pi}. \tag{2.24}$$

This, together with Eq. (2.17), allows a generalization of Ohm's law,

$$\vec{J}_{tot} = \frac{1}{4\pi}\frac{\partial}{\partial t}\vec{D} + \vec{J} = \left(\tilde{\sigma}_1 + \frac{i\omega}{4\pi}\tilde{\epsilon}_1\right)\vec{E} = \left(\tilde{\sigma} + \frac{i\omega}{4\pi}\mathbf{1}\right)\vec{E}, \tag{2.25}$$

with the total current $\vec{J}_{tot}$.

The optical properties of a medium can be completely characterized by the dielectric and magnetic permeability tensors, $\tilde{\epsilon}_{ij}(\omega, \vec{k})$ and $\tilde{\mu}_{ij}(\omega, \vec{k})$, respectively. Both tensors depend, in general, on frequency

ω and wave vector $\vec{k}$ of the light wave. The selection of tensors $\tilde{\epsilon}_{ij}$ and $\tilde{\mu}_{ij}$ is to some extent arbitrary. The response of a medium to an electromagnetic wave can be described by an effective conductivity tensor without introducing $\tilde{\mu}_{ij}$ [14, 15, 16, 17]. The tensor $\tilde{\mu}_{ij}(\omega)$ is required to describe contributions to electronic magnetic dipole transitions, which are usually small and may be noticeable only in the vicinity of direct absorption bands in the optical spectrum[18]. We follow the argument of Landau and Lifschitz[19] and Pershan[14] that at optical frequencies $\mu = 1$, even for ferromagnets. Therefore, when studying the symmetry of the optical properties of magnetic crystals, it is sufficient to investigate the dependence of the dielectric tensor components, $\tilde{\epsilon}_{ij}(\omega, \vec{H}, \vec{k})$, on the symmetry, i.e. crystal structure, of the material. As long as the wavelength of the radiation is large compared to interatomic distances, which is the case for photon energies of several eV, as used for standard optical measurements, the $\vec{k}$-dependence can be neglected. The components of $\tilde{\epsilon}_{ij}$ satisfy the Onsager relations[20]

$$\tilde{\epsilon}_{ij}(\vec{H}) = \tilde{\epsilon}_{ji}(-\vec{H}). \tag{2.26}$$

This is strictly valid for paramagnets and diamagnets in an applied field only. For ferromagnets the field $\vec{H}$ is replaced by the intrinsic magnetization $\vec{M}$. It follows from Eq. (2.26) that the diagonal components are even functions of $\vec{H}$, whereas the off-diagonal elements of the dielectric tensor are an odd function of the field. Assuming a magnetization along z and applying general symmetry arguments[20, 21], we may write the dielectric tensor of a crystal with at least cubic symmetry, tetragonal or hexagonal symmetry and the c axis along z, or polycrystalline samples as

$$\tilde{\epsilon} = \begin{pmatrix} \tilde{\epsilon}_{xx} & \tilde{\epsilon}_{xy} & 0 \\ -\tilde{\epsilon}_{xy} & \tilde{\epsilon}_{xx} & 0 \\ 0 & 0 & \tilde{\epsilon}_{zz} \end{pmatrix}. \tag{2.27}$$

The dielectric and conductivity tensors are not independent but describe the same phenomena, and are related by

$$\tilde{\epsilon}_{ij} = \delta_{ij} - \frac{4\pi i}{\omega}\tilde{\sigma}_{ij}, \tag{2.28}$$

where we used the Kronecker δ-symbol. In the case of zero field (zero magnetization for ferromagnets), the off-diagonal components vanish and $\tilde{\epsilon}_{ij}$, as well as $\tilde{\sigma}_{ij}$, becomes diagonal. Magneto-optical effects result from magnetically induced off-diagonal elements in the dielectric and conductivity tensors.

In the following we will define the complex optical functions by

$$\tilde{\epsilon}_{ij} = \epsilon_{1ij} - i\epsilon_{2ij} \tag{2.29}$$

$$\tilde{\sigma}_{ij} = \sigma_{1ij} + i\sigma_{2ij}. \tag{2.30}$$

Setting $\mu = 1$ and applying Maxwell's equations to a plane wave, as defined by Eq. (2.1), we obtain

$$\tilde{n}^2 = (n + ik)^2 = \tilde{\epsilon}_{xx}, \tag{2.31}$$

which relates the complex index of refraction to the diagonal element of $\tilde{\epsilon}_{ij}$. We can write the dispersive and absorptive part of the dielectric function in term of the index of refraction n and absorption coefficient k:

$$\epsilon_{1xx} = n^2 - k^2 \tag{2.32}$$

$$\epsilon_{2xx} = 2nk, \tag{2.33}$$

and the conductivity according to Eq. (2.28).

2.3 Fresnel reflection coefficients

Consider the oblique reflection of an optical plane wave at the planar interface between two semi-infinite homogeneous optically isotropic media 0 and 1, with complex indices of refraction $\tilde{n}_0$ and $\tilde{n}_1$, respectively (Fig. 2.3). The total fields inside media 0 and 1 obey Maxwell's equations and the boundary conditions at the interface

$$E_{t,0} = E_{t,1} \tag{2.34}$$

$$H_{t,0} = H_{t,1} \tag{2.35}$$

$$D_{n,0} = D_{n,1} \tag{2.36}$$

$$B_{n,0} = B_{n,1}. \tag{2.37}$$

The indices t, n designate the component tangential and normal to the interface, respectively. For these boundary conditions to be satisfied, (1) the direction of the incident, reflected, and refracted waves must all lie in one plane, called the plane of incidence (defined by the wave vector $\vec{k}$ and the surface normal), (2) the angle of of incidence θ_0 must be equal to the angle of reflection, and (3) the angles θ_0 and θ_1 must be related by

$$\tilde{n}_0 \sin\theta_0 = \tilde{n}_1 \sin\theta_1, \tag{2.38}$$

which is Snell's law.

If the two media are optically isotropic the eigenpolarizations of reflection are the states of linear polarization parallel (p) and perpendicular (s) to the plane of incidence. Matching the tangential

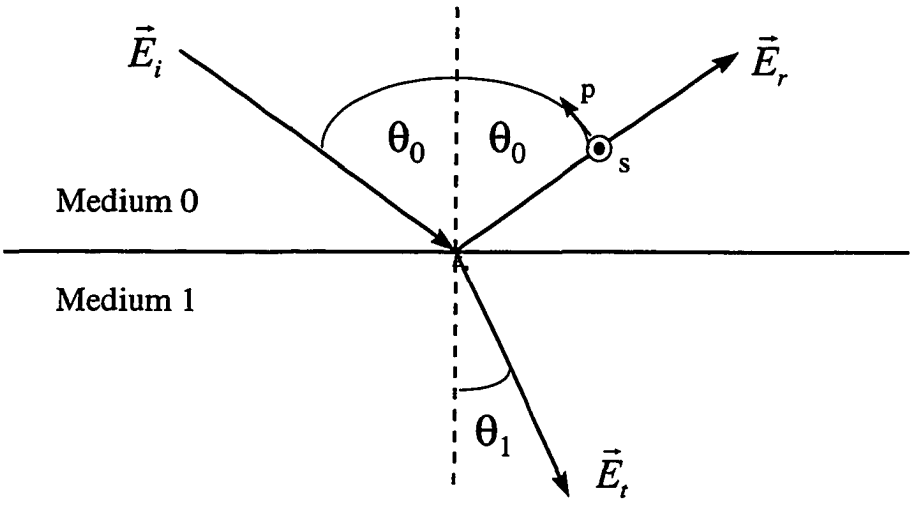

Figure 2.3 Reflection and refraction of a plane wave at the interface between two media 0 and 1. $\vec{E}_i$ is the incident, $\vec{E}_r$ the reflected, and $\vec{E}_t$ the transmitted wave. The electric field can be decomposed into the two eigenpolarizations of an optically isotropic surface, i.e. p and s-polarization, for which the electric field oscillates parallel and perpendicular to the plane of incidence, respectively.

components of $\vec{E}$ and $\vec{H}$ leads to

$$\frac{E_{rp}}{E_{ip}} = \tilde{r}_p = \frac{\tilde{n}_1 \cos\theta_0 - \tilde{n}_0 \cos\theta_1}{\tilde{n}_1 \cos\theta_0 + \tilde{n}_0 \cos\theta_1} \tag{2.39}$$

$$\frac{E_{rs}}{E_{is}} = \tilde{r}_s = \frac{\tilde{n}_0 \cos\theta_0 - \tilde{n}_1 \cos\theta_1}{\tilde{n}_0 \cos\theta_0 + \tilde{n}_1 \cos\theta_1}, \tag{2.40}$$

which are the Fresnel complex-amplitude reflection coefficients for the p and s polarizations. Indices i and r designate incident and reflected electric fields, respectively. In order to examine the amplitude and phase separately, we may rewrite Eqs. (2.39) and (2.40) as

$$\tilde{r}_p = r_p e^{i\delta_p}, \qquad \tilde{r}_s = r_s e^{i\delta_s}. \tag{2.41}$$

Notice that at normal incidence and in absence of a magnetic field ($\tilde{\epsilon}_{xy} = 0$), $\tilde{r}_p = \tilde{r}_s$, i.e. at normal incidence there is no difference between s and p-polarization.

So far, we dealt with the reflection of linearly polarized light on an isotropic surface. The Faraday effect and Kerr effect will be observed if the material is magnetized along the direction of propagation of the light. The complex Faraday effect ($\phi_F = \theta_F - i\epsilon_F$) results from different optical constants for RCP and LCP. Linearly polarized light incident on a medium may be written as a superposition of RCP and LCP waves of equal amplitude,

$$\vec{E} = \frac{E_0}{\sqrt{2}} \left\{ \hat{e}_+ \exp\left[i\left(\omega t - \frac{2\pi \tilde{n}_+ z}{\lambda_0} \right) \right] + \hat{e}_- \exp\left[i\left(\omega t - \frac{2\pi \tilde{n}_- z}{\lambda_0} \right) \right] \right\}, \tag{2.42}$$

or equivalently

$$\vec{E} = \frac{E_0}{\sqrt{2}} \exp\left[i\left(\omega t - \frac{2\pi\tilde{n}z}{\lambda_0}\right)\right]\left\{\hat{e}_x \cos\frac{\tilde{\Delta}}{2} + \hat{e}_y \sin\frac{\tilde{\Delta}}{2}\right\} \tag{2.43}$$

with the complex phase

$$\tilde{\Delta} = \frac{2\pi z(\tilde{n}_+ - \tilde{n}_-)}{\lambda_0}. \tag{2.44}$$

A wave which is linearly polarized at $z = 0$, will be elliptically polarized after propagating a distance l_0, with the major axis of the ellipse rotated by an angle

$$\theta_F = \mathrm{Re}\left[\frac{\tilde{\Delta}}{2}\right] = \mathrm{Re}\left[\frac{\pi l_0}{\lambda}(\tilde{n}_+ - \tilde{n}_-)\right] = \frac{\omega l_0}{2c}(n_+ - n_-), \tag{2.45}$$

and an ellipticity, defined as the ratio of the minor to the major axis of the ellipse

$$\begin{aligned} \epsilon_F &= -\tanh\left(\mathrm{Im}\left[\frac{\tilde{\Delta}}{2}\right]\right) = -\tanh\left(\mathrm{Im}\left[\frac{\pi l_0}{2\lambda}(\tilde{n}_+ - \tilde{n}_-)\right]\right) = \tanh\left(\frac{\omega l_0}{2c}(k_+ - k_-)\right) \\ &\approx \frac{\omega l_0}{2c}(k_+ - k_-). \end{aligned} \tag{2.46}$$

The Faraday rotation is due to the difference of the index of refraction for RCP and LCP, while the ellipticity originates from different absorption coefficients. In our experiment we observe a Faraday rotation when the light passes the optical windows of the cryostat (see Appendix C).

In the remainder of this chapter we will derive expressions that relate the polar Kerr effect to the Fresnel coefficients for RCP and LCP and to the optical conductivity tensor. Using Eqs. (2.32), (2.33), and (2.28) we can write the complex dielectric function for a right and left-circularly polarized wave as

$$\tilde{\epsilon}_\pm = \tilde{n}_\pm^2 = 1 - \frac{4\pi i}{\omega}\tilde{\sigma}_\pm \tag{2.47}$$

where $\tilde{\sigma}_\pm$ is

$$\tilde{\sigma}_\pm = \tilde{\sigma}_{xx} \mp i\tilde{\sigma}_{xy}. \tag{2.48}$$

The optical reflectivity for RCP and LCP at normal incidence ($\theta_0 = 0$) is obtained from the Fresnel equations given above. Furthermore, medium 0 will be air, i.e. $\tilde{n}_0 = 1$. We may then write the Fresnel reflection coefficients for RCP and LCP as

$$\tilde{r}_\pm = r_\pm \, e^{i\Delta_\pm} = \frac{n_\pm - ik_\pm - 1}{n_\pm - ik_\pm + 1}. \tag{2.49}$$

In the reflection configuration we distinguish between three different geometries for the Kerr effect, depending on the direction of $\vec{H}$ (or $\vec{M}$ in the case of ferromagnets) with respect to the plane of incidence and the wave vector $\vec{k}$. All three experiments are described by the same dielectric tensor $\tilde{\epsilon}_{ij}$.

However, only the polar Kerr effect, and a specific equatorial configuration, give a contribution that is linear in the magnetization[14]. In our experiment the complex magneto-optic Kerr effect,

$$\phi_K = \theta_K - i\epsilon_K, \tag{2.50}$$

is measured. In the polar configuration (Fig. 1.1) RCP and LCP are the eigenpolarizations for the magnetized surface. The MOKE can be expressed in terms of the Fresnel coefficients of Eq. (2.49),

$$\theta_K = -\frac{1}{2}(\Delta_+ - \Delta_-) \tag{2.51}$$

$$\epsilon_K = -\frac{r_+ - r_-}{r_+ + r_-}. \tag{2.52}$$

We are seeking a relation between ϕ_K and the optical conductivity. For Kerr angles up to several degrees we can make the following approximations:

$$\sin(\Delta_+ - \Delta_-) \approx \Delta_+ - \Delta_-, \tag{2.53}$$

$$\cos(\Delta_+ - \Delta_-) \approx 1, \tag{2.54}$$

$$(r_+ - r_-)^2 \ll 2r_+r_-, \tag{2.55}$$

which lead to an approximation for the complex Kerr effect,

$$\phi_K = -\frac{\tilde{r}_+ - \tilde{r}_-}{\tilde{r}_+ + \tilde{r}_-}. \tag{2.56}$$

When we substitute the Fresnel coefficients (2.49) and use Eqs. (2.47) and (2.48) we find

$$\phi_K = -\frac{\tilde{\sigma}_{xy}}{\tilde{\sigma}_{xx}\sqrt{1 + \frac{4\pi i}{\omega}\tilde{\sigma}_{xx}}}, \tag{2.57}$$

which relates the MOKE to the optical conductivity tensor. This can be solved to obtain the Kerr rotation and ellipticity in terms of the optical constants and the off-diagonal components of the optical conductivity tensor,

$$\theta_K = \frac{4\pi}{\omega}\frac{B\sigma_{1xy} + A\sigma_{2xy}}{A^2 + B^2}, \tag{2.58}$$

$$\epsilon_K = \frac{4\pi}{\omega}\frac{A\sigma_{1xy} - B\sigma_{2xy}}{A^2 + B^2}, \tag{2.59}$$

$$\tag{2.60}$$

where we used the approximation $\tilde{n} \approx (\tilde{n}_+ + \tilde{n}_-)/2$. The coefficients A and B are functions of the diagonal optical conductivity (or the complex index of refraction $\tilde{n}$),

$$A = \frac{4\pi}{\omega}(n\sigma_{2xx} - k\sigma_{1xx}) = n^3 - 3nk^2 - n, \tag{2.61}$$

$$B = \frac{4\pi}{\omega}(n\sigma_{1xx} + k\sigma_{2xx}) = -k^3 + 3n^2k - k. \tag{2.62}$$

The coefficients A and B are non-trivial functions of n and k. It is therefore necessary to measure all four quantities, i.e. (n,k) and (θ_K,ϵ_K), to determine $\tilde{\sigma}_{xy}$. In order to compare our experimental results with theoretical predictions we will need to calculate the off-diagonal conductivity in terms of the four experimental quantities:

$$\sigma_{1xy} = \frac{\omega}{4\pi}(B\theta_K + A\epsilon_K) \tag{2.63}$$

$$\sigma_{2xy} = \frac{\omega}{4\pi}(A\theta_K - B\epsilon_K). \tag{2.64}$$

2.4 Dispersion relations

It follows from the conservation of energy and the principle of causality that $\tilde{\sigma}_{ij}(\omega)$ must be an analytical function in the upper half complex plane. This leads to dispersion relations between the real and imaginary part of $\tilde{\sigma}_{ij}$. With the definition (2.30) we obtain the dispersion relations

$$\sigma_{1ij}(\omega) = -\frac{2}{\pi}\mathcal{P}\int_0^\infty \frac{\omega'\sigma_{2ij}(\omega')}{\omega'^2-\omega^2}\,d\omega', \tag{2.65}$$

$$\sigma_{1ij}(\omega) = \frac{2\omega}{\pi}\mathcal{P}\int_0^\infty \frac{\sigma_{1ij}(\omega')}{\omega'^2-\omega^2}\,d\omega', \tag{2.66}$$

where $\mathcal{P}$ is the principal value of the integral. These equations are referred to as Kramers-Kronig relations and the concept is applicable to any linear response function of a medium to an external field. Equivalent expressions can be found for the dielectric function $\tilde{\epsilon}_{ij}$[22]. In the limit of small magneto-optical effects we can derive similar expressions relating the Kerr rotation and ellipticity[23, 24],

$$\tanh^{-1}(\tan\epsilon_K(\omega)) = -\frac{2\omega}{\pi}\mathcal{P}\int_0^\infty \frac{\theta_K(\omega')}{\omega'^2-\omega^2}\,d\omega' \tag{2.67}$$

$$\theta_K(\omega) = \frac{2}{\pi}\mathcal{P}\int_0^\infty \frac{\tanh^{-1}(\tan\epsilon_K(\omega))}{\omega'^2-\omega^2}\,d\omega'. \tag{2.68}$$

The relations are consequences of strict causality and no special assumptions were made.

3 MICROSCOPIC MODEL FOR THE OPTICAL RESPONSE

3.1 The classical approach - Drude behavior and Lorentz model

According to Eq. (2.57) free carriers can contribute to the Kerr effect through both components of the optical conductivity tensor, $\tilde{\sigma}_{xx}$ and $\tilde{\sigma}_{xy}$. We will derive the optical conductivity $\tilde{\sigma}_{xx}$ from the free electron approximation. It will be our goal to calculate the current induced in a metal by an incident electro-magnetic plane wave, given by Eq. (2.1). The Lorentz force,

$$\vec{F} = e\vec{E} + \frac{e}{c}\vec{v} \times \vec{B}, \tag{3.1}$$

is acting on the charges moving in the radiation field. Since typically for an electron in a metal $v \ll c$, we can neglect the term originating from the magnetic field. Assuming a frictional term, represented by a relaxation time, τ, we may then write the equation of motion per electron as

$$\frac{d\vec{p}}{dt} = -\frac{\vec{p}}{\tau} - e\vec{E}, \tag{3.2}$$

where $\vec{p}$ is the electron momentum. The steady state solution to this equation leads to a conductivity that depends on frequency,

$$\tilde{\sigma}(\omega) = \frac{\sigma_0}{1 - i\omega\tau}. \tag{3.3}$$

This is the Drude conductivity which reduces to the dc conductivity, $\sigma_0 = ne^2\tau/m$, at zero frequency. From Eq. (2.28) we obtain the intraband dielectric function

$$\tilde{\epsilon}_{xx}^{intra} = 1 - \frac{\omega_p^2}{\omega^2 + i\omega\gamma}, \tag{3.4}$$

where the scattering frequency $\gamma = \tau^{-1}$ and

$$\omega_p = \sqrt{\frac{4\pi ne^2}{m^*}} \tag{3.5}$$

is the unscreened plasma frequency. n stands for the free carrier density and m^* for their effective mass. This model can be extended to include interband transitions, which are treated in the harmonic approximation. One starts from an equation of motion similar to that for free carriers (Eq. (3.2)).

We add a term $\omega_0^2\vec{r}$ which describes a harmonically bound charge, ω_0 being the eigenfrequency of the system,

$$m\left(\frac{d^2\vec{r}}{dt^2}+\gamma\frac{d\vec{r}}{dt}+\omega_0^2\vec{r}\right)=e\vec{E}. \tag{3.6}$$

In general, there is more than one electron per atom contributing to the absorption. If N is the electron density and f_k the fraction of electrons with eigenfrequency ω_k, we may write the interband dielectric function as

$$\tilde{\epsilon}_{xx}^{inter}=1+\frac{4\pi Ne^2}{m}\sum_k\frac{f_k}{\omega_k^2-\omega^2-i\gamma\omega}. \tag{3.7}$$

f_k is called an oscillator strength and we will justify this terminology in Section 3.2 when we derive the quantum mechanical expression for the optical conductivity. In the case of $\omega_k=0$, Eq. (3.7) reduces to the intraband dielectric function.

We now take a look at the free carrier contribution to $\tilde{\sigma}_{xy}$ in diamagnetic and paramagnetic materials. The classical Drude theory is more adequate to describe the magneto-optical response of free carriers. We start from an equation of motion similar to Eq. (3.6), but we take the full expression for the Lorentz force (3.1) and set $\omega_0=0$, i.e. we treat free electrons. We will need to solve

$$m\left(\frac{d^2\vec{r}}{dt^2}+\gamma\frac{d\vec{r}}{dt}\right)=e\vec{E}+\frac{e}{c}\frac{d\vec{r}}{dt}\times\vec{B}, \tag{3.8}$$

Entering this equation of motion with an Ansatz

$$\vec{r}_\pm(t)=r_\pm\hat{e}_\pm e^{i(\omega t-\vec{k}\cdot\vec{r})} \tag{3.9}$$

and an electric field of the form (2.1), we obtain the dielectric function for the states of right and left-circular polarization

$$\tilde{\epsilon}_\pm=1+\frac{4\pi Ne}{E_\pm}r_\pm=1+\frac{\omega_p^2}{\omega(-\omega+i\gamma\pm\omega_c)}, \tag{3.10}$$

where ω_p is the plasma frequency we already found earlier and $\omega_c=eB/m^*c$ is the cyclotron frequency. Equation (3.10) shows that the dielectric constants for RCP and LCP are different. This is observed as a splitting of the plasma edge in paramagnetic materials, which can lead to relatively large Kerr rotations of several 10^{-3} degrees, as observed by Schnatterly[25] on paramagnetic silver.

In ferromagnetic metals the conduction electrons can also contribute to the off-diagonal conductivity and their effect might be orders of magnitudes larger than for paramagnetic metals. It was Hulme[26] who proposed that spin-orbit interaction is the driving force for large magneto-optic effects in ferromagnets. Spin-orbit interaction couples the momentum of an electron to its spin and thus allows the circularly polarized light wave to couple to the magnetization of the material. We will present the results of the skew scattering theory developed by Erskine and Stern[27] with the correction by Reim

et al.[28]. Intraband transitions contribute to the off-diagonal absorption, σ_{2xy}, with two different frequency dependencies, i.e. $\sigma_{2xy} \propto \omega^{-1}$ and $\sigma_{2xy} \propto \omega^{-3}$. Erskine and Stern[27] consider the response of free carriers to an electric field of the form $E_0\delta(t)\hat{x}$. Using the relaxation-time approximation,

$$-\frac{d\vec{k}}{dt} = \frac{\vec{k}}{\tau} + \frac{\vec{s}\times\vec{k}}{\tau_s} \tag{3.11}$$

where the right-hand side contains a normal scattering lifetime τ and a skew scattering lifetime τ_s, which accounts for spin-orbit asymmetric scattering in ferromagnetic metals[29], the off-diagonal optical conductivity is given by

$$\tilde{\sigma}_{xy} = \frac{\omega_p^2}{4\pi}\langle\sigma_z\rangle\left\{\frac{\Omega}{(\omega-i\gamma)^2-\Omega^2} + \frac{|\vec{P}_0|}{ev_F}\left(1-\frac{\omega(\omega-i\gamma)}{(\omega-i\gamma)^2-\Omega^2)}\right)\right\}, \tag{3.12}$$

where ω_p is the unscreened plasma frequency, $\Omega = \tau_s^{-1}$ is the skew scattering frequency, v_F is the Fermi velocity, and $|\vec{P}_0|$ is the maximum electric dipole moment per unit cell. The off-diagonal conductivity is proportional to the net spin polarization

$$\langle\sigma_z\rangle = \frac{n_\uparrow - n_\downarrow}{n_\uparrow + n_\downarrow}. \tag{3.13}$$

If we identify $\langle\sigma_z\rangle\Omega$ with the cyclotron frequency ω_c, the first term in Eq. (3.12) is formally identical with our result obtained from the Drude model for diamagnetic and paramagnetic materials, i.e. for $\omega \gg \Omega, \gamma$, σ_{2xy} shows the same ω^{-3} frequency dependence. In the same high frequency limit the second term in Eq. (3.12) is proportional to ω^{-1} and represents the only term previously considered to interpret magneto-optical data[27, 30, 31].

3.2 Quantum mechanical derivation

In this section we will derive the optical conductivity from the quantum mechanical point of view. We start with the unperturbed one-electron Hamiltonian

$$H_0 = \frac{\vec{p}^{\,2}}{2m} + V(\vec{r}). \tag{3.14}$$

To describe the response of a charge carrier to an electromagnetic field, we introduce the vector potential $\vec{A}(\vec{r},t)$ and the scalar potential $\phi(\vec{r},t)$. For convenience we choose the Coulomb gauge, in which

$$\phi = 0 \qquad \nabla\cdot\vec{A} = 0. \tag{3.15}$$

We may describe the motion of a charge $-e$ in an external field by replacing the electron momentum operator

$$\vec{p} \rightarrow \vec{p} + \frac{e}{c}\vec{A}. \tag{3.16}$$

Substituting this into the unperturbed Hamiltonian and using the operator definition of $\vec{p}$ we can expand the first term of H_0. Neglecting terms quadratic in $\vec{A}$ we can approximate the Hamilton operator by

$$H = H_0 + \frac{e}{mc}\vec{A}\cdot\vec{p} = H_0 + H_I, \tag{3.17}$$

where H_I is referred to as the electron-radiation interaction Hamiltonian. In the limit of small wave vectors $\vec{k}$ we may approximate H_I by

$$H_I = -e\vec{r}\cdot\vec{E}, \tag{3.18}$$

which is the more commonly used expression, also known as the electric dipole approximation. We will not include higher order terms (magnetic dipole, electric quadrupole, etc.) The electric dipole transition probability, $\Gamma_{\alpha\beta}$, for photon absorption per unit time is obtained from Fermi's Golden Rule,

$$\Gamma_{\alpha\beta} = \frac{2\pi}{\hbar}\left(\frac{e}{m\omega}\right)\left|\frac{E(\omega)}{2}\right|^2 \sum_{\vec{k}} |P_{\alpha\beta}|^2 \delta(E_\beta(\vec{k}) - E_\alpha(\vec{k}) - \hbar\omega). \tag{3.19}$$

$|\alpha\rangle$ and $|\beta\rangle$ are the occupied initial and empty final states of the transition, respectively. $E(\omega)$ is the amplitude of the radiation field and E_α, E_β are the energies of the initial and final states, respectively. $P_{\alpha\beta}$ is the dipole matrix element,

$$|P_{\alpha\beta}|^2 = |\langle\beta\,|H_I|\,\alpha\rangle|^2\,. \tag{3.20}$$

The power loss function is simply the transition probability per unit volume multiplied by the energy of the photon. This power loss can also be expressed in terms of the imaginary part of the dielectric function, ϵ_{2xx}, thus creating the link between microscopic theory and macroscopic phenomena,

$$\hbar\omega\ \Gamma_{\alpha\beta} = \frac{\omega|E(\omega)|^2}{8\pi}\ \epsilon_{2xx}. \tag{3.21}$$

We are now able to write the dielectric function in terms of matrix elements,

$$\epsilon_{2xx} = \left(\frac{2\pi e^2}{m\omega}\right)^2 \sum_{\vec{k}} |P_{\alpha\beta}|^2\ \delta(E_\beta(\vec{k}) - E_\alpha(\vec{k}) - \hbar\omega). \tag{3.22}$$

Using the Kramers-Kronig relations (Eqs. (2.65) and (2.66)) we obtain ϵ_{1xx},

$$\epsilon_{1xx} = 1 + \frac{4\pi e^2}{m} \sum_{\vec{k}} \frac{2}{m\hbar\omega_{\beta\alpha}}\ \frac{|P_{\alpha\beta}|^2}{\omega_{\beta\alpha}^2 - \omega^2}, \tag{3.23}$$

where $\hbar\omega_{\beta\alpha} = E_\beta(\vec{k}) - E_\alpha(\vec{k})$. Equation (3.23) represents the sharp limit, i.e. the life time of the excited state is infinite or the broadening (damping) term is zero, $\gamma = 0$. When we compare this expression to the result obtained from the Lorentz model (Eq. (3.7)) we find that

$$N f_k = \frac{2|P_{\alpha\beta}|^2}{m\hbar\omega_{\beta\alpha}}. \tag{3.24}$$

Nf_k is essentially the number of oscillators with frequency $\omega_{\beta\alpha}$. Since f_k is proportional to the transition matrix element it is called the oscillator strength of the optical transition.

We now want to focus on the absorptive part of the off-diagonal conductivity, σ_{2xy}. Since the contribution of spin flip transitions is negligible[11] we may write σ_{2xy} as the sum of contributions from spin-up ($\uparrow$) and spin-down ($\downarrow$) states,

$$\sigma_{2xy}(\omega) = \sigma_{2xy\uparrow}(\omega) + \sigma_{2xy\downarrow}(\omega). \tag{3.25}$$

The contributions from spin-up states is given by[17]

$$\sigma_{2xy\uparrow}(\omega) = \frac{\pi e^2}{4\hbar\omega m^2 V} \sum_{\alpha\beta} \left\{ \left|\langle\beta\uparrow|\vec{\pi}^+|\alpha\uparrow\rangle\right|^2 - \left|\langle\beta\uparrow|\vec{\pi}^-|\alpha\uparrow\rangle\right|^2 \right\} \delta(\omega_{\alpha\beta\uparrow} - \omega), \tag{3.26}$$

where the operators

$$\vec{\pi}^{\pm} = \vec{\pi}_x \pm i\vec{\pi}_y \tag{3.27}$$

are linear combinations of the kinetic momentum operator

$$\vec{\pi} = \vec{p} + \frac{\hbar}{4mc^2}\hat{\sigma} \times \vec{\nabla}V(r), \tag{3.28}$$

$\vec{p}$ being the canonical momentum operator and $\hat{\sigma} \times \nabla V(r)$ represents the spin-orbit term. In principle, this spin-orbit contribution could couple spin-up to spin-down states that would have to be included in Eq. (3.25). However, this spin-flip contribution is of second order in the spin-orbit interaction and is negligible compared to contributions conserving spin[11]. The contribution from spin-down states is formally identical to Eq. (3.26), but with spin-up states replaced by spin-down ones. Multiplying Eq. (3.26) by ω and replacing the sum over all states by an integral we obtain

$$\omega\sigma_{2xy} = \frac{\pi e^2}{4\hbar m^2} \frac{1}{(2\pi)^3} \int F_{\alpha\beta}(\omega)\delta(\omega_{\beta\alpha} - \omega)\, d\vec{k} \tag{3.29}$$

where

$$F_{\alpha\beta}(\omega) = \left|\langle\beta\uparrow|\vec{\pi}^+|\alpha\uparrow\rangle\right|^2 - \left|\langle\beta\uparrow|\vec{\pi}^-|\alpha\uparrow\rangle\right|^2 + \left|\langle\beta\downarrow|\vec{\pi}^+|\alpha\downarrow\rangle\right|^2 - \left|\langle\beta\downarrow|\vec{\pi}^-|\alpha\downarrow\rangle\right|^2. \tag{3.30}$$

Optical and magneto-optical spectra of metals contain contributions from intraband and interband transitions. In principle, Eq. (3.26) accounts for both effects. However, intraband effects can be more easily dealt with in the classical model described earlier.

3.3 Band structure calculations

Our *ab initio* band structure program is based on the local density approximation (LDA) and the tight-binding linear muffin-tin orbital method in the atomic sphere approximation (TB-LMTO-ASA)[32,

33, 34, 35]. For all band structure calculations the TB-LMTO-ASA program Version 47, developed by O.K. Andersen's group[33] was used as a starting point. Version 47 allows spin-polarized calculations. The energy bands were calculated using the LMTO technique and included the combined correction terms to the ASA[32]. The density of states (DOS) was obtained using the analytical tetrahedron method[36] with at least 2000 k-points. The self-consistent potential was calculated in the frozen core approximation and the local-spin-density approximation (LSDA) was employed for the exchange and correlation potential with the von Barth-Hedin parametrization[37]. Relativistic effects (i.e. mass velocity, Darwin shift) are included in Version 47, but spin-orbit coupling is neglected. Since magneto-optic effects are due to spin-orbit splitting, an Ames-Lab-modified version (internally called 48), which includes spin-orbit coupling, was used in most cases. In order to determine the optical conductivity we made use of an older version (Version 41) of the same program, for which there is an optical package available. This package allows us to calculate the optical conductivity. Differences between the older Version 41 and the new Version 48 are minor (e.g. convergence with Version 48 is much improved, the control file is more user friendly, etc.) and are not important for the final results. Further instructions on the program can be obtained on-line[1] or directly from Andersen's group, which has been developing the code at Max-Planck Institut für Festkörperforschung in Stuttgart, Germany.

It was found helpful to start from a non-magnetic calculation using Version 48, but excluding spin-orbit coupling. After convergence was achieved we performed a calculation for the magnetic case, where the ions carry a moment. As a starting value for the spin moments (which are the difference in the number of spin-up and spin-down electrons in a particular orbital channel) we used the results obtained by neutron diffraction or X-ray magnetic circular dichroism (XMCD), which allow orbital decomposition of the moment. However, this is not crucial to the calculation, in that it only leads to faster convergence. For most structures investigated a rough estimate of the moments will also lead to convergence after a few iterations.

A typical *stripped* control file for the TB-LMTO program is shown below. We will shortly describe the important aspects of this input file which sets the starting point for our self-consistency cycle.

```
HEADER  Gd (HCP)      2 ATOMS   spd3.5
VERS    LMASA-41
IO      SHOW=F HELP=F  VERBOS=30  WKP=F IACTIV=F
OPTIONS NSPIN=2 REL=T CCOR=T  NRMIX=2 ADNF=T LMH=F  BEGATOM=T
        Q=  NITATOM=10
SYMGRP  I R6Z MX
BZ      NKABC=16 16 12 METAL=T TETRA=T NPTS=900 SAVDOS=F
STR     RMAXS=3.0 NOCALC=F
STRUC   NBAS=2  NCLASS=1  NL=5
```

[1] Currently at *http://www.mpi-stuttgart.mpg.de/docs/ANDERSEN*

```
        ALAT=6.873345936
        PLAT=  0.8660254 -0.5   0.0
               0.0        1.0   0.0
               0.0        0.0   1.622
CLASS ATOM=Gd  Z=64 R=3.751 LMX=4 CONF=6 6 5 4 5 IDXDN=1 1 1 1 1
SITE  ATOM=Gd  POS=  0.00000     0.000000    0.000000
      ATOM=Gd  POS=  0.57735027  0.000000    0.811000
DOS    NOPTS=1000 EMIN=-1. EMAX=1.
START  NIT=199 BROY=F WC=-1. NMIX=2 BETA=0.10 CNVG=1.D-5 CNVGET=1.D-5
        BEGMOM=T
        CNTROL=F
          ATOM=Gd  P=6.65 6.45 5.90 4.92 5.10  6.65 6.45 5.70 4.42 5.10
          Q=0.38 0.0 0.0  0.19 0.0 0.0  0.59 0.0 0.0  0.17 0.0 0.0
            0.1 0.0 0.0
            0.39 0.0 0.0  0.31 0.0 0.0  0.98 0.0 0.0  6.98 0.0 0.0
            0.1 0.0 0.0
HARTREE XO=0. 0. 0.
BOUND=1. 0. 0.   0. 1. 0.
TEXT
```

This control file was used to calculate the optical conductivity of Gd. We need to take a close look at the token **CLASS** where we *define* the electronic configuration of the ions, i.e. for Gd we included $6s$, $6p$, $5d$, $4f$, and $5g$ orbitals in the calculation. All lower orbitals are treated as core states and do not contribute to the optical conductivity. It is important to note that although the Gd-$5g$ orbitals are not necessary to obtain a self-consistent electronic structure, they are very important for the calculation of the optical properties of this material. From a mere look at the band structure or the density of states, a calculation without $5g$ states can hardly be distinguished from one including $5g$ states. However, there is a large change in the optical conductivity due to $4f \rightarrow 5g$ transitions as shown in Fig. 3.1. In general one should always extend the basis by one more orbital in the optical calculation than were used for the band structure calculation, in order to include transitions from occupied states below to empty states above the Fermi level. This becomes even more striking in the case of $CeAl_2$ (see Chapter 5), where we have to include higher orbitals for the Al site although they are clearly not occupied and their positions are far above the Fermi level.

The token **START Q=** contains the first three moments of the charge for down-spin and up-spin for each orbital channel. For example, we estimate 0.38 electrons for the minority spin s-band and 0.39 for the corresponding spin-up band. These were the converged charges obtained from an earlier calculation using Version 48. The second and third moments are set to zero at the beginning. Gd has a half-filled shell. This is seen in the charge distribution for the $l = 3$ channel where we estimate 6.98 and 0.17 electrons for the spin-up and spin-down bands, respectively, giving a $4f$ derived spin magnetic moment of $\mu_{4f} = (6.98 - 0.17)\mu_B = 6.82\mu_B$. The orbital moment is not calculated in Version 48. Using Version 41 the orbital magnetic moment is calculated for each iteration and one needs to check the output for

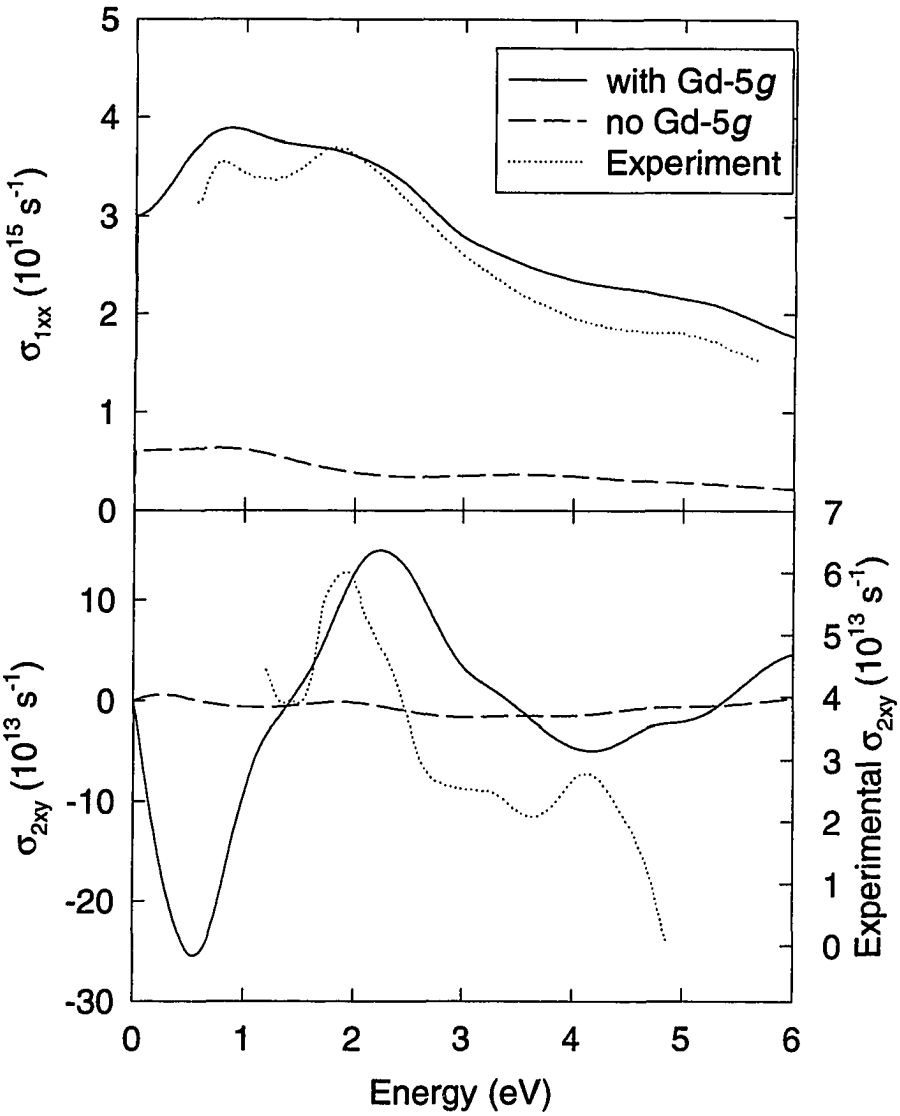

Figure 3.1 Effect of $5g$ states on the optical conductivity of Gd metal obtained from a relativistic band structure calculation including spin-orbit coupling. A lifetime broadening of 0.3 eV was used in the calculated spectra. Upper panel shows the absorptive part of the diagonal component σ_{1xx} and the lower panel shows that of the off-diagonal component σ_{2xy}. The dotted curves show experimental values as obtained by Erskine and Stern. Note the different scales for σ_{2xy}.

detailed information.

In order to check the results of our optical calculation we started with Ni, which has been discussed in detail[38, 39, 40], and Gd metal[27, 30, 41, 42]. Wang and Callaway[38] showed that band structure calculations describe the optical response (diagonal and off-diagonal conductivity) of elemental Ni rather well. We found excellent agreement of our calculation and earlier results, as well as experiment[38, 39, 40]. In general, this is true for all d compounds with rather wide bands (of the order of 2 eV or more; see Ref. [43] and references therein), or even $4f$ compounds in which the localized $4f$ bands are far away from the Fermi energy, e.g. $LuFe_2$[44, 45]. For Gd metal the diagonal optical conductivity agrees well with the experimental data of Erskine and Stern[27]. As shown in the upper panel of Fig. 3.1 the peak positions and magnitudes are reproduced rather well. The off-diagonal part of the optical conductivity obtained from our LDA calculation does not agree qualitatively with data shown in Ref. [27]. Experiment shows that σ_{2xy} is positive between 1 and 5 eV whereas LDA predicts a change in sign at 1.3, 3.5, and 5.2 eV. Furthermore, experiments gave a smaller magnitude for σ_{2xy} , our LDA result being about a factor of 2-3 larger. This disagreement is due to the inappropriate approximation made in the LDA. Local density theory is not capable of treating localized states, which form narrow bands. Especially the position of the $4f$ bands cannot be predicted. This is due to many body effects which are not taken into account in one-electron LDA theory. There are two major contributions that we would like to point out. First, there is a strong on-site Coulomb repulsion which the electrons in partially filled shells feel. This Coulomb repulsion has been included in band structure calculations as an additional term in the electron's energy, the so-called LDA+U method. Application of this method to elemental Gd and CeSb showed considerable improvement for the off-diagonal conductivity[46, 47, 42]. However, the method is cumbersome and a thorough analysis of the results obtained is necessary. The second effect is of excitonic origin. In optical experiments an electron absorbs energy from the incoming photon and is transferred to a higher band leaving behind a hole. There is a Coulomb attraction between the electron and the hole which is not included in our calculation.

Optical transition frequencies are determined by the one-electron excitation spectrum which is obtained form the ground-state band structure including the energy dependence of the self-energy. In an empirical approach one includes this self-energy correction in the calculation of the optical conductivity. Based on the work of Sham and Kohn[48], Janak *et al.*[49] made some simplifying approximations that led to an energy shift that is proportional to the energy of a band with respect to the Fermi level. The corrected energy is given by

$$E'_n(\vec{k}) = E_n(\vec{k}) + \lambda[E_n(\vec{k}) - E_F]. \tag{3.31}$$

This is equivalent to a modified exchange potential. This potential differs from the ground-state exchange-correlation potential by a term that is energy dependent but independent of position. Thus, there is no change in the one-electron wave functions, and, in particular, there is no change in the matrix elements when calculating the optical conductivity. Inserting the corrected band energies (3.31) into the equation that determines the optical conductivity, $\tilde{\sigma}$, we find the self-energy corrected conductivity

$$\tilde{\sigma}'(E) = \frac{1}{(1+\lambda)^2}\,\tilde{\sigma}\left(\frac{E}{1+\lambda}\right). \tag{3.32}$$

It should be noted that for this corrected conductivity the sum rule is not conserved. It is also important to note that the approximation made in Eq. (3.31) is strictly valid only in the vicinity of E_F, i.e. for bands within about 10 eV. Since the matrix elements are not influenced by the self-energy correction, we can evaluate the optical conductivity from the one-electron band structure and use Eq. (3.32) to account for the self-energy. This self-energy correction was applied to Cu[49], a large number of semiconductors[50], Cr[51], the $3d$ metals Fe, Co, and Ni[40], Pt_3Mn and Pt_3Co[43], and $LuFe_2$[44, 45]. Self-energy corrected spectra showed improved agreement with experiment in all cases.

In general the self-energy is complex. The real part describes a shift of the excited state quasiparticle energies, due to electron-hole and electron-electron interactions, as described above. The imaginary part represents a finite lifetime of the excited quasiparticle. This lifetime broadening will be included in our spectra by convolution of the optical conductivity, as obtained from the band structure calculation, and a Lorentzian with width equal to the imaginary part of the self-energy[52]. Calculations for Ni showed that lifetime broadening is proportional to E^2[53, 54]. However, since we will be dealing with a very limited spectral range a constant broadening will be assumed.

4 EXPERIMENTAL TECHNIQUES

Spectroscopic ellipsometry and Kerr spectroscopy can be used to fully determine the dielectric or conductivity tensor of a material. It is the purpose of this chapter to give a brief introduction into the experimental techniques. Sufficient background information will be provided to understand the principle of each experiment. Since neither system is commercially available, we will give detailed information on the mechanical, electronic, and optical components used. However, an in depth discussion of the experiment is beyond the scope of this work and we refer to the operation manuals available in our laboratory for more information. Additional details about the measurements can be found in the source code of the data acquisition programs.

Both experiments are designed for the near-infrared to near-ultraviolet spectral range, i.e. between about 1.35 and 5.5 eV (220 - 920 nm). The spectral range is limited by the detectors, polarizing prisms, monochromator gratings, and, in the case of the Kerr spectrometer, the modulator. This range can only be covered under optimum conditions, i.e. with high light intensities, as obtained with evaporated thin film samples. For polished samples the surface is microscopically not flat, and a surface roughness of the order of the finest abrasive, which is about 50 to 250 nm, leads to a considerable loss of intensity in the short wavelength range. Typically spectra are reliable between 1.4 and 5 eV.

4.1 Spectroscopic ellipsometry

4.1.1 The principle

Reflection ellipsometry is based on measurement of the state of polarization of a wave reflected from a surface, which yields the ratio $\tilde{\rho}$ of the complex Fresnel reflection coefficients for p and s-polarizations, as defined in Eqs. (2.39) and (2.40):

$$\tilde{\rho} = \frac{\tilde{r}_p}{\tilde{r}_s} = \tan\psi \, e^{i\Delta}, \tag{4.1}$$

where ψ and Δ are the conventional ellipsometric angles[55]. We will now consider the rotating analyzer ellipsometer (RAE) shown in Fig. 4.1. A similar design was presented by Aspnes and Studna[56].

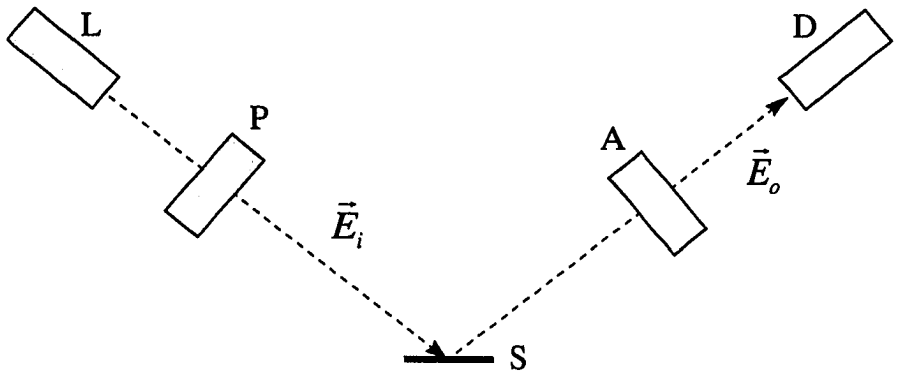

Figure 4.1 A rotating analyzer ellipsometer (RAE) consists of the light source L, polarizer P, sample S, analyzer A rotating with frequency ω, and detector D.

Linearly polarized light, with electric field vector $\vec{E}_i$ (Eq. (2.3) at an azimuth angle $\theta = P$), is reflected from an optically isotropic surface. The Jones matrix describing reflection is

$$S = \begin{pmatrix} \tilde{r}_p & 0 \\ 0 & \tilde{r}_s \end{pmatrix}. \tag{4.2}$$

When the incident wave is p (s) polarized, the reflected wave will also be p (s) polarized. For any other polarization state the reflected light will, in general, be elliptically polarized. This is an immediate consequence of the different Fresnel reflection coefficients for s and p-polarizations. The relative amplitude, as well as the phase between the two mutually perpendicular components of the incident light, will change upon reflection. The reflected light is then passed through another polarizing prism, which we refer to as analyzer, rotating at a mechanical frequency ω. Since we cannot distinguish between linearly polarized light with $\theta = \alpha$ and $\theta = \alpha + 180°$, this corresponds to a modulation of the optical signal with frequency 2ω. The Jones vector of the analyzer is given by Eq. (2.12) with $\theta = \omega t$:

$$A = \begin{pmatrix} \cos^2(\omega t) & \sin(\omega t)\cos(\omega t) \\ \sin(\omega t)\cos(\omega t) & \sin^2(\omega t) \end{pmatrix} \tag{4.3}$$

Using matrix algebra, we can now calculate the Jones vector of the light incident on the detector,

$$\vec{E}_o = A \cdot S \cdot \vec{E}_i. \tag{4.4}$$

For this sequence of elements we obtain the irradiance at the detector

$$I(t) = I_0 \left[1 + \alpha_2 \cos(2\omega t) + \beta_2 \sin(2\omega t)\right], \tag{4.5}$$

with the normalized Fourier coefficients

$$\alpha_2 = \frac{\tan^2\psi\cos^2 P - \sin^2 P}{\tan^2\psi\cos^2 P + \sin^2 P} \tag{4.6}$$

$$\beta_2 = \frac{2\tan\psi\cos\Delta\tan P}{\tan^2\psi + \tan^2 P}. \tag{4.7}$$

From the measured Fourier coefficients we can now determine ψ and Δ,

$$\tan\psi = \sqrt{\frac{1+\alpha_2}{1-\alpha_2}}\tan P \tag{4.8}$$

$$\cos\Delta = \frac{\beta_2}{\sqrt{1-\alpha_2^2}}\tan P, \tag{4.9}$$

where $0 \leq \psi \leq \pi/2$ and $-\pi < \Delta \leq \pi$. The uncertainty in the sign of Δ is a manifestation of the fact that, with a rotating analyzer ellipsometer, it is not possible to determine the handedness of the elliptical polarization. Finally, we determine the dielectric function from $\tilde{\rho}$,

$$\tilde{\epsilon}_{xx} = \left(\frac{1-\tilde{\rho}}{1+\tilde{\rho}}\right)^2 \tan^2\phi_0 \sin^2\phi_0 + \sin^2\phi_0. \tag{4.10}$$

So far we assumed an ideal system and ideal components. We have to take into account a misalignment of the polarizer and analyzer elements, i.e. the mechanical zero does not need to be at the same position as the optical zero. That means, we will have to replace $P \rightarrow P - P_S$ in Eqs. (4.6) and (4.7). The irradiance, Eq. (4.5), is converted to an electrical signal with an assumed linear detector, but the filtering necessary to reduce noise inevitably leads to a frequency-dependent gain and phase shift. The phase shift can be adjusted, by allowing for a phase factor in the analyzer position, i.e. $(2\omega t) \rightarrow (2\omega t + A_S)$. An additional parameter η^{-1} is required, which represents the attenuation of the ac component at 2ω with respect to the dc component. P_S, A_S, and η are obtained from a calibration of the instrument. Calibration procedures for the rotating analyzer ellipsometer were first described by Meulen and Hien[57] and by Aspnes[58]. Both methods are similar, relying on the fact that a light wave reflected from the surface of an isotropic sample will be linearly polarized, if the incident wave is linearly polarized in the p or s-direction. In these methods, calibration is performed in the polarizer-sample-analyzer (PSA) configuration using a sample mounted and aligned for normal measurement. Depending on the sample properties, i.e. the absorption at the calibration energy, we may chose between a residue calibration, a phase calibration, or a regression calibration (for more detailed information see Refs. [56, 58, 59, 60]). Thus, when an actual measurement is performed at a known polarizer angle (typically chosen for optimum precision), leading to a single pair of Fourier coefficients (α', β'), knowledge of η and A_S from the calibration allows one to deduce the corrected coefficients (α, β) of Eqs. (4.8) and (4.9):

$$\alpha_2 = \eta\left[\alpha_2'\cos(2A_S) + \beta_2'\sin(2A_S)\right] \tag{4.11}$$

$$\beta_2 = \eta[-\alpha_2' \sin(2A_S) + \beta_2' \cos(2A_S)]. \tag{4.12}$$

Then, using P_S, one can determine (ψ, Δ) from α_2 and β_2.

4.1.2 Experimental considerations

The experimental realization of the RAE used in our laboratory is shown in Fig. 4.2. The entire experiment is controlled through a personal computer. We will describe this in more detail at the end of this chapter. First we would like to give the specifications of the optical components used in this setup.

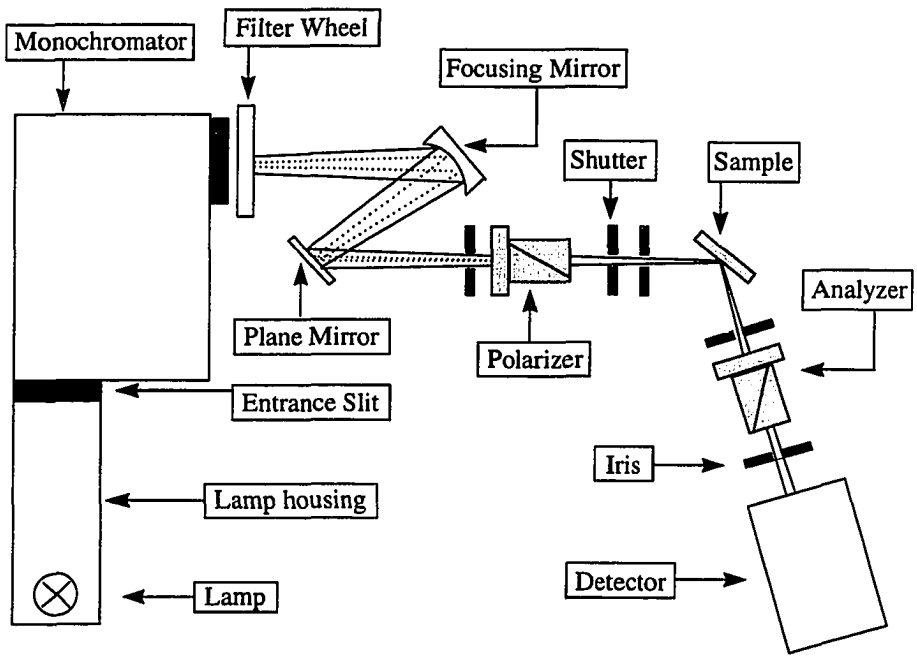

Figure 4.2 Experimental setup of a rotating analyzer ellipsometer.

The optical part of this experiment can be divided into three parts: generation of polarized light, interaction with the sample, and characterization of the polarization of the reflected light. The entire illumination system was designed by Photon Technology Inc. (PTI). The PTI LPS220/250 power supply can be used with xenon or tungsten lamps. The standard broad-band source for use in spectroscopic ellipsometry from the near-IR to the near-UV is a Xe lamp with a short arc for stability. The lamp is enclosed in a special PTI housing, which allows adjustment of the lamp with three set screws. A parabolic mirror focuses the light onto the entrance slit of a computer controlled PTI 102 double monochromator (1/4 m). Entrance and exit slits can be adjusted continuously to achieve the desired

resolution or light intensity. We usually operate the monochromator with a slit width of 2 mm, which gives a resolution of 4 nm. The monochromator disperses the light using two gratings with 1200 grooves/mm, blazed at 500 nm. Each of the two grating turrets can hold two gratings back-to-back and the optical range of the monochromator can easily be extended to the IR using the second grating, with 600 grooves/mm, blazed at 1600 nm. Due to the lamp holder the output of the monochromator is a bright ring with a dark center. A quartz diffuser is mounted at the focal point of the lamp, i.e. at the exit slit. Since scattered light and higher order reflections from the gratings are not blocked by the monochromator, additional filtering is necessary. An automated filter wheel is mounted onto the output slit of the monochromator. One of up to six filters can be selected using a special interface card. Currently we use RG850, RG630, OG515, WG345, and WG305 glass filters from Schott. One filter position is left blank, since for wavelengths below 360 nm there is no second order light (lamp output at 180 nm is negligible), and filtering is not necessary.

All mirrors used in this setup are UV enhanced aluminum mirrors, i.e. Al with MgF_2 coating. A spherical mirror focuses the output of the monochromator onto the sample. The apex angle of the light cone is about 1°. Several irises are used to block stray light. They also serve for easy alignment of the optical bench. A detailed description of the alignment procedure for this particular instrument was given in Ref. [61]. Before the light reaches the sample it is polarized by a Glan-Taylor-type calcite prism from Opto Sigma. The prism is mounted in a rotary stage, which is driven by a stepper motor with a resolution of 0.001°. The light incident on the sample is polarized at 30° with respect to the plane of incidence. The angle of incidence is kept constant at 70°. The sample can be aligned in the beam path with an adjustable sample holder. The reflected light passes through the analyzer, which is a Rochon quartz prism (CVI). The cutoff frequency of quartz is higher than that of calcite, thus providing higher light intensity near the high energy limit of our instrument. On the other hand, the Rochon prism is a birefringent polarizer, i.e. it separates the ordinary and extra-ordinary beam by about 3°, and only a fraction of the light that is reflected from the sample can be used for detection. Most of the light must be blocked with an iris in front of the analyzer, in order to achieve sufficient separation between the two beams at the detector. The analyzer prism is mounted in the hollow shaft of a dc motor, which is driven at a mechanical frequency of 45 to 50 Hz. The light then passes another iris in front of the detector, which blocks the deviated beam. A photomultiplier tube (PMT) or Si diode can be used as a detector.

Although we will not present IR data in this work, we were able to extend the spectral range to 0.57 eV, below which energy the calcite prisms absorb most of the light. As mentioned earlier, the

Xe light source is replaced by a W lamp. For IR measurements we use a single instead of the double monochromator, with a 600 lines/mm grating, blazed at 1600 nm. The polarizer remains unchanged. However, due to the long time constant of the PbS photoconductive cell, which is used as the detector, we need to replace the continuously rotating analyzer by a second rotary stage, which holds a Glan-Taylor polarizer. The light is then focused onto the PbS cell with a lens. Since the PbS detector is operated with a 40 to 60 V bias, the beam needs to be chopped. For optimum performance we set the chopping frequency to 400 to 500 Hz. The output from the PbS cell is fed into an EG&G lock-in amplifier, whose output is read by the same multimeter used in the near-IR to near-UV setup (see Fig. 4.3).

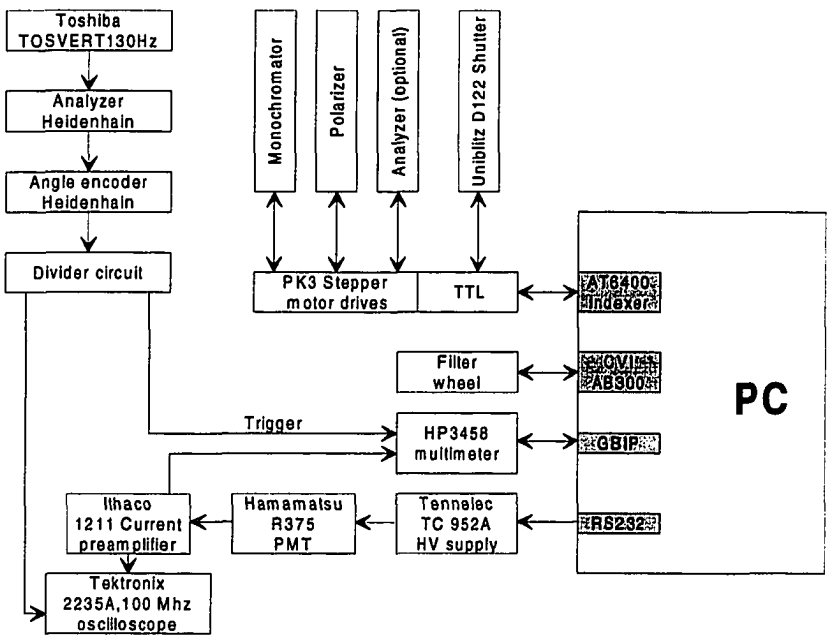

Figure 4.3 Schematic design of the rotating analyzer ellipsometer. Arrows indicate the direction of data transfer.

We now continue with the electronic components and briefly describe how they interact with the computer. Figure 4.3 is a diagram of the experiment. The computer communicates through four different interfaces with the other components. The Parker Daedal AT6400 indexer card controls up to four stepper motors, which are powered by Parker Daedal PK3 stepper motor drives. Additional digital I/O ports are available on the same board. One TTL channel is used to open and close a Uniblitz D122 shutter. The CVI AB300 filter wheel is a separate unit, controlled by its own interface card. The General Purpose Interface Bus (GPIB) reads data from the Hewlett Packard 3458 multimeter. No

other devices are attached to the GPIB. The Tennelec high voltage supply is controlled via the RS232 port of the PC. The anode current of the Hamamatsu R375 PMT is is fed into an Ithaco 1211 current preamplifier, which is set to a gain of 10^{-6} to 10^{-7} A/V. A time constant of 100 ms gives sufficient filtering without distortion of the signal (reduced amplitude, phase shift, etc.). During measurements the high voltage is adjusted to keep a constant 3 V dc signal.

A Toshiba TOSVERT130Hz linear inverter drives the dc motor of the analyzer (Heidenhain GmbH, Germany) at 45 to 55 Hz. The angle decoder, which is mounted onto the dc motor, gives 2048 pulses per revolution. A divider circuit decreases this number to 512 pulses per revolution. During each revolution the angle decoder sends one zero pulse, which is used as a calibration point. This zero pulse also triggers an oscilloscope, which serves for alignment of the sample. The HP multimeter has on-board memory. When a measurement is initiated by the computer, the multimeter takes one data point at each pulse it receives from the divider circuit until the total number of points requested it reached, at which time the entire data set is transferred to the PC. During a typical scan we take 147 cycles (memory limitation of the HP multimeter) with open shutter and 50 dark cycles, i.e. with the shutter closed. After taking the average of all open and all dark cycles, respectively, the dark current is subtracted. A Fast Fourier transform yields second harmonic Fourier coefficients, from which the optical constants of the sample can be determined (see the previous chapter). Large first and fourth order coefficients indicate insufficient alignment or nonlinearities of the detection system. Even for samples with poor surface quality the sum of the squared first order coefficients should be kept below $5 \cdot 10^{-4}$ and that of the fourth order coefficients below 10^{-5}.

4.2 Kerr spectroscopy

4.2.1 The intensity method

As shown in Fig. 4.4, the Kerr spectrometer consists of four basic parts: the polarizer, the sample, the modulator, and the analyzer. In contrast to the ellipsometer, described in the previous section, the MOKE can be measured without any *moving* parts, i.e. light modulation is achieved with a photoelastic modulator (PEM). A PEM is an oscillating quartz bar that is driven at its resonance frequency (50 kHz in our experiment). Due to stress, induced by the longitudinal oscillation, the phase velocities for light polarized along the two mutually perpendicular optical axes of the modulator are different. That means one component will experience a periodically modulated phase shift with respect to the other component. The transfer characteristic of a PEM is described by the Jones vector J_R in Eq. (2.13),

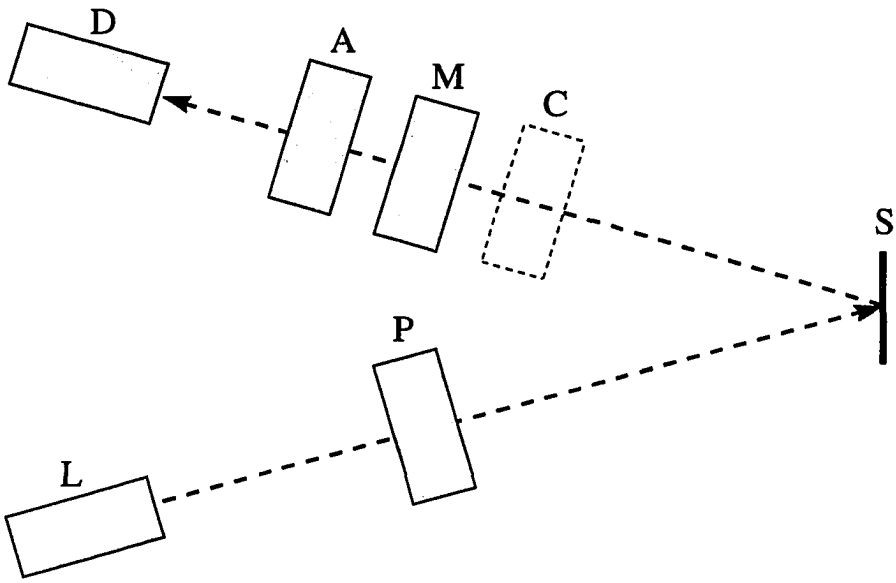

Figure 4.4 Magneto-optical Kerr spectrometer. L is the light source. The light passes a linear polarizer P before it is reflected on a magnetized sample S. The emerging light is modulated by a photoelastic modulator M and passes the analyzer A. The intensity of the emerging light is measured with the detector D. To measure the Kerr ellipticity with the compensation method a Soleil-Babinet compensator C is inserted into the beam (see Section 4.2.2).

with a sinusoidal phase retardation, $\delta = \delta_0 \sin(\omega t)$.

Since our experimental setup is different from that used earlier by Lee[44], and we are not aware of any report describing this configuration, we will present the most important steps to calculate the irradiance at the detector in more detail. For reasons that will become clear when we discuss the compensation method, we place the modulator after the sample, i.e. we employ the polarizer-sample-modulator-analyzer (PSMA) configuration, whereas all earlier measurements were performed in the PMSA setup described by Lee[44]. A similar configuration was used by van Engen *et al.*[3] and Reim *et al.*[62]. They used a Faraday cell instead of a PEM. A Faraday cell modulates the azimuth angle of the light. The Kerr rotation is then determined from the $1f$ component of the modulated signal.

In the PMSA configuration one is forced to use the reflection matrix of the magnetized sample

$$S = \begin{pmatrix} \tilde{r}_{ss} & -\tilde{r}_{sp} \\ \tilde{r}_{sp} & \tilde{r}_{pp} \end{pmatrix}. \tag{4.13}$$

Determination of the Kerr effect in the PSMA setup requires some approximations regarding the reflection coefficients for RCP and LCP[44]. As will be shown, we can obtain an exact solution for the

detected signal in the PSMA configuration. Linearly polarized light (Eq. (2.3) at an azimuth angle $\theta = \psi$) is reflected from a magnetized sample. Upon reflection the light is elliptically polarized with an ellipticity ϵ_K. The major axis of the polarization ellipse is rotated by the Kerr angle Θ_K. The Jones vector of the reflected light is therefore given by Eq. (2.8) with $\theta = \psi + \Theta_K$,

$$\vec{E}_S = E_0 \begin{pmatrix} \cos(\psi + \Theta_K)\cos\epsilon_K - i\sin(\psi + \Theta_K)\sin\epsilon_K \\ \sin(\psi + \Theta_K)\cos\epsilon_K + i\cos(\psi + \Theta_K)\sin\epsilon_K \end{pmatrix}. \tag{4.14}$$

The analyzer is kept at a fixed angle. Its Jones matrix, A, is given by Eq. (2.12) with $\theta = \phi$. Using matrix algebra we can write the light at the detector as a product of Jones matrices,

$$\vec{E}_o = A \cdot J_R \cdot \vec{E}_S. \tag{4.15}$$

We are then able to calculate the intensity of the detected light using Eq. (2.10). If we keep terms up to second order in the expansion of $e^{i\delta_0 \sin(\omega t)}$, the signal at the detector consists of a dc component and two ac components at ω and 2ω. Without loss of generality, we may set the analyzer angle to $\phi = 45°$, which greatly simplifies the result. With the amplitude of the radiation field $E_0 = 1$, the three components are given by

$$I_{dc} = \frac{1}{4}[1 + J_0(\delta_0)\cos(2\epsilon_K)\sin(2(\psi + \Theta_K))] \tag{4.16}$$

$$I_{1\omega} = -\frac{1}{2}J_1(\delta_0)\sin(2\epsilon_K) \tag{4.17}$$

$$I_{2\omega} = \frac{1}{2}J_2(\delta_0)\cos(2\epsilon_K)\sin(2(\psi + \Theta_K)), \tag{4.18}$$

where the J_i are i-th order Bessel functions. If we chose the amplitude of the modulation, δ_0, such that $J_0(\delta_0) = 0$, the dc component will be constant. For $\delta_0 = 2.41$ the 0-th order Bessel function vanishes and J_1 and J_2 are within 90% of their maximum values. We will use this retardation in all measurements.

Normalization of $I_{1\omega}$ and $I_{2\omega}$ with I_{dc} allows us to directly determine the Kerr ellipticity and rotation,

$$\epsilon_K = -\frac{1}{4AJ_1(\delta_0)}\frac{I_{1\omega}}{I_{dc}} \tag{4.19}$$

$$\Theta_K = \frac{1}{4BJ_2(\delta_0)}\frac{I_{2\omega}}{I_{dc}}, \tag{4.20}$$

where A and B are amplification constants which can be determined by a calibration procedure. These equations are valid for small angles (ϵ_K, Θ_K). We call this technique the intensity method since it determines the MOKE from the intensity of the dc and ac components of the signal. More detailed information on this method, including calibration procedures, can be found in Refs. [63, 64, 65, 66, 67, 68, 69, 70, 44]. However, the method fails for low light intensities, as was seen by Lee[44] for small

rare-earth-Fe_2 single crystals. False signals are also obtained when measurements are performed under a high magnetic field, which leads to a considerable background due to Faraday rotation in the cryostat windows. This becomes more pronounced at high photon energy, i.e. $E > 3.5$ eV (see Appendix C). We will therefore use a compensation method to measure the magneto-optic Kerr effect. Since this is an integral part of this thesis, we will briefly outline this technique.

4.2.2 The compensation method

According to Eq. (4.18) the 2ω-component of the signal vanishes for $\psi = -\Theta_K$. For $|\psi + \Theta_K| \ll 1$, $I_{2\omega}$ depends linearly on ψ. Since the polarizer is mounted in a computer-controlled rotary stage, we can measure $I_{2\omega}$ as a function of ψ. The intercept determined from a linear regression is $-\Theta_K$. Using the intensity method, the error increases with increasing $I_{2\omega}$. This problem obviously does not occur for the compensation method, since signals are always small and we are measuring in a range of high sensitivity. Compared to the intensity method, Kerr rotation and ellipticity cannot be determined simultaneously, which is the major drawback of this method. A second scan is required to obtain the ellipticity. However, in order to expedite the measurement, we may use the compensation method to determine the Kerr rotation accurately, and measure the ellipticity simultaneously using the intensity method. We see from Eq. (4.17) that $I_{1\omega}$ does not depend on the polarizer angle, and we can take $I_{1\omega}$ at any arbitrary setting of ψ. We adopted this *mixed* method for our measurements.

The Kerr ellipticity can also be measured by the compensation method. However, it requires a separate scan after the Kerr rotation has been determined. Assume Θ_K is known for the entire spectral range. A compensator is inserted in the beam path between the sample and the modulator, as indicated in Fig. 4.4. We compensate for the Kerr rotation by setting the polarizer to $\psi = -\Theta_K$. Thus the reflected light is elliptically polarized with the major axis of the ellipse along x. We start from Eq. (4.14) with $\psi = -\Theta_K$. The Jones vector of the reflected light is given by

$$\vec{E}_r = \begin{pmatrix} \cos\epsilon_K \\ i\sin\epsilon_K \end{pmatrix}, \tag{4.21}$$

where the amplitude of the radiation field is $E_0 = 1$. The compensator is aligned with its major axes along x and y, and adjusted to function as a quarter wave plate. The Jones matrix of the linear retarder (Eq. (2.13)) with $\delta = \pi/2$ is

$$J_C = \begin{pmatrix} 1 & 0 \\ 0 & i \end{pmatrix}. \tag{4.22}$$

After the light passed the compensator it is linearly polarized with an azimuth angle $-\epsilon_K$, i.e.

$$\vec{E}_C = J_C \cdot \vec{E}_r = \begin{pmatrix} \cos(-\epsilon_K) \\ \sin(-\epsilon_K) \end{pmatrix}. \tag{4.23}$$

We can then determine the irradiance at the detector, which is analogous to the calculation described earlier for the intensity method, the only difference being the polarization state of the light incident upon the modulator. Carrying out the matrix multiplications leads to a set of equations similar to Eqs. (4.16)–(4.18),

$$I_{dc} = \frac{1}{4}\left[1 - J_0(\delta_0)\sin(2(\epsilon_K - \psi))\right] \tag{4.24}$$

$$I_{1\omega} = 0 \tag{4.25}$$

$$I_{2\omega} = -\frac{1}{2}J_2(\delta_0)\sin(2(\epsilon_K - \psi)). \tag{4.26}$$

We are able to determine the ellipticity from the intercept of a plot of $I_{2\omega}$ versus ψ.

Since this technique is relatively new to our laboratory, we have not been able yet to obtain ellipticity data using the compensation method. However, the compensator was installed and most of the software has been written. The calibration procedures for the compensator should be working in near future (see Appendix A). Upgrade to the compensation method has led to improved results for the Kerr rotation data, i.e. smaller errors, extended spectral range, and higher magnetic field, and we expect a similar improvement for the ellipticity.

4.2.3 Experimental considerations

After introducing the compensation method in the previous section, we will now focus on the experimental realization of the Kerr spectrometer (Fig. 4.5). First we would like to describe the optical setup including the specifications of the components employed. In the second part of this section we will discuss the most important aspects concerning data acquisition and explain how the experiment is controlled.

Like the RAE described in Section 4.1, the Kerr spectrometer was designed for the near-IR to near-UV spectral range, i.e. for operation between 1.4 and 5.5 eV. The setup is shown in Fig. 4.5. The output of a Xe short arc lamp is focused onto the sample using a spherical mirror. All mirrors are Al base with MgF_2 coating for high reflectivity in the UV. The light is linearly polarized by a Glan-Taylor calcite prism (Opto Sigma), which is mounted in a rotary stage with 0.001° resolution. The measurement of the polar Kerr effect, as described in the previous sections, is performed near normal incidence, the angle of incidence being less than 4°. The reflected light is focused onto the entrance slit of a

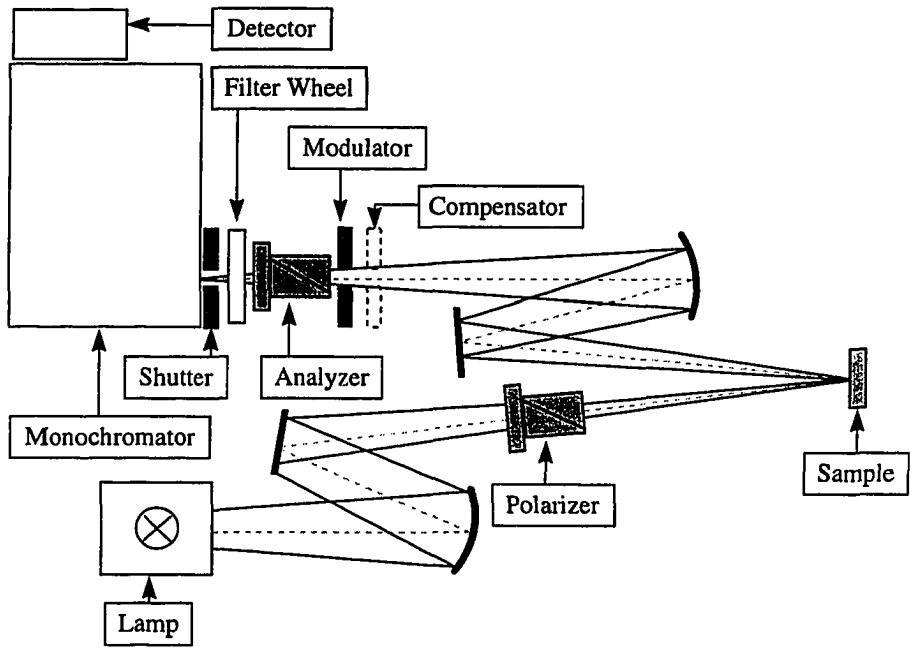

Figure 4.5 Experimental setup of a Kerr spectrometer.

CGA/McPherson monochromator. Light modulation is achieved using a Hinds PEM-80 photoelastic modulator (the alignment procedure is described in Appendix A). The analyzer, which is also a Glan-Taylor prism, is at a fixed angle ($\phi = 45°$ with respect to the optical axes of the modulator). In order to avoid higher order diffraction of the monochromator, a filter wheel is mounted in front of the entrance slit. According to the wavelength one of four filters is chosen. We use WG305, GG395, and GG495 glass filters from Schott and one UV interference filter (see Appendix E). The monochromator is calibrated for gratings with 1200 lines/mm. In order to enhance the performance at small wavelengths (i.e. high photon energy) a ruled grating, blazed at 250 nm, was installed. A PMT mounted onto the exit slit of the monochromator serves as the detector. We also indicate the position of the Soleil-Babinet compensator in Fig. 4.5. The compensator (Bernhard Halle Nachfl. GmbH, Germany) is made of quartz (full transmission above 230 nm) and has a 12 mm aperture. A stepper motor and limit switch were mounted to the shaft of the compensator and retardation can be controlled by the computer.

A split-coil superconducting magnet system from Cryomagnetics (CM), enclosed in an optical cryostat by Cryoindustries of America (CIA), can produce magnetic fields up to 7 T. We will discuss some of the problems regarding the optical access to the sample in Appendix C. It is our experience that this cryostat needs a lot of attention and special skills. The sample space, which is accessed from the top of the cryostat, is connected to the liquid He reservoir by a capillary. Helium flow is controlled with

a needle valve. Evacuating the sample space with a rotary pump allows one to cool the sample below 4.2 K. However, temperature stabilization can be a problem below 3.5 K. Using two pumps we were able to reach 2 K without accumulating liquid He in the sample space. Accurate temperature control is achieved using a Lakeshore DRC-91CA. The magnet can be operated manually or by the computer using the GPIB interface. The magnet and temperature control components are marked by a black background in Fig. 4.6. The CM CIM-16 unit is the interface between the GPIB and the actual magnet power supply. The CM IPS-100 power supply can deliver up to 100 A of magnet current, which can be reversed using the CM CRS-100 current reversing switch, i.e. we may reverse the magnetic field using the CRS-100. Using the GPIB option we are able to control the magnet and measure the Kerr rotation of a sample as a function of field.

The motion control part of our experiment is shown with a light gray background in Fig. 4.6. The monochromator receives TTL pulses from a Keithley Dascon-1 AD/DA board. Attempts to control the monochromator using one of eight TTL compatible programmable ports provided by the new Newport MM2000 Standard Interface Module, were not successful. The pulses generated by the MM2000-SIM were too long, and the monochromator cannot be moved at sufficient speed. However, we use one of the TTL ports to switch a solenoid shutter (directly) and a second port to rotate the filter wheel (via a stepper motor driver). The MM2000 motion control card provides up to four axes, which may be chosen as any combination of stepper motors and dc motors. We operate two Newport URM80ACC rotary stages, which are driven by dc motors with an encoder on the motor axis. One rotary stage is utilized to move the polarizer prism, thereby allowing 1) easy alignment of the polarizer and 2) measurement of the Kerr rotation using the compensation method. The second rotary stage can be used to adjust the analyzer or compensator. In future it is planned to mount the compensator on the rotary stage and keep the analyzer in a manually adjustable precision mount. The compensator can then be rotated about its optical axis. The retardation is set using a stepper motor which is powered by an external drive (Ramco Electronics).

The third part of our experiment deals with data acquisition and is indicated by a white background in Fig. 4.6. A Hamamatsu R562 PMT is the detector in our experiment. A voltage signal is obtained from a DL Instruments 1641 current preamplifier. Only the lowest setting (10^4 V/A) provides sufficient bandwidth for our experiment (600 kHz, compared to a modulation at 2f = 100 kHz). High voltage is supplied by a Stanford Research PS325, whose output, between 0 and 1500 V, is set by a 0 to 6 V input. The Stanford SR510 analog lock-in detector is connected to the RS232 interface of the PC. It offers two analog outputs (0-10 V), one of which sets the high voltage. Through the other output we

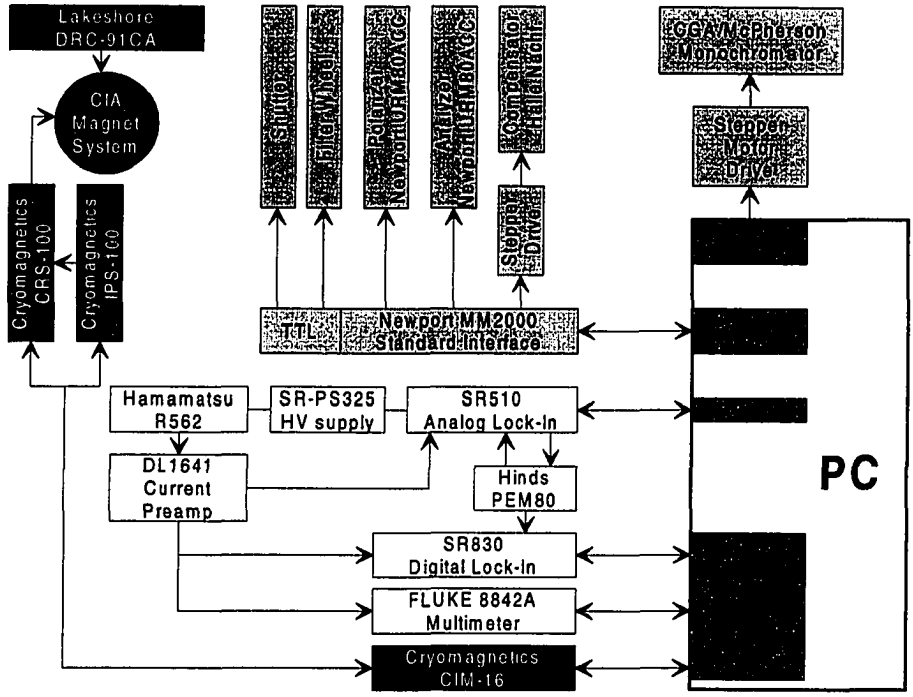

Figure 4.6 Schematic design of the Kerr spectrometer. Arrows indicate the direction of data transfer. Dark gray shade indicates interfaces between the PC and the experiment. According to the background we separate the experiment into three parts: light gray is motion control, white is data acquisition, and black is magnet and temperature control.

control the retardation of the PEM80. The PEM80 offers two reference outputs at 1ω and 2ω, which are fed into the SR510 and SR830 lock-in amplifiers, respectively. The SR830 digital lock-in measures the 2ω component of the signal and is used for most of our measurements, in particular, when using the compensation method. A FLUKE8842 multimeter measures the dc component of the signal. During measurements the high voltage is adjusted such that a 5 mV dc signal is obtained.

5 OPTICAL PROPERTIES AND ELECTRONIC STRUCTURE OF A MAGNETIC KONDO SYSTEM: A CASE STUDY OF THE LOCAL MOMENT MAGNETS RAl_2 (R=La, Ce, Pr)

5.1 Introduction

Many Ce systems are classified as intermediate valence or heavy Fermion systems. In intermediate valence (or valence fluctuation) systems the Ce partially *loses* its single $4f$ electron due to strong mixing of the $4f$ state with conduction band states. The Ce ion is no longer trivalent but a mixture of Ce^{3+} and Ce^{4+} (or $4f^1$ and $4f^0$). This change in valence is manifested in many physical properties, the most striking one being a volume collapse of the unit cell. The case of weaker hybridization is the formation of a Kondo state. In the static interpretation the local moments on the trivalent Ce^{3+} ions are screened by a cloud of conduction electrons. This can also be seen as resonant spin-flip scattering of conduction electrons by local moments. In compounds showing the Kondo effect, bands in the vicinity of the Fermi level show strong f character. This leads to an increase of the density of states at the Fermi level. It can be observed experimentally as a massive increase in the linear specific heat coefficient γ. Due to strong electron correlations the electrons in the solid appear to be up to several thousand times heavier than in ordinary metals. Cu has a γ of 0.695 mJ/mol K^2 whereas $CeAl_3$ shows a linear specific heat coefficient of 1620 mJ/mol K^2. Since electrons are Fermions we refer to materials with a large γ (usually above 500 mJ/mol K^2) as heavy-Fermion compounds[71].

Early measurements on $CeAl_2$ indicated a large linear specific heat coefficient (135 mJ/mol K^2) despite magnetic order at low temperature (T_N=3.8 K). The magnetic transition was observed in specific heat[72], resistivity[73], magnetic susceptibility[74], and thermal expansion measurements[75]. The Kondo effect was invoked to explain the reduced magnetic moment that was observed in neutron scattering. $CeAl_2$ provides an example of a magnetic Kondo lattice (or concentrated Kondo system). Other examples of this class of materials are CeB_6 (discussed in Chapter 8.2), $CeIn_3$, $CeCu_2$, and some CeT_2Ge_2 and CeT_2Si_2 compounds with T being a metal with a filled or nearly filled d shell[76]. The

Kondo temperature is 5 K in $CeAl_2$ and is about the same as the ordering temperature[77]. $CeAl_2$ shows competition between magnetic order and the Kondo effect which wants to form a non-magnetic singlet ground state. An increase of the density of states at the Fermi level is believed to give rise to a pure Kondo ground state in $CeAl_3$. Due to magnetic ordering, the Kondo effect in $CeAl_2$ remains incomplete. Bredl *et al.*[78] estimated from specific heat measurements above the Kondo regime that $CeAl_2$ would become an extreme heavy Fermion material if magnetic order did not occur. Their extrapolated value for zero temperature is ten times the measured value, i.e. 1740 mJ/mol K^2. Patthey and co-workers[79] estimated an even larger value (2400 mJ/mol K^2) based on their photoemission studies at 15 K.

The Ce nearest neighbor distance in $CeAl_2$ is in between that of α-Ce and γ-Ce. Due to strong hybridization α-Ce has no local moment. Direct $4f$ overlap leads to a finite $4f$ bandwidth, i.e. itinerant $4f$ electrons, similar to CeN and puts α-Ce in the group of valence fluctuation systems. In γ-Ce, on the other hand, the $4f$ states are localized and have a magnetic moment which leads to long-range magnetic order. $CeAl_2$ is a limiting case in which we still have local moments but also a considerable $4f$-$4f$ overlap. We have a competition between direct overlap interaction and RKKY (Ruderman-Kittel-Kasuya-Yoshida[80, 81, 82]) indirect exchange which is mediated by conduction electrons and is the major contribution to magnetic interactions in compounds containing rare-earths.

Local magnetic moments and strong mixing of the $4f$ bands with conduction electron states makes $CeAl_2$ a very interesting system for magneto-optical experiments. The optical response between 1.5 and 5.5 eV is believed to be governed by interband transitions involving p and d bands. Due to small matrix elements $4f$ contributions are sometimes difficult to identify from reflectance measurements. However, since they are extremely narrow and have large spin-orbit splitting, they can give large peaks in the magneto-optical signal. We will compare $CeAl_2$ to the isostructural compounds containing La and Pr. $LaAl_2$ has no $4f$ electrons which reduces the $4f$ character below E_F. It will be taken as a reference to investigate the contribution of f states to the optical signal. The third compound in this group is $PrAl_2$. It is more of the *conventional type of rare-earth compound* in that it behaves much like heavier rare-earth Laves phase intermetallic compounds, i.e. it has localized $4f$ states and orders ferromagnetically at 35 K.

5.2 Sample preparation and characterization

RAl_2 (with R being La, Ce, Pr) were grown by the flux growth technique [83, 84, 85] from a binary melt, i.e. a self flux. The starting materials were 99.995% Ames Lab (La, Ce, Pr) and 99.999% Johnson Matthey Al. Crystals of this structure (discussed below) often grow preferentially along [111] and

hence have an octahedral morphology. Our optical measurements in this and the following chapter on RFe_2 will be performed on (111) planes. For $LaAl_2$, single crystals of octahedral morphology of about $3 \times 3 \times 3$ mm^3 with clean triangular facets were obtained by the flux growth method described above. No further surface treatment was necessary and ellipsometric measurements were performed on the as-grown crystals. In the case of Ce the crystals had a slight hoppered morphology, i.e. no clean facets, unlike $LaAl_2$. The Pr growth produced a giant sample (about 1 g) with a morphology similar to that of $CeAl_2$. $CeAl_2$ and $PrAl_2$ are not very reactive and were therefore polished first using a very fine silicon carbide abrasive paper (1200 grade) followed by alumina powder with grain sizes starting at 3 down to 0.05 μm. The results were not very promising in that the surface was still not good enough for reflection experiments. We then polished the samples using silicon carbide spray with grades of 6, 1, and 0.25 μm. In addition to giving a better surface we can avoid the contact with water which is used in conjunction with alumina abrasives. Water is known to enhance oxidation. The sample surface was microscopically clean after rinsing off residue from the polishing agent using acetone and isopropanol. The samples were mounted on the sample holder and transferred into the sample chamber within 5 minutes where an inert atmosphere protected the samples from further oxidation. After the polishing procedure annealing can often relieve strain in the surface layers of a sample and improve the optical response by up to a factor of two. However, rare-earth compounds are prone to oxidation. Complete oxidation of the surface occurred in one sample during the annealing process and we obtained better results using as-polished samples for our experiments.

RAl_2 compounds (as well as RFe_2, Chapter 6) crystallize in the cubic $MgCu_2$ Laves phase structure (C15, space group O_h^7, $Fd\bar{3}m$) shown in Fig. 5.1. The rare-earth atoms (large white spheres) are arranged on a diamond lattice at positions $(0,0,0)$ and $(\frac{1}{4},\frac{1}{4},\frac{1}{4})$. The transition metal is in a tetrahedral coordination at $(\frac{5}{8},\frac{5}{8},\frac{5}{8})$, $(\frac{5}{8},\frac{7}{8},\frac{7}{8})$, $(\frac{7}{8},\frac{5}{8},\frac{7}{8})$, and $(\frac{7}{8},\frac{7}{8},\frac{5}{8})$[86, 87, 88]. We have two formula units, i.e. six atoms, per unit cell. The measured lattice constants are 8.148, 8.059, and 8.024 Å for the La[89], Ce[90], and Pr[88] compound, respectively. It should be noted that this lanthanide contraction already indicates a trivalent Ce^{3+} ion, i.e. similar to $\gamma-$Ce which has a local magnetic moment. At higher pressure (above 65 kbar or 7% volume compression) a volume collapsed phase similar to that of mixed valent $\alpha-$Ce has been observed[91]. Thermal expansion data do not show any change in the Ce valence down to 2K[75]. Recently, Delin and Johansson[92] were able to show, employing a full-potential linear muffin-tin orbital method, that $CeAl_2$ is far from valence degeneracy. They found the $4f^0$ state 1.61 eV above the trivalent $4f^1$ ground state.

To characterize the samples, magnetization measurements were performed on $CeAl_2$ and $PrAl_2$[93].

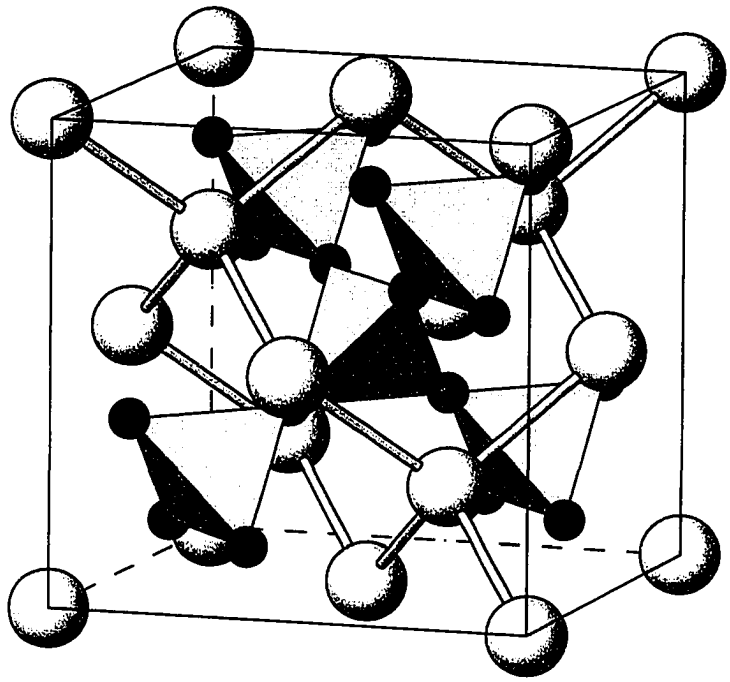

Figure 5.1 Cubic $MgCu_2$ Laves phase structure. The big white spheres are rare earth atoms which form a diamond lattice. Dark small symbols show tetrahedral coordination of the transition metal atoms. Bonds and tetrahedra are shown for clarity.

$LaAl_2$ does not carry a moment and is therefore of no further interest in this respect. The upper panel of Fig. 5.2 shows M/H at 1 kOe with the magnetic field aligned along [111], which is the easy axis in this compound[94]. We can clearly see that there are two transitions. Plotting $d(\chi T)/dT$ allows us to determine the transition temperatures. According to Fisher[95] the critical temperature can be estimated from the maximum in $d(\chi T)/dT$ which is proportional to the magnetic component of the specific heat close to an antiferromagnetic transition. At 3.7 K we observe the first transition. This peak is due to $CeAl_2$ which orders in a sinusoidal antiferromagnetic structure at 3.8 K[86]. In this structure Ce moments in successive [111] planes are aligned antiparallel and the magnitude of the moments on the Ce site are modulated sinusoidally along $[1\bar{1}0]$[86]. This modulation, which persists to lower temperatures, cannot be explained with thermal effects, i.e. disorder, but rather by formation of a singlet ground state. Although $CeAl_2$ is clearly antiferromagnetic there are strong ferromagnetic interactions in this compound as was shown by an extrapolation of the Curie constant for $Pr_{1-x}Ce_xAl_2$ alloys which yields $T_C \sim 5$ K. This explains the incommensurate propagation vector with a period of roughly 9 interatomic distances. The Kondo effect is believed to reduce the Ce moment in this compound giving rise to the

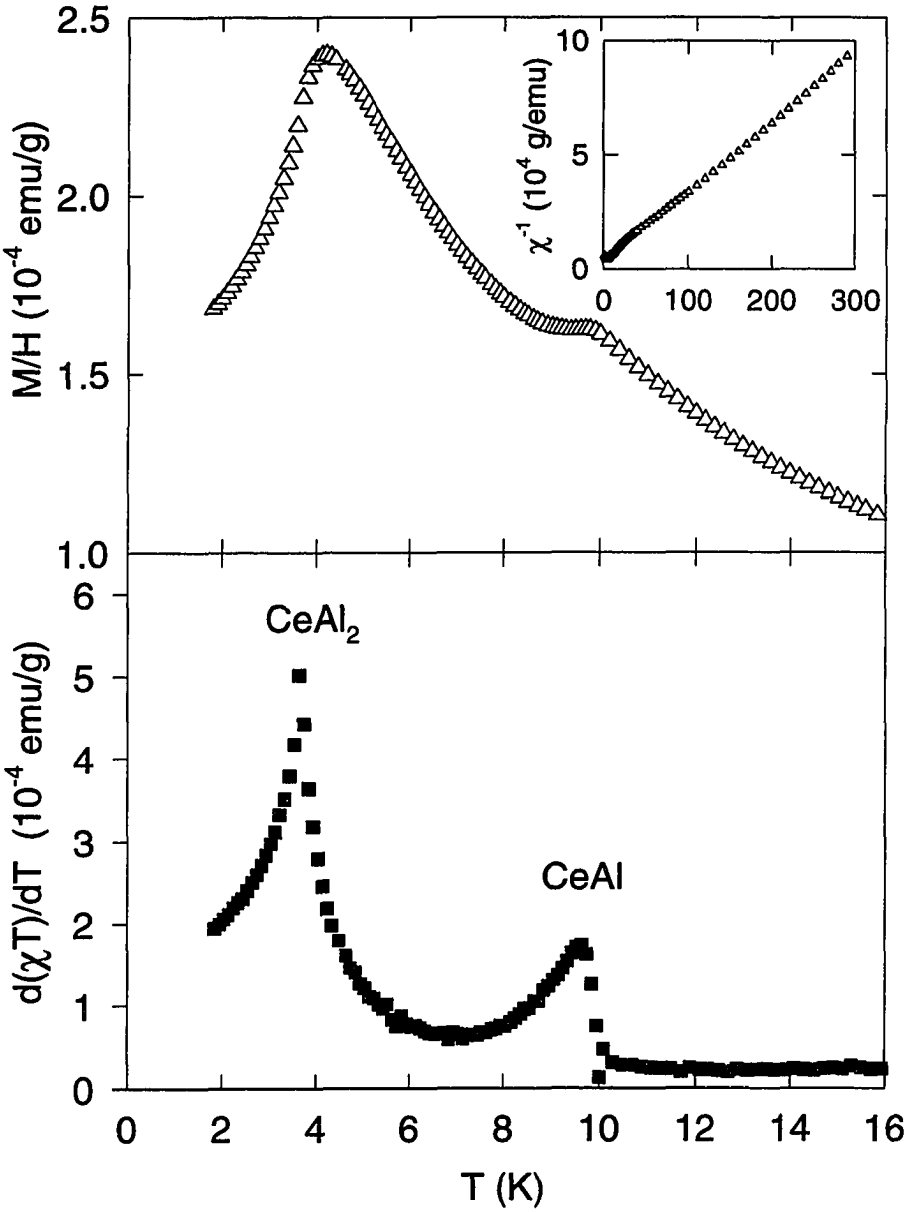

Figure 5.2 Magnetization of $CeAl_2$ in an applied field of 1 kOe parallel to [111]. The upper panel shows M/H for $CeAl_2$. Two transitions are observed. The lower panel has $d(\chi T)/dT$ as a function of temperature. The transition at 3.7 K originates from $CeAl_2$ (T_N=3.8 K). At 9.7 K we observe a second antiferromagnetic transition which is due to CeAl contamination of the sample. The inset in the upper panel shows χ^{-1}. From a fit between 150 and 350 K we obtain an effective moment of 2.18 μ_B and $\Theta = -3.4$ K.

sinusoidal variation of the Ce moment along [1$\bar{1}$0]. From residual quasielastic linewidth of neutron scattering data and specific heat measurements Steglich *et al.*[77] derived a Kondo temperature of 5±2 K. This shows that correlation effects are strong above the magnetic ordering temperature. At lower temperature the RKKY indirect exchange interaction becomes stronger than the Kondo effect. The Kondo effect favors a non-magnetic singlet ground state resulting from a negative exchange interaction between localized $4f$ and conduction electrons, also referred to as s-f interaction. Since $T_N \sim T_K$ $CeAl_2$ belongs in the category of magnetic concentrated Kondo systems. From the high temperature inverse susceptibility (inset in Fig. 5.2) we estimate $\Theta = -3.5$ K which is in good agreement with the ordering temperature obtained from $d(\chi T)/dT$. A linear fit yields an effective moment of 2.18 μ_B. The cubic crystal field splits the sixfold degenerate J=5/2 Ce^{3+} state into a Γ_7 doublet and a fourfold degenerate Γ_8 excited state 100 K above the ground state[72] (Appendix D). The calculated moment for the free Γ_7 is 2.54 μ_B. This means we observe an effective moment which is decreased by about 14% from the free ion value. A similar trend was observed by Vasil'kevich in Ce_3Al, Ce_3Al_{11}, and CeAl[96]. This behavior is likely due to the effect of Kondo spin compensation.

We should also note the second transition at 9.7 K. This transition is much weaker than the other transition in the $CeAl_2$ sample. It originates from a second phase contamination of the sample. Of the related compounds, CeAl and Ce_3Al_{11} show antiferromagnetic and ferromagnetic transitions at 9 K, respectively[97, 98]. Inspection of the binary phase diagram[99] shows that one is likely to obtain CeAl along with $CeAl_2$ in the flux growth process. We therefore assign this peak to CeAl contamination of our sample.

Figure 5.3 shows the magnetization versus field for $CeAl_2$ at two different temperatures. At 2.1 K, well below T_N, we observe a linear increase of M until we reach the critical field of 40 kOe where $CeAl_2$ undergoes a metamagnetic phase transition to a field-induced ferromagnetic structure. This transition was also observed by Barbara *et al.*[86] and Ōnuki *et al.*[100]. Comparison with the magnetization curves shown in Ref. [86] shows that at 55 kOe, which is the limit of our instrument, the moment per Ce is strongly increasing with increasing field. Saturation cannot be achieved up to 150 kOe. With our optical cryostat we can measure in fields up to 70 kOe which corresponds to a moment of 0.75 μ_B per Ce. At 3.3 K, which is fairly close to the transition temperature, this antiferromagnetic to field-induced ferromagnetic transition is hardly visible in our data.

We have second-phase contamination in our sample. Since $CeAl_2$ is a system with competing long range interactions we would expect to see an effect of the second phase on either the moment or the transition temperature. As seen from our data this is not the case and we conclude that the amount

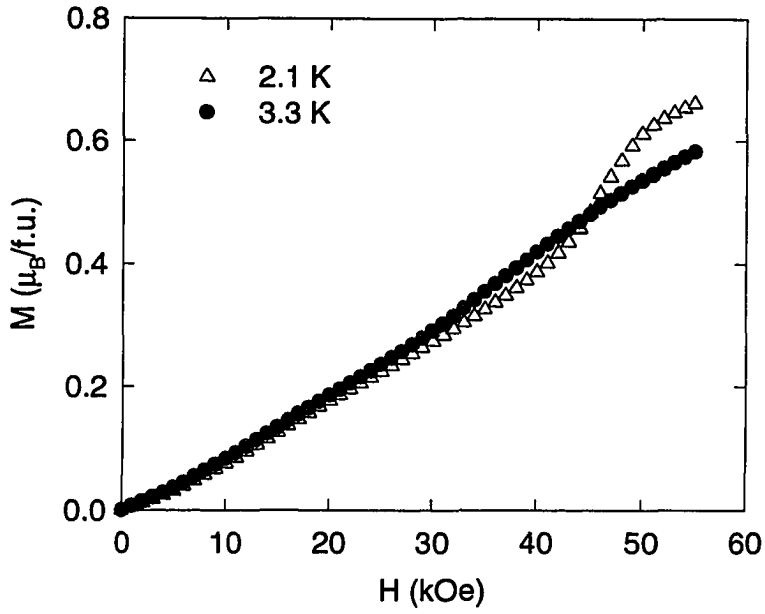

Figure 5.3 Magnetic moment per Ce as a function of field with H || [111]. We show one scan well below $T_N = 3.7$ K and another one very close to it. At 40 kOe we see the onset of a field induced antiferromagnetic to ferromagnetic phase transition.

of second phase is small and does not affect the physical properties of the sample. A more accurate analysis would require x-rays which would allow one to estimate the amount of CeAl second phase in the sample.

$PrAl_2$ orders ferromagnetically at 33 K[101, 102]. The saturated moment is 2.88 μ_B/Pr[94]. Due to CEF effects $PrAl_2$ shows a fairly large anisotropy in the magnetization. The largest magnetization is reached for H || [100]. For H || [111] a moment of 2.45 μ_B is reached at 80 kOe[94]. For H || [110] an increased moment of 2.55 μ_B was measured[94]. Our magnetization data, which were taken along two arbitrary directions (parallel and perpendicular to $[xyz]$), are shown in Fig. 5.4. Data were taken at 5 K which is well below the ordering temperature. The anisotropy is obvious from our two scans. We obtain a maximum moment of 2.59μ_B at 50 kOe. From the magnitude of the saturated moment it becomes clear that H $\perp$ $[xyz]$ in our case corresponds to an alignment which is very close to H || [110]. The susceptibility was measured in order to determine T_C. Figure 5.5 shows data taken in a field of 1 kOe applied perpendicular to $[xyz]$. From the inverse susceptibility (shown in the inset) we estimate $T_C = 33$ K which agrees well with earlier results. Note that the line shown indicates how we determined T_C and is not a fit. χ^{-1} shows non-linear behavior at higher temperatures which is due to temperature independent contributions to the susceptibility. These originate from a diamagnetic sample

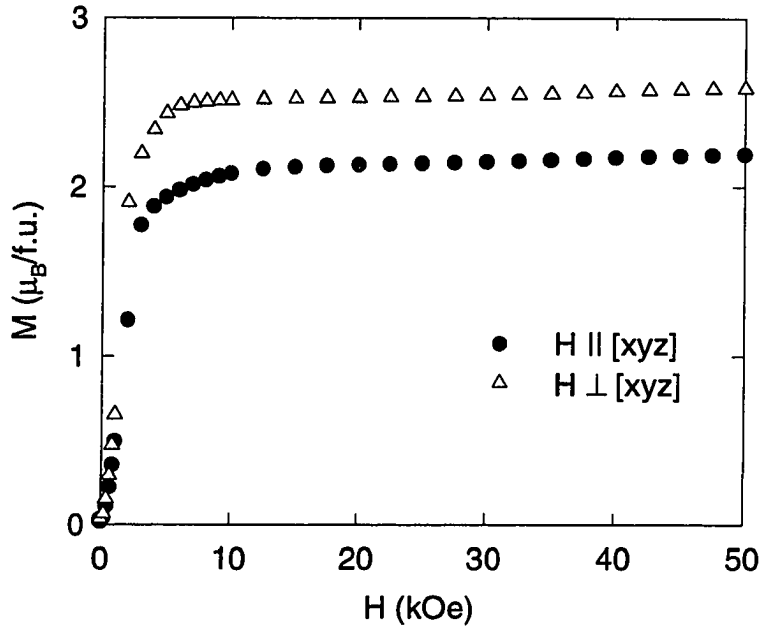

Figure 5.4 Magnetization of $PrAl_2$ measured along two arbitrary perpendicular directions. The observed saturation moment of 2.59 μ_B indicates that H⊥ [xyz](△) corresponds to H|| [110].

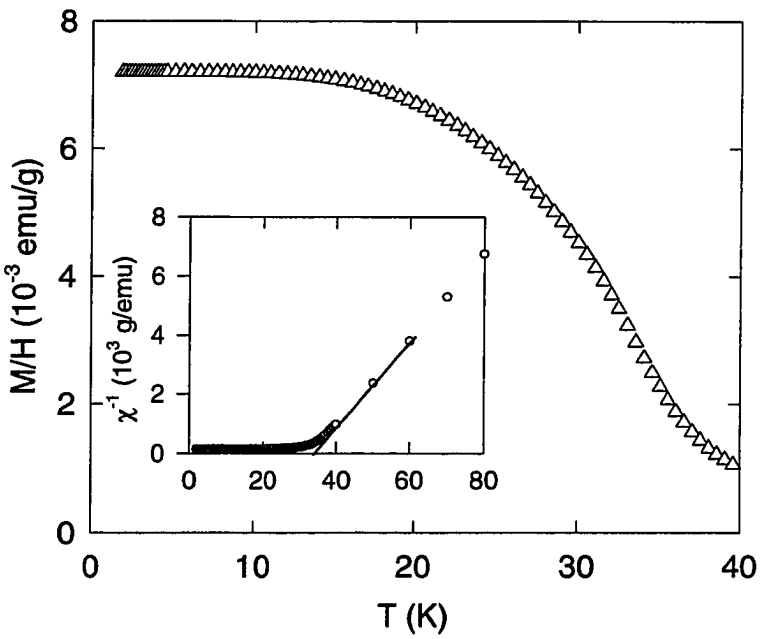

Figure 5.5 Magnetization of $PrAl_2$ in an applied field of 1kOe parallel to [110]. From χ^{-1} (shown in the inset) we estimate $T_C = 33K$. The line shows how we obtained T_C and is not a fit. From a fit of χ we determined an effective moment of 3.36 μ_B/Pr and Θ=35 K.

holder, Larmor diamagnetism of the core electrons, and Pauli paramagnetic and Landau diamagnetic contributions from the conduction electrons. We therefore prefer to fit the susceptibility. A fit of χ with a Curie-Weiss law yields an effective moment of 3.36 μ_B/Pr which agrees well with the Hund's rule ground state value of 3.58 μ_B/Pr. This indicates that our sample is of high quality which is supported by the observed T_C.

5.3 Electronic structure

The first band structure (BS) calculations for *non-4f* materials YAl_2, $LaAl_2$, and $LuAl_2$ were reported by Switendick[103]. A non-spin-polarized augmented plane wave method (APW) was used to calculate the BS and density of states (DOS). For YAl_2 and $LuAl_2$ good agreement with the experimentally observed linear specific heat coefficient γ was found[103, 89]. For $LaAl_2$ the deviation was larger, the calculated DOS at the Fermi energy being only 1/3 of what would be expected from specific heat measurements. Even including $4f$ orbitals did not lead to an improved estimate for γ. At the time those results were published, computational resources were limited and k-space sampling could not be performed with the accuracy needed leading to an error of $\pm 20\%$ in the calculated values. However, the BS obtained is very similar to later results[87, 104, 90, 105]. Hasegawa and Yanase[87] reported a self-consistent relativistic APW study of the Fermi surface of $LaAl_2$ which shows excellent agreement with experimental results. States contributing to the Fermi surface are mostly Al-p and La-d states with only little f character ($< 3\%$). The calculated extremal cross sectional areas are within 3% of the experimental values[87, 106]. They did not include spin-orbit coupling and suggest that this might lead to degenerate bands at E_F giving a value for γ that is larger than that obtained experimentally[87, 89]. A very similar investigation on $LaAl_2$ was published by Pickett and Klein[90]. They compared the DOS obtained from the semirelativistic APW method with X-ray photoelectron spectroscopy (XPES)[107] and found good agreement. Finally there are two reports by Jarlborg *et al.*[104, 105] who used a self-consistent spin-polarized LMTO scheme to calculate the BS for $LaAl_2$ and non-magnetic, forced ferromagnetic and antiferromagnetic $CeAl_2$. They actually succeeded in showing that this compound orders in an antiferromagnetic structure. The ferromagnetic spin structure was stable with an external applied field ($\sim$ 4.6 MOe) which is accounted for by adding a spin dependent field energy to the potential in each iteration until self-consistency was achieved[105]. In the following we will discuss our results and point out the differences to the calculations that were mentioned above.

Using the TB-LMTO scheme we calculated the BS and DOS for RAl_2 (R=La, Ce, Pr). In BS calculations La, having no $4f$ electrons, can be seen as a *rare-earth without the trouble*, i.e. the empty

$4f$ bands are far above the Fermi energy (about 3 eV in this compound, compare our Fig. 5.6 and Ref. [87]) and do not contribute to the ground-state properties. It is well known that strongly localized states cannot be treated properly in LDA since there is a large on-site Coulomb repulsion which is not accounted for in local density calculations. This results in a pinning of the Fermi energy to the lower edge of the $4f$ band. Additional strong mixing of the $4f$ levels with the $5d$ bands consequently leads to a DOS at E_F that can be an order of magnitude larger than for the same compound containing the $4f$-free rare-earth element La (see Table 5.1).

We used the experimental lattice constants given in the previous section. The radii of the overlapping Wigner-Seitz (WS) spheres were chosen in such a way as to fill the entire unit cell. The rare-earth spheres

Table 5.1 Results of charge and moments inside the Wigner-Seitz spheres in $LaAl_2$, $CeAl_2$, and $PrAl_2$ from self-consistent spin-polarized BS calculations including spin-orbit coupling. Charges are in electrons, moments in μ_B/ion, and the DOS at the Fermi energy $N(_F)$ in states/eV cell.

	rare-earth					Al			
	s	p	d	f	Total	s	p	d	Total
$LaAl_2$									
$n_\downarrow$	0.21	0.24	0.91	0.15	1.51	0.56	0.81	0.13	1.50
$n_\uparrow$	0.21	0.24	0.91	0.15	1.51	0.56	0.81	0.13	1.50
$n_\downarrow + n_\uparrow$	0.41	0.48	1.81	0.30	3.02	1.13	1.61	0.26	3.00
$N(E_F)$	0.1	0.2	1.0	0.2	1.5	0.1	1.0	0.2	1.3
$CeAl_2$									
$n_\downarrow$	0.22	0.25	0.89	0.37	1.73	0.56	0.79	0.13	1.48
$n_\uparrow$	0.23	0.25	0.97	0.87	2.33	0.56	0.80	0.14	1.50
$n_\downarrow + n_\uparrow$	0.45	0.50	1.86	1.24	4.06	1.12	1.60	0.26	2.97
μ_S	0.01	0.00	0.08	0.50	0.60	-0.00	0.01	0.01	0.02
μ_L	-	0.00	0.00	-0.35	-0.34	-	-0.00	0.00	0.00
$N(E_F)$	0.2	0.2	1.4	9.9	11.6	0.1	0.9	0.4	1.5
$PrAl_2$									
$n_\downarrow$	0.21	0.24	0.82	0.19	1.46	0.57	0.79	0.12	1.48
$n_\uparrow$	0.24	0.25	0.92	2.22	3.62	0.56	0.80	0.13	1.49
$n_\downarrow + n_\uparrow$	0.45	0.49	1.74	2.41	5.08	1.12	1.59	0.25	2.96
μ_S	0.03	0.01	0.11	2.02	2.17	-0.01	0.01	0.01	0.01
μ_L	-	0.00	-0.01	-2.17	-2.18	-	-0.00	0.00	0.00
$N(E_F)$	0.1	0.2	0.9	30.3	31.5	0.1	0.8	0.3	1.2

had radii 3.736, 3.697, and 3.679 a.u. for La, Ce, and Pr, respectively. The corresponding sphere radii for Al were 3.050, 3.019, and 3.004 a.u. Self-consistent calculations were carried out using 72 k-points within the irreducible wedge (1/48) of the Brillouin zone (BZ), i.e. on a 12 × 12 × 12 mesh. As basis functions we chose rare-earth-6s, 6p, 5d, and 4f orbitals and Al-3s, 3p, and 3d wave functions.

The self-consistent charges and moments inside the WS spheres are shown in Table 5.1. Although the electronic structure and ground state properties of these compounds are expected to be very different due to the change in 4f occupancy we notice that the results are surprisingly similar. In Figs. 5.6, 5.9, and 5.12 we show the BS of the three compounds along the principal symmetry lines of the BZ together with the total DOS. Inspection of the BS shows that below -2 eV the bands are basically identical, the only difference being an increase in the spin-orbit splitting as we move from La to Pr. Similar structures are also observed at higher energies where the distortion of the conduction bands due to 4f states is negligible. For $LaAl_2$ (see Figs. 5.6-5.8) we find a complex of empty f states centered at 3 eV above E_F in agreement with Hasegawa and Yanase[87]. For $CeAl_2$ we notice considerably narrower 4f bands pinned at the Fermi energy (shown in Figs. 5.9-5.11). Due to small exchange splitting they appear as one broader band in the BS and total DOS. $PrAl_2$ shows two exchange split 4f bands with the partially occupied lower one at 0.2 eV and the unoccupied minority spin band at 1.5 eV with respect to E_F (Figs. 5.12-5.14). Conduction band states in the vicinity of the 4f bands are distorted due to strong mixing with the flat and localized 4f states. LDA therefore predicts a change in the Fermi surface as we add more 4f electrons. de-Haas-van-Alphen (dHvA) measurements did not indicate any significant difference between the Fermi surfaces of $LaAl_2$ and $CeAl_2$[106, 108, 109, 110, 111]. Even the metamagnetic phase transition does not lead to considerable changes of the Fermi surface in $CeAl_2$[111]. We therefore conclude that the 4f states are sufficiently localized and do not participate in the formation of the Fermi surface. Photoemission experiments show a feature close to E_F (within 0.2-1 eV) and another one at 2.5 eV ($CeAl_2$) and 3.75 eV ($PrAl_2$) below E_F[107, 112]. There was some controversy about the origin of this 2 eV feature, i.e. whether it was due to 5d or 4f emission (see Ref. [112] and references therein). From resonant UPS and the energy dependence of the emission cross section it became evident that this is a 4f related feature[112]. This also supports the picture of rather *inactive* 4f states. The 4f peak at E_F corresponds to a screened 4f photohole whereas the peak at 2 eV below is an unscreened hole. Band structure calculations are not able to identify this peak. The second peak at lower binding energy is due to many-body effects which LDA does not take into account. The Anderson model was successfully applied to this problem and the two f related features could be explained in terms of different screening mechanisms.

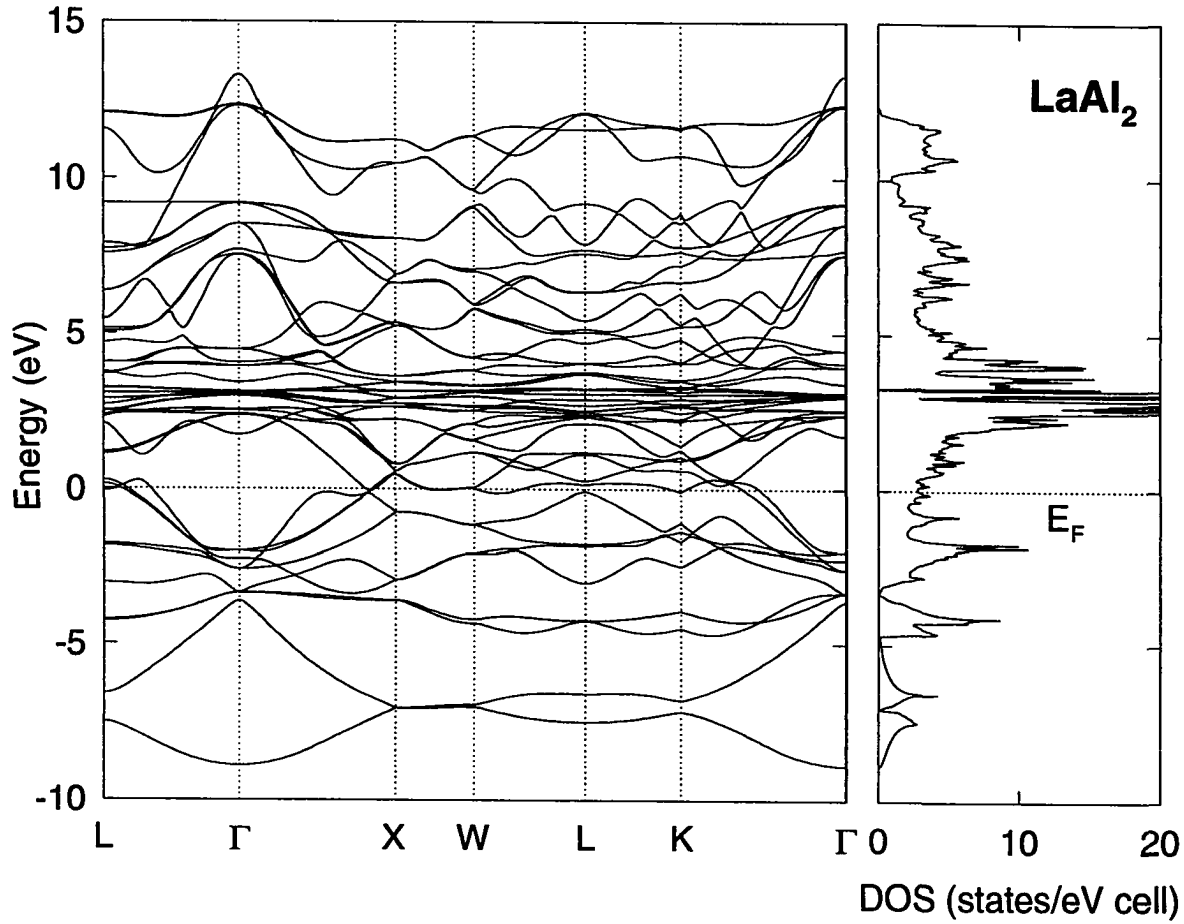

Figure 5.6 Spin-polarized relativistic band structure and total DOS for $LaAl_2$ including spin-orbit splitting.

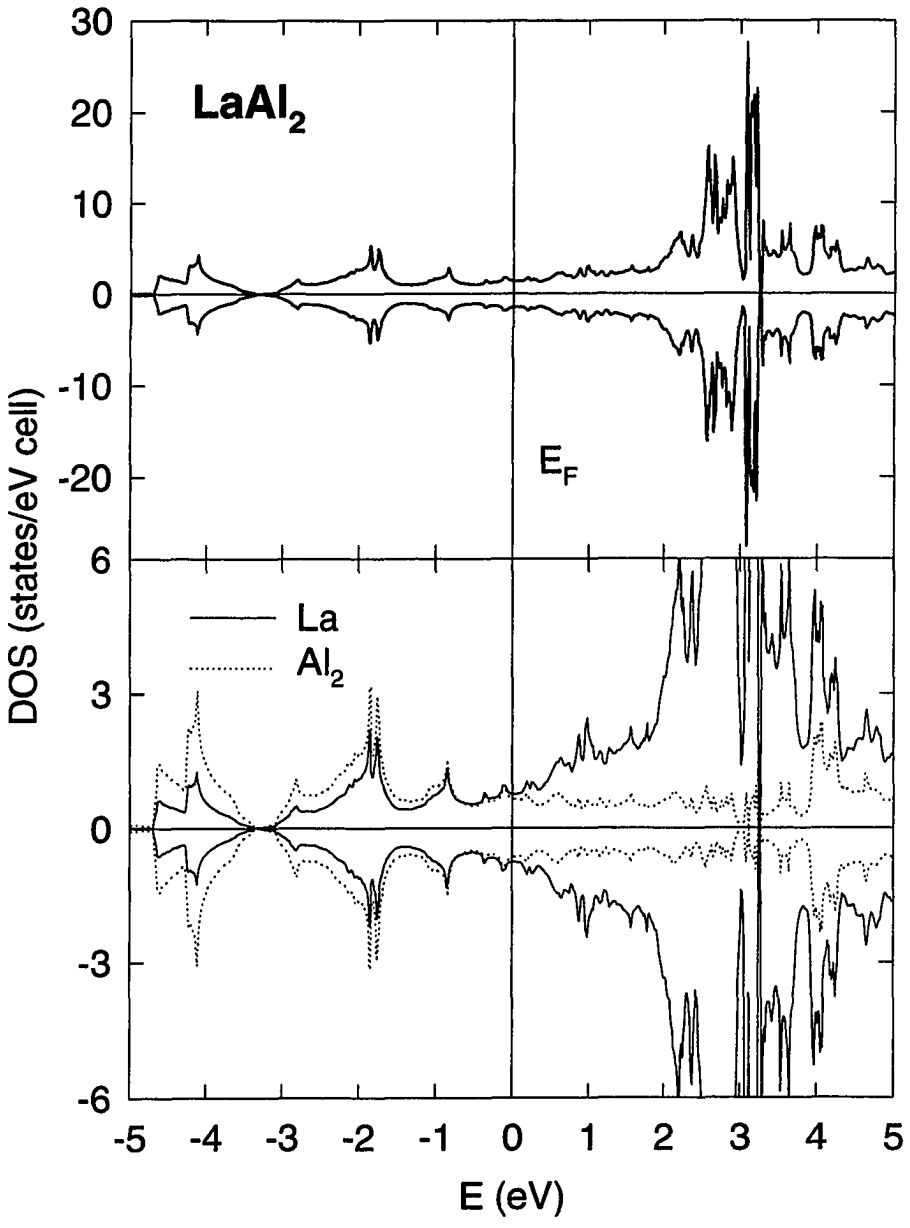

Figure 5.7 Total DOS for $LaAl_2$ (upper panel) and partial DOS (lower panel).

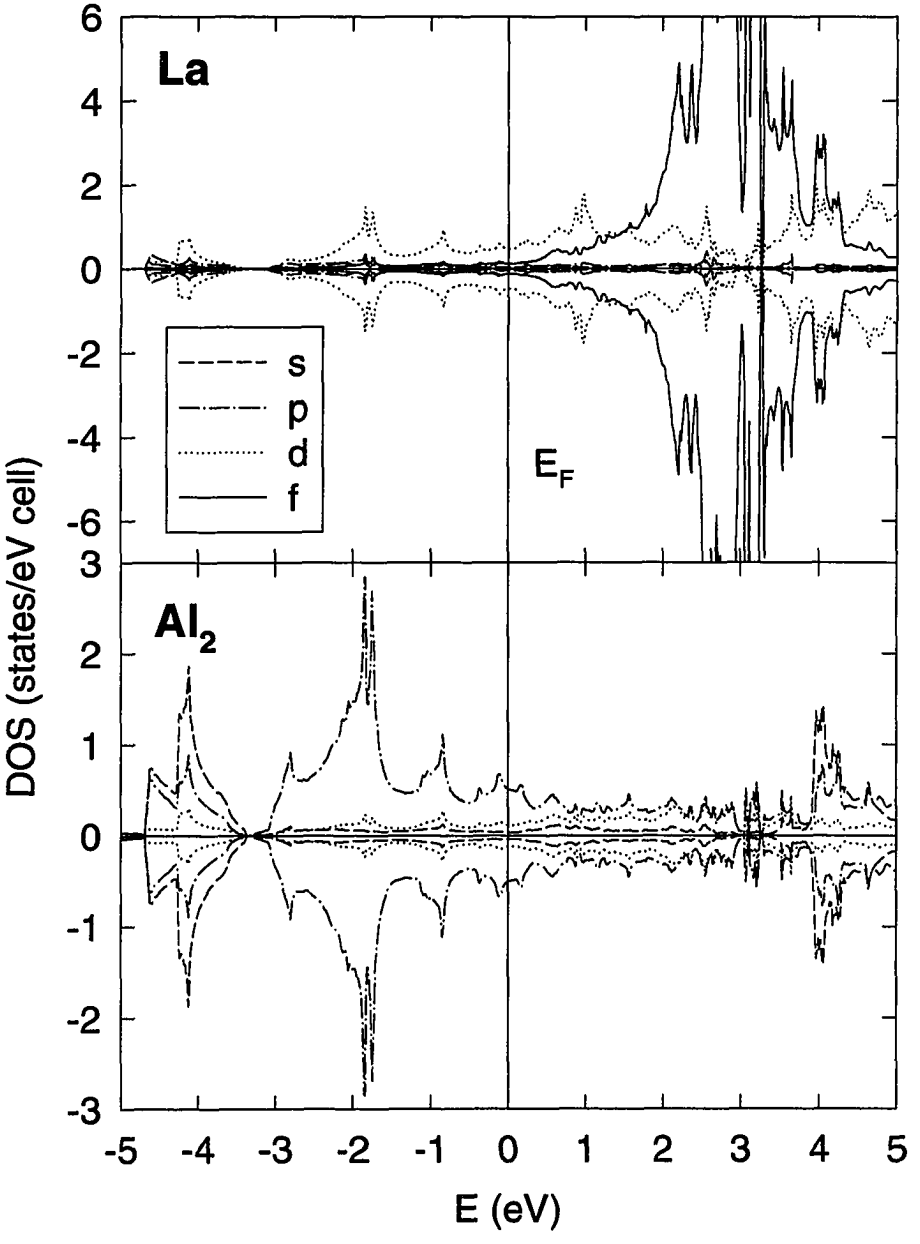

Figure 5.8 Orbital decomposition of the DOS for $LaAl_2$.

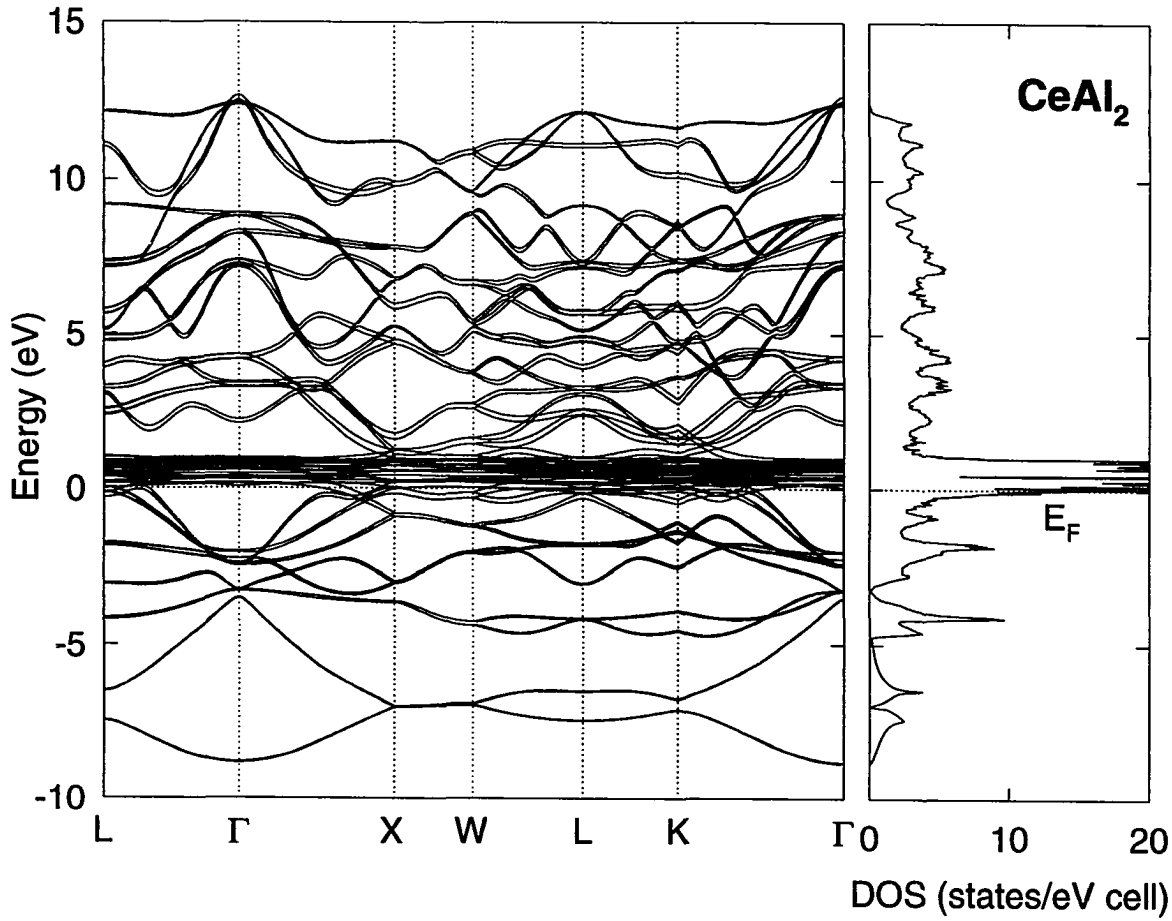

Figure 5.9 Spin-polarized relativistic band structure and total DOS for $CeAl_2$ including spin-orbit splitting.

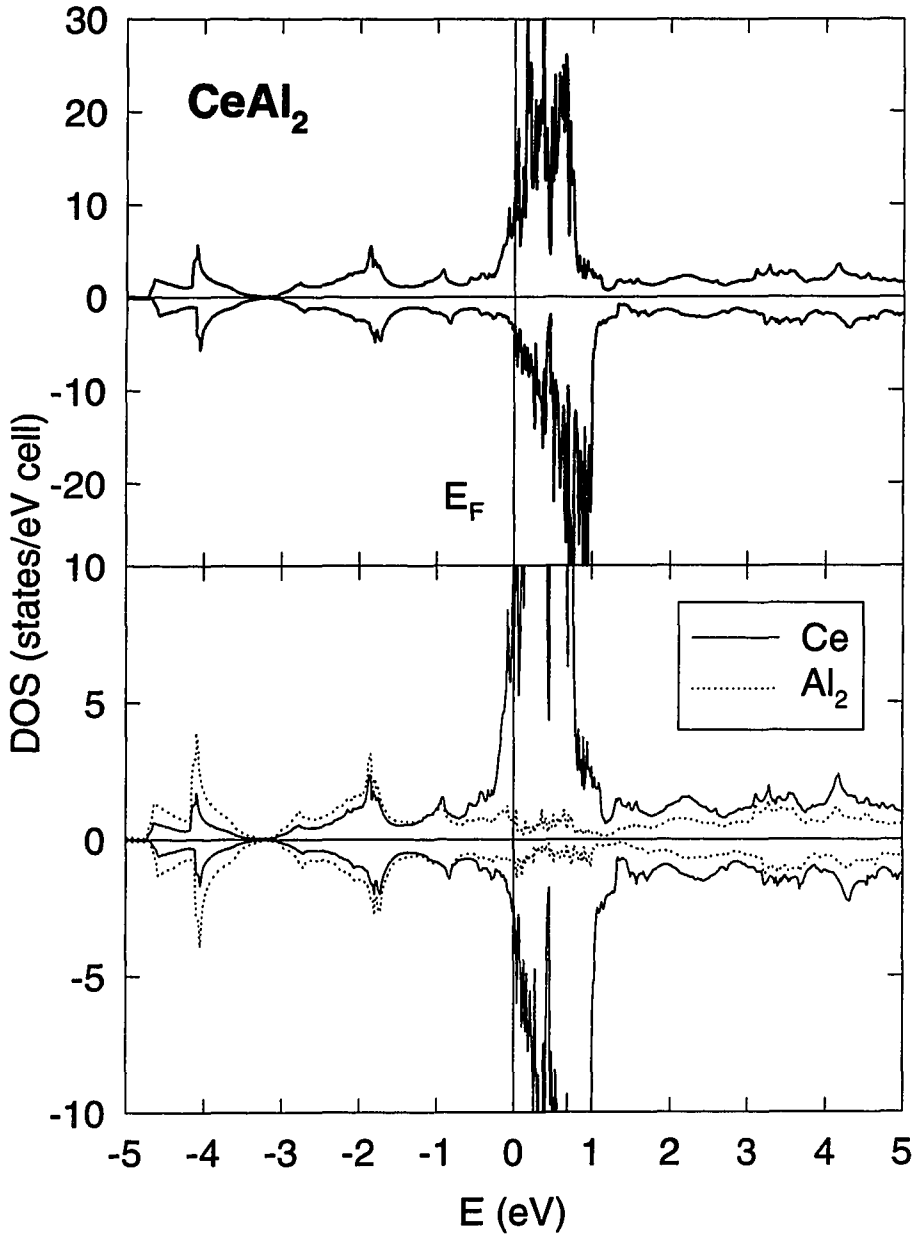

Figure 5.10 Total DOS for $CeAl_2$ (upper panel) and partial DOS (lower panel).

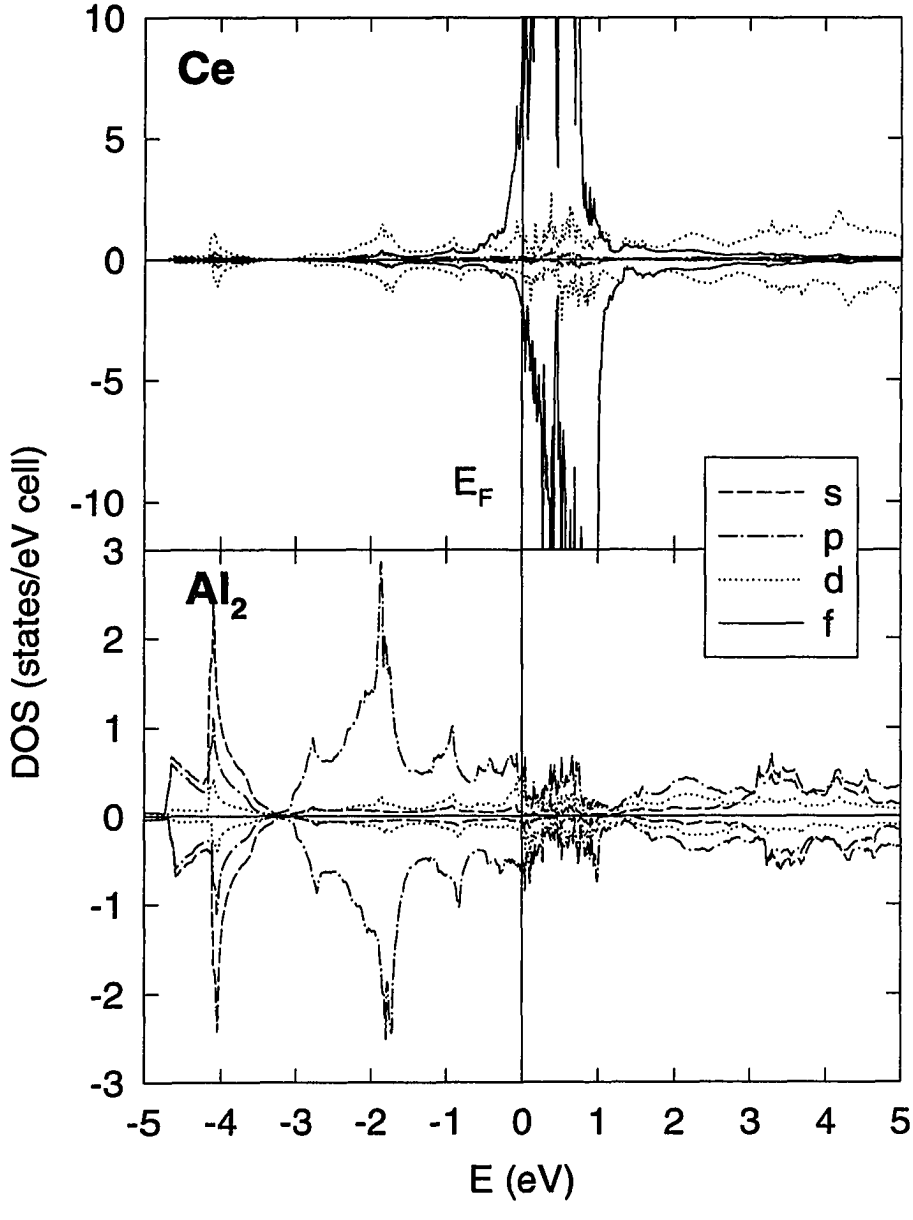

Figure 5.11 Orbital decomposition of the DOS for $CeAl_2$.

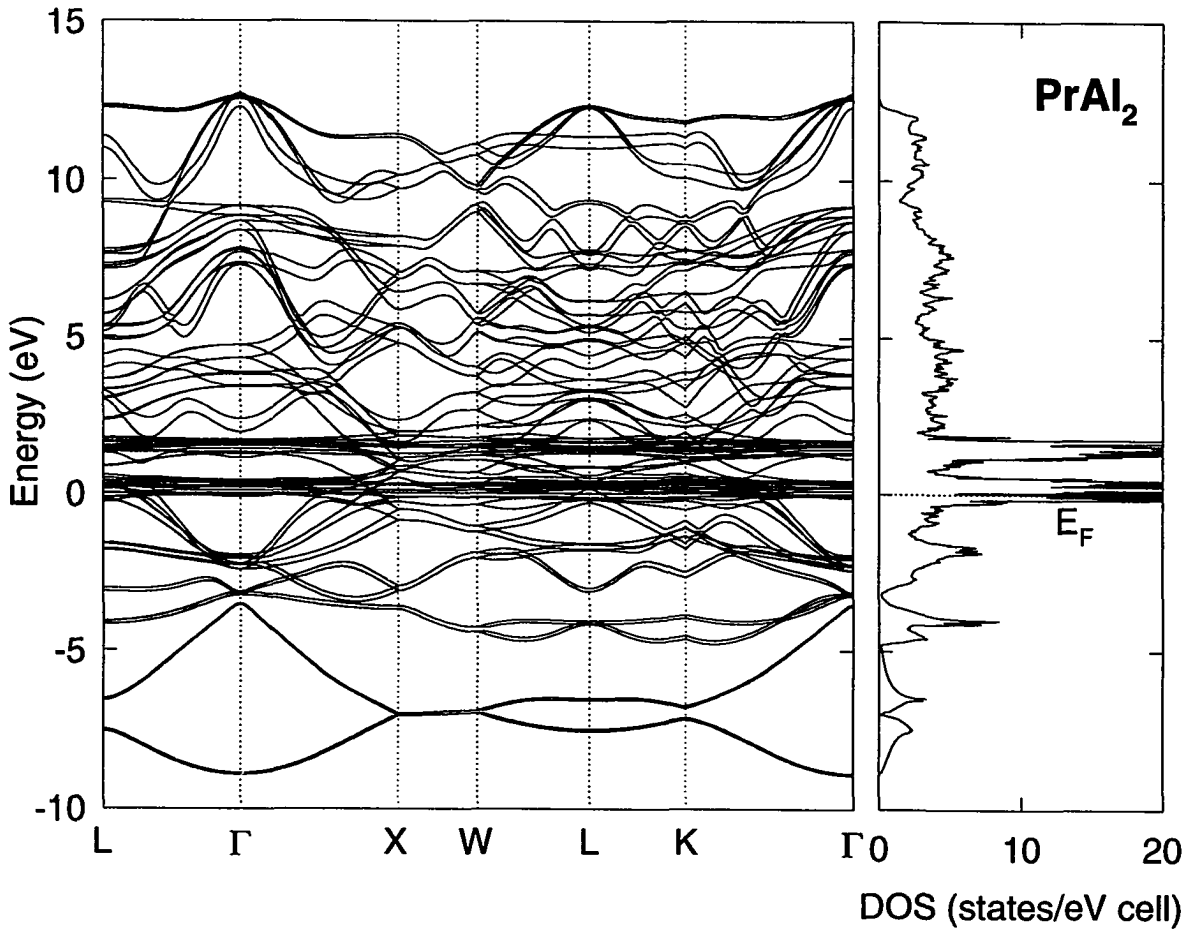

Figure 5.12 Spin-polarized relativistic band structure and total DOS for $PrAl_2$ including spin-orbit splitting.

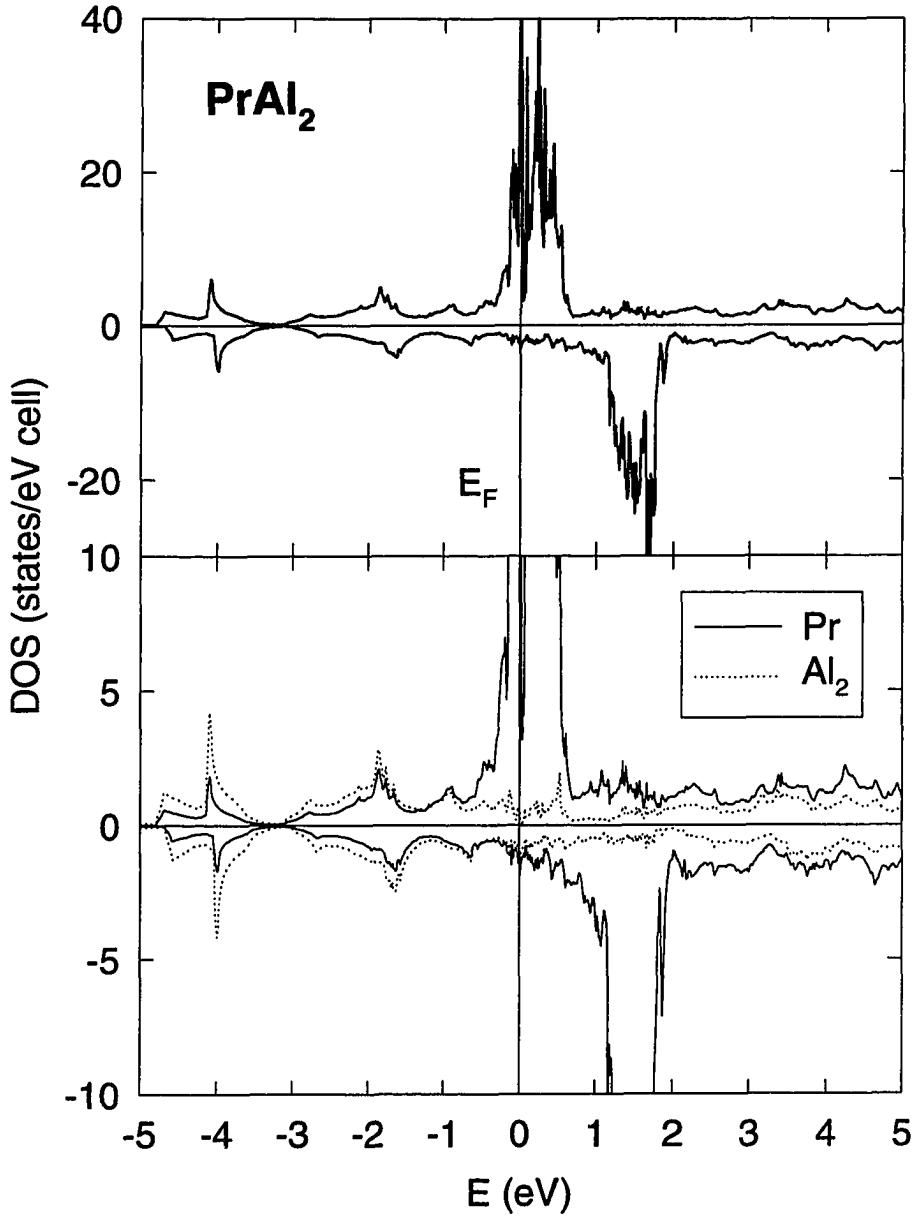

Figure 5.13 Total DOS for $PrAl_2$ (upper panel) and partial DOS.

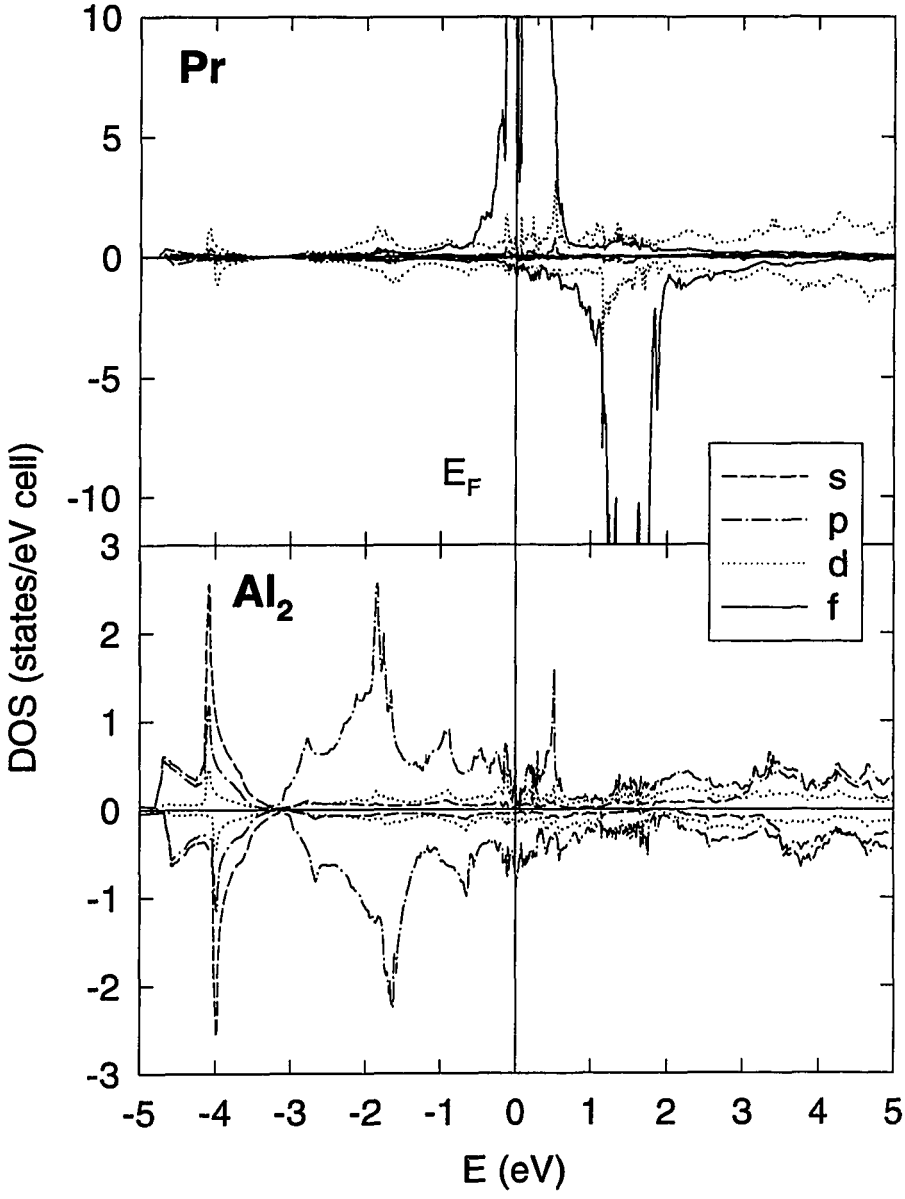

Figure 5.14 Orbital decomposition of the DOS for $PrAl_2$.

As mentioned earlier the LDA is not reliable in the limit of localized states and often is not able to predict the correct position of the $4f$ level. In La the $4f$ levels are centered 3 eV above the Fermi level and contribute only little to the DOS at E_F. We have 7% f character whereas the major contribution is due to Al-p and La-d states which both contribute about 36%. This supports Hasegawa's results[87] of less than 10% f character at E_F. Switendick reported about 13% partial f-DOS at E_F which clearly overestimates the contribution from f derived states. When we compare the rare-earth d-DOS at E_F with the other two compounds we find that it is nearly constant. The difference is clearly the DOS originating from the f orbital. For $CeAl_2$ and $PrAl_2$ the Fermi level is at the bottom of the $4f$ majority spin band, i.e. the $4f$ band leaks below E_F to accommodate the additional electron(s). For the Ce compound we have 11.6 $4f$-states per eV and unit cell at the Fermi energy. In $PrAl_2$ this is larger by a factor of 3. It should be noted that the contribution from Al is independent of the rare-earth ion indicating negligible mixing of Al derived states with the localized $4f$ levels at E_F. From the DOS at E_F we can estimate the electronic contribution to the specific heat which is given by

$$\gamma = \frac{\pi^2}{3} N(E_F) k_B^2 (1 + \lambda), \tag{5.1}$$

where k_B is Boltzmann's constant and λ is the enhancement due to electron-phonon interaction. Thus we can determine the *unenhanced* γ (λ=0) using the DOS from Table 5.1. We calculate 7, 31 and 77 mJ/mol K^2 for $LaAl_2$, $CeAl_2$, and $PrAl_2$, respectively. This is in fair agreement with specific heat data which indicate a γ of 11 mJ/mol K^2 for $LaAl_2$[89]. For $PrAl_2$ γ is clearly overestimated which can be attributed to an inadequate treatment of the Pr-$4f$ states. LDA predicts narrow $4f$ bands at the Fermi level leading to a large DOS. For $CeAl_2$ we underestimate γ which was shown to be about 135 mJ/mol K^2[78]. It was observed earlier that in $CeAl_2$, despite the increased DOS at the Fermi level, an electron-phonon coupling enhancement of about 8 is needed to account for the observed γ[105]. It is worth noting that the mass enhancement deduced from dHvA data is of the same order[113]. However, the increased linear specific heat coefficient is a many-body effect and LDA can merely indicate trends but does not yield a quantitatively reliable result.

The charge on the Al site does not change as we move from La to Pr. We find a constant charge of 1.12 in the s-orbital and 1.61 in p-orbitals which are the major contributions to the Al atoms. This can be verified from the DOS for Al which are shown in Figs. 5.8, 5.11, and 5.14. The DOS for all three compounds shows a large Al-p derived peak about 1.8 eV below the Fermi energy. Another peak which has about 50% s as well as p character can be seen at 4 eV below E_F. A peak in the PES spectrum at this energy was identified by Croft *et al.*[107] as Al derived states. From Figs. 5.8, 5.11, and 5.14 those regions with high DOS can be identified as atomic-like $3s$ and $3p$ bands with some $5d$ character. In the

BS (Figs. 5.6, 5.9, and 5.12) those bands can be seen to be well separated from the higher rare-earth $4f$ bands. The lowest $5d$ bands of the rare-earth site are nearly independent of the rare-earth element and strong mixing with the Al p-derived states is evident. It leads to a large DOS peak around -0.9, -1.8 eV, and -4.1 eV which agrees well with PES measurements[112]. Al-d character is negligible below the Fermi level but contributes considerably to the Al DOS above E_F (Figs. 5.8, 5.11, and 5.14), i.e. we need to take that into account in the following section when we calculate the optical properties of the material.

Let us turn to the differences caused by increasing $4f$ occupation number. The change of rare-earth conduction electron states is independent of the number of $4f$ electrons. In all three compounds our calculation yields a total of about 0.45 electrons with s and 0.5 with p character. Those are also the states in the vicinity of the Fermi level. La, which is non-magnetic, has 1.81 d electrons which is about the same as found in the Ce and Pr structures. However, whereas in La the occupancy of spin-up and spin-down states is the same we notice a strong polarization of the $5d$ states for the magnetic compounds. It should be noted that our calculation yields a ferromagnetic ground state. Jarlborg *et al.*[104, 105] found the simple antiferromagnetic structure to be the ground state with a Ce moment of $0.89\mu_B$ which is close to the experimental moment deduced from neutron scattering experiments[86]. The antiferromagnetic spin alignment can be understood in terms of nesting features of the underlying Fermi surface of $LaAl_2$ and is not caused by the $4f$ states. Nesting features were observed along [111] and [110]. Please note that the spins in successive (111) planes are aligned antiparallel and the modulation is along $[1\bar{1}0]$. A study of the generalized susceptibility similar to that of Rhee *et al.*[114] for $HoNi_2B_2C$ could possibly lead to an estimate for the propagation vector for the spin-density wave (SDW) in $CeAl_2$. For $CeAl_2$ we calculate a spin moment of 0.08 μ_B for the d band and in the case of Pr we find an even larger moment of 0.11 μ_B. This $5d$ moment is induced by the strongly polarized $4f$ states through intra-atomic coupling. Although the exact strength of this interaction cannot be determined from our results the increase of the $5d$ moment on the rare-earth site follows the trend of a four times stronger moment due to the Pr-$4f$ state. The $4f$ state in $CeAl_2$ was shown to be of rather localized character. This is reflected in the large orbital component of the magnetic moment of the $4f$ state which becomes quenched when the $4f$ states become more delocalized and form bands (see Chapter 6). LDA clearly overestimates the orbital contribution. Comparing with experimental results found in in the previous section we find that the rare-earth spin moments agree well with those observed in $CeAl_2$ and $PrAl_2$[86, 94] (see Table 5.1). In all cases Al carries a small spin moment and there is no orbital contribution as would be expected for conduction electron states. In previous studies the orbital

contribution to the total moment was not mentioned, either because the BS program did not calculate orbital moments or because agreement is worse when we take into account orbital moments. $PrAl_2$ is a striking example. The spin moment is fully compensated by a large orbital contribution and $PrAl_2$ is, according to our LDA results, basically without a magnetic moment. It is clear that the calculation fails to reproduce the magnetic moments which are mostly $4f$ in character.

5.4 Optical and magneto-optical properties

Let us turn to the optical properties of rare-earth dialuminides, especially in the energy range between 1.4 and 5.2 eV. Kim and Lynch[115] reported reflectivity data for $CeAl_2$ and $LuAl_2$. Combining reflectivity measurements and ellipsometry they obtained the optical conductivity between 0.04 and 4.1 eV. Lu has filled $4f$ bands (14 electrons) which are located well below the Fermi level and do not contribute in optical transitions in the low energy region (< 5 eV)[116]. Therefore the latter material was used as a reference to probe the contribution of the single Ce-$4f$ electron. However, the electronic structure of $LuAl_2$ is very different from that of $CeAl_2$ due to complete filling of the $4f$ shell and a larger nuclear charge. Is seems therefore useful to compare spectra to $LaAl_2$ instead. The nuclear charge differs by only one and the empty $4f$ levels are located above E_F (see the previous section). This is supported by PES experiments where no $4f$ contribution could be detected[107]. A major drawback is the position of the empty $4f$ states which LDA predicts about 3 eV above E_F, i.e. there could be contributions from $d \rightarrow f$ transitions to the optical conductivity. Kim and Lynch[115] found similar structures in the spectra of $CeAl_2$ and $LuAl_2$ at higher energies. Both compounds show an absorption peak at 2 eV. For the Ce compound there is another peak in σ_{1xx} at 3 eV. A structure which is believed to be of the same origin is found at 4 eV in $LuAl_2$. Based on the calculated DOS they assign this peak to transitions involving p derived bands as final states, i.e. $6s \rightarrow 6p$ and $5d \rightarrow 6p$ transitions. Below 2 eV $CeAl_2$ shows two more peaks in σ_{xx} which were not found for $LuAl_2$. Therefore an assignment of those peaks to transitions involving Ce derived f states seems obvious. $CeAl_2$ shows transitions at 0.1 and 1 eV. The former is believed to originate from $d \rightarrow f$ transitions while the latter peak is associated with transitions from f character bands just below E_F to $5d$ final states. There is no signature in the optical conductivity which could be related to the $4f$ feature at 2.5 eV below E_F seen in PES experiments[107]. Lee recently reported ellipsometric measurements on $LuAl_2$ and divalent $YbAl_2$[44]. His results, which we reproduce in Fig. 5.15 for the sake of completeness, are in fair agreement with those obtained earlier[115]. We will show our results obtained from ellipsometry and magneto-optics and compare the experimental results to predictions based on a self-consistent BS calculation.

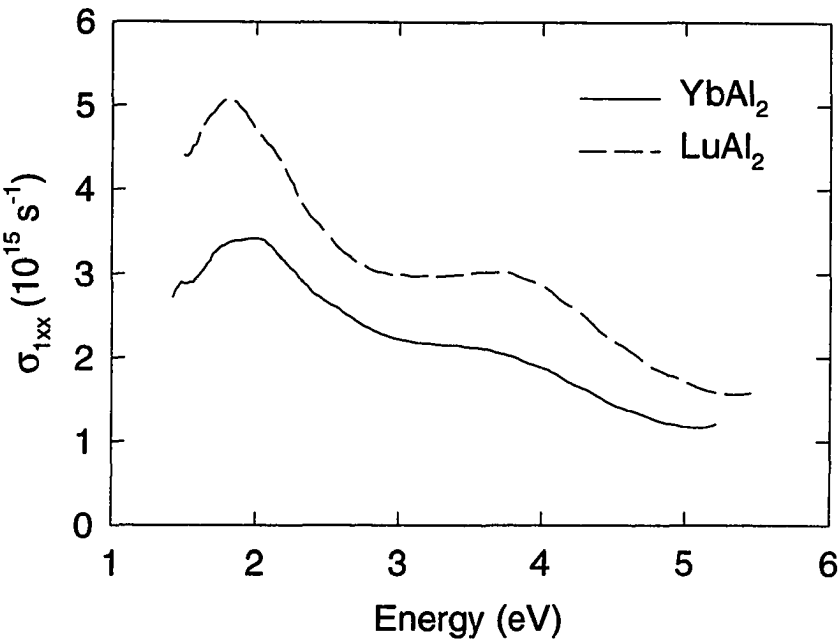

Figure 5.15 Optical conductivity of two related compounds containing the heavy rare-earths Yb and Lu.

In Fig. 5.16 we show the diagonal part of the optical conductivity of RAl_2 for R=La, Ce, Pr. The upper (lower) panel shows the absorptive (dispersive) part of σ_{xx}. First we note a decrease in the magnitude as we go from La through Ce to $PrAl_2$. The peak intensity of $LaAl_2$ at 2 eV agrees with that of $LuAl_2$ measured by Lee[44] and $CeAl_2$ in Ref. [115]. The magnitude of the absorption of $CeAl_2$ is slightly smaller and structures are not as clear. Absorption is clearly reduced for the $PrAl_2$ sample and its magnitude is close to that of $YbAl_2$[44]. However, since ellipsometry is very surface sensitive different procedures for sample preparation (e.g. polishing agents and duration, annealing temperature and time, etc.) may give different results. Since we measured the dielectric function in air (as done in Refs. [115, 44]) surface oxidation cannot be avoided. The samples were polished with 0.05μm alumina abrasives immediately before the experiment to reduce oxide effects.

In order to make any quantitative statements about the bulk absorption multiple angle of incidence ellipsometry should be performed. If one assumes the simple case of an oxide overlayer and a sharp interface between bulk material and oxide film this technique will allow the determination of the optical properties of the *buried clean* material. Those corrections were done for semiconductors and good agreement with data obtained on clean surfaces was obtained[117]. Assuming a non-absorbing oxide overlayer with an energy independent dielectric constant (or index of refraction), it can be shown that

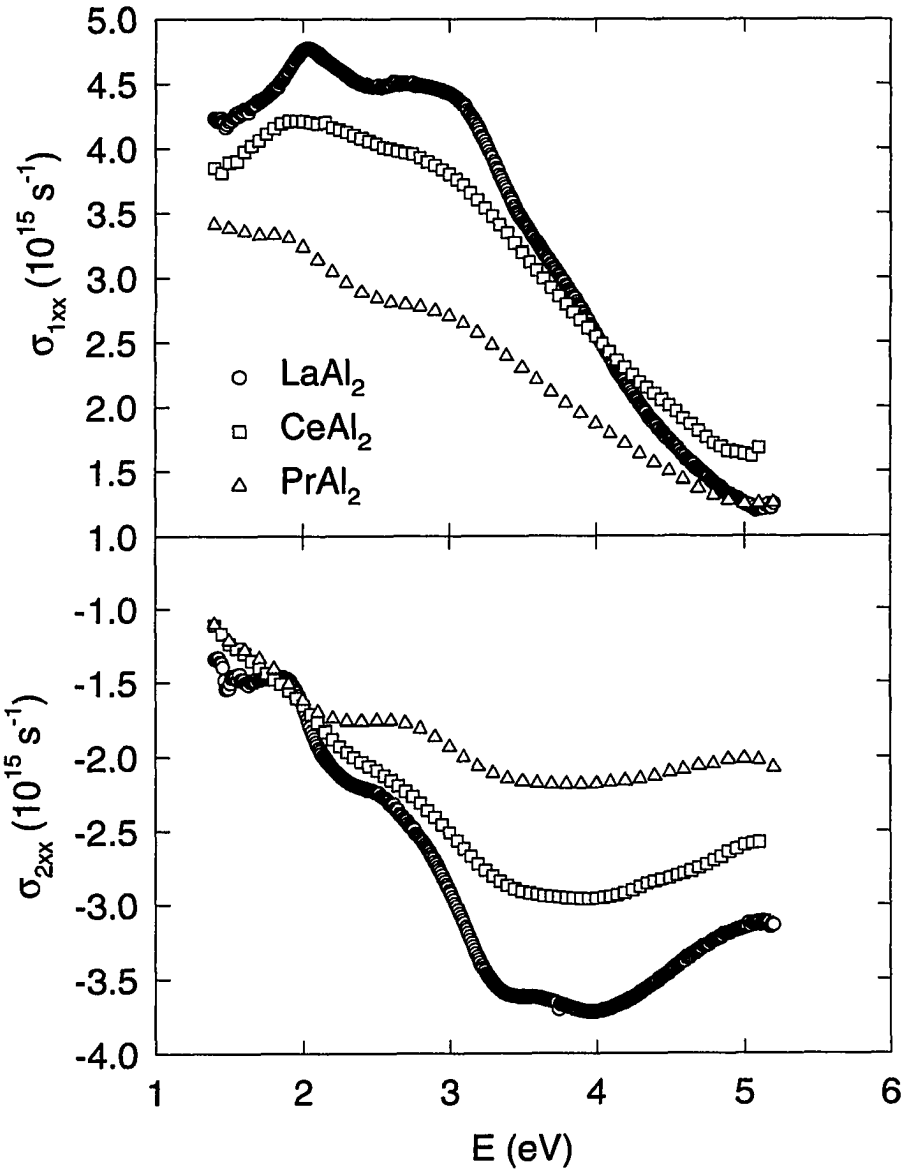

Figure 5.16 Optical conductivity of RAl_2 measured by ellipsometry at room temperature.

such a layer reduces the magnitude of the apparent dielectric function and the optical conductivity. Peak positions are not affected by a transparent oxide film (provided $\epsilon \approx$ constant). It is tempting to make similar corrections for our spectra. As Lee[44] pointed out this is not an easy task as there are too many variables, i.e. one does not know what kind of oxide makes up the surface layer. In our case it could be any combination of the rare-earth element, Al, and O. It is also possible to get different oxides that would give rise to a pseudo-dielectric function which can be modeled by the Bruggemann effective-medium theory[118]. The next problem is the determination of the oxide thickness. There are several methods available (grazing angle of incidence X-rays, secondary ion mass spectroscopy, Rutherford backscattering, Auger spectroscopy) none of which yielded conclusive results in the case of rare-earth-Fe_2 compounds. Once the oxide composition and thickness have been determined one has to find the dielectric function of each component of the effective medium. This is very difficult considering the variety of materials we are dealing with. Lee used as a first approximation a constant dielectric function (similar to that of SiO_2 which is nearly constant in the energy range of interest) and calculated the bulk properties. Furthermore a sharp interface between oxide film and bulk was assumed, a condition that certainly is not met in a real system where the surface may be some mixture of oxide and bulk or even crystalline and amorphous material. Lee[44] was able to show that the effect of an insulating overlayer on a metal is similar to that observed for semiconductors[117]. An oxide film reduces σ_{1xx} and also the Kerr effect. It does not shift the transition energies observed in ellipsometry. However, a shift in the peaks of the Kerr spectra was seen by Lee[44]. Since the Kerr effect is not a physical property of the material oxide effects should be discussed in terms of absorption coefficients or optical conductivity. Considering all the uncertainties we think it is not possible to make corrections that reflect the real situation. After careful sample preparation we will therefore use the measured optical constants without corrections. For further discussion of this subject we refer to an article by Aspnes[44] who investigated oxide effects on semiconductor surfaces in more detail.

In Fig. 5.16 we see three distinct absorption peaks in σ_{1xx}. There is a main peak centered at 2 eV for all three compounds. This transition is also observed in the heavier aluminides, as shown in Fig. 5.15. However, in the Lu and Yb compound the transition occurs at a lower energy, about 1.8 eV. In Ref. [115] the same transition in $CeAl_2$ and $LuAl_2$ was observed at about 1.8 eV. It becomes clear that there is a difference of about 0.2 eV. There is another transition between 2.8 and 3 eV which is at about the same energy in all three compounds. This peak was also seen in Ref. [115] and it appears at 3.8 and 4 eV in $YbAl_2$ and $LuAl_2$, respectively. The spectrum of $LaAl_2$ also shows a weak shoulder at about 4 eV which can hardly be discriminated in σ_{1xx} for $CeAl_2$ and is simply too weak to be detected for the

Pr compound. If we take a look at the dispersive part of σ_{xx} (lower panel of Fig. 5.16) this assignment of another transition at higher energy is clearly confirmed and even in $PrAl_2$ there is a weak structure around 4 eV. It is likely that this much weaker transition cannot be seen in the spectra of the heavier rare-earths since the more prominent peak is shifted to higher energies and actually coincides with it. From inspection of σ_{2xx} we notice a small shift of the 3 eV absorption peak for heavier elements whereas the ones at 2 and 4 eV remain at constant energy.

In Fig. 5.17 we show the optical conductivity of $LaAl_2$ and compare it with the result of our BS calculation. The dashed line is the conductivity in the sharp limit as obtained from the matrix element calculation. We then include a lifetime broadening of 0.2 eV and a self-energy correction with $\lambda = 0.2$ as described in Section 3.3. It may be noticed that the lifetime broadening is rather small. Usually a broadening of 0.4 eV gives reasonable agreement[43]. However, the effect of the self-energy correction described by Eq. (3.32) is not only a shift of the peaks in the conductivity spectra but also a broadening (sharpening) of the structures when λ is positive (negative). We reduce the lifetime broadening in the case of a positive self-energy parameter to counteract the additional broadening caused by the self-energy correction. The calculated conductivity shows a first peak at 2 eV and a second peak around 3.1 eV. These two peaks can also be seen in the experimental data. Using the dispersive part of σ_{xx} we identified a third transition at 4 eV which gives a weak shoulder in σ_{1xx}. The unbroadened spectrum shows a transition at 4 eV as well as two at higher energies which give a broad feature centered at 4.5 eV in the corrected spectrum. The spectrum including self-energy correction and lifetime broadening is in excellent agreement with experimental data, the only difference being a larger amplitude of the calculated conductivity. This is a common phenomenon and can be ascribed to a sample surface that is not ideal, i.e. it may have dislocations, an oxide overlayer, or distortions due to surface treatment. Our calculation fails completely for $CeAl_2$ and $PrAl_2$. The calculated spectra do not show the absorption peak at 2 eV that was obtained for $LaAl_2$ and can be seen in all three experimental spectra. This clearly indicates that the $4f$ states in the Ce and Pr compound are not treated appropriately. We would also like to mention that from our calculation it was not possible to identify the two peaks below 1 eV that were assigned to transitions involving f states[115]. From the similar shape of the experimental spectra we conclude that f related transitions do not contribute between 1.5 and 5.2 eV. As shown the conductivity for all three compounds can be reproduced from a calculation of $LaAl_2$ which supports our result that there are negligible (if any) f contributions.

Figures 5.18 and 5.19 show the magneto-optic Kerr spectra obtained for $CeAl_2$ and $PrAl_2$. Due to small light intensity it was not possible to obtain ellipticity data for $CeAl_2$. We therefore used the

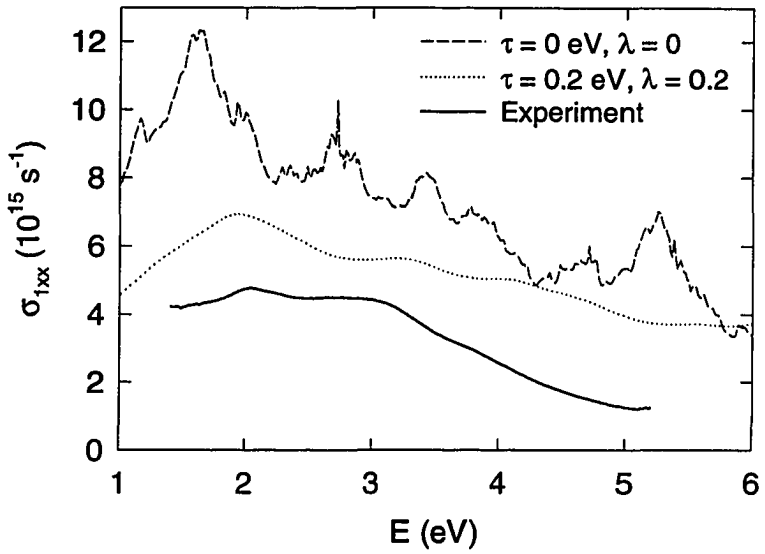

Figure 5.17 Optical conductivity of $LaAl_2$. Shown is only the absorptive part σ_{1xx}. The dashed line shows the conductivity in the sharp limit, i.e. no lifetime broadening and no self-energy correction. The dotted line is the same spectrum with a self-energy correction parameter λ=0.2 and a lifetime broadening of 0.2 eV. The thick solid line shows experimental data taken from Fig. 5.16.

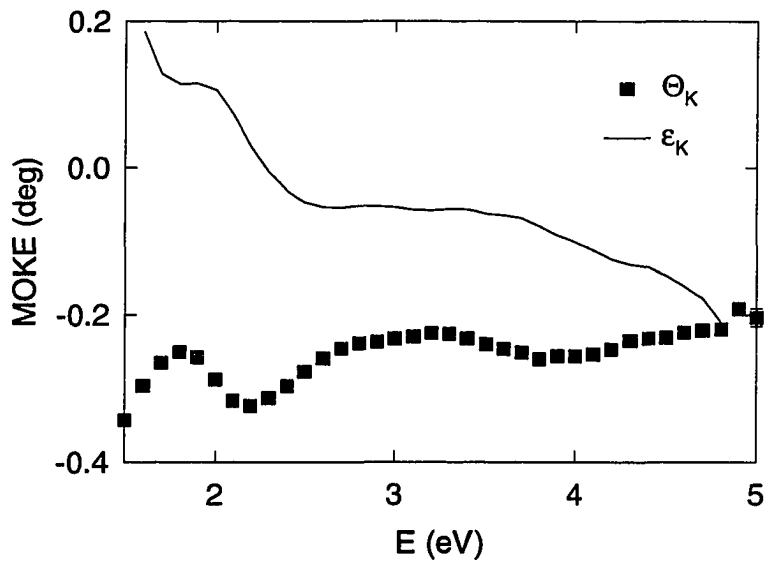

Figure 5.18 Magneto-optic Kerr effect of $CeAl_2$. ■ shows Θ_K at 2.7 K and a field of 70 kOe. The solid line represents ϵ_K obtained from Kramers-Kronig transformation.

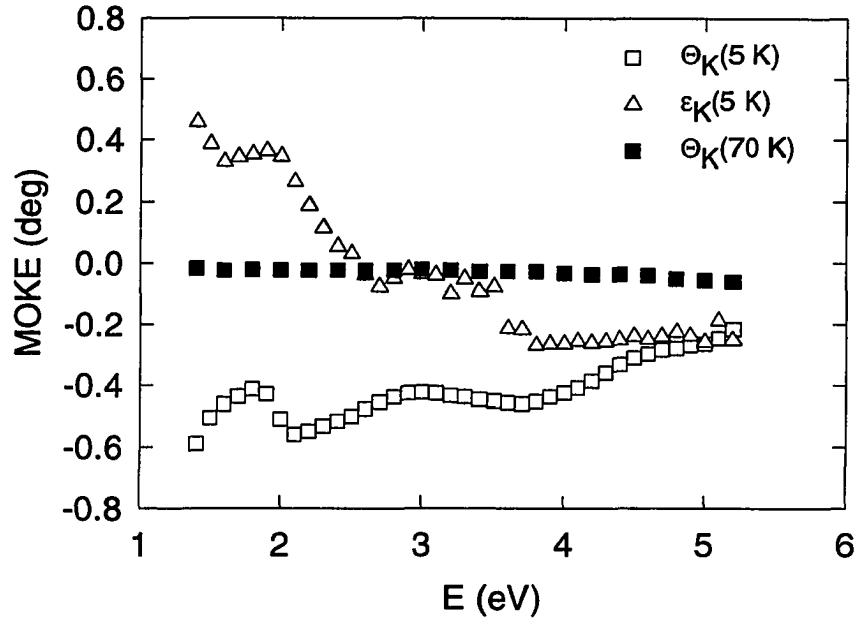

Figure 5.19 Magneto-optical Kerr effect in $PrAl_2$. For comparison we also show a spectrum taken above the ordering temperature (T_C=33 K).

Kramers-Kronig transformation to calculate the ellipticity from the measured Kerr rotation. Data for $CeAl_2$ were taken at 2.7 K and a field of 70 kOe. Referring to the magnetization data shown in Fig. 5.3 this field is sufficient to induce ferromagnetic spin-alignment. Since the ordering temperature of $PrAl_2$ is an order of magnitude higher than that of $CeAl_2$ we measured Kerr spectra at 5 K in a field of 10 kOe which is sufficient to reach saturation, as shown in Fig. 5.4. The spectra for both compounds are very similar, showing a negative Kerr rotation over the entire spectral range. Under the given conditions $PrAl_2$ has a magnetic moment that is at least a factor of three larger than that of $CeAl_2$. However, the amplitude of the Kerr rotation is only twice that found in $CeAl_2$. We notice a first maximum in the Kerr rotation at 1.8 eV followed by a minimum at 2.2 eV. This low energy structure dominates the magneto-optic spectra in these compounds. At 3 eV we have a very weak peak in the Kerr rotation which can be identified as a shoulder in the ellipticity data. There is another weak minimum at 3.8 eV. At higher energies the Kerr rotation returns to zero.

Next we measured the field dependence of the Kerr rotation. Figure 5.20 shows Θ_K versus field for $CeAl_2$. The upper panel shows data taken at the energy of minimum Kerr rotation in Fig. 5.18. For temperatures below T_N we have a very sharp metamagnetic transition to field-induced ferromagnetism. It should be noted that the spectra for 2.7 K and 3.3 K are basically identical whereas data taken at 2.1

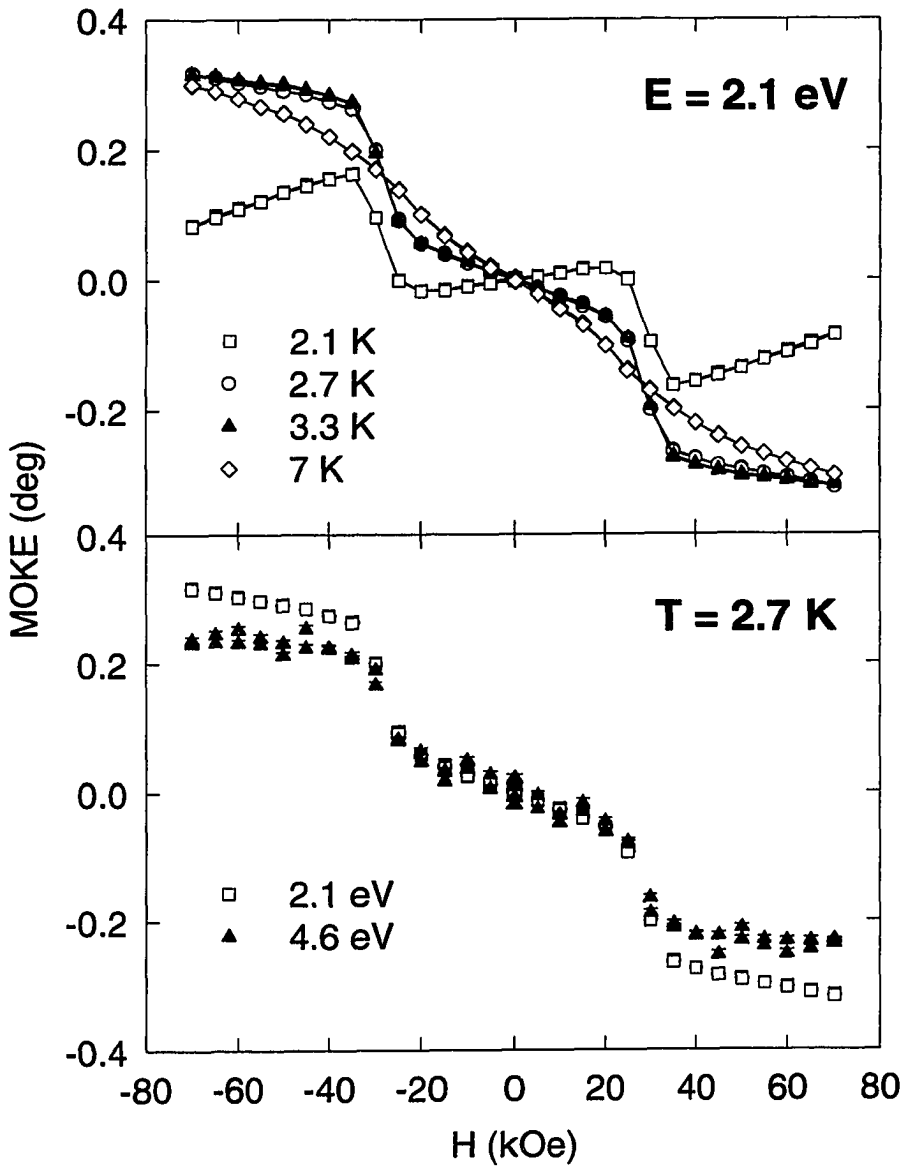

Figure 5.20 Field dependence of the Kerr rotation. Field scans at constant energy are shown in the upper panel. Note the difference between the spectra below and above $T_N = 3.8$ K. The metamagnetic transition to a field-induced ferromagnetic structure begins at 30 kOe. The lower panel shows the energy dependence of the saturation behavior of Θ_K below T_N.

K are clearly different. The Kerr rotation is smaller than at higher temperatures and we attribute this to stronger antiferromagnetic interactions at lower temperatures. Furthermore we note a decrease of the Kerr rotation with increasing field. This is unusual since magnetization data indicate an increase of the magnetization, even at lower temperatures. Similar anomalies have been observed in CeSb[13]. Pittini *et al.*[13] explained this as the "direct contribution of the external field to the Kerr rotation" which is not obvious to us. Even at 7 K, which is above T_N, we can still identify the phase transition which is already too small to detect in the magnetization data we obtained at 3.3 K (Fig. 5.3). Our Kerr rotation data show stronger saturation effects than those observed in M(H) although complete saturation of the Kerr rotation cannot be achieved up to 70 kOe. The lower panel of Fig. 5.20 shows data taken at 2.7 K at different parts of the spectrum. The curves are very similar indicating the proportionality of the spin-polarization of the states involved in the transitions observed at 2.1 and 4.6 eV. The data taken at 4.6 eV show more noise due to i) lower light intensity at higher energies and ii) technical problems taking Kerr loops at higher energies where an increased Faraday rotation of the cryostat windows leads to large jumps in the Kerr signal as we scan the magnetic field. This latter problem could be overcome by appropriate corrections to the data acquisition program. The phase transition occurs between 40 and 50 kOe in M(H) and around 30 kOe in the Kerr spectra. Since the anisotropy in this compound is small we believe that this is due to different samples used in both measurements.

Figure 5.21 shows similar scans for $PrAl_2$ at 2.1 eV. Below T_C we observe ferromagnetic behavior with an increasing hysteresis at lower temperatures. At 5 K the Kerr rotation saturates at nearly 0.6° in an external field of 10 kOe. The Kerr rotation in this sample is proportional to the magnetization shown in Fig. 5.4. As expected the Kerr rotation is strongly reduced above the ordering temperature. In order to check the energy dependence of Θ_K we took Kerr loops at different energies. In Fig. 5.22 we show the normalized Kerr rotation and it is obvious that the transitions at both energies are of similar origin.

As seen earlier, Kerr rotation and ellipticity can be calculated from the optical parameters, i.e. the optical conductivity tensor. However, since the conductivity describes absorption we calculated the absorptive part of the off-diagonal conductivity $\omega\sigma_{2xy}$. Intraband contributions to σ_{2xy} are proportional to ω^{-1} and the free-electron contribution shows up as a constant (shift) in Figs. 5.23 and 5.24. Again the absorption spectra are very similar. We can identify two peaks at 2.1 and 3.8 eV in $CeAl_2$ and 2.1 and 3.4 eV in $PrAl_2$. Then absorption decreases towards higher energies and there might be another transition above 4.5 eV which gives a weak shoulder in σ_{2xy} for both compounds. Comparing the off-diagonal with the diagonal conductivity we believe that the feature at 2.1 eV is due to $p \rightarrow d$

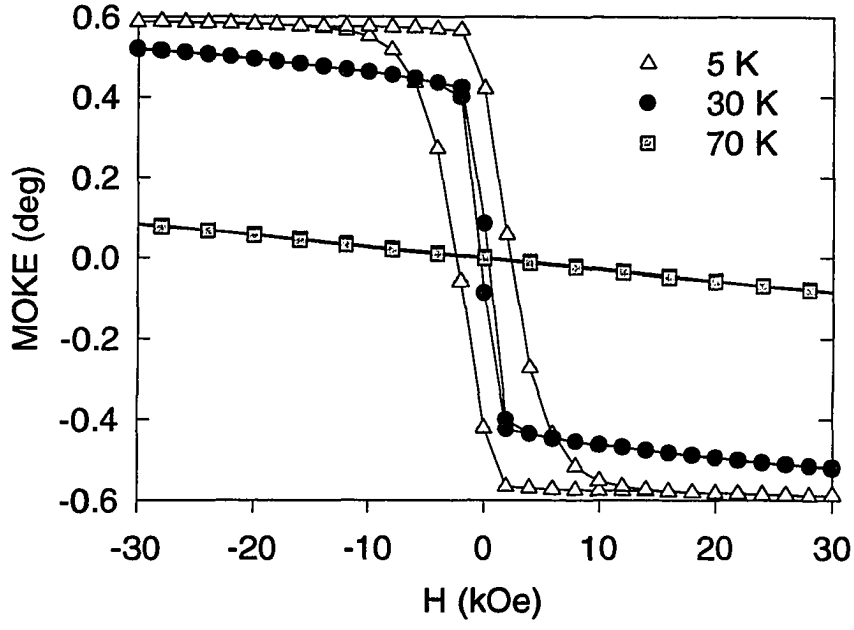

Figure 5.21 Kerr rotation versus field for $PrAl_2$ at 2.1 eV.

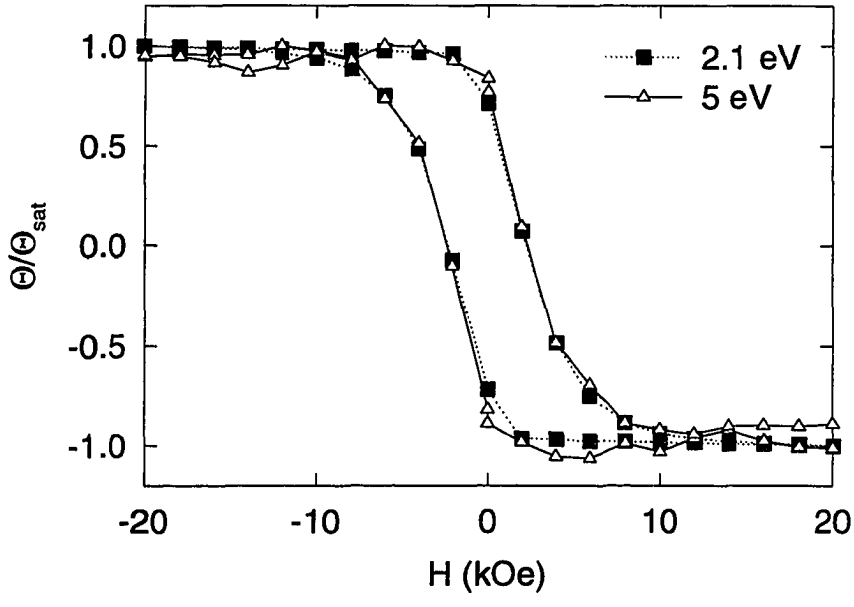

Figure 5.22 Energy dependence of the saturation Kerr rotation. The plot shows the normalized Kerr rotation versus field at 2.1 and 5 eV.

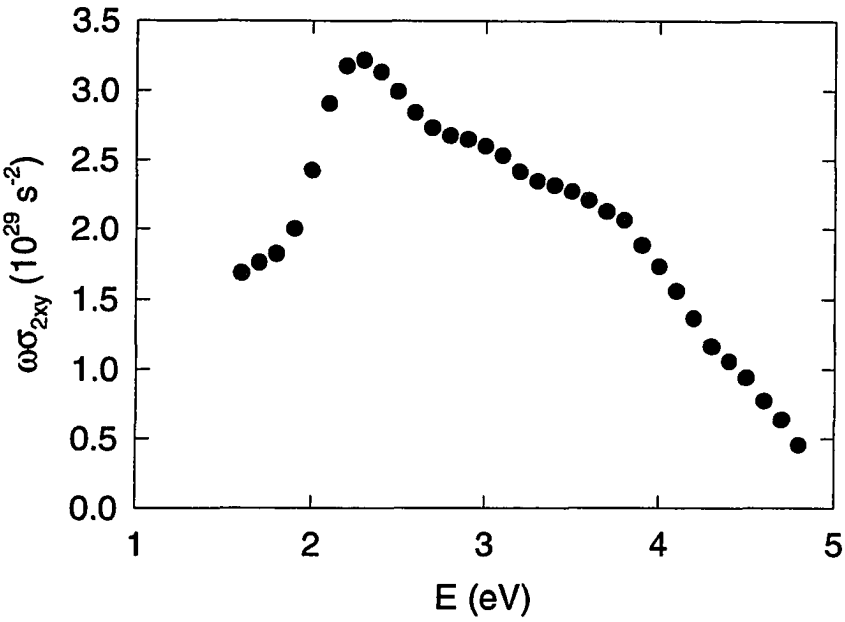

Figure 5.23 Absorptive part of the off-diagonal optical conductivity of $CeAl_2$ calculated from the optical data in Figs. 5.16 and 5.18.

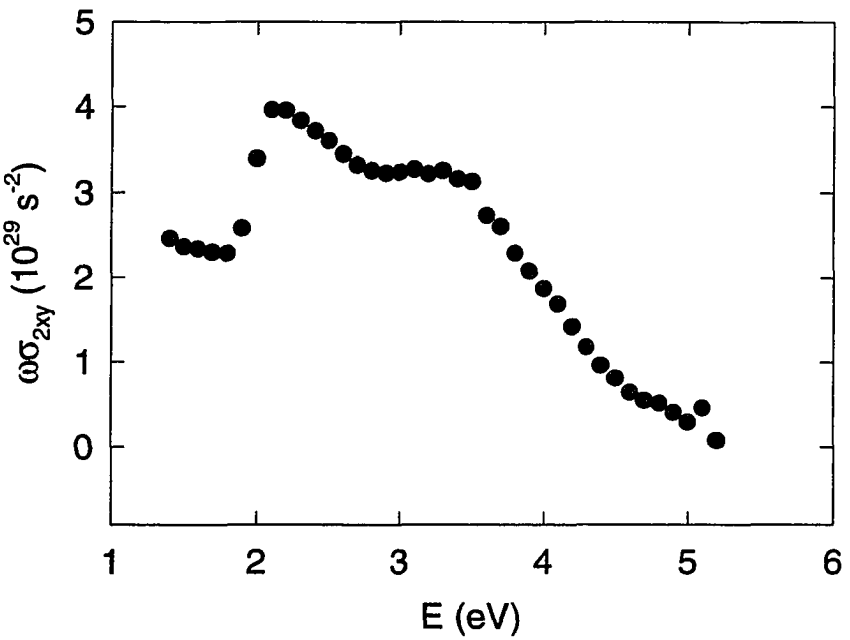

Figure 5.24 Absorptive part of the off-diagonal optical conductivity of $PrAl_2$ calculated from the optical data in Figs. 5.16 and 5.19.

transitions. The higher energy transition, which shows a redshift in $PrAl_2$ with respect to the Ce-compound, is tentatively assigned to $s \rightarrow p$ and $d \rightarrow p$ transitions. Since spin-orbit splitting for p states is small $s \rightarrow p$ transitions do not give a large contribution to σ_{xy}. However, due to large matrix elements they might be the major contribution to σ_{xx} at the same energy. The shift of this peak seems to be related to Ce. $PrAl_2$ shows transitions which are very close in energy to those observed in heavier rare-earth compounds (as shown in Fig. 5.15). This blueshift of the 4 eV absorption peak in $CeAl_2$ is therefore associated with the special role of Ce in this compound. Strong hybridization, as evidenced by the Kondo effect and the reduced moment observed even at temperatures exceeding T_K, gives rise to strong distortion of the conduction states in the vicinity of E_F. This can also be seen from the BS in Figs. 5.9 and 5.12. Below E_F the bands are very similar, the only difference being a larger spin-orbit splitting for $PrAl_2$. We therefore suggest that a distortion of the final state leads to the observed shift of that absorption peak. This can be understood from the DOS plots (Figs. 5.11 and 5.14). The majority spin DOS in both compounds is qualitatively very similar. For both spins we observe a complex with strong rare-earth-d and Al-p character 2 eV below E_F. We also note a peak in the Al-p derived DOS just above E_F which cannot be seen in $CeAl_2$. Transitions occur to empty $5d$ states up to 2 eV above E_F which hybridize with $4f$ derived bands. Comparing the DOS for $CeAl_2$ and $PrAl_2$ leads to the conclusion that the very small exchange splitting in the Ce compound is causing this difference. $PrAl_2$ (in general compounds with heavier rare-earth elements) shows a much larger splitting and the $5d$ minority spin DOS is shifted to higher energy.

5.5 Conclusions

In this chapter we have shown the optical and magnetooptical properties of RAl_2 with R=La, Ce, Pr. Similarity of the spectra for all three compounds showed that the $4f$ electrons do not contribute to the diagonal optical conductivity in the spectral range between 1.4 and 5.4 eV. However, they are highly spin-polarized and lead to a fairly large magneto-optic Kerr effect in $CeAl_2$ and $PrAl_2$. The spectra are governed by transitions involving mostly d states. Magneto-optic measurements in the infrared are needed to confirm the assignment of $d \rightarrow f$ and $f \rightarrow d$ transitions below 1 eV observed earlier[115]. From the field dependence of the magneto-optic Kerr effect it becomes clear that the states involved in transitions around 2 and 4.7-5 eV are proportional to the magnetization. This corresponds to an increasing rare-earth $5d$ moment which is induced by $4f$ electrons through intraatomic coupling. Band structure calculations produced spin magnetic moments which agree well with experiment as well as previous calculations. If we also calculate the orbital contributions to the total moment the agreement

is worse for $CeAl_2$ and LDA predicts zero moment for $PrAl_2$. This is a well known problem in local density functional theory which cannot treat localized $4f$ states correctly. Despite this failure we found fairly good agreement for the optical conductivity in the case of $LaAl_2$. Absorption peak positions as well as magnitude agree well with experiment. It shows that $4f$ states do not contribute directly to this part of the optical spectrum.

6 OBSERVATION OF A METAMAGNETIC PHASE TRANSITION IN AN ITINERANT 4f SYSTEM VIA THE KERR EFFECT: $Ce(Fe_{1-x}Co_x)_2$

6.1 Introduction

The nature of the anomalous magnetic properties of $CeFe_2$ has been of great interest for at least two decades. RFe_2 compounds with heavy rare-earths have a high ordering temperature, a large magnetocrystalline anisotropy, and a reasonably strong magneto-optic signal, which makes those materials suitable for magneto-optic device applications. $CeFe_2$ clearly is an exception. The ordering temperature is reduced to below room temperature. This already indicates some kind of instability which is manifested in a low temperature antiferromagnetic structure upon alloying with small amounts of Al, Co, or Ru[119, 120, 121, 122]. The lattice constant of $CeFe_2$[123] is smaller than expected for a rare-earth-Fe_2 compound containing a trivalent Ce ion. XPS indicates that, in fact, the Ce ion is close to the tetravalent state in $CeFe_2$. This contradicts the results of neutron scattering experiments which indicated a considerable magnetic moment which originates from $4f$ and $5d$ contributions. It is believed that $CeFe_2$ is an itinerant magnet, similar to UFe_2[124, 125], in which the $5f$ overlap is strong enough to broaden the usually localized $5f$ states into bands. Recently, strong antiferromagnetic fluctuations were found in the ferromagnetically ordered state of $CeFe_2$[123]. It emerges that our understanding of $CeFe_2$ is still poor. We decided to perform magneto-optic measurements on $CeFe_2$ to gain more insight into the electronic structure of this intriguing compound. In order to be able to separate out contributions from the $4f$ states we performed the same experiments on the Y analogue which has no $4f$ electrons but behaves chemically similar to RFe_2. We then investigated a $Ce(Fe_{1-x}Co_x)_2$ alloy from which we hope to learn more about the character of the metamagnetic phase transition and how it relates to the magneto-optical signal.

6.2 Sample preparation and characterization

Rare-earth-Fe_2 compounds were grown by the flux growth technique out of a Ce rich flux[83, 84, 85]. The crystals were grown from Ames Lab 99.995% Ce, Ames Lab 99.99% Y, and 99.999% Fe,Co from Union Carbide. The flux growth yielded plate-like crystals, with the plane of the plates perpendicular to [111]. The YFe_2 and $CeFe_2$ crystals were about $3\times5\times2$ mm^3 and had clean surfaces. No further surface treatment was necessary and we used the as-grown crystals for our experiments. It was then attempted to substitute some of the Fe to obtain $Ce(Fe_{0.8}Co_{0.2})_2$. It turned out that Co is less likely to grow in this structure and, as will be shown later, only 10% of the Fe was substituted. This growth produced crystals of octahedral morphology about $3 \times 3 \times 3$ mm^3 in size with clean triangular facets. As for the other samples of this group, polishing was not necessary giving the best samples possible for reflection experiments. However, unlike the aluminides discussed in the previous chapter, RFe_2 compounds are rather reactive and complete oxidation of a sample surface can occur in as little as one hour, giving the surface a yellowish instead of the typical metallic appearance of an unoxidized surface. Lee encountered this problem when measuring heavy rare-earth-Fe_2 compounds[44]. In many cases samples needed to be polished, which lead to thick oxide overlayers which eventually reduced the magnitude of the optical conductivity. After our samples were removed from the growth chamber and separated from the flux they were immediately sealed in quartz or pyrex. Before sealing it off, the glass tube is evacuated to 20 mTorr and backfilled with high purity argon (99.995%) to about 500 Torr three times. Samples were kept sealed until the optical experiments were performed. Immediately before the optical experiments the glass was broken, the sample epoxied to the sample holder, and transferred into the sample chamber where it was kept in a He atmosphere during the measurements. The sample is in contact with air for no longer than 5 min. Paolasini *et al.*[123] performed neutron scattering on samples grown at Ames Lab and pointed out that $CeFe_2$ is extremely sensitive to thermal shock. They transformed one sample into powder after heating it in one hour from low temperature to room temperature. Slow cooling and heating is therefore necessary with $CeFe_2$ and the Ce-Fe-Co alloy discussed in this chapter. After the magneto-optical experiment we measured the dielectric function on the same samples. Since we are not able yet to perform ellipsometry in vacuum or an inert atmosphere, the samples were exposed to air for up to 30 min during the measurement. Before each scan we polished the surface with 0.05 μm alumina to remove any oxide that might have formed on the surface. Ellipsometric spectra were within 2%, which is considered the accuracy of our instrument. However, oxidation of the top layer occurs on a much shorter time scale (on the order of ns for Al) and there will always be a native oxide overlayer if the measurements cannot be performed under UHV conditions.

RFe_2 compounds crystallize in the same cubic $MgCu_2$ Laves phase that was described in Chapter 5. The crystal structure is shown in Fig. 5.1. The lattice constants for YFe_2[126] and $CeFe_2$[123] are 7.363 and 7.304 Å, respectively. These values were also used for the band structure calculations discussed in Section 6.3. In Fig. 6.1 we show the lattice constant and Curie temperature for the RFe_2 series. From the small lattice parameter as well as from the suppressed ordering temperature it becomes clear that $CeFe_2$ plays a special role and does not behave like the *common* RFe_2 compounds. Similar anomalies are observed for $CeCo_2$ and $CeNi_2$. For comparison we included the lattice constants for those two compounds in Fig. 6.1. $CeNi_2$ is paramagnetic and $CeCo_2$ is an exchange-enhanced paramagnet with a Stoner product of 0.95, i.e. the compound is close to a magnetic instability. According to the Stoner model for itinerant electrons, a stable ferromagnetic state exists if the Stoner product, $UN(E_F) > 1$, where $N(E_F)$ is the DOS at the Fermi energy and U describes the interaction which tends to increase the number of majority spin electrons[127]. The lattice constant of $CeFe_2$ is much smaller (similar to that of $HoFe_2$) than expected for a compound containing tripositive Ce, indicating valence fluctuations[128]. Olcese[128] investigated a number of Ce compounds and determined the Ce valence from the observed ionic radius. According to his study we will find Ce^{4+} in CeB_{13}, CeB_6 (discussed later), and $CeSi_2$ but Ce^{3+} in $CeGe_2$ and $CePb_3$, to name a few. It turned out that the lattice parameter is an appropriate criterion to predict the valence of the Ce ion. However, it does not allow one to assign a specific valence, as was done in spectroscopy. X-ray absorption at the Ce L_3 edge shows two distinct absorption peaks which are assigned to $2p^*4f^15d^26s^2$ and $2p^*4f^05d^36s^2$ final states. $2p^*$ denotes a $2p$ core hole. From the integrated intensities of the two peaks, Croft *et al.*[129] assigned a valence of 3.3 to the Ce ion in $CeFe_2$. A classification of compounds containing Ce was suggested by Neifeld *et al.*[130] who distinguished the compounds by the L_3 derived valence estimate v. For $3.00 < v < 3.12$ materials show a competition of (local moment) magnetism and Kondo-type valence spin-fluctuation phenomena. $CeAl_2$ which we discussed in Chapter 5 shows all the characteristics of this group. We pointed out earlier the strong competition between interactions favoring magnetic order and the Kondo effect in $CeAl_2$. In the intermediate regime, which is assigned a valence $3.13 < v < 3.25$ there is a mixture of both valence states and the ground state can be described as a combination of $4f^1$ and $4f^0$. A total loss of the local $4f$ moment and a strong volume collapse characterize the saturated regime for which the spectroscopically derived valence is $3.26 < v < 3.35$. According to Croft et al.[129] $CeFe_2$ belongs to the saturated regime. This is also supported by the reduced volume (see Fig. 6.1). We will return to this topic when we discuss the magnetic moments in $CeFe_2$ obtained from magnetization measurements and later when we present the results of our BS calculation.

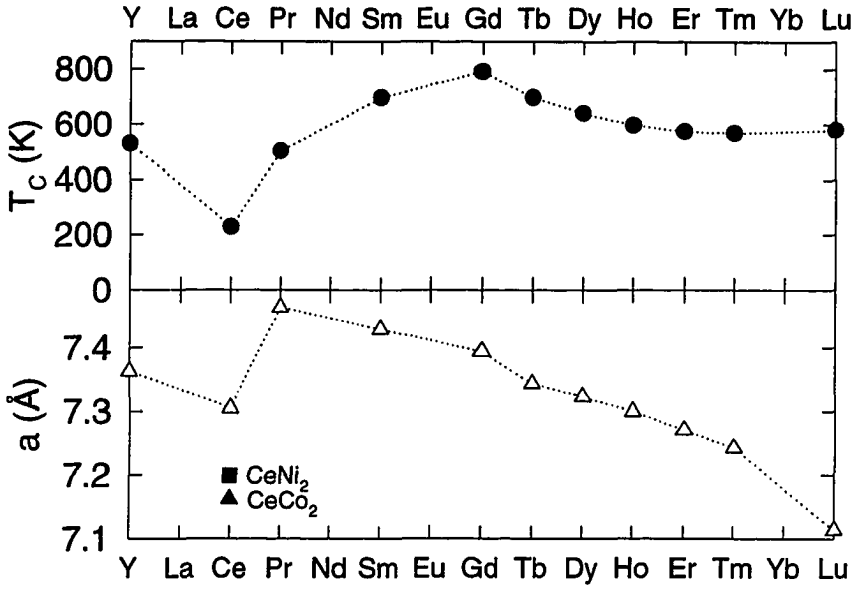

Figure 6.1 Lattice constant (a) and Curie temperature (T_C) of rare-earth-Fe_2 compounds[131]. Notice the special position of $CeFe_2$. Its lattice constant indicates an itinerant $4f$ state as does the reduced T_C.

In order to characterize the samples we performed magnetization measurements on all specimens[93]. Figure 6.2 shows M(H) for YFe_2 taken at 5 K. YFe_2 is a ferromagnet with an ordering temperature of 528 K[132]. At 55 kOe, which is the limit of our instrument, we measured a saturated moment of $2.91\mu_B/YFe_2$. This is the same value obtained by Buschow and van Stapele who measured the magnetization for many RFe_2 Laves phase compounds at 4.2 K[126]. First the moment was entirely assigned to Fe assuming zero moment at the Y site. Later polarized neutron studies by Ritter *et al.*[133] revealed a Y moment as large as $-0.67\mu_B$ coupled ferrimagnetically to an Fe moment of $1.77\mu_B$. These results agree with our magnetization data. The easy direction of magnetization in this compound is along [111], i.e. along the surface normal.

We show M(T) for $CeFe_2$ in Fig. 6.3. Measurements were taken in an external field of 1 kOe. The upper panel shows M/H between 100 and 350 K, and emphasizes the anisotropic behavior that we also found in M(H) (see Fig. 6.5). The low field magnetization data shown here indicate a spontaneous magnetization along [111] that amounts to roughly 60% of that in the (111) plane. Forsthuber *et al.*[134] reported that the easy axis is along [001] below 132 K, above which temperature the moments deviate by about 20° from the edge of the cube. In the lower panel of the same figure we plot χ^{-1} which already allows us to roughly determine the ordering temperature. From a fit of inverse χ above 280 K we obtained $T_C = 240$ K. By plotting $d(\chi T)/dT$ (shown in the inset; a technique usually reserved

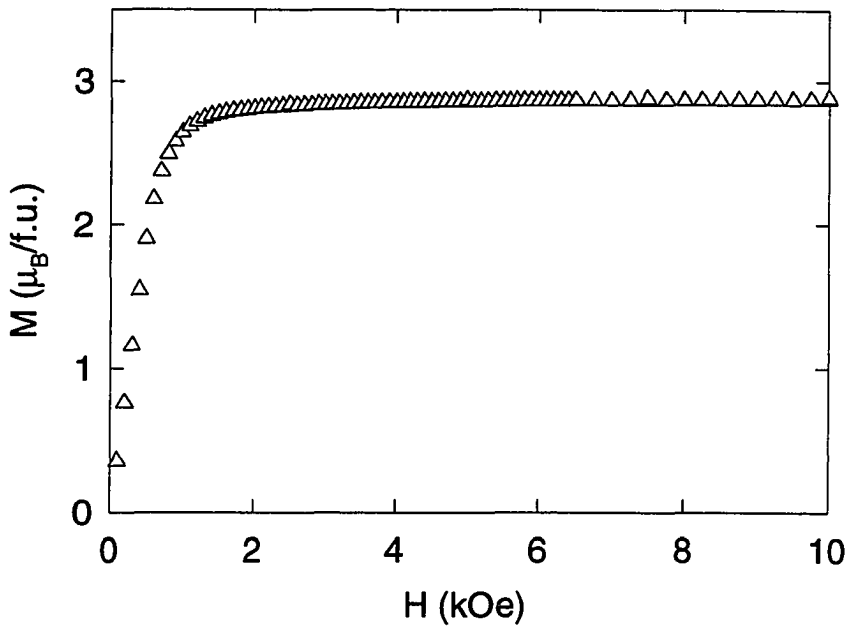

Figure 6.2 Magnetization versus field of YFe_2 at 5 K for an arbitrary field direction. At 50 kOe the saturated moment is $2.91\mu_B/YFe_2$.

for antiferromagnets, for which this quantity is proportional to the magnetic component of the heat capacity), we are able to identify a sharp feature that we associate with T_C. The value obtained by this method is 228 K, which is very close to the value obtained from the inverse susceptibility shown in Fig. 6.3. A proper determination of T_C requires detailed M(H) data for temperatures above and below the ordering temperature. In Fig. 6.4 we show M^3 versus field between 220 and 250 K with the field applied parallel to [111]. Above 2 kOe, M^3 depends linearly on the magnetic field. The high-field data are then extrapolated to zero field and the temperature for which the extrapolation intersects the origin defines T_C. From the plot in the lower panel of Fig. 6.4 we estimate $228\ K < T_C < 230\ K$. This is in excellent agreement with the 230 K measured by Farrell and Wallace[135]. From χ^{-1}, an effective moment of $4.87\mu_B$ was derived. This cannot be compared to any free ion moment (as was done for RAl_2 in the previous chapter) since in this compound we have (1) more than one magnetic ion contributing to the total moment and (2) itinerant (instead of localized) $4f$ electrons which make the interpretation of an effective moment difficult. In the case of $3d$ compounds, or itinerant magnets in general, one usually finds an effective moment that is larger than the saturation moment[127]. This is in agreement with the large effective moment observed for $CeFe_2$.

In Fig. 6.5 we show M(H) data obtained at 10 K for a $CeFe_2$ single crystal. We notice again the

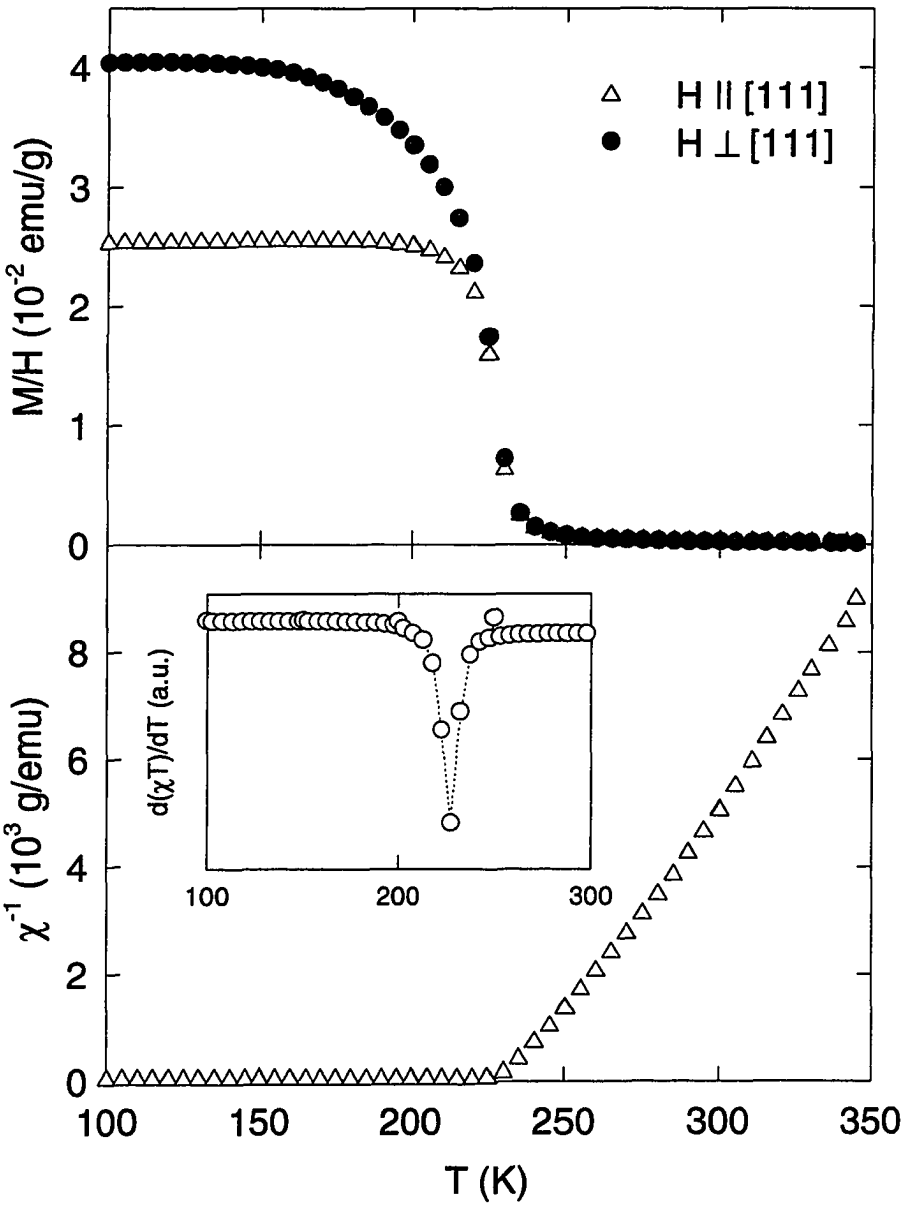

Figure 6.3 M/H (upper panel) and inverse χ (lower panel) for $CeFe_2$ at 1 kOe. Data shown in the lower panel were taken with $H||[111]$. The inset shows the corresponding $d(\chi T)/dT$ indicating a T_C of 228 K.

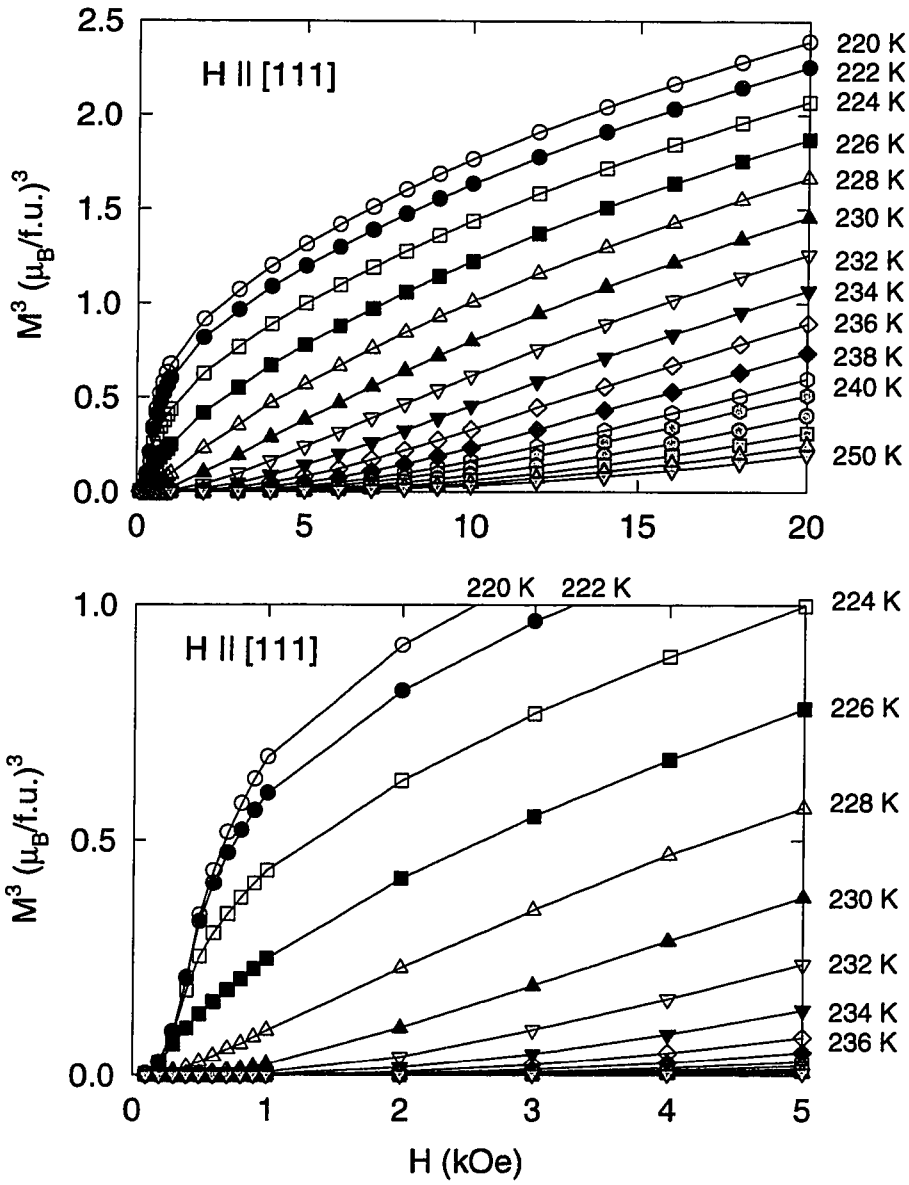

Figure 6.4 Third power of the magnetization as a function of applied field for temperatures between 220 and 250 K. From the lower plot we estimate a Curie temperature between 228 and 230 K.

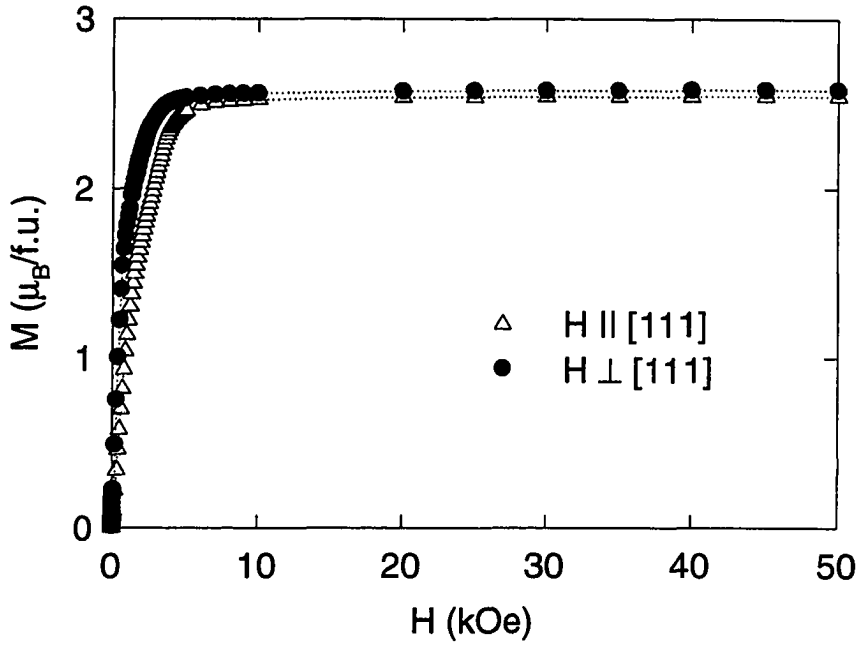

Figure 6.5 Magnetization versus field for $CeFe_2$ at 10 K. The easy direction of magnetization is perpendicular to [111]. The saturated moment for H⊥ [111] is $2.58\mu_B/CeFe_2$ at 55 kOe.

magnetic anisotropy in this compound. As seen from that plot, the easy axis is perpendicular to [111], i.e. in the surface plane. The anisotropy is small and the saturated moments differ by less than 2%. The moment reached at 55 kOe for a field applied parallel [111] is $2.55\mu_B/CeFe_2$. This is the same alignment that we used in our optical experiments (Section 6.4). In early neutron scattering experiments only an Fe moment could be resolved and no contribution from the Ce ion was detected. However, high temperature susceptibility indicates a Curie constant that is too large to be attributed solely to the Fe ions. It was concluded that there is a contribution from Ce which was also observed in later experimental studies employing polarized neutrons[136], XMCD[137, 138, 139], Compton scattering[140], and nuclear magnetic resonance (NMR)[141]. Kennedy *et al.*[142, 121] already noticed reflections that were of antiferromagnetic origin but did not investigate this in more detail. An antiferromagnetic component of $0.15\mu_B$/Fe was estimated. Upon doping with Al, Co, or Ru they found an antiferromagnetic ground state with wave vector $\left[\frac{1}{2}, \frac{1}{2}, \frac{1}{2}\right]$. In the case of $Ce(Fe_{0.8}Co_{0.2})_2$ a lattice distortion from cubic ($\alpha = 90°$) to rhombohedral symmetry with $\alpha = 90.2°$ was found[143, 142]. The most recent results from neutron inelastic scattering on $CeFe_2$ confirmed the antiferromagnetic component in the ferromagnetically ordered state[123]. It is concluded that in $CeFe_2$ there is a strong competition between the ferromagnetic ground state and an antiferromagnetic ground state with the same wave vector that was found earlier

by Kennedy *et al.*[142, 121]. The antiferromagnetic component is about $0.05\mu_B$, superimposed on a $1.2\mu_B$ ferromagnetic Fe-moment. At low temperatures these antiferromagnetic correlations extend over many unit cells. They can also be seen in Mössbauer spectra up to higher temperatures. It is therefore likely that $CeFe_2$ is close to an electronic instability and a small change in electron concentration can establish a stable antiferromagnetic ground state.

Alloying reduces T_C and, as we mentioned above, a low-temperature simple antiferromagnetic phase is found upon substitution of Fe with Co, Al, Ru, Rh, or Pd[119, 120, 121, 122]. In $Ce(Fe_{1-x}Co_x)_2$ a low temperature antiferromagnetic phase is found for $0 < x < 0.3$. For $0.3 < x < 1$ ferromagnetic order persists down to low temperatures. The paramagnetic to ferromagnetic and ferromagnetic to antiferromagnetic phase transitions were observed in neutron scattering[143, 142, 121], susceptibility[119, 120], resistivity and thermopower[122], specific heat[144, 145, 146], and thermal expansion experiments[147]. An abrupt change in the cell volume at the ferromagnetic to antiferromagnetic transition indicates that this is a first-order phase transition. The phase transition from the paramagnetic to ferromagnetic regime is accompanied by a smooth variation in cell volume and is therefore believed to be of second order.

In order to investigate the role of the delocalized $4f$ levels we decided to perform magneto-optical spectroscopy on $Ce(Fe_{1-x}Co_x)_2$. The samples were grown by the flux-growth technique from a pseudo-binary melt with a nominal $x = 0.2$[83, 84, 85]. Figure 6.6 shows magnetization versus temperature for our sample between 0 and 300 K in a 1 kOe applied field. We can clearly identify two magnetic phase transitions. From a plot of $d(\chi T)/dT$ (shown in the lower panel) we find a T_C of 191 K which indicates the paramagnetic to ferromagnetic transition. A fit of the high temperature inverse χ yields an effective moment of $4.97\mu_B$, which is slightly larger than that obtained for $CeFe_2$. The same fit gives 207 K for Θ. Considering the small temperature range available for this fit (up to 350 K) we may say that Θ agrees with the observed T_C. At lower temperature we observe a second phase transition from the ferromagnetic to an antiferromagnetic structure at $T_N = 81$ K. In the upper panel of that figure we indicate the regime of antiferromagnetic (AFM) and ferromagnetic (FM) order. Above T_C the sample behaves paramagnetically (PM). Using the values obtained for T_C and T_N and the phase diagram for $Ce(Fe_{1-x}Co_x)_2$[143, 144, 145, 148, 147] we estimate $8.5\% < x < 10\%$. We obtain a range for x since the magnetization was measured in an applied field and it is well known that T_N is field dependent[147, 148]. For an unambiguous determination of T_N we would need to measure the zero field magnetization. However, for our purposes the exact composition is not crucial and we will assume that $x = 0.1$. This was a little surprising since the nominal x was 0.2. We were aiming at that particular

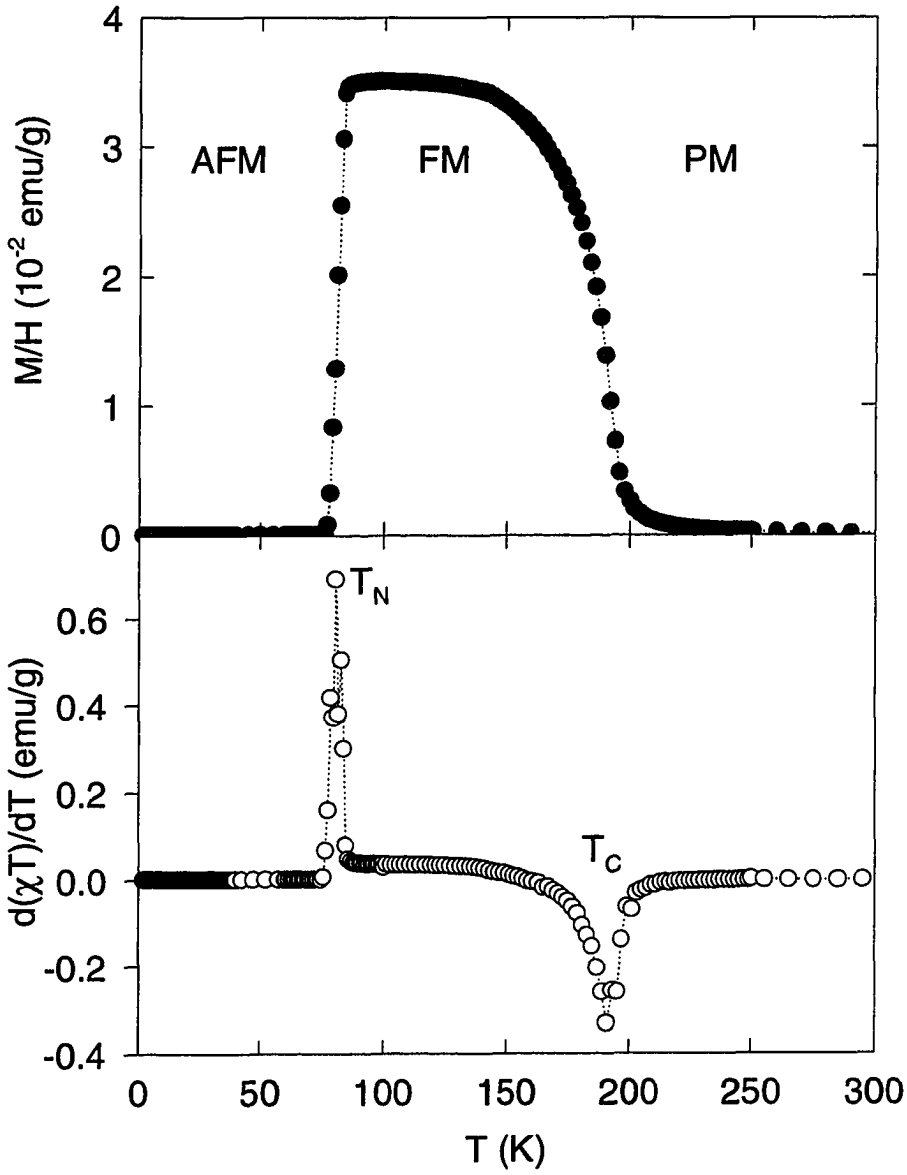

Figure 6.6 Temperature-dependent magnetization of $Ce(Fe_{1-x}Co_x)_2$ with a field of 1 kOe applied perpendicular to [111]. The upper panel shows M/H indicating two phase transitions. We show the antiferromagnetic (AFM), ferromagnetic (FM), and paramagnetic (PM) regime. From $d(\chi T)/dT$, which is shown below, we estimate T_N=81 K and T_C=191 K. Using the phase diagram this leads to x=0.1.

value since, for $x = 0.2$, T_N is at a maximum and T_C is at a minimum[143]. However, since the sample we obtained shows the same magnetic instability, we used this for our experiments.

As in the case of pure $CeFe_2$ the easy direction of magnetization is in the plane, i.e. perpendicular to [111]. For H ||[111] (not shown here) we measured a saturated moment of $2.20\mu_B$/ $Ce(Fe_{0.9}Co_{0.1})_2$ at 50 K. If we apply the field perpendicular to [111], a maximum moment of $2.33\mu_B$ is reached. In Fig. 6.7 we show the magnetization versus field for various temperatures and H $\perp$ [111]. At low temperatures we are in a stable antiferromagnetic regime and even a field of 55 kOe is not sufficient to induce ferromagnetic ordering. At the highest field the moment at 2 and 5 K is below $0.1\mu_B$. A field of about 68 kOe will eventually induce a ferromagnetically ordered state at this temperature. This metamagnetic transition was observed in the high field magnetization by Wada *et al.*[145] and is also found in our spectroscopic data (see Section 6.4). At 50 K the structure becomes unstable at a lower field and we observe a metamagnetic transition between 25 and 30 kOe leading to a field-induced ferromagnetic structure. Below the transition temperature the moment remains below $0.05\mu_B$. Saturation is reached at 50 kOe which is fairly close to the transition. We note some hysteresis which increases with decreasing temperature[145]. Garde *et al.*[122] observed hysteresis effects in the resistivity and thermopower versus temperature of Ru, Al, and Co doped samples. They attributed the hysteresis to the coexistence of ferromagnetic and antiferromagnetic phases. Depending on the alloy this range can be 35 to 50 K wide, as derived from the thermopower of $Ce(Fe_{0.96}Al_{0.04})_2$. Based on neutron experiments, which showed the coexistence of ferromagnetic and antiferromagnetic components even in the parent compound, we believe that the hysteresis in M(H) is also caused by the competition of positive and negative magnetic interactions. At 100 K we have simple ferromagnetic order (compare Fig. 6.6) and saturation is reached at 5 kOe (as the domains align in the applied field). Compared to the data at 50 K, the moment is reduced which is due to thermal disorder. The scan at 250 K indicates a linear field dependence of the magnetization as expected for a paramagnet.

From the magnetization data presented here we were able to characterize the samples. In the case of YFe_2 and $CeFe_2$ the observed moments and transition temperatures are in excellent agreement with earlier results indicating high quality of our samples. This was supported by neutron experiments on samples grown by the same group[123]. From M(T) we were able to determine the composition of the Ce-Fe-Co alloy and we estimated 10% substitutional Co. Again magnetization data indicate high quality single crystals. In the following section we will present the theoretical work we performed on this class of materials before we return to the experimental findings in section 6.4.

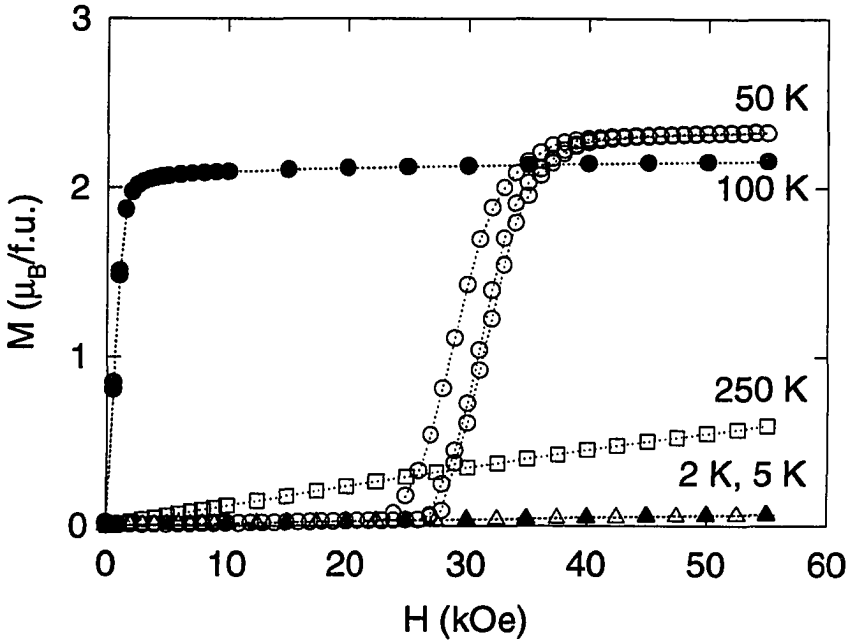

Figure 6.7 M(H) for $Ce(Fe_{0.9}Co_{0.1})_2$ with H⊥ [111].

6.3 Electronic structure and $4f$ band magnetism

In this section we will describe our theoretical work on YFe_2 and $CeFe_2$. Over the past decade rare-earth compounds have been the subject of many LDA studies due to their intriguing electronic and magnetic properties. For an excellent review on this topic we refer to an article by Brooks and Johansson[125] who investigated the ground state magnetic properties of compounds containing rare-earths and actinides. As we will see, actinides, especially U compounds, behave very similarly to Ce compounds. Before presenting our results we would like to summarize the results of previous work.

The first electronic structure calculations for Y intermetallic compounds were published by Yamada *et al.*[149]. Using a self-consistent recursion method and a tight-binding approximation they were able to calculate the DOS and magnetic moments of YM_2, with M being one of the transition metals Mn, Fe, Co, or Ni. The intra-atomic exchange integrals U_Y and U_{Fe} were chosen in such a way as to match the experimentally observed total moment. They derived a moment of $1.58\mu_B$/Fe and $-0.29\mu_B$/Y which are in fair agreement with later calculations. The moment on the Y site is only half of the moment determined from neutron scattering[133]. The first self-consistent spin-polarized electronic structure calculation were carried out by Mohn and Schwarz[150]. They used the augmented spherical wave method (ASW) to investigate the binding mechanism in YFe_2 and $ZrFe_2$. They explained the

magnetism, especially the ferrimagnetic coupling of Y and Fe moments, on the basis of hybridization between Fe-3d and Y-4d states. The coupling is the same we find in itinerant $CeFe_2$ which we will describe shortly (see also Fig. 6.8). An Fe-induced diffuse spin density gives rise to small magnetic contributions even from s and p bands. In YFe_2 this contribution was found to be as large as $0.12\mu_B$. The total moment derived from their calculation is composed of $1.66\mu_B$/Fe and -$0.42\mu_B$/Y and agrees favorably with experimental results. Later Eriksson *et al.*[151, 152, 153] determined the electronic structure and magnetic properties of many Laves phase compounds using the LMTO technique. Spin and orbital magnetism was of special interest to them. The spin moments reported for YFe_2 agree with earlier calculations. As we would expect for itinerant magnets the orbital moments were found to be small. Finally, there is a report by Rhee[154] on the electronic structure of $LuFe_2$ and YFe_2. It was the first attempt to calculate the optical conductivity of those two compounds. Since the 4f shell is either empty or completely filled, YFe_2 and $LuFe_2$ are suitable for LSDA calculations. The diagonal part of the conductivity agrees well with experimental data. However, there are some major differences between the experimental and calculated off-diagonal conductivity. This might be due to an improper treatment of the 4f states which should be included in the basis set for the optical calculation.

$CeFe_2$ poses another problem for band structure calculations due to the additional 4f charge. Our treatment of RAl_2 in Chapter 5 showed that the LDA fails completely for localized 4f states. However, since experiments revealed strongly hybridized 4f levels and possibly formation of 4f bands in $CeFe_2$, a theoretical approach using the LDA formalism seemed reasonable. Eriksson et al.[151] performed LMTO calculations on $CeFe_2$. They correctly predicted the Ce and Fe moments and the ferrimagnetic alignment which had not been observed at that time. The coupling scheme is shown in Fig. 6.8 and can be understood as follows. The Fe-3d states are lower in energy than the Ce-derived 5d levels. If a moment develops at the Fe site the majority spin band will be lowered and the minority spin band will be shifted to higher energy due to exchange interaction. This increases the energy separation between 3d and 5d states for the majority spins, i.e. the hybridization is reduced. For the minority spin direction the opposite happens and the increased hybridization with the spin-down Fe bands induces a negative 5d moment. Intra-atomic interaction couples the 5d and 4f spins ferromagnetically. In light rare-earths with localized 4f states the orbital contribution to the total moment is much larger than the 4f spin moment and spin-orbit coupling, i.e. Hund's third rule, which requires $J = L - S$ for less than half-filed shells, leads to a ferromagnetic alignment of the Ce and Fe moments. This is shown in the upper part of Fig. 6.8. The lower part shows the coupling for itinerant 4f electrons. Due to band formation the 4f orbital moment is quenched and the total moment on the Ce site is negative, giving ferrimagnetic

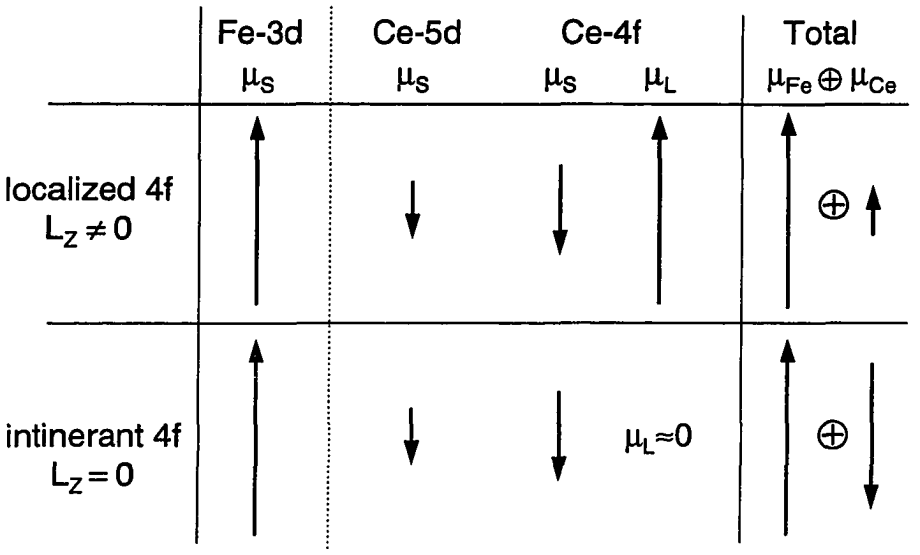

Figure 6.8 Coupling scheme for localized and itinerant $4f$ states in Ce intermetallic compounds. For localized states the large orbital contribution compensates the $5d$ and $4f$ spin moments and the total Ce moment is parallel to the Fe moment. If the $4f$ electrons form bands the orbital moment will get quenched resulting in a ferrimagnetic alignment of the Ce and Fe moments.

order in $CeFe_2$. Eriksson *et al.*[151] treated the Ce-$4f$ electron as itinerant which led to the correct equilibrium lattice constant. This was a first indication that LDA could be used to investigate further the role of hybridization in Ce compounds if the $4f$ states form *reasonably* broad bands (on the order of 2 eV). Using the Stoner criterion for band magnetism it was shown that only $CeFe_2$ would order magnetically, whereas $CeCo_2$ and $CeNi_2$ are non-magnetic. $CeCo_2$ has a Stoner product of 0.95 and is therefore close to a magnetic instability. This was later confirmed by measurements on $Ce(Fe_{1-x}Co_x)_2$ alloys which indicate that alloying of $CeCo_2$ with small amounts of Fe leads to ferromagnetic order at low temperature[143].

Johansson *et al.*[124] pointed out that the situation in Ce intermetallics is very similar to that in the corresponding Y compounds where YFe_2 is magnetic but YCo_2 and YNi_2 are non-magnetic. They also included UFe_2 in their work and found striking similarities to $CeFe_2$, i.e. the $5f$ electrons appear to be rather itinerant in character. This was investigated again in more detail in terms of the hybridization strength[155]. In UFe_2 magnetism is driven by Fe. Replacing Fe by Ni leads to filling of the $3d$ band which in turn reduces hybridization between $3d$ and $5f$ states. In UNi_2 the $5f$-derived peak in the DOS coincides with E_F and we observe magnetism that is driven by U-$5f$ states. This is again very similar to $CeFe_2$ and $CeNi_2$. It was also shown that the position of the $4f^1$ state can be predicted

from LDA if the hybridization is strong enough and the resulting bands wide enough. The agreement between LDA and inverse photoemission (or Bremsstrahlen isochromat spectroscopy, BIS) is excellent for $CeNi_2$ and fair for $CeCo_2$. Best results are obtained for $CeRh_3$ which is believed to be the compound with the strongest hybridization. That LDA can be successfully used to calculate $4f$-band systems was supported by Delin *et al.*[92] who reported the optical conductivity of CeN. Experimental features were well reproduced when the $4f$ states were treated as valence states. All absorption peaks below 5 eV vanished when the $4f$ levels were treated as core states and the spectra were similar to those of the heavier Ce pnictides which show localized $4f$ states. Trygg *et al.*[156] used the full potential LMTO method to investigate the asymmetry of the charge and spin distribution. They also included orbital polarization. The major difference to other calculations is a larger Fe spin moment and an increased orbital component for the Ce-$4f$ level.

Finally we would like to mention the work by Khowash[157]. The anomalous magnetic behavior of CeM alloys was explained in terms of d-d-f hybridization similar to the scheme presented above (Fig. 6.8). The observed instabilities in $Ce(Fe_{1-x}M_x)_2$ were explained by band filling and a reduced hybridization for $x > 0$.

We performed BS calculations for YFe_2 and $CeFe_2$. Experimental lattice constants were used. The WS sphere radii were chosen as 3.379 and 3.350 a.u. for Y and Ce. The Fe radius was 2.759 and 2.735 a.u., respectively. Self-consistent calculations were carried out on a $12 \times 12 \times 12$ mesh giving 72 k-points in the irreducible wedge of the BZ. As basis functions we included Ce-$6s$, $6p$, $5d$, and $4f$ orbitals and $4s$, $4p$, and $3d$ wave functions on the Fe site. For YFe_2 we treated $5s$, $5p$, $4d$, and $4f$ as valence states. The Fe site was chosen as in the case of $CeFe_2$.

Figures 6.9 and 6.10 show the BS and total DOS for the two compounds. Below -3 eV the band structures are very similar and bands are mostly of Fe-s and rare-earth s, p-character. Looking at the lowest bands we notice the larger spin-orbit splitting in the case of $CeFe_2$. We then observe a complex of Fe-derived bands below and crossing E_F. Above 3 eV the BS are again similar. Between -2 and 2 eV we find Ce-$4f$ bands which strongly distort the BS around E_F. Table 6.1 summarizes the results of our self-consistent calculation. First we would like to point out that the charge as well as the magnetic moments on the Fe site are very similar in both compounds. This confirms the assumption that Y and Ce behave chemically similar. The most significant difference is found in the $3d$-charge where we find an increase of 0.05. This is accompanied by a decrease in the magnetic moment which can be attributed to an increased number of minority carriers and a slightly decreased number of majority electrons in $CeFe_2$. This can be understood in terms of hybridization of Fe-derived states with states originating

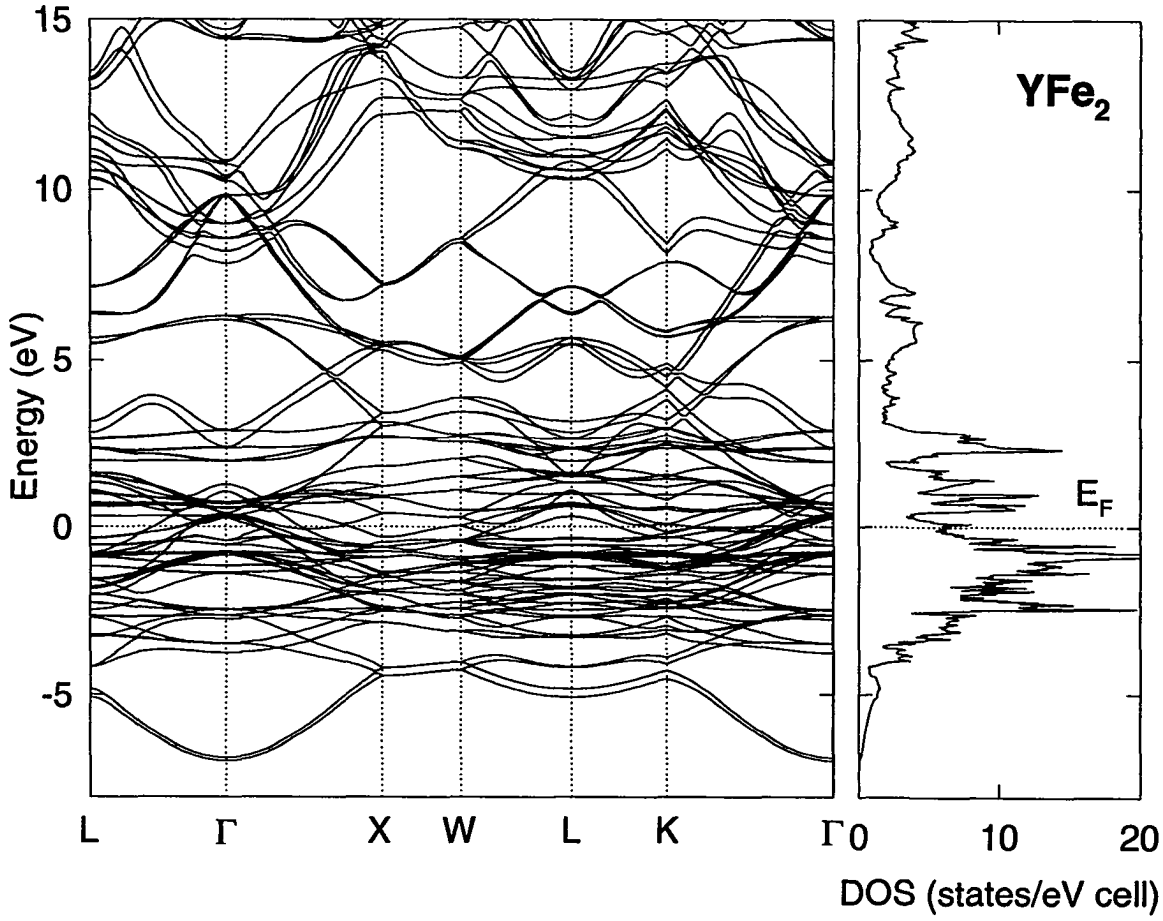

Figure 6.9 Spin-polarized relativistic band structure and total DOS for YFe_2 including spin-orbit splitting.

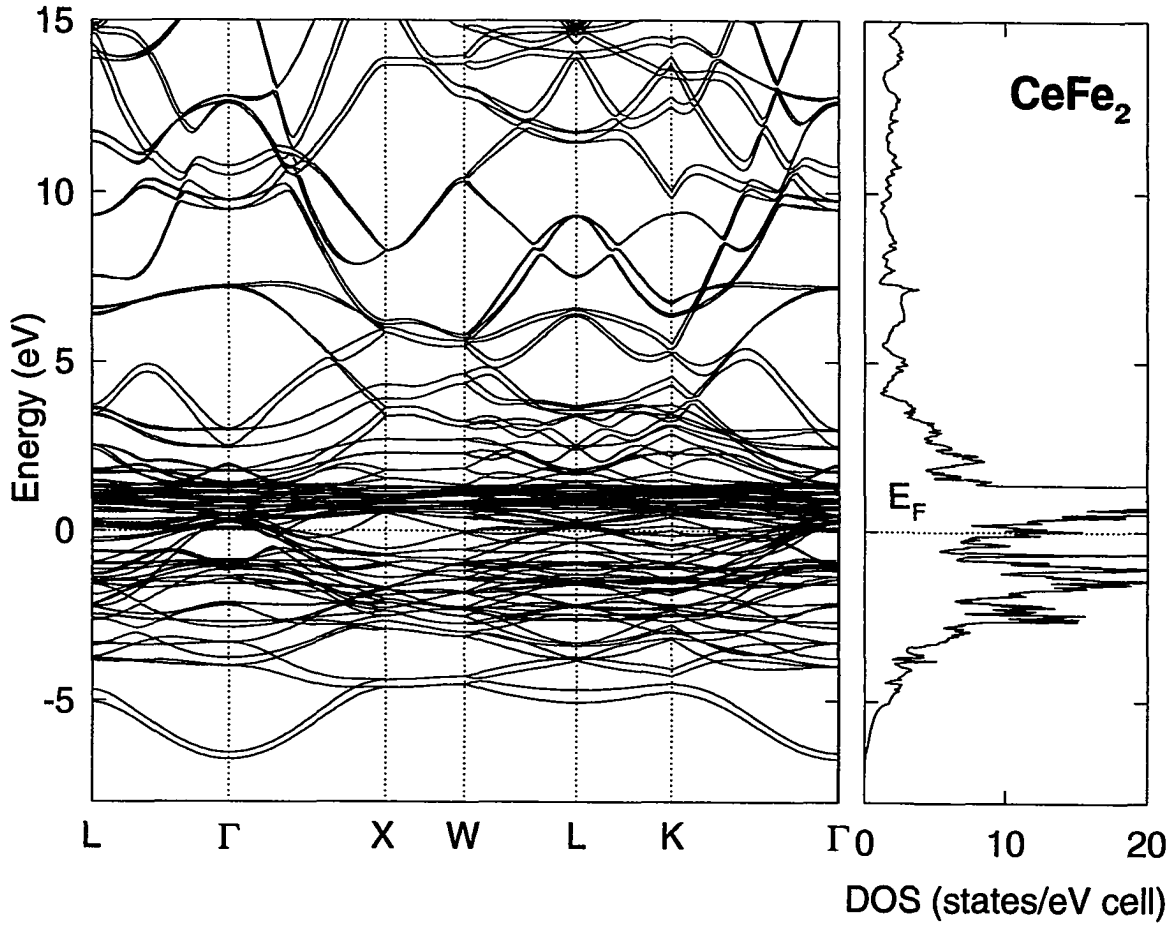

Figure 6.10 Spin-polarized relativistic band structure and total DOS for $CeFe_2$ including spin-orbit splitting.

Table 6.1 Charges and moments within the Wigner-Seitz sphere for YFe_2 and $CeFe_2$ as obtained from self-consistent spin-polarized band structure calculations including spin-orbital coupling. Charges are given in electrons, moments in μ_B/ion, and $N(E_F)$ in states/eV cell.

	Rare-earth					Fe			
	s	p	d	f	Total	s	p	d	Total
YFe_2									
$n_\downarrow$	0.30	0.37	0.95	0.07	1.69	0.36	0.38	2.44	3.18
$n_\uparrow$	0.25	0.27	0.64	0.07	1.23	0.35	0.32	4.19	4.86
$n_\downarrow + n_\uparrow$	0.55	0.64	1.59	0.14	2.92	0.71	0.70	6.63	8.04
μ_S	-0.05	-0.10	-0.31	0.00	-0.46	-0.01	-0.06	1.75	1.68
μ_L	-	0.00	0.00	0.00	0.00	-	0.00	0.05	0.05
$N(E_F)$	0.17	0.18	0.65	0.06	1.06	0.07	0.78	4.68	5.53
$CeFe_2$									
$n_\downarrow$	0.22	0.20	1.05	0.79	2.27	0.35	0.37	2.54	3.26
$n_\uparrow$	0.18	0.18	0.80	0.38	1.54	0.35	0.34	4.14	4.83
$n_\downarrow + n_\uparrow$	0.40	0.38	1.85	1.18	3.81	0.70	0.71	6.68	8.09
μ_S	-0.04	-0.02	-0.35	-0.42	-0.73	0.00	-0.03	1.60	1.57
μ_L	-	0.00	0.01	0.12	0.13	-	0.00	0.06	0.06
$N(E_F)$	0.13	0.19	0.67	3.27	4.27	0.08	0.86	6.33	7.27

from the rare-earth site. The magnetic moment on Y is due to $4d$ electrons which carry about 2/3 of the total moment. In $CeFe_2$ $5d$ and $4f$ states contribute about 50% each to the total magnetic moment. Since the mixing of Fe-$3d$ with Y-$4d$ states is stronger than that with Ce-$5d$,$4f$ states, the induced moment of the Fe site is larger in YFe_2. The rare-earth-s charge remains unchanged but the charge in the Ce-$6p$ channel is only 60% of what we find in the Y-$5p$ orbital. In addition, in the case of YFe_2, the p orbitals contribute $-0.1\mu_B$ to the spin-moment. This is rather large considering that the s and p states can be considered conduction bands and can usually be neglected in terms of their magnetic contribution. The d charge and moment found in both compounds is very similar. The $4f$ states, which are empty in Y and do not carry a magnetic moment, are clearly the major difference between the two compounds. In $CeFe_2$ we find a total of 1.18 electrons within the WS sphere. The occupancy, which depends sensitively on the sphere radius, is the same as found by Eriksson *et al.*[151]. Finally, we notice that the total charge difference on the Y and Ce site is about 1, which is due to the additional $4f$ charge on Ce.

The DOS at the Fermi level can be compared to experimental data, specifically the linear specific

heat parameter γ (Eq. (5.1)). YFe_2 has a total of 6.59 states/eV cell which is derived from Fe-3d (71%), Fe-4p (12%), and Y-4d (10%) states. This results in γ = 15.5 mJ/K^2 mol which agrees favorably with the 12.3 mJ/K^2 mol observed experimentally[158]. For $CeFe_2$ we obtained a DOS at E_F that is nearly twice that observed in YFe_2. Strong mixing with the Ce-4f bands leads to an increase of the rare-earth-derived DOS by a factor of 4. The difference is due to the 4f channel since the DOS for the other orbitals remains constant. The Fe-3d DOS can be seen to be increased due to mixing with the f orbitals. Still, the value for γ derived from this calculation (27.2 mJ/K^2 mol) amounts to only 50% of that observed by Roy and Coles[119]. This indicates a considerable electron-phonon interaction. The 53 mJ/K^2 mol measured for $CeFe_2$ is very close to the value of 45 mJ/K^2 mol reported for UFe_2 by Franse *et al.*[159]. UFe_2 also shows similarities in the magnetic behavior and transport properties and can be considered the 5f analogue of $CeFe_2$.

Let us take a closer look at the DOS for the two compounds. Figures 6.11 and 6.12 show the site and orbital decomposition of the DOS for YFe_2. The major contribution can be seen to be due to Fe-3d states. We find a peak in the total DOS at E_F which shows mostly Fe character. This leads to a Stoner type instability, i.e. magnetic order, in this compound. The minority spin band on the Fe site is split by about 1.8 eV separating filled and empty 3d states. Empty Y-4d states are predicted between 2 and 3 eV above E_F, strongly mixed with Fe-d minority spin bands. From Fig. 6.12 we see that strong mixing induces a peak in the DOS of the Y-4d minority spin carriers about 0.8 eV below E_F as well as an increased DOS for Fe-p states. This is the main peak in the minority DOS below E_F for Y and results in the negative magnetic moment observed at the Y site. It should be noted that even s states are mixed with higher orbitals leading to large contributions between -2 and -4 eV (upper panel).

When we compare the DOS for $CeFe_2$ (Figs. 6.13 and 6.14) with that of $CeAl_2$ (Figs. 5.10 and 5.11) we first notice that the empty states above E_F, which are mostly Ce-4f states, are broadened in $CeFe_2$. The 4f-bandwidth is about 1.5 eV which should give reasonable agreement between results derived from LDA and experiment. The top of the Ce-4f band is about 1.5 eV above the Fermi level for both spin directions. Whereas in $CeAl_2$ majority and minority spin bands were of equal width and separated by the exchange splitting, this is not as clear in $CeFe_2$. The center of mass of the f minority spin band is shifted to lower energy by band broadening due to strong mixing with Fe-3d states. This leads to a tail that extends to nearly 2 eV below E_F, giving a negative spin polarization on the Ce site. The Fermi energy is seen to coincide with a peak in the DOS derived from Fe-d and Ce-f states. The contribution of Fe-3d states is about the same as found in YFe_2. However, the splitting of the 3d minority spin band is reduced, giving a 4 eV wide d-band with a high DOS that extends from below to

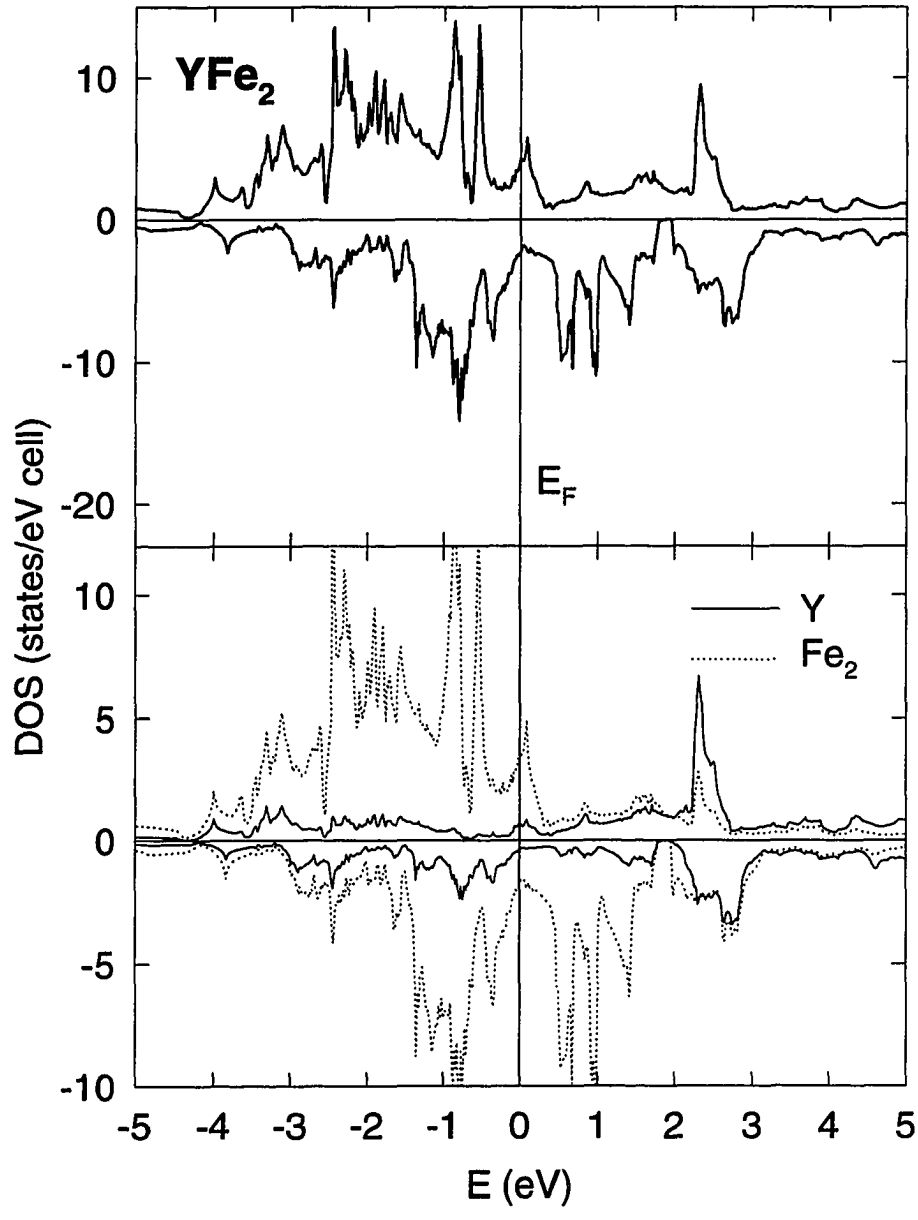

Figure 6.11 Total DOS for YFe_2 (upper panel) and partial DOS.

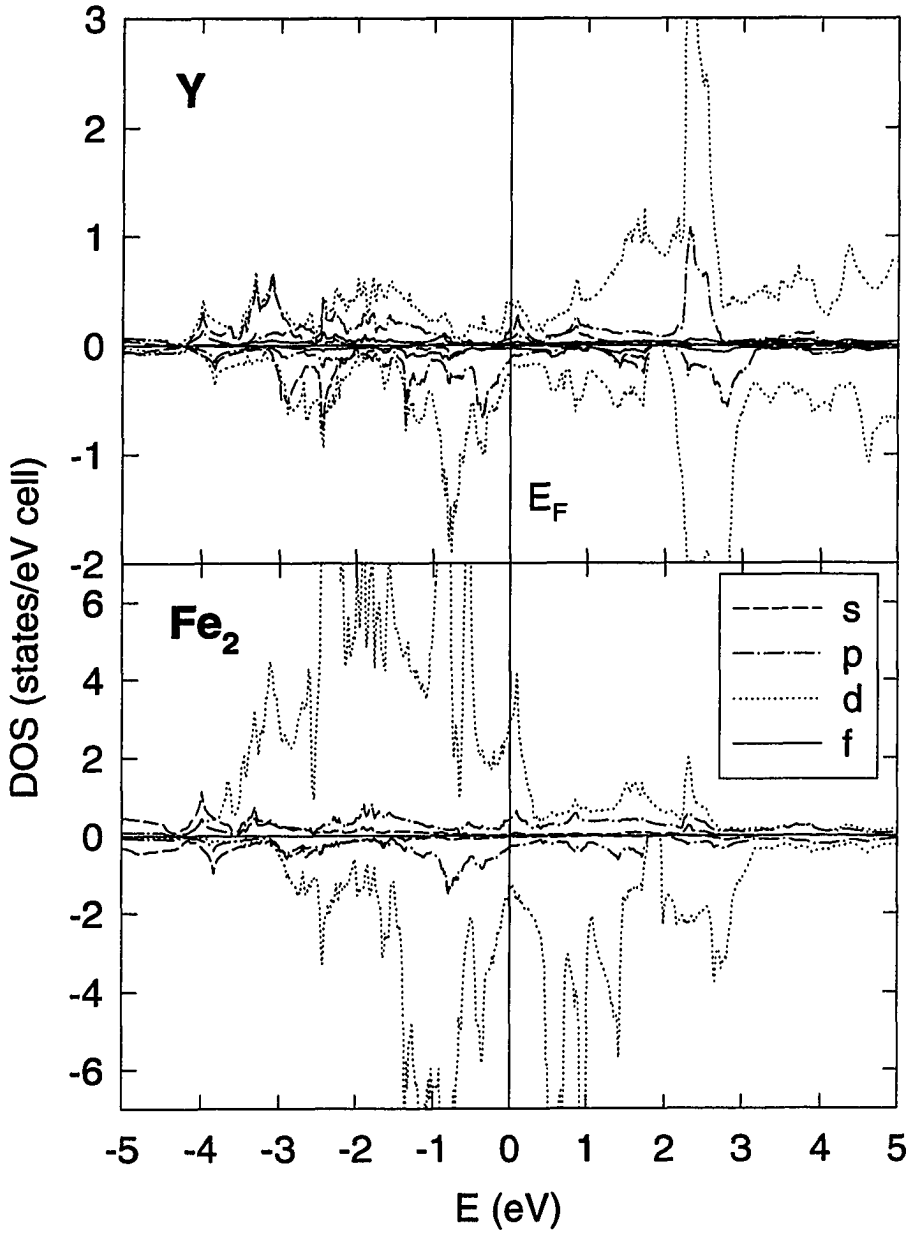

Figure 6.12 Orbital decomposition of the DOS for YFe_2.

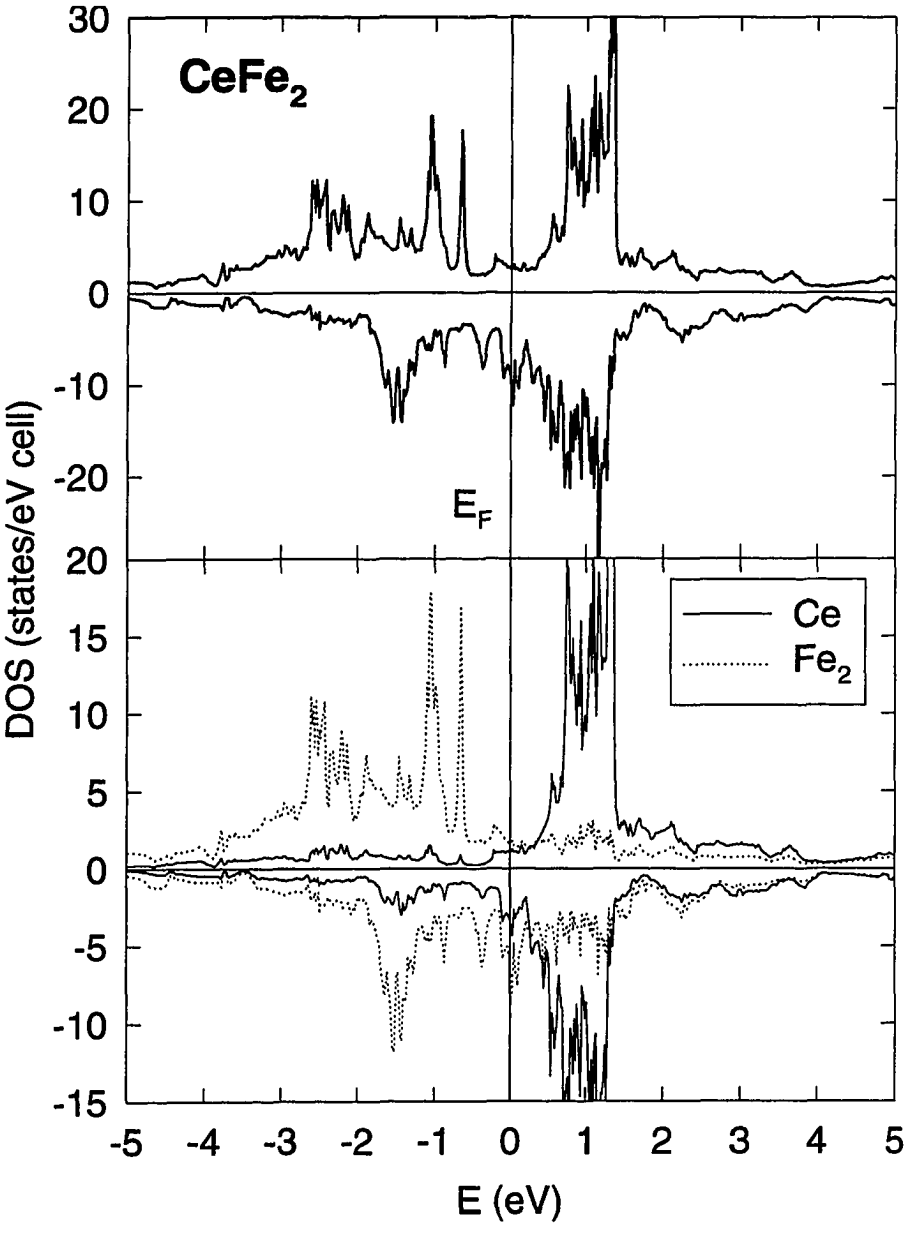

Figure 6.13 Total DOS for $CeFe_2$ (upper panel) and partial DOS.

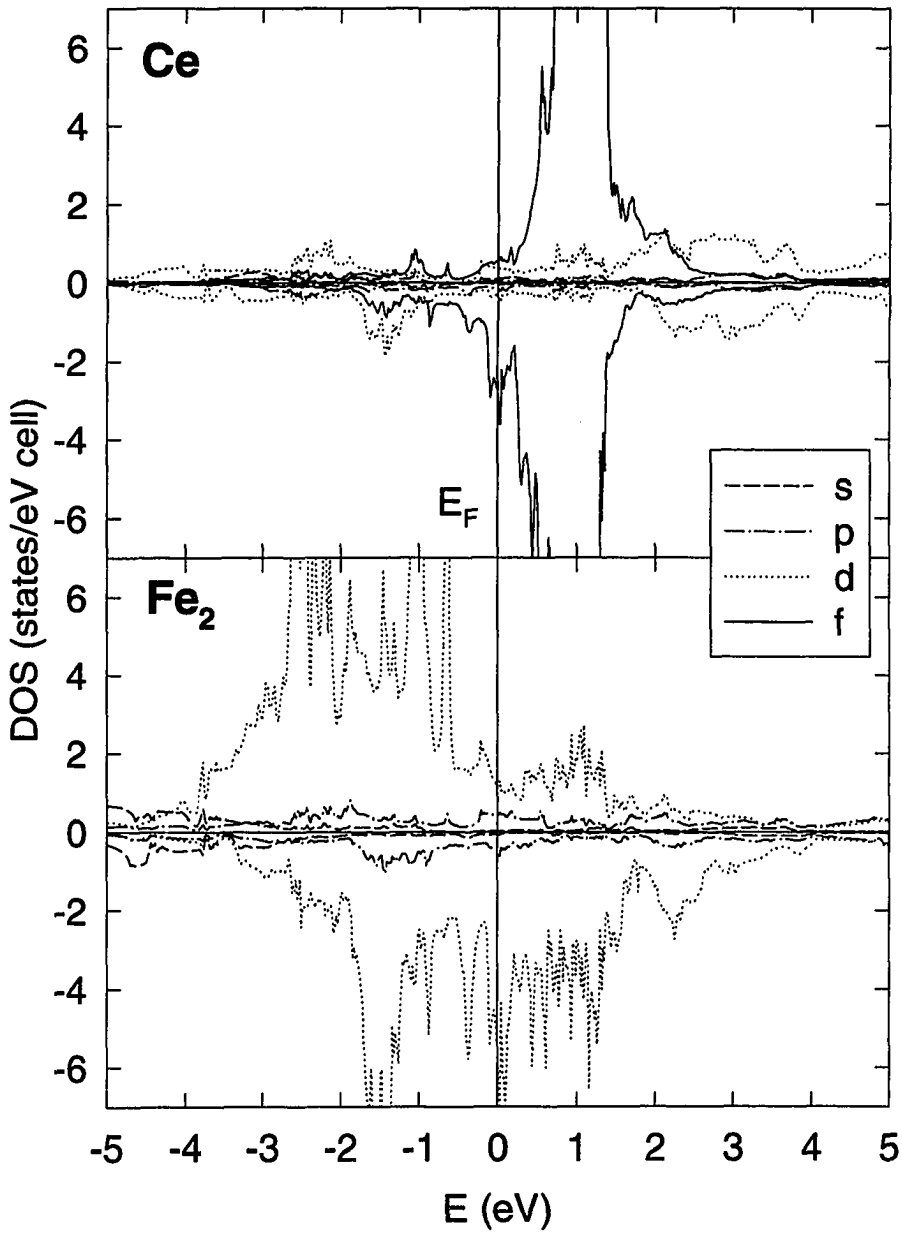

Figure 6.14 Orbital decomposition of the DOS for $CeFe_2$.

above E_F. The magnetic instability in $CeFe_2$ can now be understood in terms of a shift of the Fermi level due to a change in the carrier concentration. Alloying with Co adds d electrons and eventually E_F will be shifted and moved away from the peak in the minority DOS (Fig. 6.13).

Finally we would like to compare the ground state properties predicted by our calculation with other theoretical and experimental results (Table 6.2). We already pointed out that the specific heat coefficient is in agreement with experimental findings. For YFe_2 results agree well with those of Eriksson *et al.*[153]. Experimental data on the orbital decomposition of the magnetic moment are not available to our knowledge. Neutron scattering yields a Fe moment that is only slightly larger than that predicted by our self-consistent calculation. However, we underestimate the magnetic moment on the Y site by 30%. The total moment of $3.00\mu_B/YFe_2$ compares well with the saturated moment of $2.91\mu_B$ obtained from magnetization data. We would like to point out that there are significant differences between our work and that by Rhee[154]. The total moment derived by Rhee[154] is 6% smaller than our result although the same BS programs were used for the calculations. Rhee also found a DOS at the Fermi level that amounts to only 50% of the one deduced from our calculation. The difference is likely to be due to the choice of WS sphere radii and different downfolding used in the BS calculation. It was observed that downfolding can change the magnetic moment by up to $0.1\mu_B$/ion.

In $CeFe_2$ the rare-earth carries a moment that is composed of a spin moment due to $4f$ and $5d$ states as well as a small orbital contribution from the $4f$ states. From neutron studies the $4f$ spin moment was determined to be $-0.10\mu_B$. Later experiments did not confirm a magnetic moment on the Ce site in $Ce(Fe_{0.9}Co_{0.1})_2$. However, it was estimated that a small moment ($< 0.1\mu_B$) could exist on the Ce site. There is some uncertainty in these results since the form factors used to interpret the scattering data were those which were derived earlier for Ce^{3+}. The rhombohedral distortion, observed at T_N, is accompanied by a spin reorientation from [001] to [111]. According to the model by Cullen and Clark[160] the lattice distortion is caused by magneto-elastic coupling. A prerequisite for this effect is the occurrence of a $4f$ magnetic moment. This is supported by LDA calculations which were shown to give an even larger Ce moment. We therefore believe that there is a moment at the Ce site in $Ce(Fe_{0.9}Co_{0.1})_2$.

For $CeFe_2$ our results agree well with earlier LSDA studies, the only difference being a larger moment at the Fe site predicted by our calculation. LDA is known to overestimate the total moment per Fe ion. This results in a magnetic moment per unit cell that is 16% larger than the saturation moment observed experimentally. Spin and orbital contributions on the Ce site are very similar to those derived by Eriksson *et al.*[151]. Especially we notice that the orbital component of the $4f$ moment is strongly

Table 6.2 Site and orbitally decomposed magnetic moment for YFe_2 and $CeFe_2$ as obtained from several different experiments as well as LDA calculations.

	Fe			rare-earth				
	μ_S^{3d}	μ_L^{3d}	μ_{tot}^{3d}	μ_S^{4f}	μ_L^{4f}	$\mu_S^{4d,5d}$	$\mu_{tot}^{d,f}$	μ_{RFe_2}
YFe_2								
Polarized neutrons [133]	1.42	0.35	1.77[2]				-0.67[2,3]	2.87
LSDA [153]	1.82	0.07	1.81[2]				-0.47	3.15
LSDA [154]			1.64[2]				-0.45[2]	2.83
LSDA[1]	1.75	0.05	1.73[2]			-0.31	-0.46[2]	3.00
Magnetization [126]								2.90
Magnetization[1]								2.91
$CeFe_2$								
LSDA [151]	1.41	0.08	1.49	-0.42	0.15	-0.3	-0.57	2.41
LSDA [156]	1.77	0.05	1.82	-0.54	0.19	-0.22	-0.56	3.08
	1.77	0.09	1.86	-0.55	0.29	-0.22	-0.47	3.25
LSDA[1]	1.60	0.06	1.63[2]	-0.42	0.12	-0.35	-0.60[2]	2.66[2]
Polarized neutrons [136]		1.17	1.17	-0.10	0.03	-0.07	-0.14	2.20
Compton scattering [140]	1.40			-0.08		-0.63	-0.71	2.10
	1.18			-0.17		-0.11	-0.28	2.10
XMCD [139]	1.24	0.10	1.34	-0.37	0.21	-0.13	-0.29	2.39
Magnetization [126]								2.48
Magnetization[1]								2.55

[1]This work.

[2]Includes contributions from s and p states.

[3]Composed of $\mu_S = -0.54\mu_B$ and $\mu_L = -0.13\mu_B$.

reduced due to band formation. $5d$ and $4f$ states contribute about 50% each to the total Ce moment. There is still some controversy about the size of the Ce-$4f$ orbital moment. Neutron scattering predicts only very little contribution whereas a fairly large moment of $0.21\mu_B$ was derived from XMCD spectra[139]. Since TB-LMTO assumes spherically symmetric potentials, Trygg *et al.*[156] performed full potential LMTO calculations. They showed that non-spherical spin densities at the Ce and Fe site exist and result in an increased orbital moment for the $4f$ states. However, considering the experimental uncertainties it does not seem justified to conclude that one calculation describes the problem better than another one. It seems that the approximations made in the LMTO method are valid. But we may say that hybridization reduces the Fe moment (compared to α-Fe) and induces a $4f$ bandwidth that quenches the orbital moment of the Ce-f states.

6.4 Optical and magneto-optical response

The magneto-optic Kerr effect of RFe_2 compounds containing one of the heavy rare-earths Gd, Tb, Dy, Ho, or Er was measured by Katayama and Hasegawa[161]. At low energy the room temperature Kerr rotation is positive and it crosses zero between 2.5 and 3.5 eV. $GdFe_2$ is an exception showing positive Kerr rotation over the entire energy range from 1.7 to 5.2 eV. The other compounds show a minimum Kerr rotation around 4.3 eV which is decreasing in magnitude with increasing atomic weight, i.e. the largest Kerr angle, of more than -0.4°, is observed in $TbFe_2$. A weak local minimum is found at 2 eV in the spectra of $GdFe_2$, $TbFe_2$, and $DyFe_2$. This minimum becomes weaker with increasing atomic number and disappears for the heaviest rare-earths in this series. Recently, Lee re-measured the optical properties of some heavy RFe_2 compounds (R=Gd, Tb, Ho, Lu) using single crystals[44, 45]. It was found that the Kerr rotation for polycrystalline $GdFe_2$ is indeed positive for the measured range. Kerr spectra for single crystals of $GdFe_2$ reveal a larger structure than polycrystalline samples at low energy and a zero crossing at 3 eV which leads to a minimum at 3.5 eV. The spectra obtained for a single crystal of $GdFe_2$ are similar to those observed for the heavier elements[161]. Kerr data for $TbFe_2$ and $HoFe_2$ agree with those of Katayama and Hasegawa[161]. However, since Lee had single crystals available and measurements could be performed at low temperatures he found a larger Kerr rotation (up to $-1°$ in $HoFe_2$)[44]. The optical conductivity showed metallic behavior. The absorptive part of σ_{xx} decreases with increasing energy and shows a broad shoulder around 2.5 eV. At higher energies there is an increase in absorption which could be due to small light intensities and is a well-known effect in ellipsometry.

We measured the dielectric function of YFe_2, $CeFe_2$ and $Ce(Fe_{0.9}Co_{0.1})_2$ at room temperature in zero field. As mentioned earlier the samples were exposed to air during the measurements. Before each scan the sample surface was slightly polished with 0.05μm alumina abrasive to remove the oxide overlayer. Figure 6.15 shows the diagonal part of the optical conductivity. The absorptive part (upper panel) of YFe_2 is similar to that of the other rare-earth-Fe_2 compounds measured by Lee[44] and agrees well with the conductivity measured by Sharipov *et al.*[162]. σ_{1xx} decreases monotonically showing a weak shoulder around 2.7 eV. This feature is more pronounced in σ_{2xx}. The two compounds containing Ce are very similar. The small difference in magnitude ($< 10\%$) is likely to be caused by oxidation effects. We also notice an increase of σ_{1xx} above 5 eV which is ascribed to small light intensity which gives a false signal in ellipsometric measurements. The absorption peak found in YFe_2 is washed out in these two compounds. However, analyzing σ_{2xx} we recognize a shoulder at 3 eV which coincides with the maximum found for YFe_2. It seems justified to say that we observe the same basic structure in all

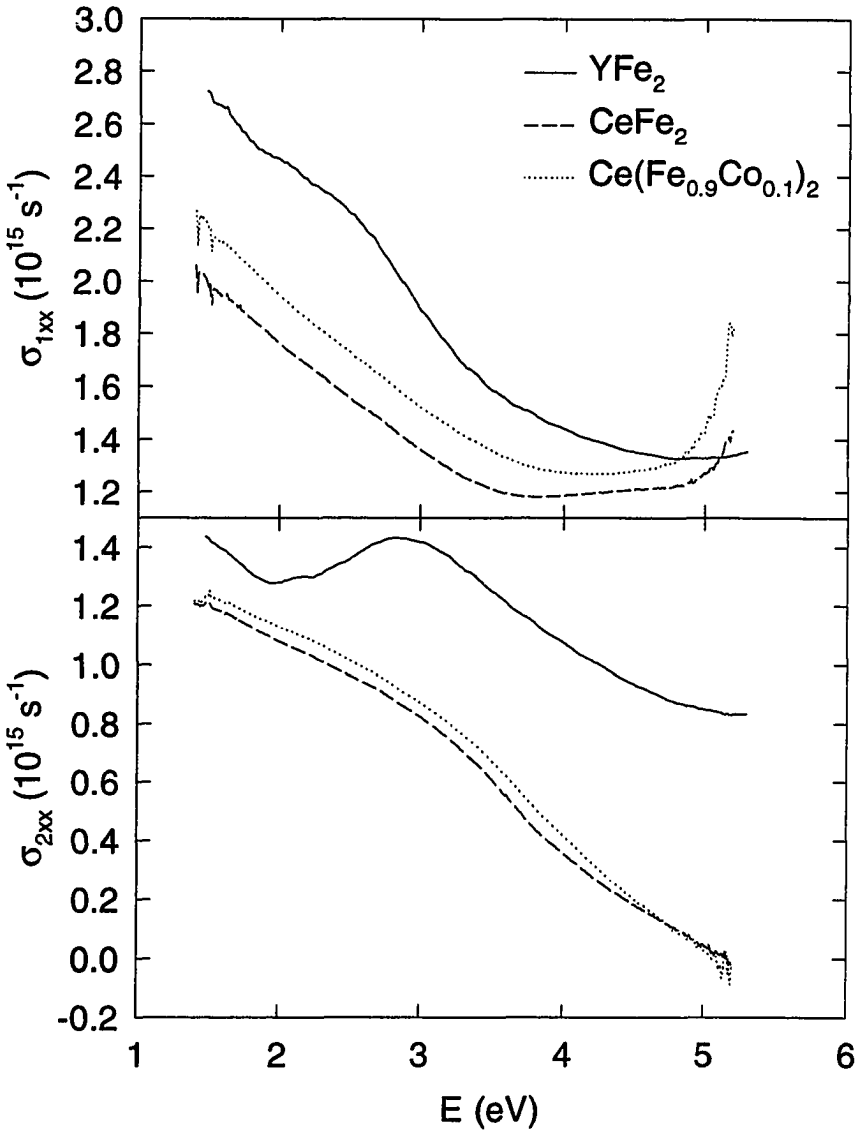

Figure 6.15 Diagonal part of the optical conductivity for YFe_2, $CeFe_2$, and $Ce(Fe_{0.9}Co_{0.1})_2$ measured at room temperature. The upper (lower) panel shows the absorptive (dispersive) part of σ_{xx}.

three compounds with a decrease of the absorption at 2 eV for $CeFe_2$ and $Ce(Fe_{0.9}Co_{0.1})_2$. Rhee found transitions occurring around the Γ point to give the main contribution to the 2.5 eV shoulder in YFe_2 and $LuFe_2$. In Fig. 6.9 we notice a region around Γ where the bands disperse very little, leading to a large DOS. The bands around 0.5 to 1 eV below E_F are of Fe-(p,d) and Y-(p,d) character. Flat bands are also found about 2 eV above E_F. From Fig. 6.11 we see that the bands in that range are of Fe-d as well as Y-d character mixed with equal amounts of Y-derived (s,p) character. Transitions involving p-derived states give large contributions to the optical conductivity and we agree with the assignment suggested by Rhee that the prominent feature in σ_{1xx} originates from transitions around the center of the BZ.

We also measured the Kerr effect of YFe_2 and $CeFe_2$. Figure 6.16 shows the Kerr rotation and ellipticity for the two compounds. YFe_2 was measured at 3.5 K with a 15 kOe field. From the inset we see that the Kerr rotation saturates at 10 kOe which is significantly higher than the magnetization which shows saturation at only 2 kOe at 5 K (Fig. 6.2). The magnitude of the Kerr effect is rather small, reaching a minimum rotation of nearly $-0.3°$ at 4.6 eV. The ellipticity shows a maximum of 0.42° at 4 eV. The overall shape of the spectrum closely resembles that of the heavier RFe_2 compounds[161, 44]. The lower panel shows data for $CeFe_2$ taken at 10 K and 10 kOe. Saturation is reached at 10 kOe (see inset) whereas the magnetic moment was observed to saturate at 6 kOe (Fig. 6.5), even if the field is applied perpendicular to the easy axis. The shape of the Kerr spectrum is very similar to that of single crystal $GdFe_2$. However, the Kerr rotation is negative over the entire energy range. A local minimum appears in the Kerr rotation at 2 eV and a minimum Kerr rotation of $-0.8°$ is found at 4.2 eV. This compares with the rotation measured for $HoFe_2$ despite the much smaller magnetic moment in $CeFe_2$. In Table 6.3 we summarize the experimental results by Lee[44] and compare them to our data. First we note that there is no obvious systematic variation in the position of maximum Kerr effect, E_{max}, in Lee's data[44]. The largest Kerr rotation is found in $HoFe_2$ and the smallest rotation angle is observed for $GdFe_2$. If the Kerr effect were simply proportional to the net spin-polarization (or magnetization), as derived from a simple model for the off-diagonal conductivity, we would extrapolate a Kerr rotation of less than $-0.5°$ for $HoFe_2$. This indicates that there are other important factors which determine the off-diagonal optical conductivity in these compounds. Misemer[11] presented a systematic study of the size of magneto-optic effects and their dependence on spin-orbit splitting and exchange interaction. It was found that the off-diagonal conductivity is proportional to the spin-orbit interaction but shows no simple relationship with the magnetization. This is supported by the specific Kerr rotation, which is also shown in Table 6.3. We define the specific Kerr rotation as the maximum observed Kerr rotation

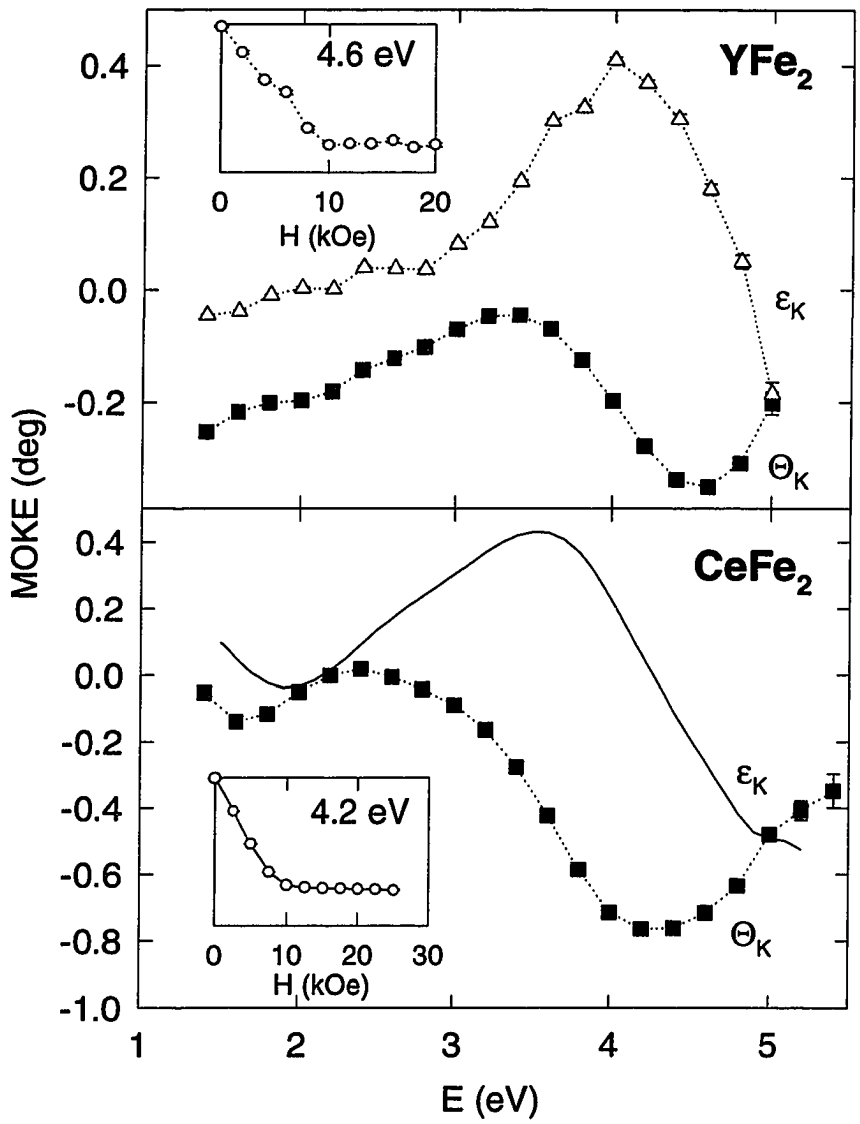

Figure 6.16 Kerr rotation (Θ_K) and ellipticity (ϵ_K). Upper panel: YFe_2 at 3.5 K and 15 kOe. Lower panel $CeFe_2$ at 10 K and 10 kOe. ϵ_K (solid line) was calculated from Θ_K by Kramers-Kronig transformation. The insets show the field dependence of Θ_K at the energy of maximum Kerr rotation.

Table 6.3 Maximum Kerr rotation $\Theta_{K,max}$ reached at energy E_{max}. Temperature T and field H at which the data were taken are given together with the sample magnetization M under those conditions. The last column gives the specific Kerr rotation per Bohr magneton.

	E_{max} (eV)	$\Theta_{K,max}$ (°)	T (K)	H (kOe)	M (μ_B/f.u.)	$\Theta_{K,max}$/M (°/μ_B)
YFe_2	4.6	-0.35	3.5	15	2.91	-0.12
$CeFe_2$	4.2	-0.76	10	10	2.58	-0.29
$GdFe_2$[1]	3.8	-0.28	7	14	3.50	-0.08
$TbFe_2$[1]	4.6	-0.48	295	5	2.00	-0.24
$HoFe_2$[1]	3.6	-1.1	7	16	5.90	-0.19
$TbFe_2$[2]	4.5	-0.42	295			
$DyFe_2$[2]	4.2	-0.25	295			
$HoFe_2$[2]	4.1	-0.18	295			
$ErFe_2$[2]	4.0	-0.08	295			

[1]Ref. [44]
[2]Ref. [161]

per magnetic moment. This indicates that $CeFe_2$ is the most *effective* material showing a Kerr rotation of $-0.29°/\mu_B$, which is similar to the value for $TbFe_2$. It becomes evident from the scattering of these values that there is no clear scheme that would allow us to predict the size of the Kerr rotation based on the sample magnetization. As pointed out by Misemer[11], the Kerr effect is also proportional to the spin-orbit splitting. This trend is found for $GdFe_2$, $TbFe_2$, and $HoFe_2$ in order of increasing spin-orbit interaction and Kerr rotation. However, YFe_2 and $CeFe_2$ do not fit in this scheme.

In order to compare our experimental results with LDA calculations we determined the off-diagonal optical conductivity from the optical constants (Fig. 6.15) and the Kerr parameters (Fig. 6.16). We show the experimental σ_{1xx} together with the calculated conductivity in the upper panel of Fig. 6.17. The calculated conductivity is reduced by a factor of 3. We would like to stress the structure of the spectra shown rather than the magnitude. A self-energy correction with $\lambda = -0.1$ and a life-time broadening of 0.5 eV were used for the theoretical spectrum. The shoulder at 2.8 eV is well reproduced and a broad shoulder around 4.8 eV can be identified in the calculated spectrum. The off-diagonal conductivity (lower panel) agrees well with the calculated σ_{2xy}. The absorption falls off monotonically reaching a minimum at 3.4 eV. There is a shoulder at 2 eV which is also seen in the calculated spectrum. The spectrum is similar to that for $LuFe_2$ measured by Lee *et al.*[44, 45]. Absorption then increases again towards higher energy and another transition is found at 4.5 eV.

A comparison of the absorptive part of the off-diagonal conductivity of YFe_2 with that of $CeFe_2$ is shown in Fig. 6.18. The upper panel shows σ_{xy} for $CeFe_2$. The spectrum is similar to Fig. 6.17. Even

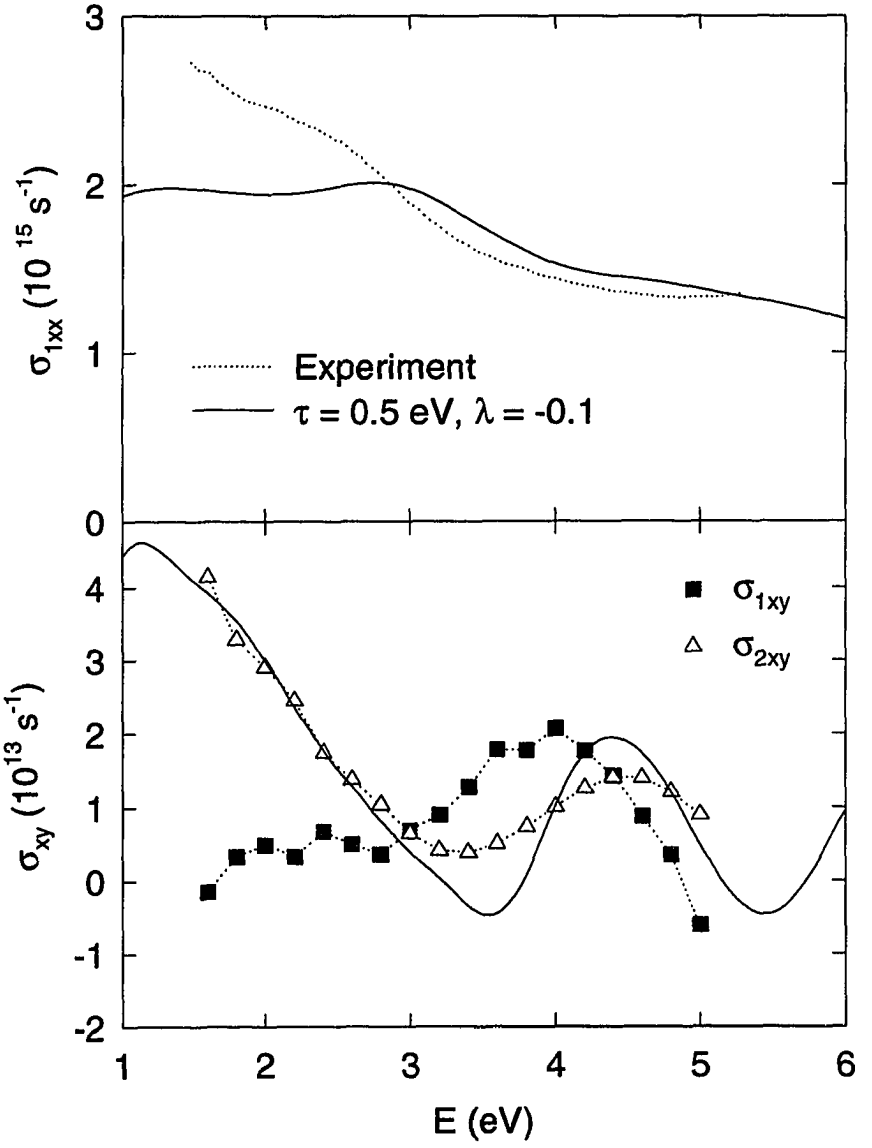

Figure 6.17 Upper panel shows the absorptive component of the diagonal part of the conductivity of YFe_2. The solid line indicates the result obtained from our calculation including a self-energy correction with $\lambda = -0.1$ and a life-time broadening of 0.5 eV. The lower panel shows the off-diagonal optical conductivity. The solid line represents the theoretical result. The magnitude of the calculated σ_{1xx} and σ_{2xy} has been reduced by a factor of 3.

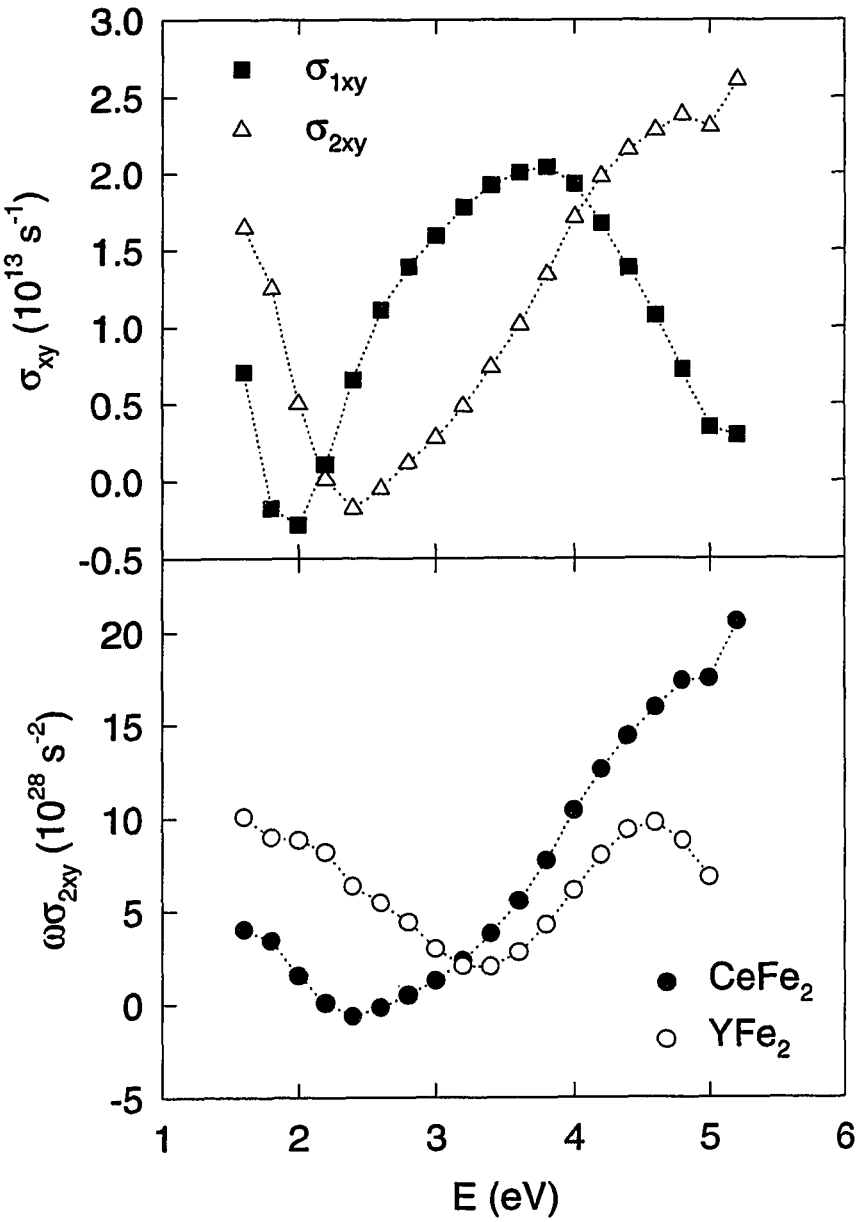

Figure 6.18 The off-diagonal optical conductivity of $CeFe_2$ is shown in the upper panel. The lower part shows $\omega\sigma_{2xy}$ for YFe_2 and $CeFe_2$.

the shoulder at 2 eV is present in this compound. The contribution of free carriers is proportional to ω^{-1}. To remove the effects of free carriers we show $\omega\sigma_{2xy}$ in the lower panel of that figure. Also shown is the spectrum for YFe_2. This emphasizes the similar structures observed in both compounds. The amplitude of the transition at 4.5 eV is smaller and the minimum occurs at a higher energy in YFe_2 than in $CeFe_2$. This implies that this transition is contributed by Fe. Contrary to the Kerr effect, which shows a structure around 2 eV in $CeFe_2$ but not in YFe_2, $\omega\sigma_{2xy}$ is very similar for the two compounds. This would lead to the conclusion that this part of the spectrum is either Fe related or due to transitions involving rare-earth d states, which are very similar in both compounds.

After describing the spectra for YFe_2 and $CeFe_2$ let us now turn to the most intriguing sample of this chapter. At 50 K $Ce(Fe_{0.9}Co_{0.1})_2$ orders antiferromagnetically in zero field. It was shown that a metamagnetic transition to a state with long range ferromagnetic order occurs at 30 kOe. In our experiment we apply a field parallel to [111], i.e. perpendicular to the easy axis in this compound, and the magnetization data in Fig. 6.7 do not necessarily represent the actual magnetization of the sample in our experiment. However, since the anisotropy is small, the net magnetization at 20 kOe will be very small. In Fig. 6.19 we show Kerr spectra taken at 50 K in a field of 20 and 50 kOe, respectively. Despite the small moment at 20 kOe we observed a large Kerr rotation that nearly reaches $-1°$. The broad maximum around 4.6 eV is the dominant feature of the spectrum and compares well with that found in $CeFe_2$. There is a very weak structure at 2 eV. At the same position we found a feature in $CeFe_2$. This indicates that the transition might still be present but is weaker due to different magnetic order. In a larger field (50 kOe) we induce ferromagnetic order and the shape of the Kerr rotation resembles that of $CeFe_2$. The main difference to the data taken at lower field is the reappearance of the 2 eV structure. This was expected since in the ferromagnetic state $CeFe_2$ and $Ce(Fe_{0.9}Co_{0.1})_2$ should be similar. To emphasize the difference we compare the Kerr rotation at 20 and 50 kOe with that of $CeFe_2$ in Fig. 6.20. The minimum in Θ_K is shifted by 0.2 eV to higher energy with respect to $CeFe_2$ and the maximum rotation is increased by nearly 0.2°. Let us focus on the difference between the 20 and 50 kOe data. At 2 eV the Kerr rotation is larger in the ferromagnetic state whereas for $E > 2$ eV the Kerr rotation in the antiferromagnetic state is larger. In order to check this field dependence of the Kerr rotation we measured Kerr loops at different temperatures and energies (Fig. 6.21). Please note that Kerr loops were taken on a different sample. Thus the reduced magnitude of the Kerr rotation indicates a thicker oxide layer on this specimen. The center panel shows the same experimental conditions discussed above. We measured the Kerr rotation at 50 K at 1.8 and 4.0 eV. At 1.8 eV Θ_K increases to about $-0.05°$ and saturates before we induce ferromagnetic order at 40 kOe and Θ_K increases to

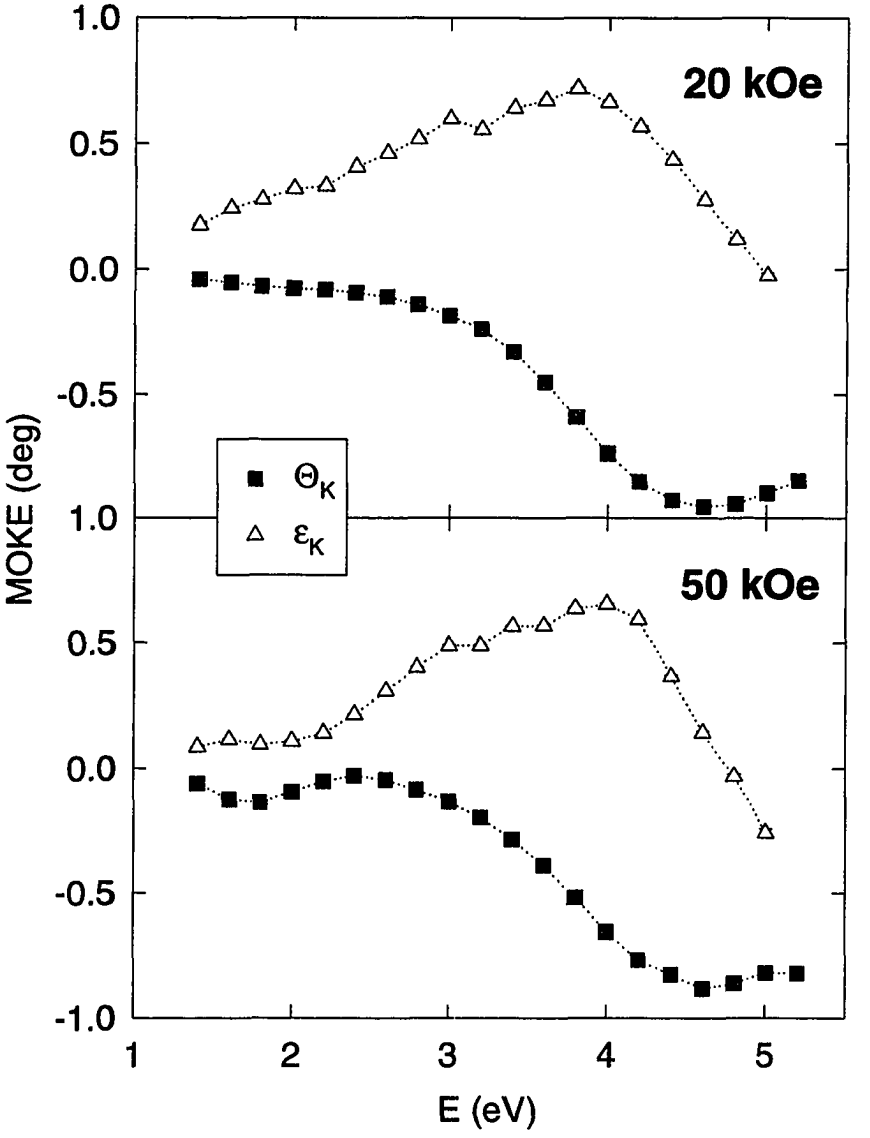

Figure 6.19 Kerr rotation (Θ_K) and ellipticity (ϵ_K) for $Ce(Fe_{0.9}Co_{0.1})_2$ at 50 K.

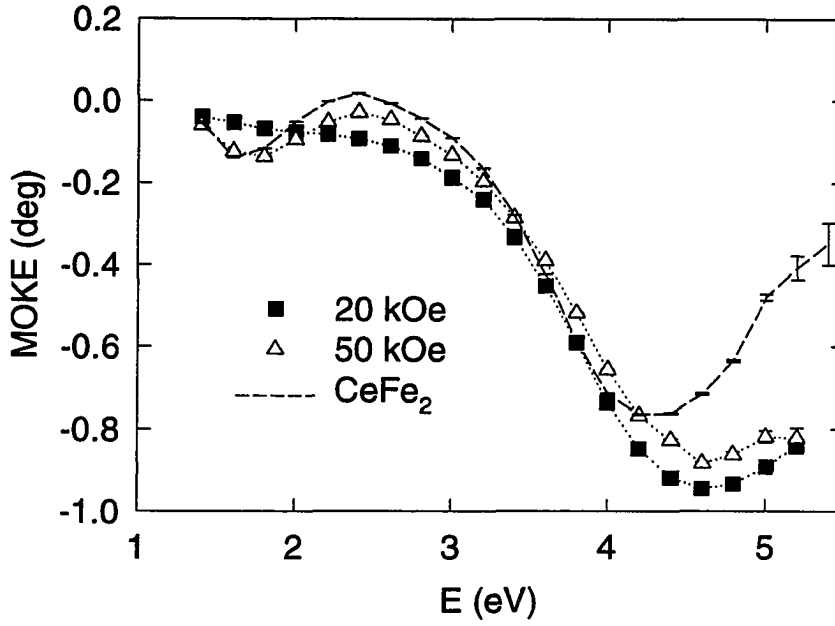

Figure 6.20 Kerr rotation for $Ce(Fe_{0.9}Co_{0.1})_2$ at 50 K in the antiferromagnetic (20 kOe) and ferromagnetic (50 kOe) state. We also show the Kerr rotation of $CeFe_2$ in the saturated regime.

$-0.14°$. Θ_K saturates and remains constant up to 70 kOe. The situation is much more dramatic at 4 eV. Despite a small magnetic moment the Kerr rotation reaches $-0.45°$ and shows the same field induced transition at 40 kOe. But this time the transition occurs to a smaller Kerr rotation, i.e. the magnitude of the Kerr rotation is reduced for an increased magnetization. This is very unusual and we performed measurements on another sample which confirmed our observation. Due to instrumental limitations it was not possible to see a phase transition at 5 K in the magnetization data. Our optical cryostat allows fields up to 70 kOe and we actually found the same transition to occur between 65 and 70 kOe at 5 K. This is shown in the upper panel of Fig. 6.21. Θ_K is similar to the loops taken at 50 K, the only difference being an increased hysteresis at lower temperature. The same transition is seen to occur at 68 kOe in a polycrystalline sample of similar composition[145]. The metamagnetic transition is observed at even higher field but data were taken at a lower temperature, which increases the critical field. What makes this material so interesting is the large Kerr rotation at 4 eV in a region of very low magnetization. In the lower panel of Fig. 6.21 we compare data taken at 4 eV for three different temperatures. The magnitudes of the Kerr rotation observed at 5 and 50 K are in good agreement. For both temperatures Θ_K has the same value in the ferromagnetic as well as in the antiferromagnetic phase. The only difference is a stronger hysteresis due to a higher critical field at lower temperature. At

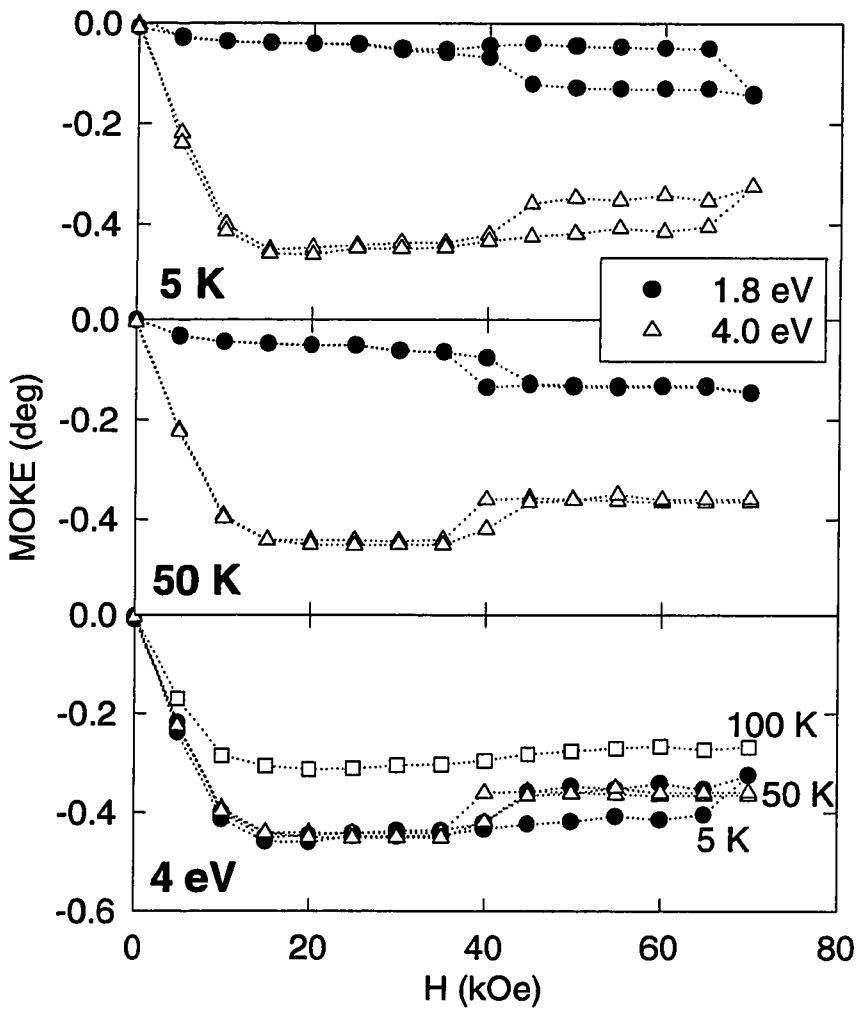

Figure 6.21 Field and temperature dependence of the Kerr rotation of $Ce(Fe_{0.9}Co_{0.1})_2$. The upper two panels show the Kerr rotation at 1.8 and 4 eV taken at 5 and 50 K, respectively. The lower panel shows the Kerr rotation at 4 eV at 5, 50, and 100 K.

100 K the sample is in the ferromagnetic state and Θ_K saturates at 10 kOe. The magnitude is reduced compared to that in the field induced ferromagnetic phase. This is due to a reduced magnetization (see Fig. 6.7).

Finally we would like to present the off-diagonal optical conductivity for $Ce(Fe_{0.9}Co_{0.1})_2$ for both magnetic phases. Figure 6.22 shows again the difference between the two absorption spectra. It becomes clear that the absorption peak centered at 1.8 eV is not present in the antiferromagnetic phase. Absorption is larger in the AF phase for $E > 2.2$ eV. Another small structure is found in the FM phase at 3.6 eV. This transition does not appear in the Kerr rotation (Fig. 6.20) due to the strong negative peak at higher energy.

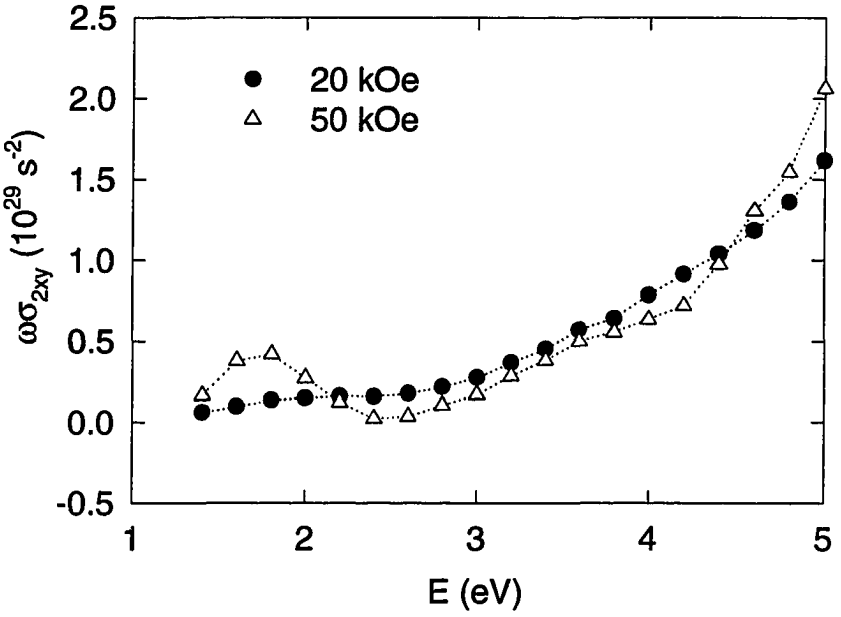

Figure 6.22 Absorptive part of the off-diagonal optical conductivity of $Ce(Fe_{0.9}Co_{0.1})_2$ at 50 K.

6.5 Conclusions

Comparing the shape of our spectra in Fig. 6.16 with those of heavier rare-earth-Fe_2 compounds[161] we find that all spectra show a broad minimum in the Kerr rotation between 3.5 and 5 eV. The measurements by Katayama and Hasegawa[161] show a decrease of the magnitude of Θ_K with increasing atomic number of the rare-earth. Furthermore, the minimum shifts to lower energy in compounds with heavier rare-earths. However, the structure of the spectra changes very little for different compounds.

We therefore ascribe this part of the spectrum to Fe-d derived transitions. This structure is absent in the spectra of RAl_2 (Figs. 5.18 and 5.19) which supports our conclusion. If we take a look at the low energy absorption we will find that the spectra of RAl_2 and RFe_2 are very similar. Rare-earth p and d states do not change significantly as the f-shell is filled, and we observe similar structures in Θ_K in the heavy RFe_2[161, 44]. We assign the structure around 2 eV to rare-earth derived transitions involving d states. As expected, this absorption is also found in the σ_{2xy} spectrum of YFe_2. Rare-earth f states polarize the d states which yields an appreciable magneto-optical signal. As found for RAl_2, the d moment itself can be rather small (Table 5.1).

In the case of RAl_2 we found Θ_K to be proportional to the sample magnetization. This is due to the simple magnetic structure of those compounds. Only the rare-earth carries a moment (which is more than 80% $4f$) and through intra-atomic coupling the spin-polarization of the $5d$ states is proportional to the magnetization. For RFe_2 the situation is more complicated since the rare-earth, as well as the Fe, carry a moment. In Fig. 6.16 we showed the saturation behavior for YFe_2 and $CeFe_2$. There is a nearly linear increase in Θ_K and saturation sets in at 10 kOe. This corresponds to a ferrimagnetic alignment of the Fe and rare-earth magnetic moment along [111].

From magnetization and Kerr angle versus field data for $Ce(Fe_{0.9}Co_{0.1})_2$ it emerges that there is a fairly large absorption despite a quite minute net magnetic moment at 50 K and 20 kOe. Magnetization increases linearly until H approaches the critical field. It differs from the Kerr rotation which saturates at an external field of 20 kOe. This is indicative of saturation of the magnetic sublevel which contributes to this absorption, presumably the Ce-$5d$ state. According to neutron scattering the Ce-$5d, 4f$ moment is small ($< 0.04\mu_B$) and cannot be seen in our magnetization measurements. Above the metamagnetic transition the Fe moments align ferromagnetically which leads to a steep increase in the magnetization. However, the change in the magneto-optic signal is an order of magnitude smaller. It appears that we are able to detect a much smaller magnetic moment using the Kerr effect, which selectively probes particular electronic states. The exact origin of the absorption at 1.8 and 4 eV cannot be determined unambiguously. One should keep in mind that there are other effects that we have not considered in the previous analysis. There is a structural distortion at T_N which is reversed as the field is increased and ferromagnetic order on the Fe sublattice is restored. This distortion can lead to splitting of bands which will change the absorption spectrum. Furthermore the BZ in the antiferromagnetic regime is smaller than for the ferromagnetic structure, i.e. the chemical unit cell is doubled due to antiferromagnetic spins on the Fe ions in consecutive (111) planes. This may lead to band folding and opening of gaps which are not present in the ferromagnetic BS.

7 SUPERCONDUCTIVITY, MAGNETISM, AND HEAVY-FERMION BEHAVIOR: RNi_2B_2C

7.1 Introduction

The observation of superconductivity in quarternary compounds with composition RNi_2B_2C by Cava *et al.*[163, 164] has motivated intensive experimental research. They are particularly interesting because of their relatively high transition temperature (T_C=17 K for $LuNi_2B_2C$) and their layered structure, which is similar to that of the high-T_C cuprates. It was found that superconductivity occurs not only in non-magnetic Y and Lu compounds but also in compounds with magnetic rare-earth ions (R=Dy, Ho, Er, Tm). At low temperature, long-range magnetic order and superconductivity, which are usually mutually exclusive, coexist. The effects of the local $4f$ moments on superconductivity, the influence of the crystalline electric field, and the magnetic character of the Ni sublattice have been investigated in great detail[165, 166]. $TmNi_2B_2C$ is a superconductor which orders antiferromagnetically below 1.5 K. $LuNi_2B_2C$ has a filled $4f$ shell and does not order magnetically. Both materials show superconductivity below 11 and 17 K, respectively. Based on de Gennes scaling, superconductivity would also be expected for $YbNi_2B_2C$. Magnetization measurements do not show any signature of magnetic ordering or superconductivity above 0.34 K. Strong hybridization of Yb-f states with conduction electrons is believed to give rise to the observed anomalies in the magnetic susceptibility. The mixing leads to an enhanced specific heat coefficient (530 mJ/K^2 mol) which places $YbNi_2B_2C$ among the heavy-Fermion compounds. We will use optical spectroscopy to investigate the role of $4f$ mixing and the contribution of $4f$ states to the optical response between 1.4 and 5 eV.

It is not known how the optical properties change when the $4f$ states are strongly hybridized. We therefore decided to compare $YbNi_2B_2C$ to a non-hybridizing compound of the same series. Recently, Eskildsen *et al.*[167] showed that the symmetry and degree of order of the flux line lattice in superconducting $TmNi_2B_2C$ can easily be modified by an applied magnetic field. Our research was inspired by the idea that is should be possible to observe the flux line lattice of $TmNi_2B_2C$ using magneto-optical

Kerr microscopy[1]. The modulation of the magnetic field, due to the vortex lattice in the mixed state, can be probed using the Kerr effect, provided the modulation of the Kerr rotation or ellipticity is large enough to be detected[168, 169]. As a preliminary step we measured the magneto-optic response of $TmNi_2B_2C$ between 1.4 and 5 eV. We also show the field dependence of the Kerr rotation and estimate the critical field, H_{c2}.

7.2 Sample preparation and characterization

Polycrystalline stochiometric RNi_2B_2C (R=Tm, Yb) was synthesized by arc melting together high purity Tm (Ames Lab: 99.99%), Yb (Ames Lab: 99.99%), Ni (Aesar: 99.95%), B (Eagle-Picher: 99.5% isotopic), and C (Carbone: 99.99%). In order to compensate for the loss of Yb due to high vapor pressure at elevated temperatures, excess Yb was added to the growth for $YbNi_2B_2C$. Single crystals were then grown by a NiB_2 flux method[170, 171]. The growths yielded large plate-like samples of up to $10 \times 10 \times 1$ mm^3. After removing the crystals from the flux there was still some residual flux on the surface. We used silicon carbide abrasives with grain sizes of 6, 1, and 0.25 μm to clean the samples. RNi_2B_2C is rather hard and polishing yields flat and highly reflective surfaces. Samples are not very reactive and can be prepared and transferred into the sample chamber without degrading the sample quality due to oxidation.

The samples were characterized by Cho *et al.*[172] and Yatskar *et al.*[173]. We will discuss the most important features and refer the reader to the original work for more detailed information. Powder XRD measurements of pulverized crystals show a single-phase pattern without any of the second phases that were seen in polycrystalline samples, except for a small $(2,1,1)$ peak originating from the Ni_2B flux that remained on the surface of the crystal. RNi_2B_2C crystallizes in the body centered tetragonal $ThCr_2Si_2$-type structure (structure type Al_4Ba, space group D_{4h}^{17}, I4/mmm) with an additional C atom at the 2b site in the basal plane. The crystal structure is shown in Fig. 7.1. This layered structure is similar to that of many of the cuprate high-T_C superconductors, consisting of alternating planes of RC and Ni_2B_2 stacked along c. Powder XRD on ground $YbNi_2B_2C$ gave $a = 3.575$ Å and $c = 10.606$ Å. These values are consistent with the lattice parameters reported by Siegrist *et al.*[174], and indicate that Yb is close to trivalent at room temperature. The lattice parameters for $TmNi_2B_2C$ are $a = 3.48$ Å and $c = 10.60$ Å. XRD on single crystals indicate that the crystallographic c axis is normal to the surface of the platelets. The observed atom positions[174] yield nearly ideal NiB_4 tetrahedra with a Ni-B bond length of 2.1 Å. The bond distance for Ni-Ni is about 2.45 Å, i.e. smaller than in fcc Ni (2.50

[1] V. Kogan, private communication.

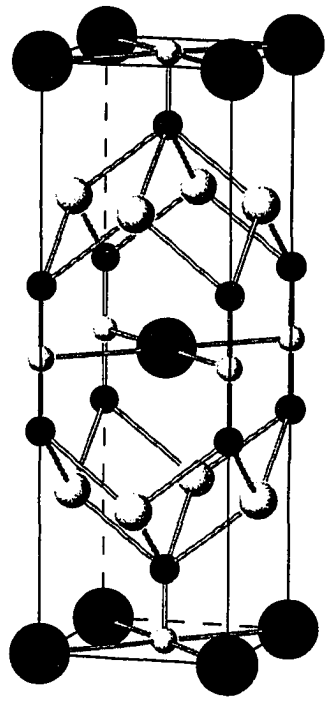

Figure 7.1 Crystal structure of RNi_2B_2C. The large black spheres are rare-earth atoms, the small black spheres are B atoms, the large white spheres are Ni atoms, and the small white spheres are C atoms. The Ni-B-C framework is indicated by bonds.

Å), indicating metallic bonds in this plane. The B-C bond length (1.47 Å) is slightly smaller than the value for hexagonal B_4C (1.64 Å).

In Fig. 7.2 we show M(T)/H for $TmNi_2B_2C$. Measurements were taken with a 1 kOe field applied parallel to c. Above 11 K the magnetization follows the Curie-Weiss law due to the paramagnetic Tm^{3+} ions. At 10.5 K a maximum in M/H indicates the onset of diamagnetic contributions at lower temperature. Below 10.5 K we notice a decrease in M/H which is reversible down to 7 K. Below 7 K M/H becomes field-history dependent with the field-cooled magnetization (FCW) being larger than the zero-field-cooled magnetization (ZFC). This is consistent with conventional type-II superconductivity below T_C with reversible behavior between 7 K and T_C. The peak in M/H is the onset of superconductivity. This anomaly at T_C is also seen in the resistivity which shows a sharp drop at the same temperature[175]. $TmNi_2B_2C$ orders antiferromagnetically at 1.52 K[176] which cannot be seen in our data. From a fit of M/H we obtain an effective moment of $7.72\mu_B$/Tm and $\Theta = -1.73$ K. The effective moment is in good agreement with the theoretical value of $\mu_{eff} = 7.57\mu_B$ for the Hund's Rule ground state of the

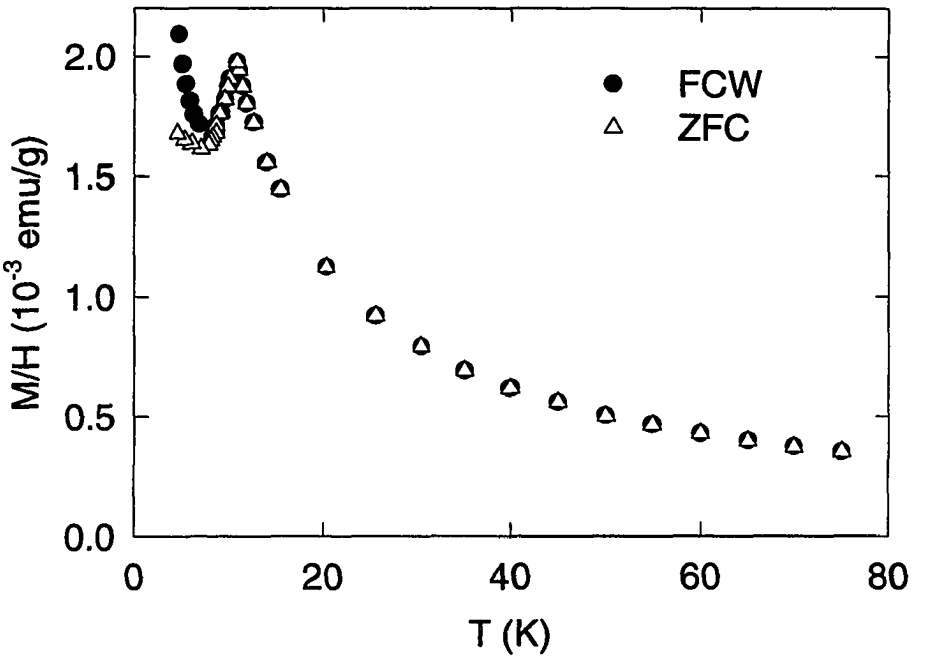

Figure 7.2 M/H versus temperature for a single crystal of $TmNi_2B_2C$ with H = 1 kOe parallel to c. Zero field cooled (ZFC) and field cooled (FCW) data are shown.

Tm^{3+} ion[177]. Θ estimated from M/H is close to the observed T_N indicating strong antiferromagnetic interactions in this compound.

In order to further characterize the role of magnetic order in this compound we show M(H) in Fig. 7.3. Measurements were taken at 2 K with H||c. The magnetic moment saturates at about 20 kOe and reaches nearly $5\mu_B$ at 50 kOe. In the case of H$\perp$ c the magnetization does not saturate and the moment is strongly reduced ($< 2.8\mu_B$ at 50 kOe). The anisotropic magnetization is most likely due to CEF splitting of the J=6 ground state multiplet of the Tm^{3+} ion. It is believed that the CEF ground state is a mixture of the J=6 states, which leads to a Tm magnetic moment that is much smaller than the single ion moment. CEF effects are also observed in specific heat measurements where a splitting of 39 K between the ground state and the first excited level was estimated[176]. Taking the derivative of the magnetization with respect to applied field, we can estimate the critical field H_{c2}, above which superconductivity disappears. $\Delta M/\Delta H$ is shown in the lower panel of Fig. 7.3. The derivative was calculated from M(H) shown in the upper panel of the same figure. The solid lines indicate the different slope of the curve below and above H_{c2}. From that plot we estimate a critical field of 8 kOe at 2 K. In general, the critical field is smaller for H||c than for H$\perp$ c. H_{c2} shows a broad maximum at 5 K and

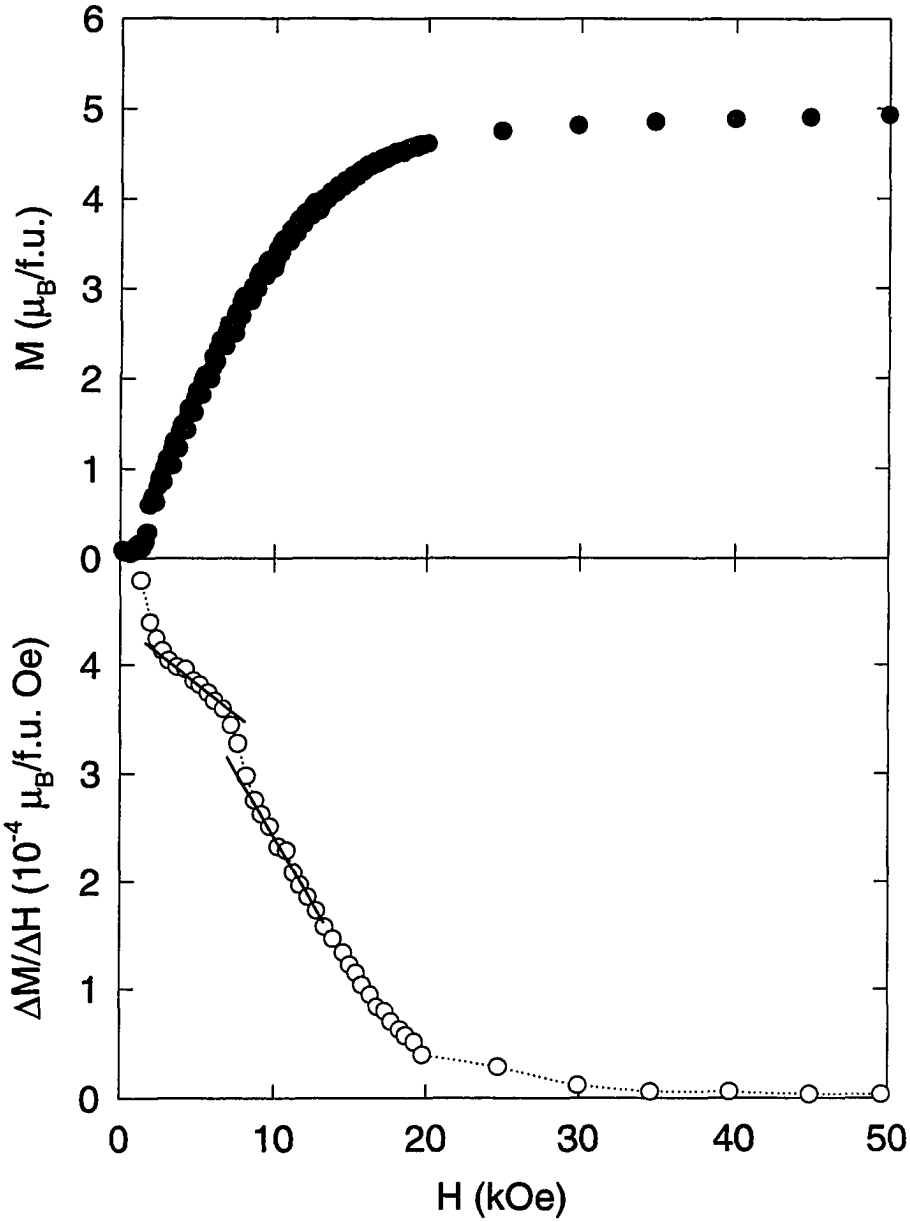

Figure 7.3 Upper panel: Magnetization versus field for a single crystal of $TmNi_2B_2C$. Data were taken at 2 K with H||c. Lower panel: Derivative of M with respect to field, $\Delta M/\Delta H$, determined from M(H) shown above. The lines indicate the different slope of $\Delta M/\Delta H$ below and above H_{c2}.

is suppressed as T approaches T_N[171], which is common in antiferromagnetic superconductors and consistent with resistivity measurements on polycrystalline $TmNi_2B_2C$[175].

In Fig. 7.4 the magnetization of a single crystal of $YbNi_2B_2C$ is shown for H||c and H$\perp$ c. As in the case of $TmNi_2B_2C$ the crystallographic c axis is seen to be the easy axis of magnetization in this compound, giving a larger magnetization over the entire temperature range. The anisotropic magnetization is caused by CEF splitting of the J=7/2 manifold of the Yb^{3+} ground state. The tetragonal crystal field splits the ground state multiplet into four doublets. Thermal excitations of those levels are observed in the specific heat and the first excited level is estimated to be separated from the ground state by 100 K. When inverse χ is plotted (lower panel) we observe Curie-Weiss behavior above 150 K for both field directions. From the high temperature slopes we estimate $\mu_{eff} = 4.85, 4.67\mu_B$ for H$\perp$ c and H||c, respectively. These values are slightly larger than the effective moment for the Hund's Rule ground state of the Yb^{3+} ion ($4.54\mu_B$)[177]. The Weiss temperatures are -191.0 and -63.6 K, indicating that antiferromagnetic correlations are important in this compound. However, neither magnetic ordering nor superconductivity are observed above 0.34 K. The large Weiss temperature is an anomaly of this compound. For other compounds of this series (R=Dy, Ho, Er, Tm) the magnetization follows a Curie-Weiss law to temperatures close to the ordering temperature and the Weiss temperature is close to T_N[178, 172, 179]. Deviations from Curie-Weiss behavior below 100 K and the large Weiss temperature indicate that the $4f$ levels of Yb may be significantly hybridizing with the conduction electrons.

This was taken as a first indication that $YbNi_2B_2C$ might be a new heavy-Fermion compound. The Sommerfeld coefficient was obtained from a fit of the specific heat below 1 K[173]. An enhanced electronic specific heat coefficient of 530 mJ/K^2 mol was estimated which is large enough to classify $YbNi_2B_2C$ as a heavy-Fermion compound. For $LuNi_2B_2C$ a fit of the specific heat below the superconducting transition (T_C=16 K) yields $\gamma = 11$ mJ/K^2 mol. $TmNi_2B_2C$ and $LuNi_2B_2C$ are superconductors with transition temperatures of 10.5 and 16.3 K, respectively. Following de Gennes scaling we would expect $YbNi_2B_2C$ to be a superconductor, too. Scaling of T_C with the de Gennes factor is based on the assumption that the coupling between the magnetic moments and the conduction electrons is constant across the rare-earth series. That this transition is not observed supports the greatly enhanced pair breaking due to strong electron correlations in this compound. Unlike compounds such as YbBiPt (see Chapter 8), the energy scales in $YbNi_2B_2C$ are largely separated. Since no transition was observed we conclude that, assuming $YbNi_2B_2C$ has a phase transition, the ordering temperature, as well as the superconducting transition temperature, are below 0.34 K. This is much lower than the spin-fluctuation

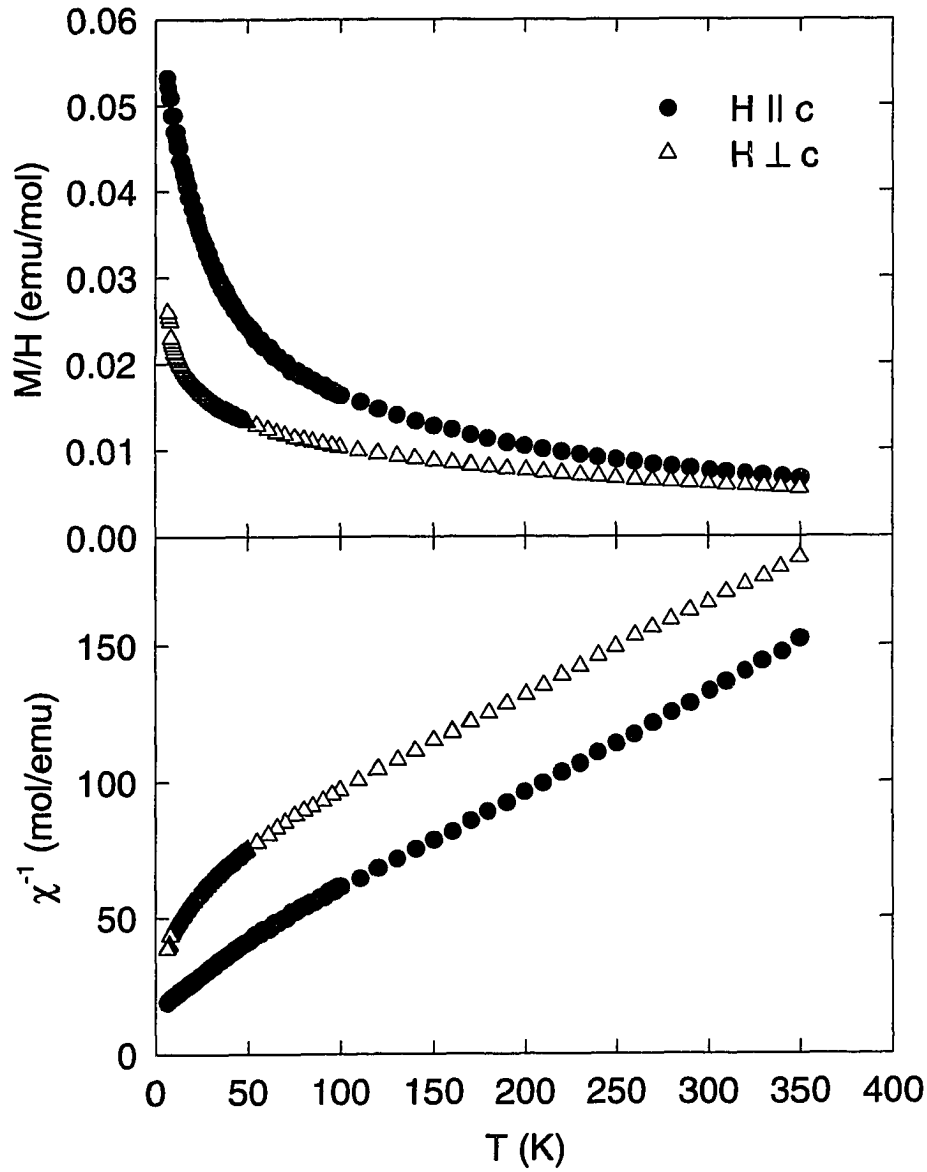

Figure 7.4 Upper panel: anisotropic magnetization for a single crystal of $YbNi_2B_2C$. Measurements were performed with an external field of 1 kOe applied parallel and perpendicular to the crystallographic c axis. Lower panel: χ^{-1} determined from the magnetization shown in the upper panel.

temperature which is estimated to be around 11 K[173]. Crystal field excitations, as seen in specific heat measurements, become important above T_{CEF}=100 K, i.e. T_C, $T_N \ll T_K \ll T_{CEF}$.

7.3 Electronic structure of RNi_2B_2C

Two of the first band structure calculations for RNi_2B_2C were published nearly simultaneously shortly after the initial discovery of superconductivity in this new class of materials[163, 164] and their crystal structure[174]. Pickett and Singh[180] and Mattheiss[181] used a scalar-relativistic version of the linear augmented-plane-wave (LAPW) method. It turned out that the electronic structure of nickel-borocarbides does not show any similarities to the well known high-T_C cuprates. Despite the two dimensional (2D) layered structure the electronic properties of $LuNi_2B_2C$ are of 3D character. This can be seen from the dispersion of bands along different directions of the BZ and is also confirmed by the DOS at E_F. All atoms contribute to $N(E_F)$ which indicates extended bonding throughout the material. The BS of $LuNi_2B_2C$ was compared to that of the isotropic superconductor YNi_2B_2C. The BS as well as the DOS of both compounds are strikingly similar. It is assumed that the rare-earth atom does not drastically alter the electronic properties of the material. A fairly complex band at E_F, strongly coupled to phonons, seems to be responsible for the robust superconductivity in this series of compounds. LDA results suggest that $LuNi_2B_2C$ is a conventional, rather than a high-T_C, superconductor.

In a series of reports Kim *et al.*[182, 183, 184] used *ab initio* pseudo-potential calculations to investigate electron-phonon interactions in $LuNi_2B_2C$. Recently Johrendt *et al.*[185] performed LMTO BS calculations of $ThCr_2Si_2$-type transition metal compounds. The bonding mechanism of $LuNi_2B_2C$ was compared to that of non-superconducting $SrRh_2P_2$. Before we present our results we would like to comment on the calculations available so far. BS calculations were performed using different techniques. Comparing the results it emerges that the DOS is in good agreement. However, it is evident that there are some differences in the calculated BS. Since Γ is a point of high symmetry we expect the bands, i.e. position and degeneracy, to be the same independent of the method used. Comparing some of the results mentioned above (e.g. Refs. [181, 180] and [185]) it is obvious that this is not the case. Unfortunately, the authors do not address this problem. Since the degeneracy of bands at Γ depends on the point symmetry only, it must be a different symmetry that is responsible for the observed deviations. Since we are also using the LMTO method we expect our results to agree with those of Johrendt *et al.*[185].

We used the experimental lattice constants for $YbNi_2B_2C$ to calculate the BS of $LuNi_2B_2C$ and $YbNi_2B_2C$. Due to the localized nature of the $4f$ states involved it was not possible to achieve con-

vergence for $TmNi_2B_2C$. We therefore chose to calculate the BS of $LuNi_2B_2C$ which is electronically similar except that the $4f$ shell is completely filled. We expect the BS to be distorted in the vicinity of the $4f$ bands which are well below E_F in compounds containing Lu. The atomic positions are given in Table 7.1. As basis functions we chose $(6s, 6p, 5d, 4f)$ for the rare-earth when the $4f$ states were treated as valence states. We also performed a calculation where the Yb-$4f$ states were core-like, i.e. $5f$ (instead of $4f$) states were included in the basis set. On the remaining sites we included Ni-$(4s, 4p, 3d)$, B-$(2s, 2p, 3d)$, and C-$(2s, 2p, 3d)$ states. In order to achieve space filling an empty sphere was inserted and $(1s, 2p)$ wave functions were added to the basis set. Self-consistent potentials were calculated on an 8 x 8 x 16 mesh, i.e. with 149 k-points in the irreducible wedge of the BZ. The BS was calculated after self-consistency had been achieved with one iteration using 16 x 16 x 32 points.

Table 7.1 Atomic positions for RNi_2B_2C (R=Yb, Lu) in units of lattice constants a = 3.48 Å and c = 10.60 Å. We also show the radius of the Wigner Seitz spheres, R, in atomic units and the basis functions included for the TB-LMTO calculation. E designates the empty sphere that was inserted in order to achieve space filling.

Atom	x (a)	y (a)	z (c)	R (a.u.)	Basis set
Yb, Lu	0	0	0	3.701	$(6s6p5d4f)$
Ni	1/2	0	1/4	2.669	$(4s4p3d)$
B	0	0	0.3621	1.573	$(2s2p3d)$
C	1/2	1/2	0	1.581	$(2s2p3d)$
E	0	0	0.2292	1.136	$(1s2p)$

The large unit cell in addition to localized $4f$ orbitals on the rare-earth site make the BS calculation rather unstable and we were not able to perform spin-polarized calculations for all RNi_2B_2C compounds. It is therefore preferred to calculate the non-magnetic BS and compare the two compounds. Since predictions for the off-diagonal conductivity, i.e. the Kerr effect, will not be reliable for this kind of material we may also neglect spin-orbit coupling. In Table 7.2 we show the self-consistent charges inside the WS spheres for $LuNi_2B_2C$ and $YbNi_2B_2C$ (with $4f$ states treated as valence and as core states). It is evident that the two calculations yield very similar results and hybridization of Yb-$4f$ with conduction electron states does not change the charge distribution. This is somewhat unexpected considering the fact that it is s-f hybridization that leads to the anomalous magnetic, electronic and thermal properties of this material. The largest difference is found for the C-$2s$ and C-$2p$ charges which are increased by 0.04 electrons each when the $4f$ states are treated as core states. This may indicate that there is a strong correlation between Yb and C derived states. However, the two cases (core and valence $4f$) are quite different and such drastic changes in the electronic structure may be responsible

Table 7.2 Charge inside the Wigner-Seitz spheres in $YbNi_2B_2C$ and $LuNi_2B_2C$ from self-consistent non-spin-polarized BS calculations. Relativistic corrections are included, but spin-orbit coupling is neglected. Charges are given in electrons.

	s	*p*	*d*	*f*	Total
$YbNi_2B_2C_2$, $4f$ core					
Y	0.70	1.30	2.10	0.00	4.10
Ni	0.72	0.95	8.70		10.37
B	0.61	1.10	0.04		1.75
C	0.96	2.16	0.02		3.14
E	0.14	0.04			0.18
$YbNi_2B_2C_2$, $4f$ valence					
Yb	0.69	1.28	2.13	14.30	18.40
Ni	0.72	0.95	8.70		10.37
B	0.58	1.09	0.04		1.71
C	0.92	2.12	0.02		3.06
E	0.15	0.04			0.19
$LuNi_2B_2C_2$, $4f$ valence					
Lu	0.74	1.35	2.53	14.69	19.31
Ni	0.72	0.98	8.70		10.40
B	0.58	1.09	0.04		1.71
C	0.91	2.16	0.02		3.09
E	0.15	0.04			0.19

for the observed change in the C charge. The results for $LuNi_2B_2C$ are similar (see Table 7.2). It is worth noting that the only difference is a promotion of the rare-earth $5d$ charge and a larger $4f$ charge. For $LuNi_2B_2C$ we obtained 0.4 more d electrons at the Lu site. Together with the increased $4f$ occupancy this leads to a charge that is 0.91 larger for Lu than for Yb, which is due to the additional $4f$ electron of Lu. However, the $4f$ occupancy for Yb is fairly large, indicating strong mixing of Yb-d and Yb-f states. In summary, we can say that the charges in the ligand muffin-tin spheres are not affected by the rare-earth atom.

The BS and DOS will give more insight into the electronic structure, especially the s-f interaction in $YbNi_2B_2C$. Figures 7.5 and 7.6 show the BS along the symmetry directions in the BZ and the total DOS for $LuNi_2B_2C$ and $YbNi_2B_2C$. The BS for both compounds show similarities. The significant difference is the position of the rare-earth $4f$ bands, which are 5 eV below E_F in $LuNi_2B_2C$ and right below E_F for $YbNi_2B_2C$. We noticed this behavior already in Chapter 5, where we found empty f levels well above E_F for $LaAl_2$ and localized f bands just above E_F for $CeAl_2$. The case discussed here

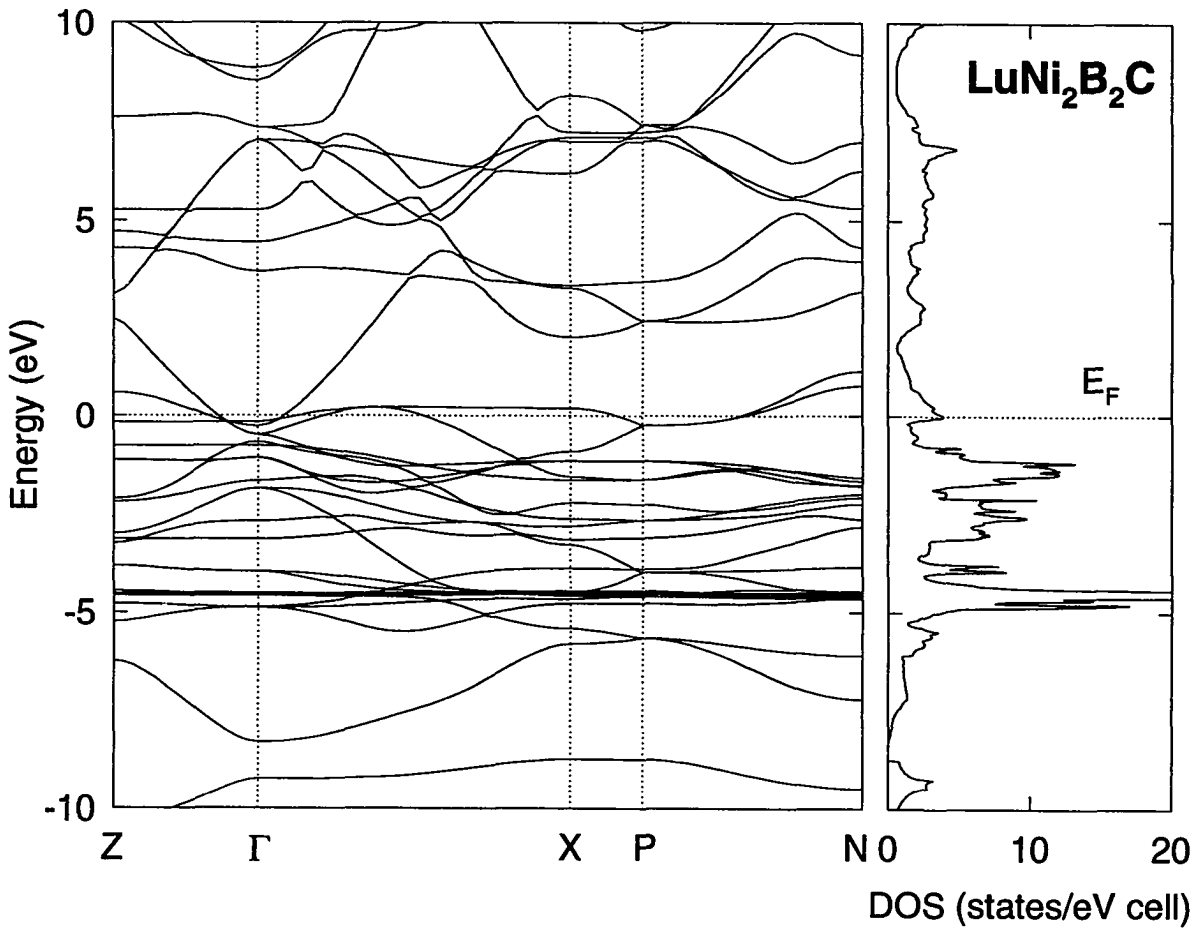

Figure 7.5 Relativistic band structure and total DOS for $LuNi_2B_2C$. Spin-orbit splitting is not included.

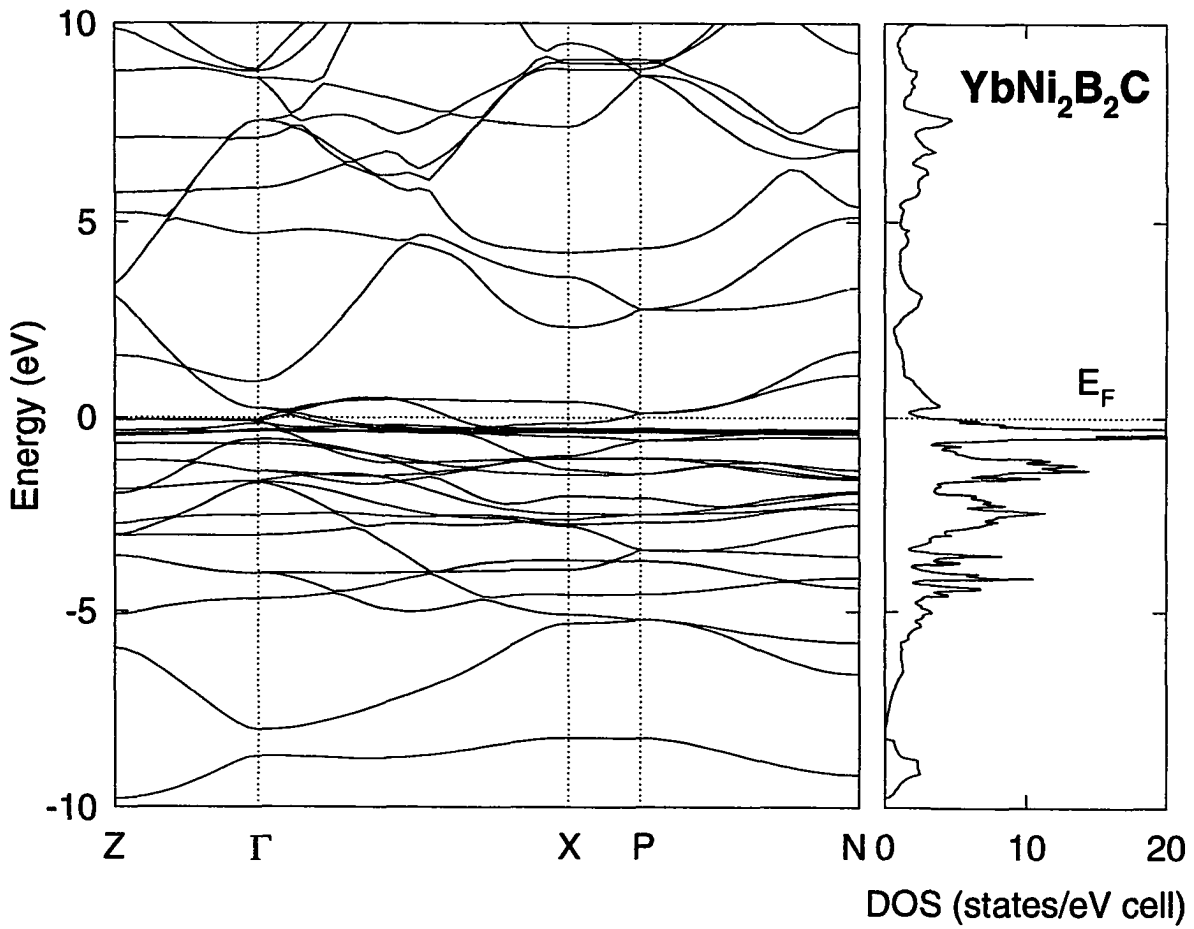

Figure 7.6 Relativistic band structure and total DOS for $YbNi_2B_2C$. Spin-orbit splitting is not included.

is analogous and we may substitute empty with full states, i.e. electrons with holes. The arguments and the underlying physics remain the same. The Lu-4f states are well below the Fermi level and do not contribute to the ground state properties of this material. In particular, we do not expect any contributions to the optical conductivity below 5 eV. In the Yb compound the 4f bands are found close to the Fermi level and strong hybridization with conduction electrons is evident. This is supported by magnetization measurements as discussed in the previous section. The lowest bands (below -10 eV, not shown here) originate from C-2s levels. If we plot the DOS (Figs. 7.7–7.10) we can identify the bands around -10 eV as B-2s and C-2p derived bands mixed with some rare-earth 5d character. Between -7 and -5 eV, bands originate from C-2p and B-2p states. From -5 eV to E_F, a broad Ni-3d complex dominates the DOS. As seen from the DOS at E_F, all atoms contribute to the ground state properties of RNi_2B_2C. For $LuNi_2B_2C$ the Fermi level coincides with a peak in the DOS which originates from Ni-d bands, which are split-off from the main Ni complex below E_F. This increased DOS, similar to the one that triggers the magnetic instability of Ni, may be the reason for superconductivity in this compound. The total DOS at the Fermi level is 3.90 states/eV cell, which is composed of 0.69/Lu, 2.61/Ni_2, 0.35/B_2, and 0.23/C. On a per Ni basis this is about the same as calculated for a typical cuprate superconductor such as La_2CuO_4, where $N(_F)$=1.3 states/eV Cu[186]. For $YbNi_2B_2C$ the Ni contribution is reduced but the DOS at E_F is increased due to the presence of 4f bands. A total DOS of 4.18 states/eV cell was calculated for $YbNi_2B_2C$ with 2.27/Yb, 1.56/Ni_2, 0.14/B_2, and 0.19 states/eV C. The peak in the Ni DOS is found at about 0.3 eV above E_F indicating a charge transfer from Ni to other sites. This shift, in addition to strong mixing of 4f and conduction electrons, is assumed to be responsible for the suppression of superconductivity in $YbNi_2B_2C$.

Our DOS agrees with earlier calculations. The total DOS and its decomposition at E_F is the same as found in Ref. [185]. Bands are similar but small differences can be found throughout the entire BZ. This is surprising since the same method (and presumably the same LMTO code) was used for our calculation. At this point we are not able to confirm any of the results published. Since there is still some controversy about the electronic structure we would like to suggest a more thorough investigation of RNi_2B_2C which is beyond the scope of this work. Despite these inconsistencies our experimental results can be interpreted based on the BS obtained from our calculation.

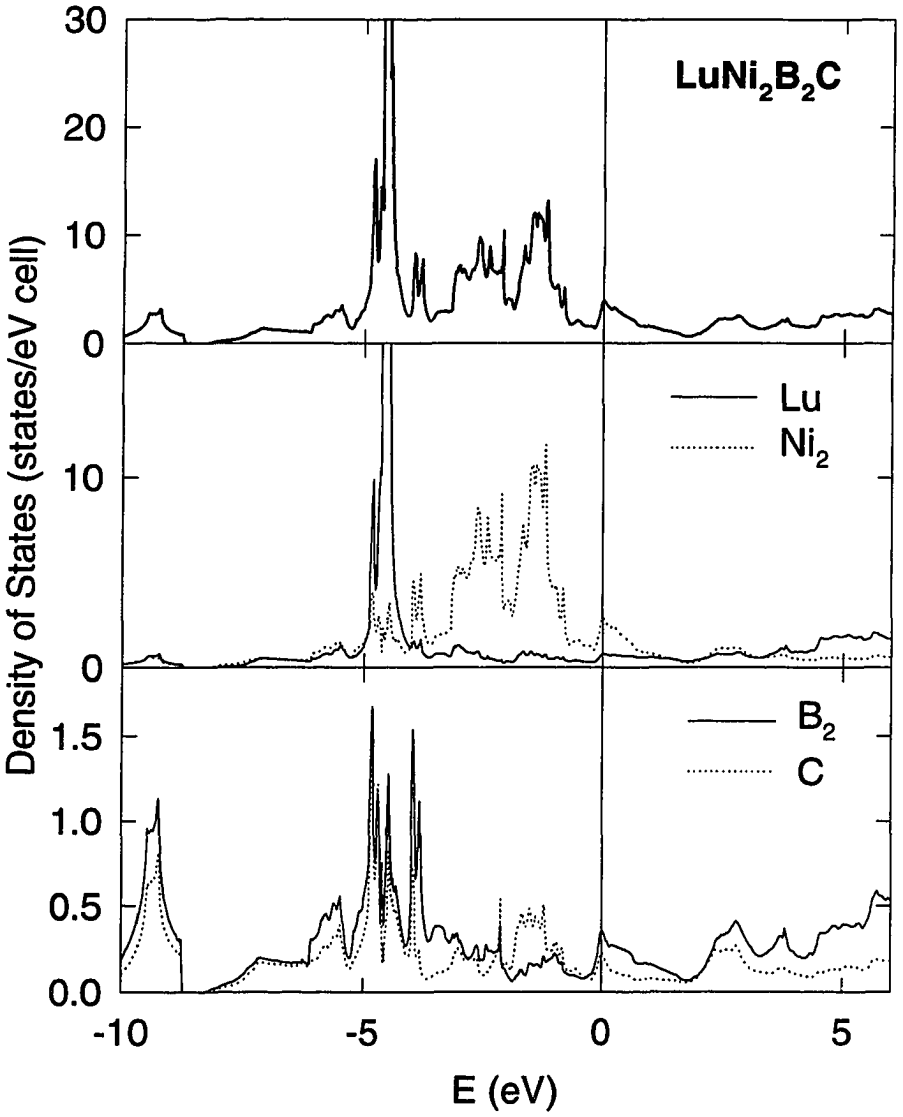

Figure 7.7 Total and partial DOS for $LuNi_2B_2C$.

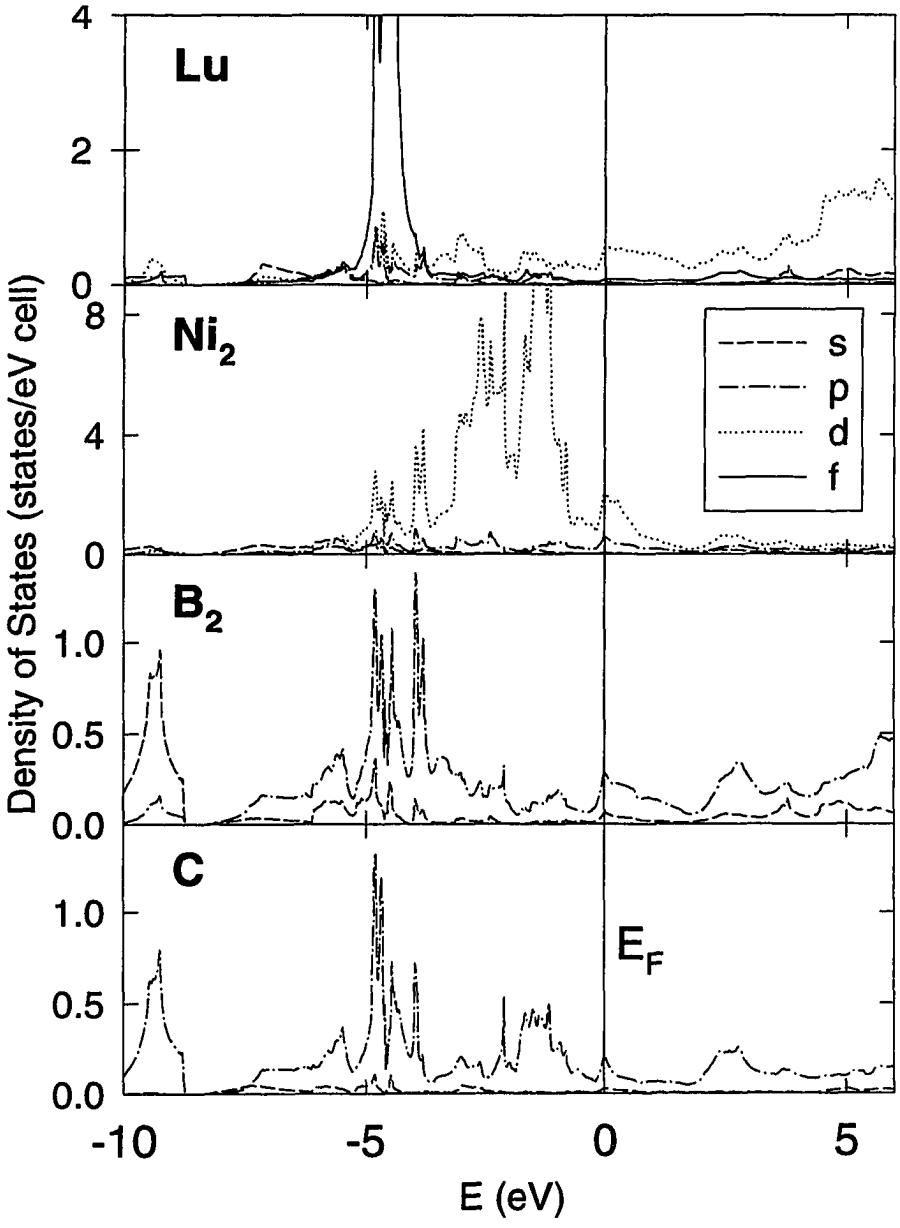

Figure 7.8 Partial DOS and orbital decomposition for $LuNi_2B_2C$.

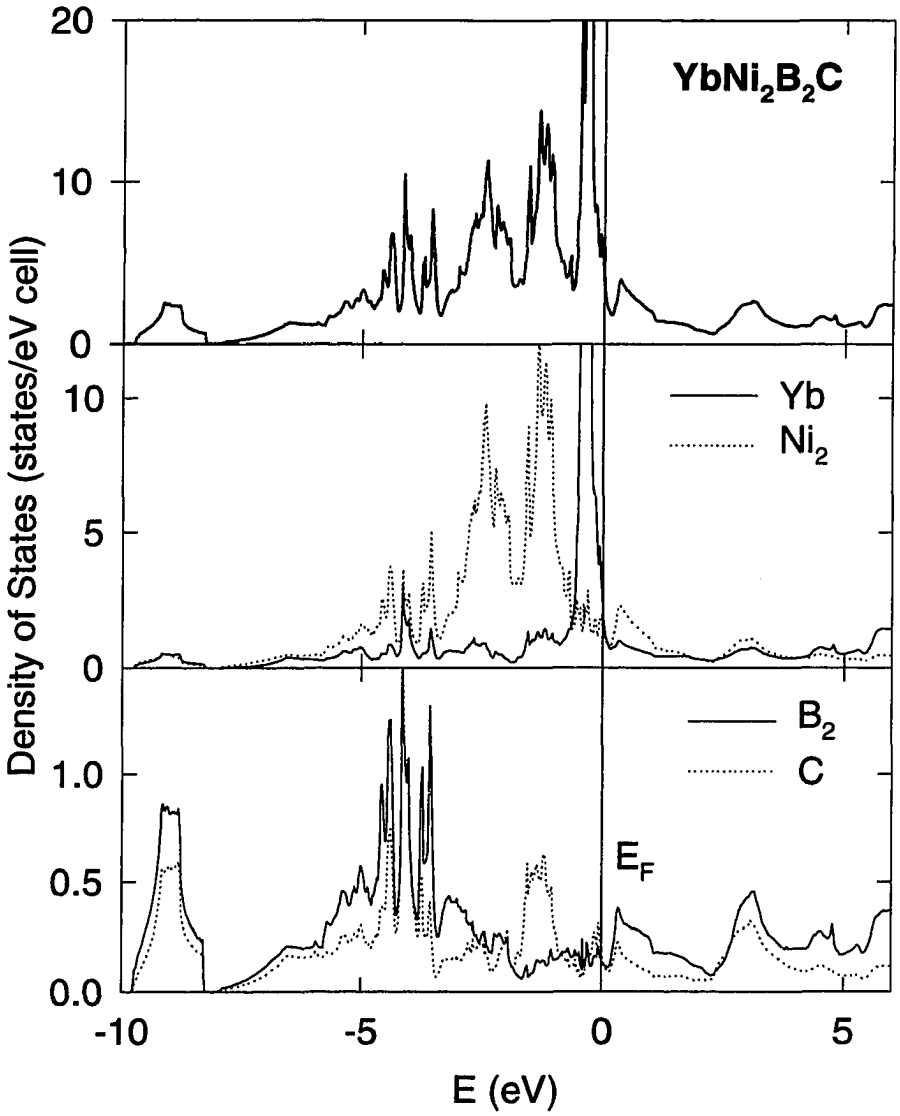

Figure 7.9 Total and partial DOS for $YbNi_2B_2C$.

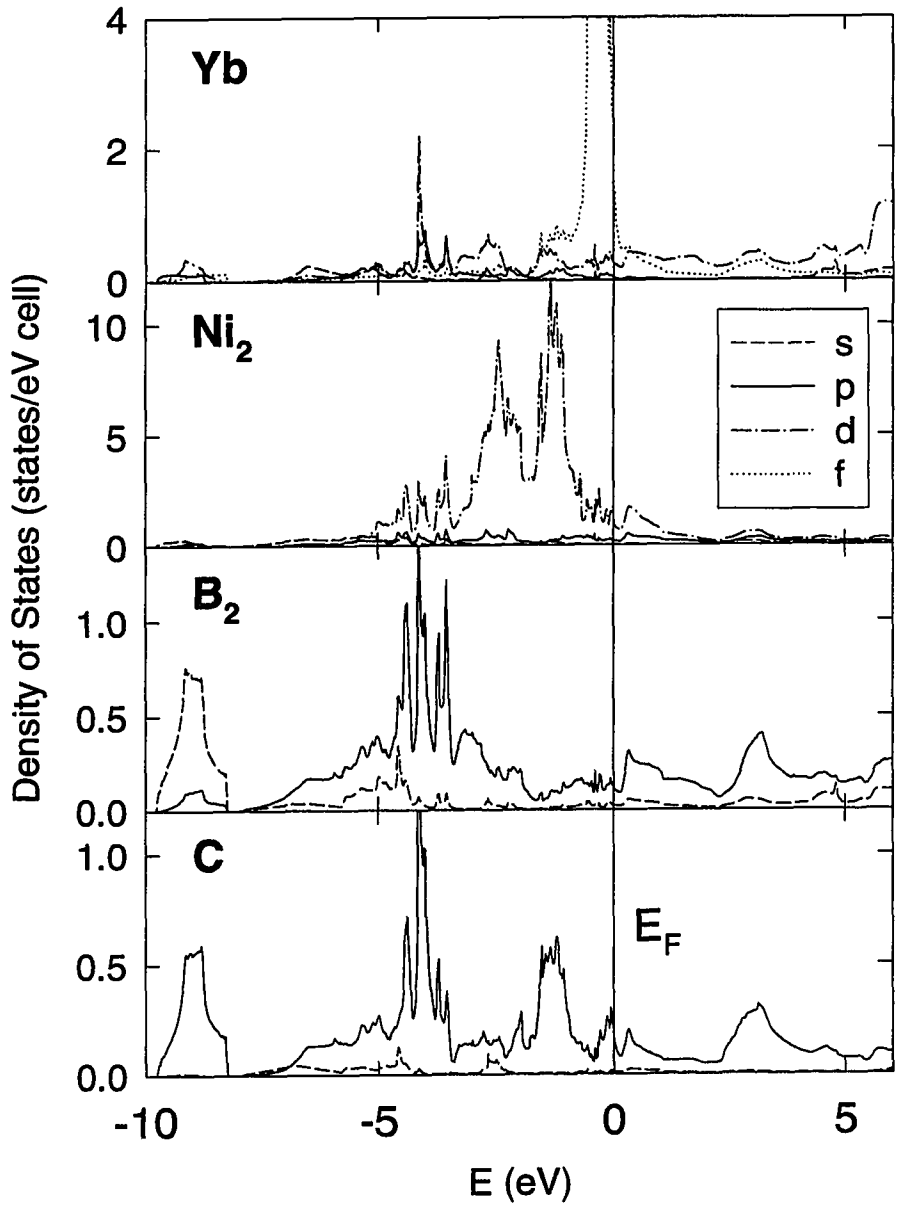

Figure 7.10 Partial DOS and orbital decomposition for $YbNi_2B_2C$.

7.4 Optical properties

So far there have been only few reports on the optical properties of RNi_2B_2C. Bommeli *et al.*[187, 188, 189] measured the normal state and superconducting reflectivity of isotropic non-magnetic YNi_2B_2C and $LuNi_2B_2C$ between 1.8×10^{-3} and 12.4 eV. Their work focused on the optical response of the free carriers in these materials. From the far-infrared optical conductivity they were able to identify a superconducting gap of 5.6 meV and 6.9 meV for the Lu and Y compound, respectively.

We performed ellipsometry on RNi_2B_2C (R=Tm, Yb) at room temperature with no magnetic field applied. From the dielectric function we determined the diagonal optical conductivity, presented in Fig. 7.11. The absorptive part, σ_{1xx}, shows an interband absorption at 2.6 eV in $YbNi_2B_2C$. The same peak can be seen in the $TmNi_2B_2C$ spectrum at a slightly lower energy ($\approx$ 2.5 eV). This is the main peak observed in our spectral range. σ_{1xx} increases below 2 eV and, extrapolating σ_{2xx}, we estimate another interband absorption at about 1.2 eV. From reflectivity measurements a transition at 1.2 eV was derived for $LuNi_2B_2C$[187]. Since the sample surfaces are of good quality for optical experiments and light intensity is sufficient even at high energies, the increase in σ_{1xx} indicates another transition above 5 eV. Absorption at higher energy was observed in reflectivity measurements on YNi_2B_2C (8 eV) and $LuNi_2B_2C$ (6.5 eV)[187]. The absorption spectra for RNi_2B_2C (R=Tm, Yb, Lu) show structures that are also seen for YNi_2B_2C indicating that there might be only little, if any, contributions involving $4f$ states in this energy range.

The (non-magnetic) BS for RNi_2B_2C (Figs. 7.5 and 7.6) is less complex, i.e. has fewer bands around E_F, than those of the Laves phase compounds discussed earlier (RAl_2 in Chapter 5 and RFe_2 in Chapter 6). It is therefore feasible to identify interband transitions combining BS and DOS plots. We will attempt this for $LuNi_2B_2C$ which shows similar spectral features[187]. Bands with small dispersion (flat bands) give large contributions to the DOS. Parallel bands lead to Van Hove singularities in the joint DOS (JDOS)[190, 177, 22]. The JDOS can be seen as the constant matrix element approximation to the optical conductivity. Calculating the JDOS does not give the correct absorption spectrum, but parts of the BZ, with possibly large contributions, can be mapped out using this simple approach. However, if matrix elements are small at a Van Hove singularity no transition will be observed. One case where this becomes dramatically clear is the small contribution of spin-flip transitions to the optical conductivity, despite a possibly large JDOS[11].

Considering the small number of bands in the region of interest (-5 to 5 eV) we are able to identify interband transitions using the BS and DOS for $LuNi_2B_2C$ (Figs. 7.5, 7.7, and 7.8). In addition we show the atomic and orbital character of the bands in Fig. 7.12. Between Γ and X is a large region

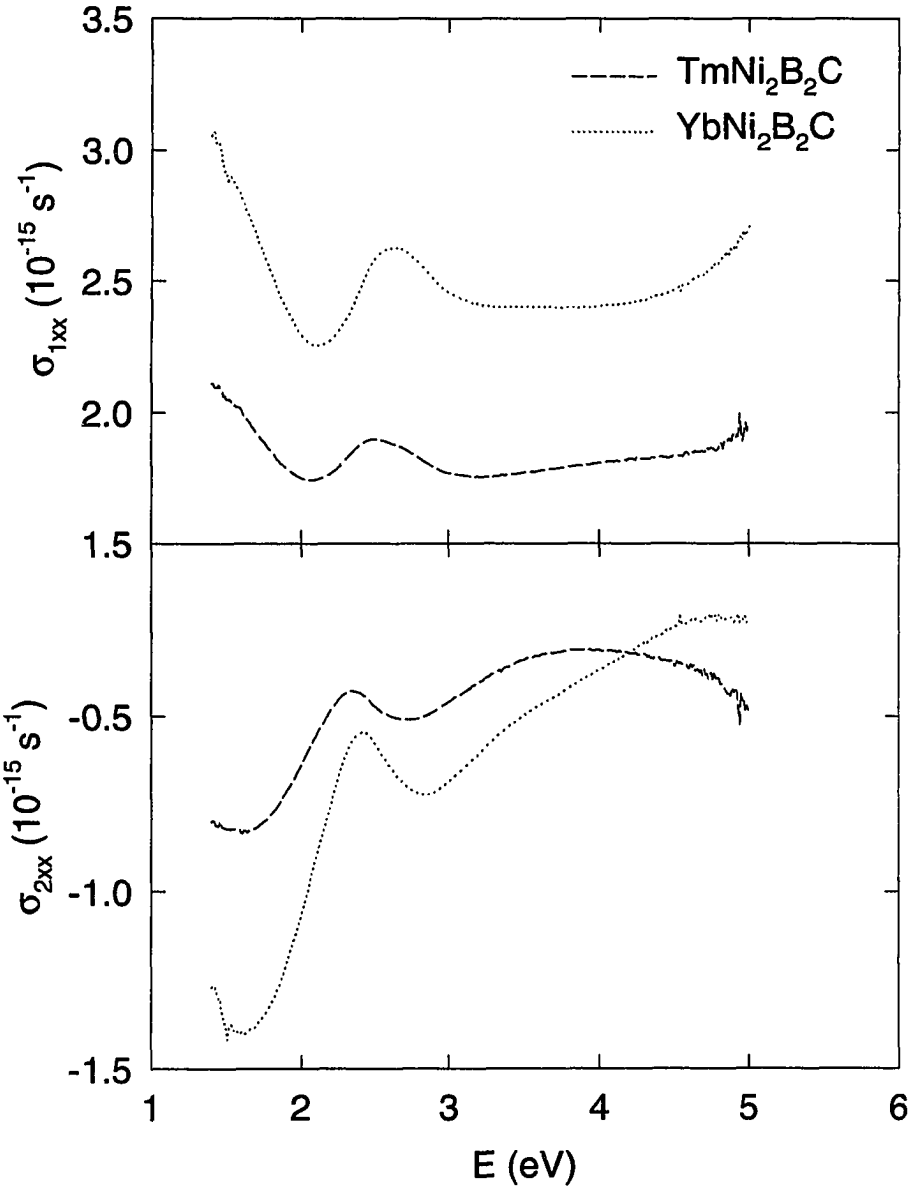

Figure 7.11 Room temperature optical conductivity of RNi_2B_2C (R=Tm, Yb) measured by ellipsometry in zero field.

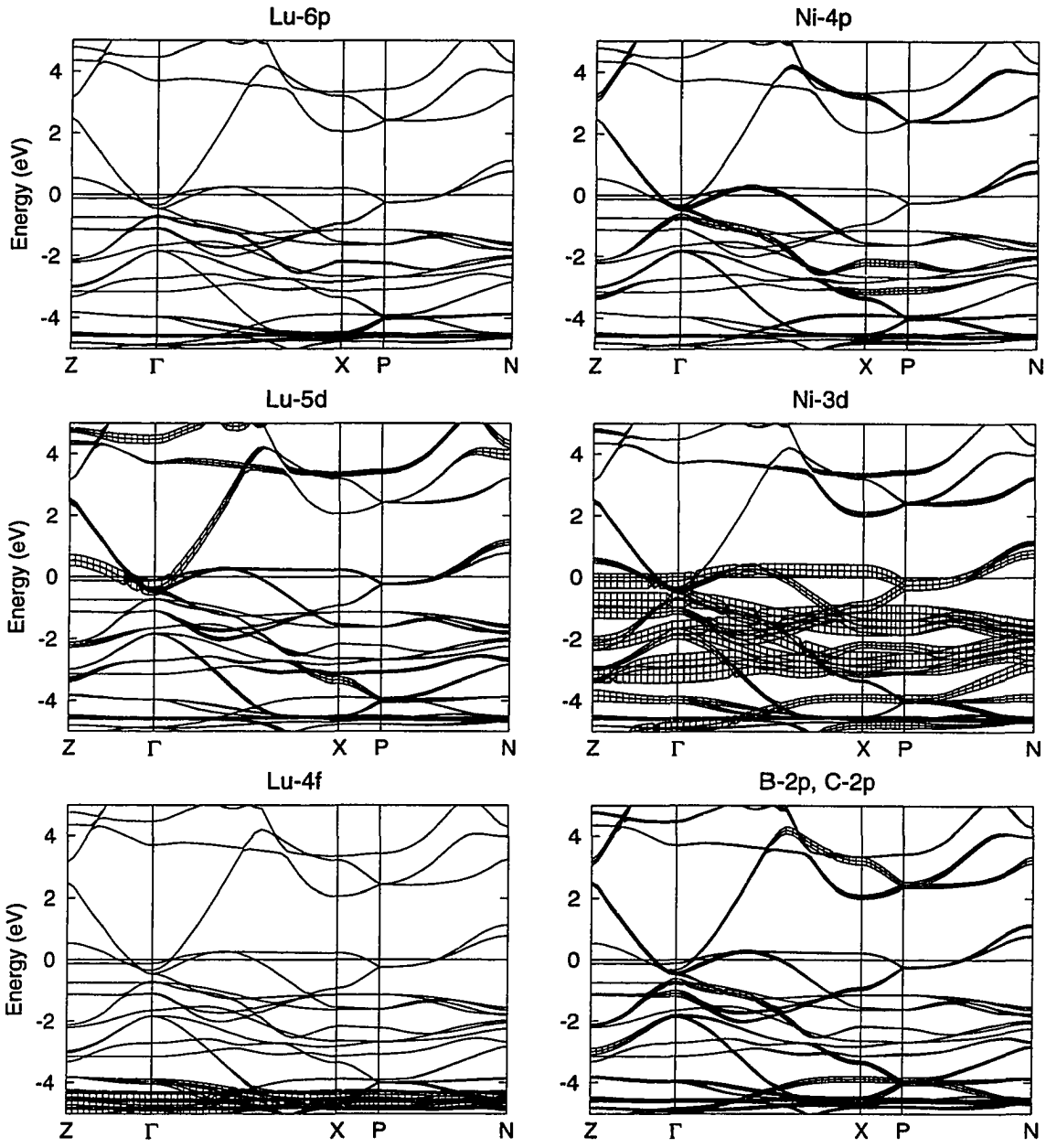

Figure 7.12 Band structure of $LuNi_2B_2C$ projected on the atomic and orbital character. The width of the hatched bands is proportional to the amount of a particular character in a band.

with flat bands about 1 to 1.2 eV below the Fermi level. These bands are composed of Ni-d and C-p character with small amounts of B-p and Lu-d. Transitions occur to a band 0.1 to 0.2 eV above E_F which disperses only weakly. It originates from Lu-d and Ni-d states. We assign the peak in σ_{1xx} at 1.2 eV to transitions from the top of the C-p complex to Lu-d and Ni-d derived states above E_F. In Fig. 7.13 we reproduce the BS of $LuNi_2B_2C$ for the energy range of interest. Solid arrows indicate the region where we expect large contributions to the 1.2 eV absorption. Dashed arrows around P show transitions from Ni-d derived bands to empty bands about 2.5 eV above E_F. The final state is composed of C-p and B-p character. We also expect transitions from Ni-p and C-p to Ni-d derived bands around the X point to contribute to this structure. Absorption at higher energies (dash-dotted arrows) is most likely due to $p \rightarrow d$ and $d \rightarrow p$ transitions. Bands that might contribute are found between Z and Γ. Between P and N we indicate a region where we expect contributions from B-p and C-p to empty states of mostly Lu-d character between 4 to 5 eV above E_F. In the same region Ni-d to B-p and C-p transitions may contribute to σ_{1xx}. The transitions we have found do not depend on the rare-earth element and can also be found in the BS of RNi_2B_2C (R=Tm, Yb). Most of the states involved are independent of the position of the f bands, and hybridization is not believed to affect the high energy (> 1 eV) optical properties of RNi_2B_2C (R=Tm, Yb).

In Fig. 7.14 we show the magneto-optic Kerr rotation and ellipticity for RNi_2B_2C (R=Tm, Yb). Data were taken at 2.5 K and 40 kOe for $TmNi_2B_2C$, and at 2 K and 70 kOe for $YbNi_2B_2C$, respectively. In both cases the field was applied along the crystallographic c axis. Θ_K shows a minimum at or below 2 eV for Tm and Yb, respectively. The minimum in the Tm compound is larger by a factor of 5. Above 2 eV the Kerr rotation returns to zero. There is another weak structure at 3 eV in the case of $TmNi_2B_2C$ which cannot be seen in the Yb compound. Above 4 eV the Kerr rotation for $TmNi_2B_2C$ decreases and reaches $-0.25°$ at 5 eV. For $YbNi_2B_2C$, Θ_K decreases above 2.7 eV and shows a broad minimum at 4.5 eV with a peak rotation of $-0.12°$. At even higher energy the rotation returns to zero. The inset in the lower panel of that figure shows $\Theta_K(H)$ at 2 eV and 2.8 K. Θ_K increases linearly with applied magnetic field up to 70 kOe, in agreement with paramagnetic Yb ions in this compound. $\Theta_K(H)$ for $TmNi_2B_2C$ is shown in Fig. 7.15. Data were taken at the local minimum (2.1 eV). We notice a linear increase at low field. Θ_K saturates at higher field although complete saturation cannot be achieved up to 60 kOe. At low field the sample is in a mixed (or vortex) state. We observe a change in the slope of $\Delta M/\Delta H$ (Fig. 7.3) at the critical field, H_{c2}, above which the sample does not superconduct. We calculated $\Delta\Theta_K/\Delta H$ (lower panel in Fig. 7.15). Solid lines indicate that the slope changes as we increase the magnetic field. The critical field estimated from the Kerr rotation is 10 kOe, which is in

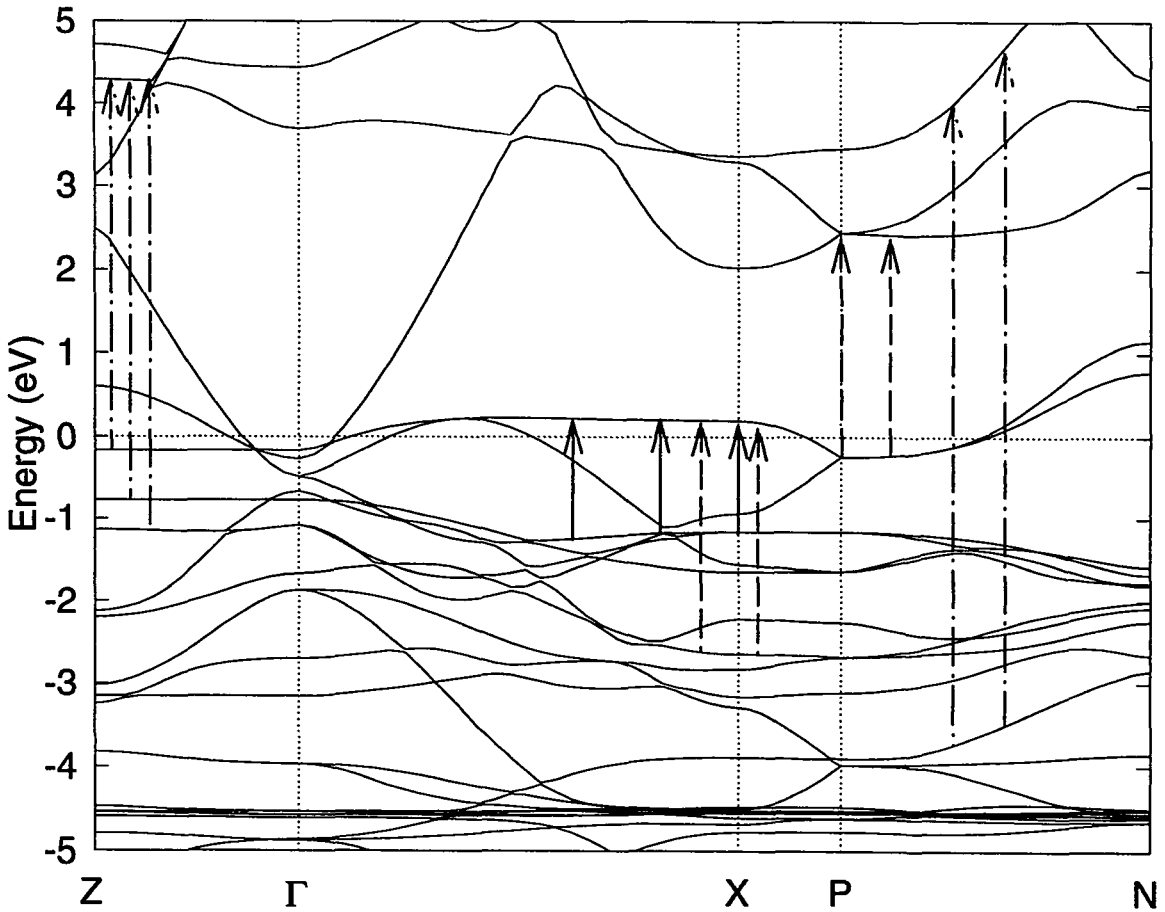

Figure 7.13 Expanded plot of the BS of $LuNi_2B_2C$. Arrows indicate regions with large contributions to the optical absorption at 1.2 eV (solid lines), 2.5 eV (dashed lines), and above 5 eV (dash-dotted lines).

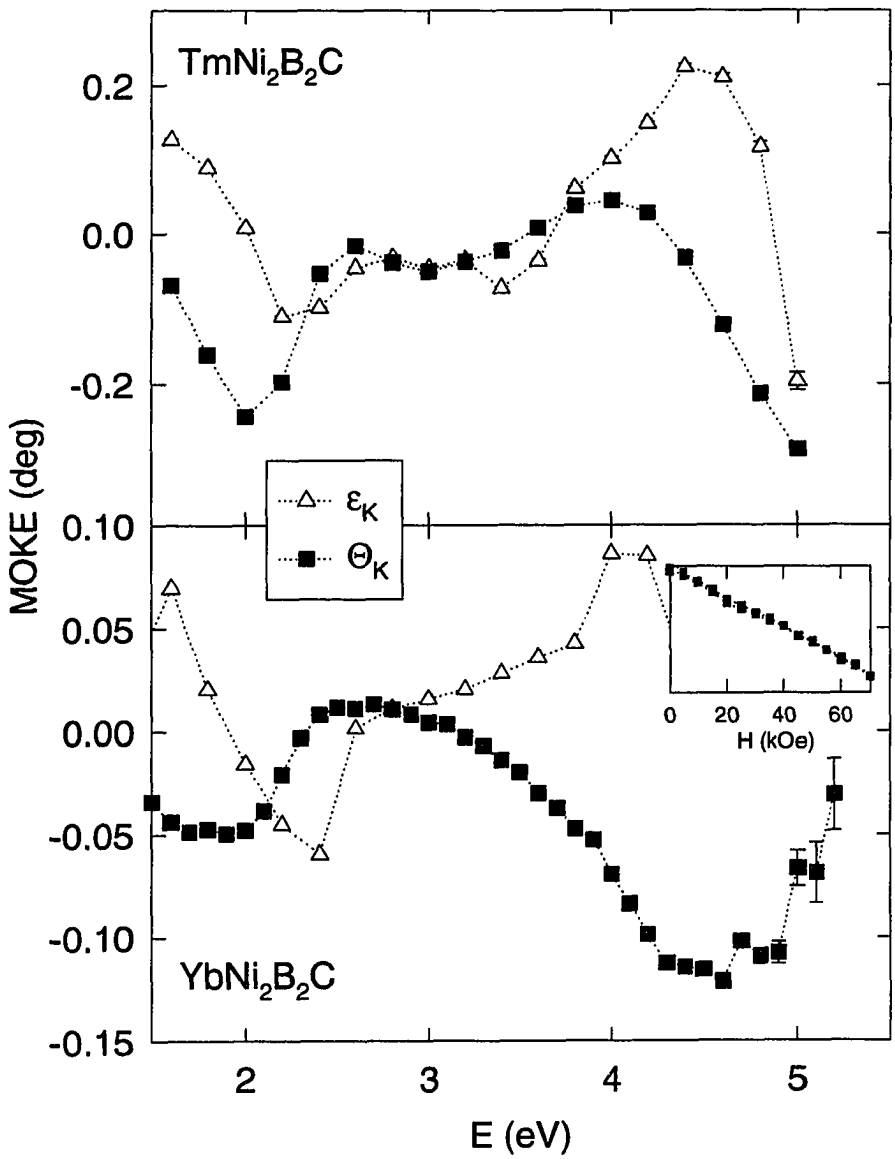

Figure 7.14 Magneto-optic Kerr rotation (Θ_K) and ellipticity (ϵ_K) for RNi_2B_2C. Upper panel: R=Tm at 2.5 K and 40 kOe. Lower panel: R=Yb at 2 K and 70 kOe. The inset shows Θ_K(H) at 2 eV and 2.8 K.

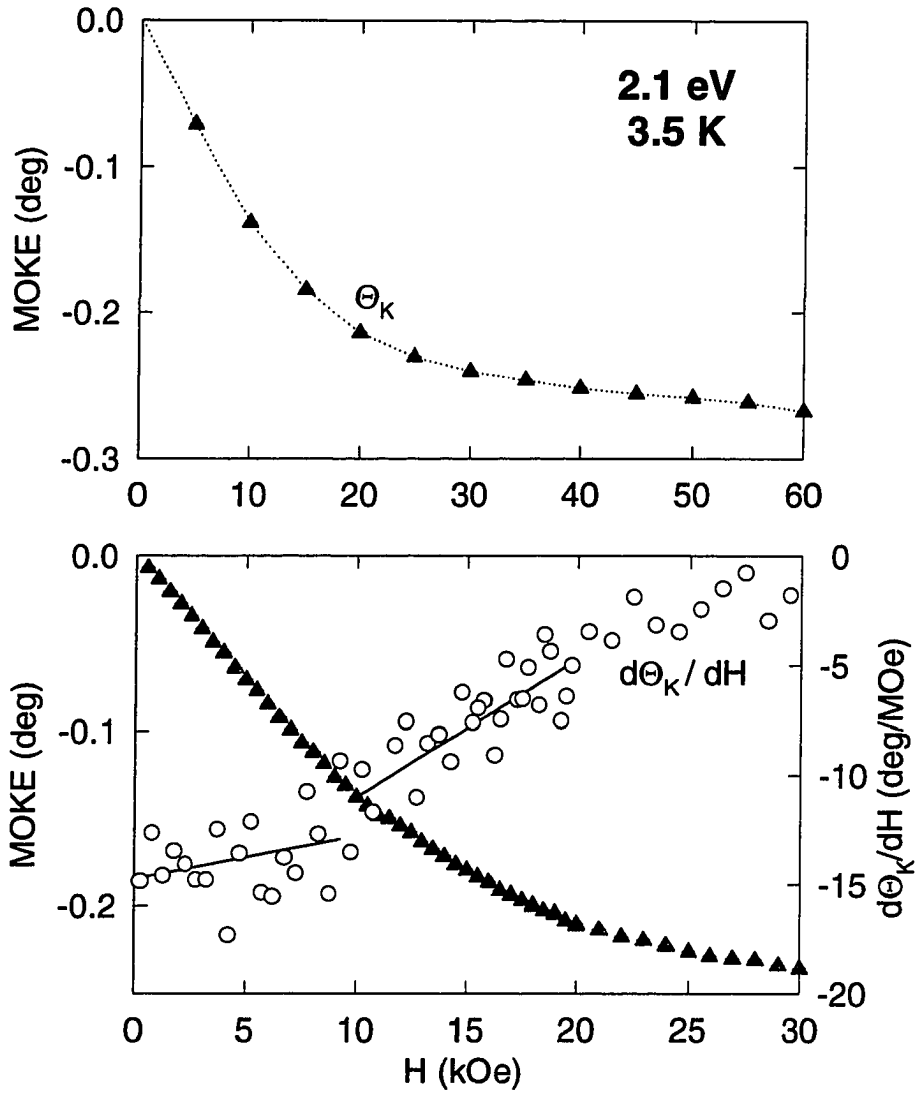

Figure 7.15 Kerr rotation (Θ_K) versus field for $TmNi_2B_2C$ at 2.1 eV and 3.5 K. The lower panel shows low-field data and the derivative of Θ_K with respect to the applied field. Solid lines indicate the different slopes below and above $H_{c2} \approx 10$ kOe.

excellent agreement with magnetization measurements ($H_{c2} \approx 8$ kOe at 2 K). Θ_K behaves similarly to the magnetization in this compound and we believe that the change in $\Delta\Theta_K/\Delta H$ originates from the magnetization and is not a direct consequence of the superconducting state, in which the electrons could give a different contribution to the optical signal than in their normal state[168, 169].

As mentioned earlier, the off-diagonal optical conductivity, rather than the magneto-optic parameters, should be compared to BS calculations. In Fig. 7.16 we show the dispersive (upper panel) and absorptive (lower panel) component of the off-diagonal conductivity for RNi_2B_2C. Note that we plot $\omega\sigma_{2xy}$ in order to suppress the free-electron contribution. Despite the quite different Kerr spectra, σ_{1xy} is similar for both compounds. The magnitude of the off-diagonal absorption of $YbNi_2B_2C$ is smaller than that of $TmNi_2B_2C$. If we compare $\omega\sigma_{2xy}$ with σ_{1xx} (Fig. 7.11) we notice that the transition at 2.5 eV also appears in the off-diagonal conductivity. The shape of the structure indicates a diamagnetic line shape, i.e. the absorptive part shows a dispersive line shape, whereas we find the common Lorentzian absorption peak in σ_{1xy}. For the diagonal optical conductivity one will always find a Lorentzian absorption peak in σ_{1xx}, whereas σ_{2xy} can have either shape. If σ_{2xy} has the shape of an absorption peak one calls it a paramagnetic line shape. If, however, σ_{2xy} exhibits dispersive behavior one speaks of a diamagnetic transition (for further details on the origin of this terminology we refer to Ref. [7]). In some cases the shape of σ_{2xy} can give additional information on the origin of the transition or the states involved.

The low-energy transition that we predicted based on the shape of σ_{1xx} becomes evident in σ_{xy}. We also confirm the interband transition above 5 eV, which results in an increasing absorption above 4.2 and 4.6 eV for $YbNi_2B_2C$ and $TmNi_2B_2C$, respectively. From σ_{1xy} above 4 eV we conclude that this transition is of paramagnetic character and a peak in $\omega\sigma_{2xy}$ can be expected between 5 and 5.5 eV for both compounds.

7.5 Conclusions

RNi_2B_2C (R=Tm, Yb) were investigated using ellipsometry and magneto-optical spectroscopy. Spectra for the two compounds are similar. The Kerr effect in magnetic $TmNi_2B_2C$ was found to be larger than in $YbNi_2B_2C$. $\Theta_K(H)$ shows paramagnetic behavior for $YbNi_2B_2C$, in agreement with magnetization measurements. For $TmNi_2B_2C$ the Kerr rotation saturates around 40 kOe. We were able to observe the superconducting transition in the Kerr rotation. From $\Delta\Theta_K/\Delta H$ at 2.8 K (which is above $T_N = 1.85$ K) a critical field $H_{c2} = 10$ kOe was estimated. Research investigating the possibility of observing the flux line lattice using Kerr microscopy is still in progress. The σ_{1xx} and σ_{2xy} spectra

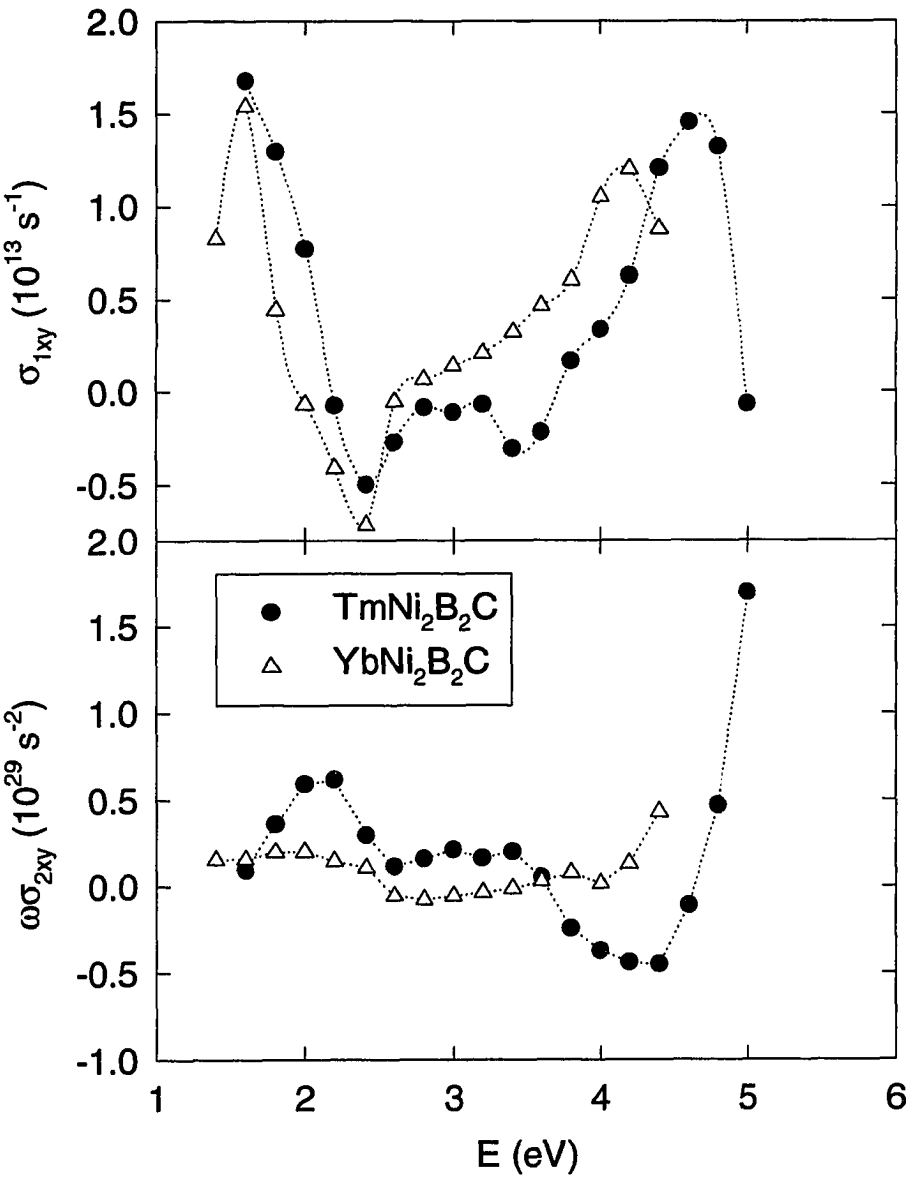

Figure 7.16 Off-diagonal optical conductivity of RNi_2B_2C determined from the optical constants in Fig. 7.11 and the Kerr parameters shown in Fig. 7.14. In the lower panel we plot $\omega\sigma_{2xy}$ to eliminate free-electron contributions.

indicate three transitions at 1.2, 2.5, and above 5 eV. These transitions were also found to occur in non-magnetic YNi_2B_2C and $LuNi_2B_2C$[187]. Combining the BS (including atomic and orbital character) and DOS we were able to identify the main contributions to the optical conductivity. The optical response between 1 and 6 eV is governed by $p \rightarrow d$ and $d \rightarrow p$ transitions. All atoms contribute to the states involved which supports earlier suggestions that RNi_2B_2C behaves like a 3D metal despite its 2D layered crystal structure.

8 MAGNETO-OPTICAL RESPONSE OF LOW CARRIER CONCENTRATRION, STRONGLY CORRELATED ELECTRON SYSTEMS

8.1 Introduction

In the previous chapters we dealt with compounds showing a variety of different properties due to s-f interaction, ranging from magnetic HF compounds to VF systems. We would like to investigate yet another group of materials, namely concentrated Kondo systems with a low carrier concentration that order magnetically. A low concentration of carriers leads to a plasmon energy in the visible to near infrared spectral range, which should be readily observable in our experiment. A plasma edge, in adition to interband absorption, can lead to a large magnetooptical Kerr effect[4]. Two representative examples are CeB_6 and YbBiPt. CeB_6 is a *moderate* HF compound, whereas YbBiPt shows the largest Sommerfeld constant observed so far (8 J/K^2 mol)[191]. Investigation of CeB_6 indicated that, although the Ce-4f states drive the magnetism in this compound, the Fermi surface is quite similar to that of LaB_6. So far, no experimental results on the Fermi surface of YbBiPt are available. LDA predicts, assuming the enhanced linear specific heat coefficient is entirely due to heavy quasiparticles, electron masses up to $4000m_e$.

Our optical investigation was clearly motivated by the low carrier concentration found in these compounds. In the following sections we will deal with CeB_6 (Section 8.2) and YbBiPt (Section 8.3), their magentic and optical properties, and compare the results to our LDA calculation.

8.2 CeB_6

8.2.1 Sample preparation and characterization

Using the flux growth technique[83, 84, 85], single crystals of CeB_6 of up to $7 \times 4 \times 4$ mm^3 were grown from Ames Lab Ce (99.995%) and Eagle-Picher B (99.5% isotopic). The samples have a blue to purple appearance, unlike common metals. The crystals did not have clean facets and polishing was

necessary. We used silicon carbide abrasive paper to obtain a flat surface. For the final step silicon carbide abrasives with grain sizes of 6, 1, and 0.25 μm were used. The sample surface was highly reflective but showed flux inclusions. This is a common problem with the flux growth technique. Due to large amounts of B in the sample the crystals are inert and oxidation is not a problem. However, in order to ensure highest sample quality the sample was transferred into the sample chamber immediately after the polishing procedure.

CeB_6 crystallizes in the simple cubic CaB_6 crystal structure (space group $Pm\bar{3}m$, O_h^1). This structure is derived from the CsCl type with Ce in the body center and B_6 octahedra located at the corners of the cubic cell (shown in Fig. 8.1). Ce is at position $(\frac{1}{2}, \frac{1}{2}, \frac{1}{2})$ and B is located at $(0.301, 0, 0)$. Powder XRD patterns (Fig. 8.2) show all reflections of the cubic structure and no second phase can be detected. From our XRD data we estimate a lattice constant of 4.115Å, which is in good agreement with earlier reports[192, 193, 194].

Due to its intriguing low temperature magnetic and transport properties CeB_6 has attracted much interest. For an extensive review on CeB_6 we refer to Ref. [195]. CeB_6 has an extremely rich phase diagram at low temperature[196, 193, 194]. Below T_N (2.4 K in zero field) CeB_6 shows simple antiferromagnetic order. Horn *et al.*[196] performed magnetization measurements on single crystalline CeB_6. At low field the largest magnetization was found for a field applied parallel to [001]. Since a field that is applied perpendicular to the antiferromagnetic axis most effectively turns the local moments, this indicates that [001] is perpendicular to the easy axis of magnetization. This, in turn, leads to the conclusion that [111], which is the easy axis for a Γ_7 ground state, is not the easy axis of magnetization. The ground state $J = 5/2$ manifold of Ce^{3+} is split into a Γ_7 doublet and a Γ_8 quartet by the cubic crystal field. An easy axis different from [111] already suggests that Γ_8 (or a mixture of Γ_7 and Γ_8) might be the ground state. A steep increase of the magnetization up to a moment larger than the expected saturation for a Γ_7 doublet ($0.71\mu_B$) supports this view. However, the moment remains well below the full moment for the Γ_8 ground state ($1.54\mu_B$). Anomalies in the specific heat[197] are consistent with an additional splitting of the Γ_8 ground state into to doublets. This splitting is caused by a reduced symmetry, which either is the result of a dynamic Jahn-Teller-like effect, involving low-energy acoustic phonons, or might originate from anisotropic p-f and d-f hybridization[198]. Raman scattering confirmed a splitting of the fourfold degenerate Γ_8 state into two doublets, separated by 30 K[198]. The crystal field transition to the Γ_7 state was identified near 530 K[198]. A CEF splitting of $T_{CEF} = 540$ K was derived from the temperature dependence of the elastic constants, considering quadrupolar exchange interactions[199, 200, 201].

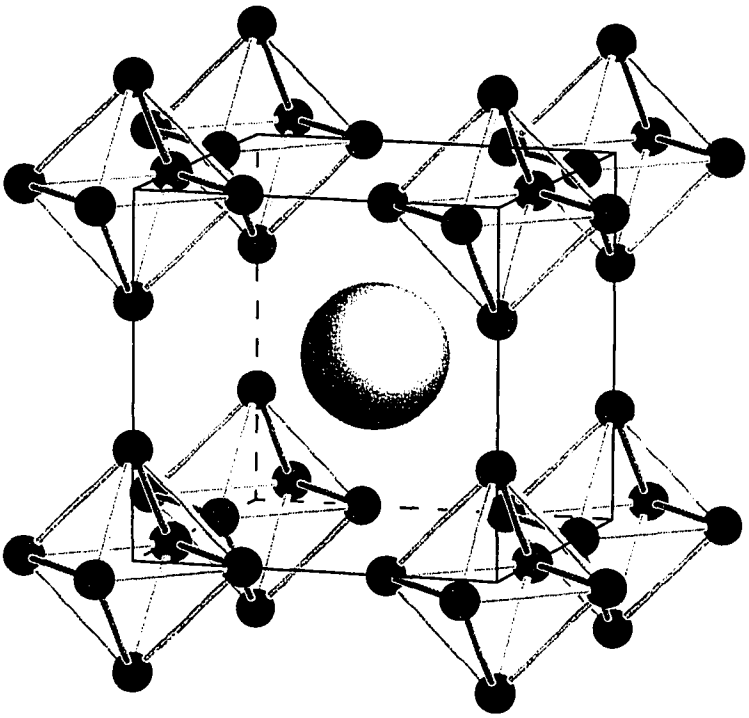

Figure 8.1 Crystal structure of CeB_6. Atomic positions are $(0.5, 0.5, 0.5)$ for Ce (white) and $(0.30, 0, 0)$ for B (black). Bonds indicate the octahedral coordination of B.

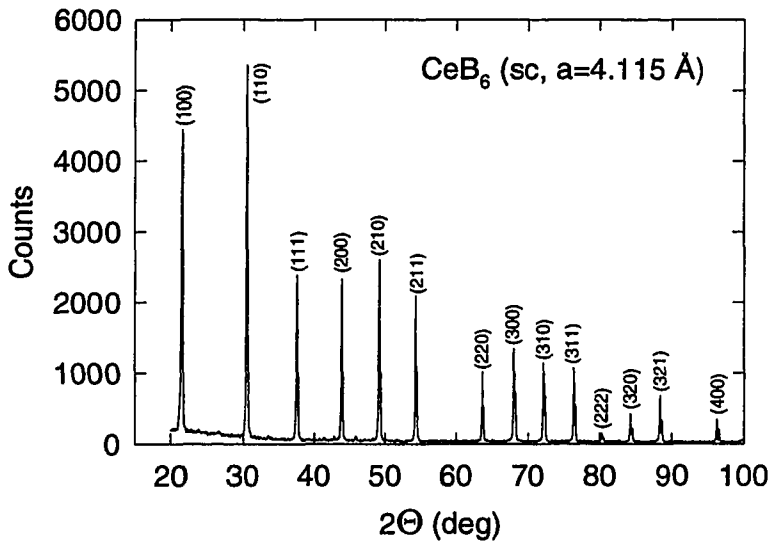

Figure 8.2 Powder X-ray pattern for CeB_6. Reflections for the simple cubic cell are indicated.

From the low-temperature width of the quasielastic neutron line, a Kondo temperature of 3 K was derived, i.e. $T_K \approx T_N$. This value is in agreement with resistivity measurements by Tanaka *et al.*[202]. In CeB_6 Kondo fluctuations are believed to be on-site interactions, i.e. mixing of Ce-4f states with Ce derived conduction electron states. In zero field the Kondo effect prevents quadrupolar order, but with increasing field the Kondo effect is suppressed and antiferroquadrupolar order can develop. The high temperature phase above T_Q (3.2 K in zero field) is paramagnetic and characterized by the incoherent Γ_8 ground state. For temperatures between T_N and T_Q, the compound displays antiferroquadrupolar ordering, which was not observed in zero field. As commonly seen in dense Kondo systems, the linear specific heat coefficient is enhanced ($\gamma = 260$ mJ/K^2 mol)[203].

We measured M versus H at 2 K for an arbitrary alignment (Fig. 8.3)[93]. Our data do not indicate any saturation up to 55 kOe. A reduced moment of $0.44\mu_B$ was observed at the highest obtainable field. When we plot the derivative of the magnetization with respect to the applied field (inset in Fig. 8.3), we see a structure at around 20 kOe, which presumably marks the transition from the simple antiferromagnetic to the field induced ferromagnetic phase. Above 20 kOe $\Delta M/\Delta H$ decreases indicating the onset of saturation. However, this effect is weak and it is not observed in M(H). Inverse χ versus temperature is shown in Fig. 8.4. Above 150 K, χ^{-1} is linear and a fit to a Curie-Weiss law yields a Weiss temperature of -66 K, which agrees well with $\Theta = -62$ K, as reported by Kawakami *et al.*[204]. The large negative Weiss temperature, and deviations from Curie-Weiss behavior at low temperature, confirm strong hybridization of the Ce-4f levels. This is consistent with the strongly reduced effective moment, $\mu_{eff} = 2.18\mu_B$, compared to the moment of an isolated Ce^{3+} ion ($2.54\mu_B$)[177]. It should be noted that the transitions at T_Q and T_N are not observed. We attribute this to strain induced in the sample during the growth process. This strain, we believe, is strong enough to prevent magnetic order and upset the delicate balance between magnetic and Kondo-type interactions in this compound.

8.2.2 Electronic structure

Band calculations for CeB_6 were first reported by Yanase[205], who used a self-consistent APW method to investigate the degree of 4f delocalization in several Ce compounds. It was found that 4f hybridization in CeB_6 is quite different from that observed in other compounds. It occurs only in a small part of the BZ, i.e. at Γ and along Σ. Van der Heide *et al.*[206] measured the dielectric function of RB_6 (R=La, Ce) and compared it to the optical conductivity obtained from an ASW-type calculation. However, they assumed constant matrix elements, an approximation that is certainly not justified when f states contribute to the optical response. Therefore, the assignment of spectral features based on this

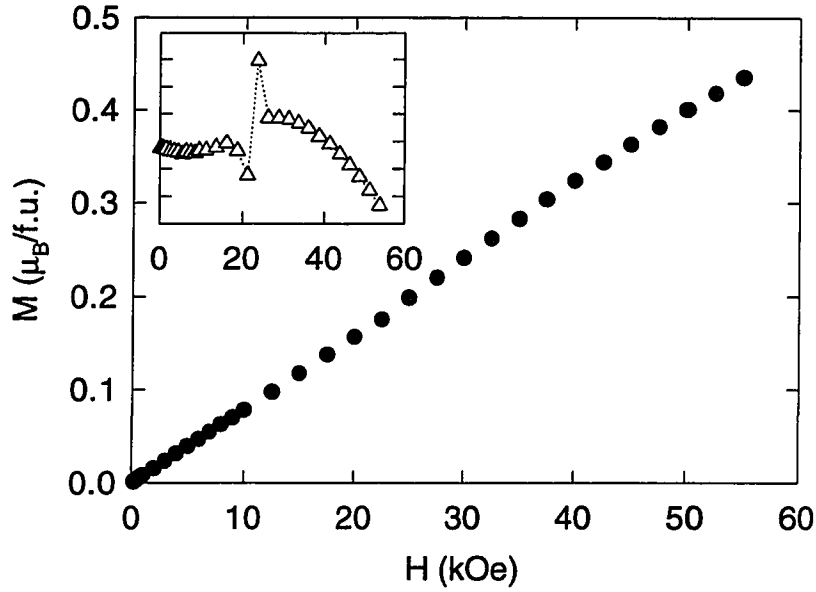

Figure 8.3 Magnetization versus field for a CeB_6 single crystal at 2 K. Inset: Derivative of magnetization with respect to field.

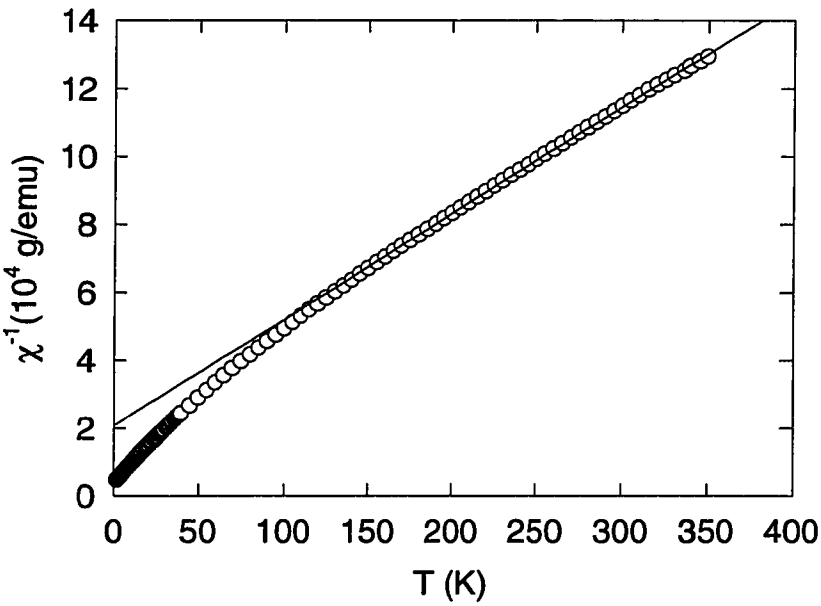

Figure 8.4 Inverse magnetic susceptibility versus temperature for a CeB_6 single crystal at $H = 1$ kOe. A fit of $\chi^{-1}(T)$ to a Curie-Weiss law above 150 K (solid line) yields $\mu_{eff} = 2.18\mu_B$/Ce and a Weiss temperature of -66 K.

calculation is questionable. Their BS is similar to that by Yanase[205], but shows distinct deviations, such as different band splittings and band positions throughout the BZ.

With the advancement of BS calculations, spin-polarized calculations for CeB_6 became feasible. There is a series of reports on the Fermi surface and enhancement effects in CeB_6 by Temmerman *et al.*[207, 208, 209, 210]. They used the LMTO method in the ASA. Their nonmagnetic BS is, again, similar to that by Yanase, but shows important deviations at the X, Γ, and R points. From their spin-polarized calculation, which assumes ferromagnetic order, they derived a spin moment of $0.94\mu_B$ and an orbital contribution of $-1.06\mu_B$. The calculated Fermi surface is in fair agreement with experimental results. Another, very peculiar, result is the DOS for the ferromagnetic case. They found a narrow majority spin $4f$ band pinned at the Fermi level. The minority spin DOS shows diffuse bands of $4f$ and $5d$ character about 3 eV above E_F. This would imply an exchange splitting of the same order, which is rather unusual. It is not clear how LDA can produce a splitting of this magnitude in a Ce compound. Their treatment of CeB_6 is inconsistent with our results, as will be pointed out below.

Finally, we would like to mention the most recent electronic structure calculation for CeB_6. Ripplinger *et al.*[211] investigated the charge distribution in hexaborides using the full-potential LAPW method. They found the B charge (within the WS sphere) to be proportional to the valence charge concentration. LaB_6 and CeB_6 deviated from this linear dependence. However, agreement was improved upon treating the (localized) $4f$ electrons as core, rather than as valence, states.

We performed BS calculations for CeB_6 for the non-magnetic and the hypothetical ferromagnetic case. We used the experimental lattice constant of 4.115 Å. Muffin-tin sphere radii and atomic positions are given in Table 8.1. In addition to Ce and B, two empty spheres were inserted in order to achieve space filling. As basis functions we chose Ce-($6s6p5d4f$) and B-($2s2p3d$) orbitals. ($1s2p3d$) wave functions were included on the empty sites. Calculations were carried out using 84 k-points in the irreducible wedge of the BZ (1/48), i.e. on a 12 × 12 × 12 mesh. After convergence was achieved, one iteration on a 24 × 24 × 24 mesh was used to calculate the BS and DOS.

We first performed a non-magnetic calculation, in which spin-orbit coupling was neglected. It turned out that the charge in the empty spheres amounted to as much as 0.21 per s and 0.03 per p channel, indicating a fairly large amplitude of the total wave function in the interstitial region. This is not a *physical* charge, in the sense that it is caused by an expansion of orbitals centered at neighboring sites rather than by an ion positioned at that lattice site. The charge in the d orbitals of the empty spheres was negligible. Charges inside the Ce and B spheres are shown in Table 8.2. We disagree with the charge distribution reported by Langford *et al.*[208]. We believe that our approach, using empty

Table 8.1 Atomic positions for CeB_6 in units of lattice constants $a = 4.115$ Å. We also show the radius of the Wigner Seitz spheres, R, in atomic units and the basis functions included for the TB-LMTO calculation. E and E1 designate empty spheres that were inserted in order to achieve space filling.

Atom	x (a)	y (a)	z (a)	R (a.u.)	Basis set
Ce	1/2	1/2	1/2	3.412	($6s6p5d4f$)
B	0	0	0	1.763	($2s2p3d$)
E	1/2	0	0.2825	1.410	($1s2p3d$)
E1	0.207	0.207	0.207	1.005	($1s2p3d$)

Table 8.2 Results of charge and moments inside the Wigner-Seitz spheres in CeB_6 from self-consistent spin-polarized BS calculations. Spin-orbit coupling was included only in the magnetic calculation. Charges are given in electrons; Moments in μ_B; DOS at E_F in states/eV cell.

	Ce				B	
	s	p	d	f	s	p
Non-magnetic						
n	0.18	0.43	1.01	1.23	0.72	1.48
N(E_F)	0.00	0.06	0.22	5.31	0.02	0.49
Ferromagnetic						
$n_\downarrow$	0.08	0.18	0.43	0.31	0.36	0.73
$n_\uparrow$	0.08	0.18	0.44	0.93	0.36	0.73
n_{tot}	0.16	0.36	0.87	1.24	0.72	1.46
μ_S	0.00	0.00	0.01	0.62	0.00	0.00
μ_L	0.00	0.00	0.00	-0.35	0.00	0.00
N(E_F)	0.00	0.03	0.19	8.59	0.01	0.35

spheres, instead of increased radii for the Ce and B spheres, yields a better description of the electronic structure. It is our experience that sphere radii larger than 3.9 a.u. for Ce can lead to drastic changes of the electronic structure. One can account for the increased radius by including higher-order wave functions (e.g. $4f$, $5g$) on the Ce and B site. This was neglected in Ref. [208], and led to an increased charge at the Ce and B site, which is physically not meaningful. In particular, they found a charge of 2.20 and 2.11 electrons per Ce-d and Ce-f orbital, respectively. This compares to 1.01 and 1.23 electrons per Ce-d and Ce-f channel obtained from our calculation. The B-$2p$ charge differs by as much as 31%. The DOS at E_F is in fair agreement. The DOS due to Ce-$4f$ states is nearly twice as large in Ref. [208]. We attribute this difference to spin-orbit coupling, which was neglected in our non-magnetic calculation. The ferromagnetic calculation yields a much larger Ce derived DOS at the Fermi level,

which agrees with the one calculated by Langford *et al.*[208]. However, it is very likely that, instead of spin-orbit, exchange interaction leads to an increased DOS at E_F. Using Eq. (5.1) and $N(E_F)$, obtained from our spin-polarized calculation, we estimate an unenhanced Sommerfeld coefficient of 23 mJ/K^2 mol. An enhancement factor $\lambda \approx 10$ is derived, which is close to the one found for $CeAl_2$ ($\lambda \approx 8$).

The Ce-d charge is reduced by 14% compared to the non-magnetic calculation (see Table 8.2). All other charges remain nearly constant. There is only negligible contribution to the spin magnetic moment from the s, p, and d channel. The Ce-f state is responsible for the magnetism in this structure, and the f-derived spin moment is in excellent agreement with a report by Horn *et al.*[196], who derived a moment of $0.65\mu_B$/Ce from neutron scattering. Since the BS, in particular the position and width of the the $4f$ bands, is similar to that of $CeAl_2$, the orbital moment will be incorrect. For strongly localized bands, LDA tends to overestimate the orbital contribution, which lead to zero net moment in the case of $PrAl_2$, although the spin moment agreed well with magnetization measurements (see Table 5.1). This tendency is also observed in the case CeB_6 for which the orbital contribution reduces the magnetic moment by over 50%.

In Figs. 8.5–8.7 we show the BS and DOS for hypothetical ferromagnetic CeB_6. Our BS is in excellent agreement with that of Yanase[205]. The spin-polarized BS can be separated into three regions. Figures 8.6 and 8.7 show that, below -2 eV, bands are mostly B-$2p$ derived with only little Ce-$5d$ character. This is confirmed by the BS, i.e. the bands in that region show negligible spin-orbit splitting. Just below E_F, Ce and B states contribute, indicating strong mixing at this energy. Especially, we notice strong hybridization with Ce-$4f$ states, which extend to about 0.5 eV below E_F. As expected, the majority spin $4f$ band is pinned to the Fermi level, separated from the minority spin band by an exchange splitting of roughly 0.5 eV. The $4f$ bands have a tail up to 3 eV, that overlaps with Ce-$5d$ states. Strong d-f mixing is found between 1 and 2 eV. Above 2 eV the DOS is dominated by contributions from B-p and Ce-d states. This is supported by Fig. 8.8, which is an expanded view of the non-magnetic BS, showing only the energy range of interest for interpretation of our optical spectra. B-$2s$ states, as well as the two lowest orbitals of Ce, are seen to be negligible between -5 and 5 eV. B-$2p$ character dominates below E_F. Around E_F bands are mostly Ce-$4f$ character, which gradually changes to Ce-$5d$ above 2 eV.

8.2.3 Optical properties and plasma edge

In compounds with a low carrier concentration the plasma resonance occurs in the near infrared to visible spectral range. This plasma edge was observed in the optical response of LaB_6, as well as in

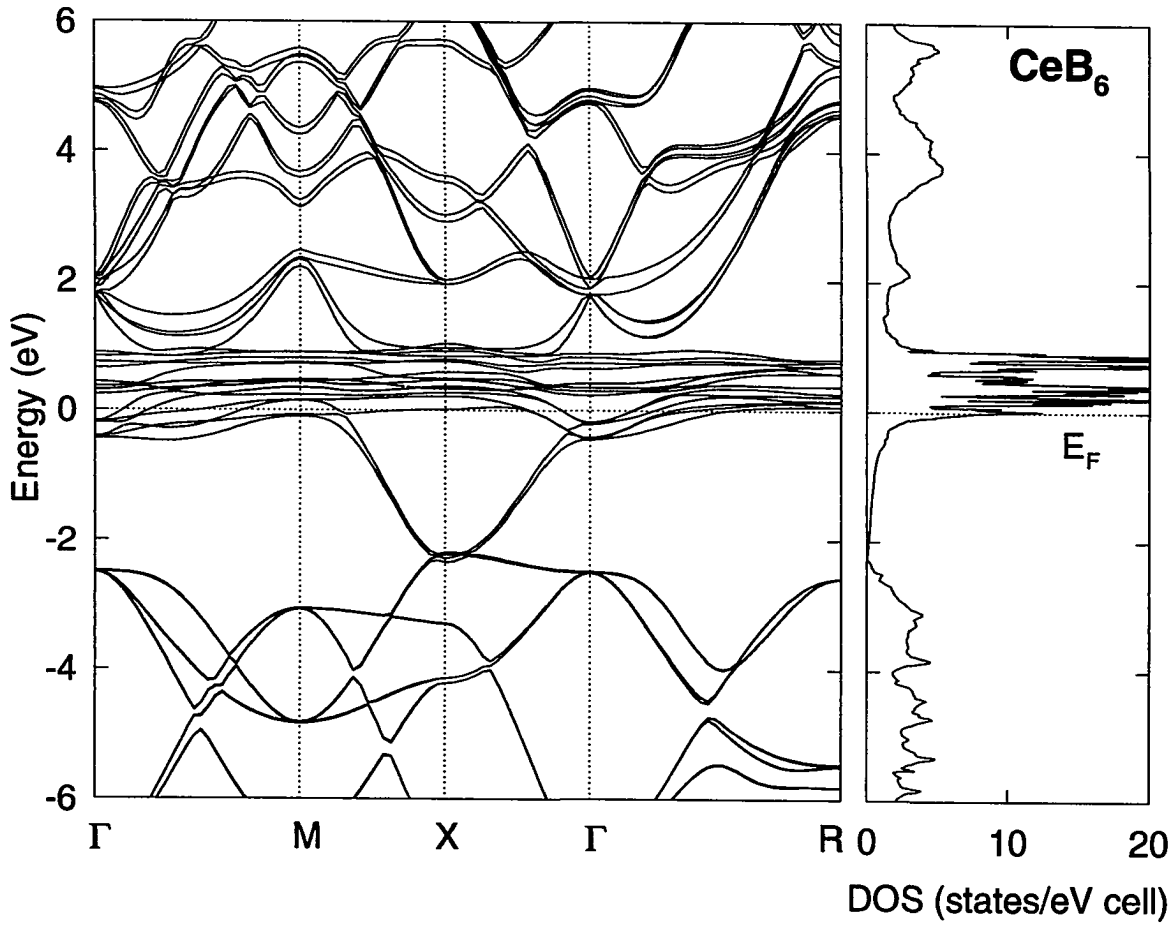

Figure 8.5 Spin-polarized band structure, including spin-orbit interaction, for hypothetical ferromagnetic CeB_6.

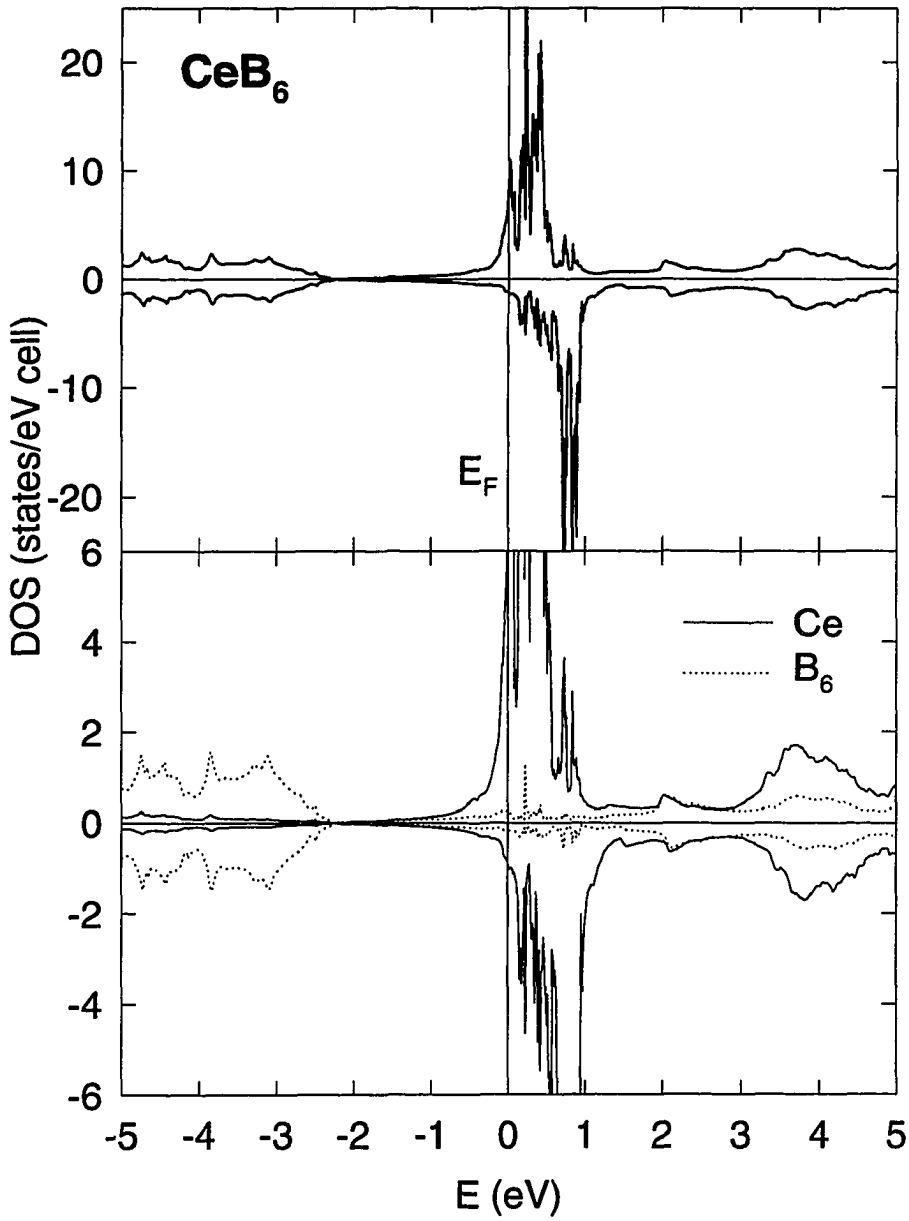

Figure 8.6 Total DOS for CeB_6 (upper panel) and partial DOS (lower panel).

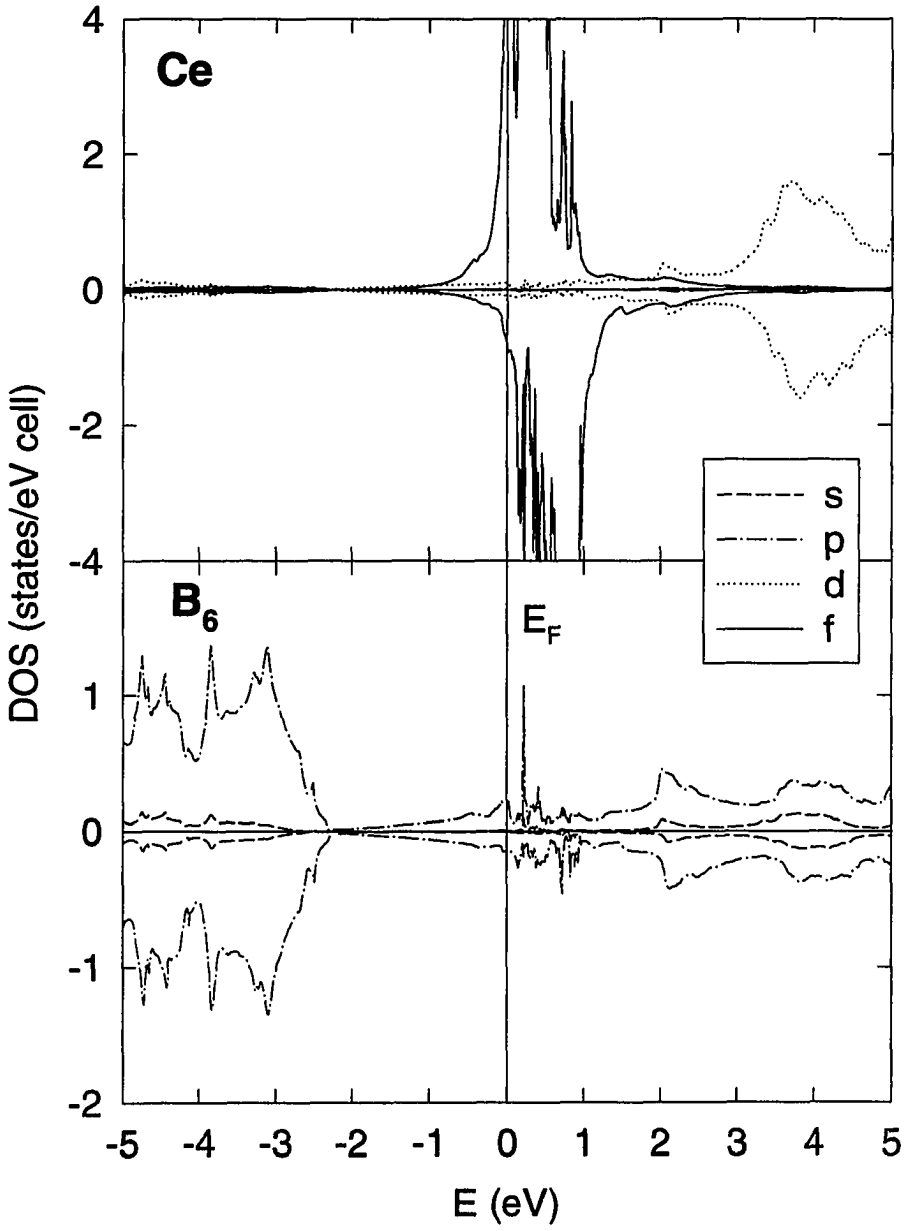

Figure 8.7 Orbital decomposition of the DOS for CeB_6.

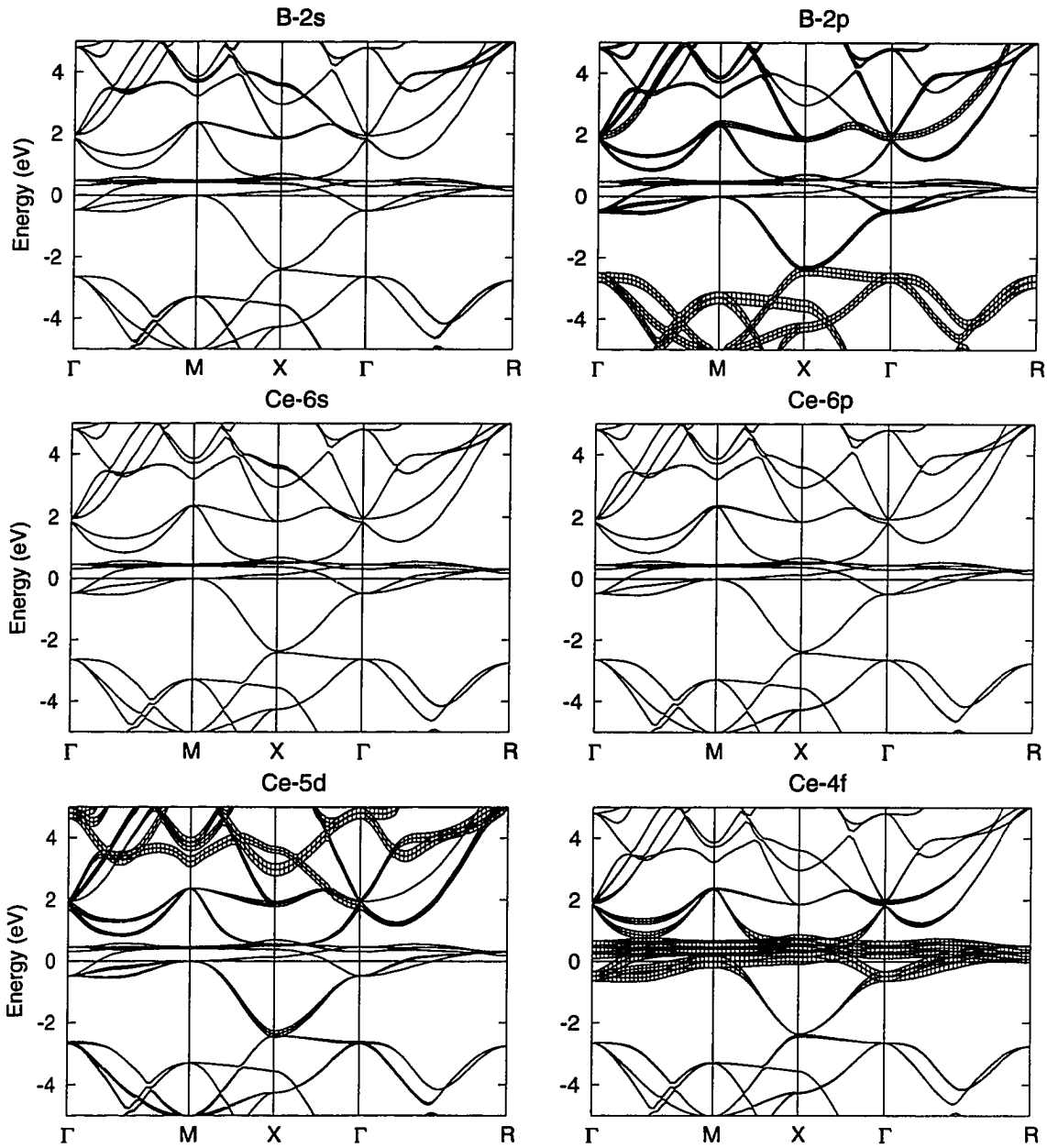

Figure 8.8 Relativistic non-magnetic band structure of CeB_6 projected on the atomic and orbital character. Spin-orbit coupling was neglected. The width of the hatched bands is proportional to the amount of a particular character in a band.

heavier rare-earth hexaborides[206, 212, 213, 214]. In the case of CeB_6, besides the reflectivity minimum at 2 eV, characteristic low-energy absorptions were observed around 0.012 eV (only at 10 K) and around 0.45 eV (at 10 and 300 K)[215]. Similar low-energy transitions (at 4 – 20 meV) have been observed in a wide variety of HF compounds, including the isostructural HF $CeCu_6$[216, 217, 218]. The periodic Anderson Hamiltonian predicts the opening of a hybridization gap in HF materials[216]. This gap gives rise to a Schottky anomaly in the specific heat, i.e. thermal excitation in a two level system. In the HF regime, the low-energy optical conductivity can be fitted with a Drude term, which originates from plasma oscillations of (heavy) quasiparticles, and a (fd)-f-type transition across a gap. The optical masses agree, in general, well with those obtained from dHvA measurements.

Aono *at al.*[219] reported angle-resolved PES experiments on LaB_6. Valence bands were in good agreement with those calculated by Hasegawa and Yanase[220]. Later PES experiments confirmed an emission peak at 2.5 eV for CeB_6, which is similar to that found in γ-Ce[107] and $CeAl_2$ (Chapter 5). In addition, a feature at E_F was found in CeB_6, but not in the other hexaborides. Although this analogy to γ-Ce is striking, the peak at E_F was not ascribed to $4f$ emission. Shino *et al.*[221] studied the electronic structure of rare-earth hexaborides using PES, BIS and optical reflectivity. Reflectivity spectra are interpreted utilizing the results of PES and BIS, forming a consistent picture of the electronic structure of RB_6 compounds.

We measured the optical response of a polished single crystal of CeB_6 between 1.4 and 5 eV. The diagonal optical conductivity (Fig. 8.9) was determined from ellipsometry. Data were taken at room temperature with no magnetic field applied. Absorption shows a minimum at about 2 eV. This minimum corresponds to a plasmon excitation. In the near-ultraviolet we observe another transition in σ_{1xx} at about 3.7 eV. Above 4.5 eV absorption increases. However, the shape of σ_{2xx} does not confirm another transition at higher energy. Intraband contributions are important below 1 eV, but can be neglected in our range.

The Kerr effect of CeB_6 is shown in Fig. 8.10. Data were taken at 70 kOe and 2 K, which is below the antiferromagnetic ordering temperature. A large negative peak in the Kerr rotation, which coincides with the plasma minimum, dominates the magneto-optic spectrum. The maximum magnitude of the Kerr rotation reaches $-1.13°$ at 1.9 eV. There is no clear structure above 3 eV. Θ_K decreases monotonically between 3 and 5 eV. The Kerr rotation at 1.9 eV was also measured versus field. Θ_K is proportional to the applied magnetic field up to 70 kOe. We show the off-diagonal conductivity in Fig. 8.11. There is a transition at 2 eV. However, the absorption amplitude is rather small. The large Kerr effect is due to small magneto-optic absorption, which interferes with the plasma edge. The transition

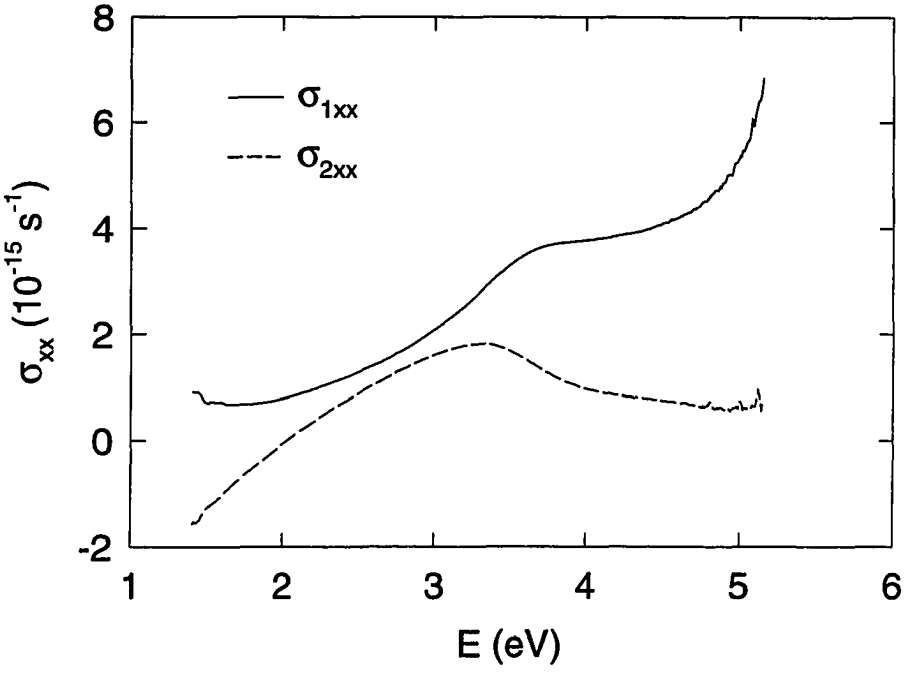

Figure 8.9 Room temperature diagonal optical conductivity of CeB_6, measured by ellipsometry in zero field.

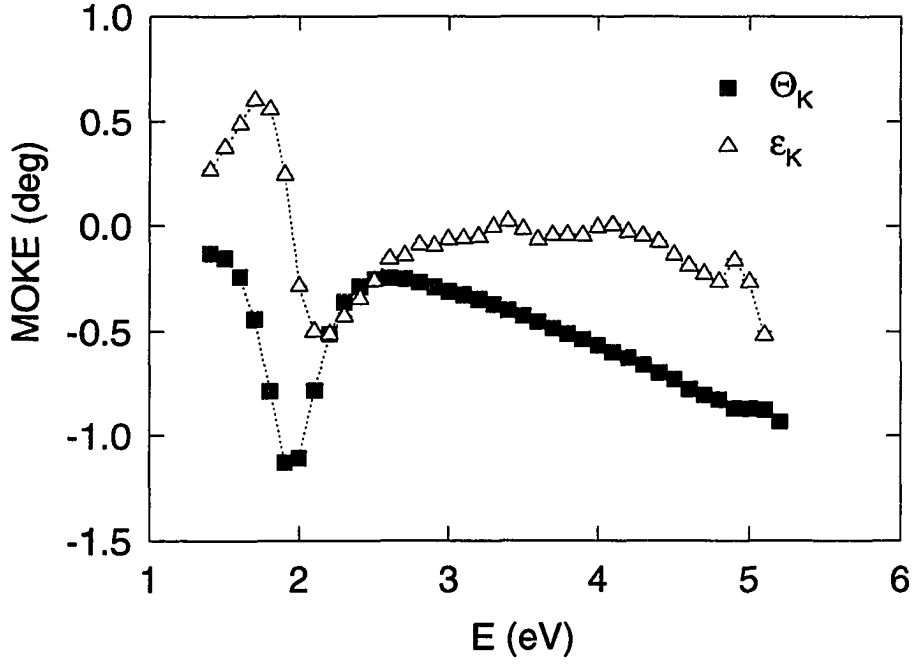

Figure 8.10 Magneto-optic Kerr rotation (Θ_K) and ellipticity (ϵ_K) of CeB_6. Data were taken at 2 K and 70 kOe.

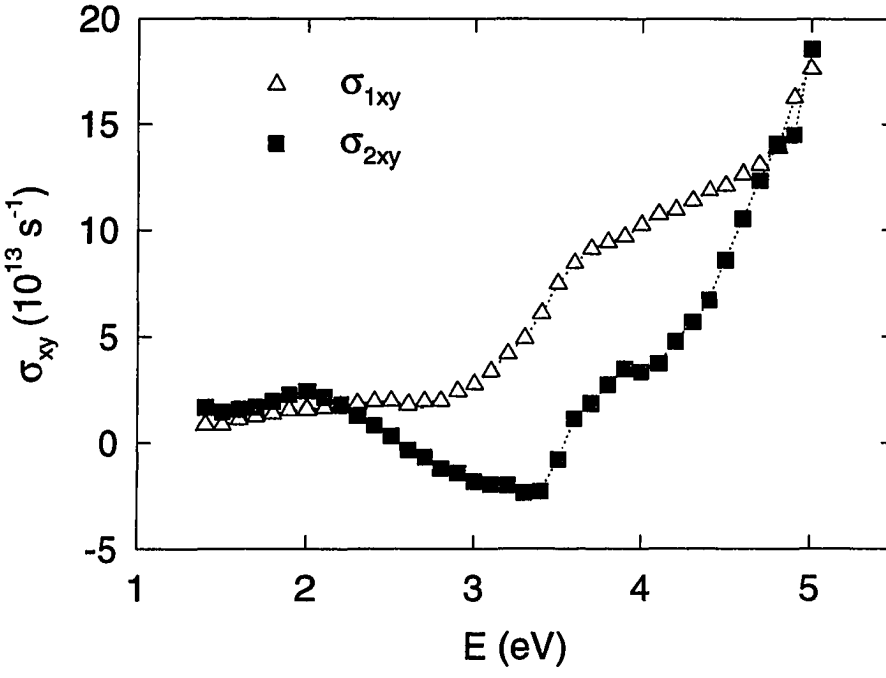

Figure 8.11 Off-diagonal optical conductivity of CeB_6, determined from the data shown in Figs. 8.9 and 8.10.

at 3.7 eV shows a weak feature in σ_{2xy}, but it leads to a broad shoulder in σ_{1xy}.

In Fig. 8.8 we show the BS of CeB_6, including the orbital character of the bands. Combining this information with the DOS plots, we can tentatively assign the absorption peaks in σ_{xx} and σ_{xy}. We believe that, due to strong dispersion of the bands along all directions of the BZ, only transitions at points of high symmetry, where bands are parallel, give rise to the absorption spectrum. This is also indicated in Fig. 8.12, where solid arrows indicate regions that probably contribute to the 2 eV absorption. We believe that the 2 eV feature in our spectra is due to transitions from occupied B-2p and Ce-5d states to empty Ce-4f bands just above E_F at the X point. Other contributions to this transition are possibly from occupied 4f to empty B-2p and Ce-5d states at Γ, and from 4f to B-2p states at the M point. Dashed arrows show points which might contribute to the transition at 3.7 eV. The four transitions we mark are: $f \rightarrow d$ along the line Γ–M, $p \rightarrow d$ at Γ, $d \rightarrow p$ at X, and $p \rightarrow f$ at M.

To summarize, we presented the magnetic properties and optical conductivity of CeB_6. There are two absorption features in both, the diagonal and off-diagonal, components of the optical conductivity. We calculated the electronic structure and found the spin magnetic moment to agree well with experimental results, while the orbital moment is overestimated by our LDA calculation. Using DOS and BS plots,

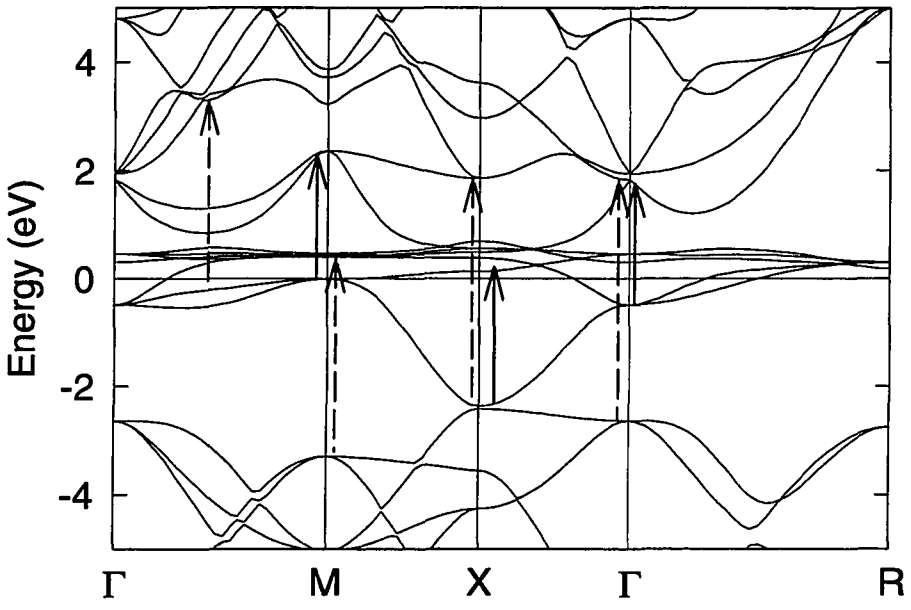

Figure 8.12 Relativistic non-magnetic band structure of CeB_6. Spin-orbit coupling was neglected. Interband transitions contributing to the 2 and 3.7 eV absorption are indicated by solid and dashed arrows, respectively.

we were able to identify the interband absorptions that were observed in the optical spectra. The large Kerr effect results from a small magneto-optic absorption in addition to a minimum in σ_{1xx}. If strongly spin polarized $4f$ states were involved, this effect could lead to Kerr rotations that are an order of magnitude larger than for CeB_6[6, 222, 223, 224, 225, 226].

8.3 YbBiPt

8.3.1 Sample preparation and characterization

Single crystals of YbBiPt were grown from excess Bi flux[83, 84, 85] using Ames Lab Yb (99.9%), Bi, and Pt. Smaller crystals (about $1 \times 2 \times 1$ mm^3) of octahedral morphology had clean triangular facets. Measurements were performed on the as-grown surfaces. Due to the small surface area, the intensity of the optical signal was rather weak. We then polished a larger crystal ($5 \times 5 \times 2$ mm^3) using silicon carbide abrasives with grain sizes of 6, 1, and 0.25 μm. After the polishing procedure the sample was epoxied to the sample holder and transferred into the sample chamber, where an inert atmosphere prevented further oxidation. The samples were characterized by transport and XRD measurements, which were

presented in Refs. [191, 227, 228]. We will discuss the results here, emphasizing the magnetic properties of YbBiPt, and refer to the original work for more detailed information.

YbBiPt crystallizes in the face-centered cubic MgAgAs structure, which is a common Heusler-alloy structure. The three elements, namely Yb, Bi, and Pt, each occupy a fcc sublattice placed at $(-\frac{1}{4},-\frac{1}{4},-\frac{1}{4})$, $(\frac{1}{4},\frac{1}{4},\frac{1}{4})$, and $(0,0,0)$, respectively. This structure can be thought of as a fictitious YbBi rock-salt structure with Pt on interstitial sites. The crystal structure, which is shown in Fig. 8.13, belongs to space group $F\bar{4}3m$. Pt is at the unique site, i.e. it has two nearest neighbors (along the body diagonal) at $(-\frac{1}{4},-\frac{1}{4},-\frac{1}{4})$ and $(\frac{1}{4},\frac{1}{4},\frac{1}{4})$. Bonds indicate the tetrahedral coordination of Yb and Bi (point-group symmetry $\bar{4}3m$). Both have one Pt atom and one empty site as nearest neighbor. Rietveld refinement of a powder XRD pattern yielded a lattice constant of 6.5953 ± 0.0001 Å[227].

Magnetization measurements were used to determine the ground state of YbBiPt. The susceptibility (Fig. 8.14) shows Curie-Weiss behavior. A fit for the high-temperature data yields an effective moment of $4.2\mu_B$ and a Weiss temperature of 2 K. The effective moment is fairly close to the full moment expected for trivalent Yb^{3+} ($4.54\mu_B$)[177]. Below 50 K, the susceptibility deviates from Curie-Weiss behavior, which is attributed to crystal field effects. To further investigate the magnetic properties the AC susceptibility was measured between 0.08 and 80 K (inset in Fig. 8.14). The peak in χ_{AC} indicates a phase transition at 400 mK and the susceptibility is consistent with antiferromagnetic order below that temperature. This is supported by resistivity and specific heat data[191, 229, 228, 230, 231], which show an anomaly at the same temperature. Although YbBiPt has a cubic crystal structure, it shows a large anisotropy in the resistivity below the ordering temperature[230, 231]. The reason for this anisotropy is not clear, but might involve (1) small localized moment order and the opening of a superzone gap, as a result of the magnetically imposed periodicity, (2) a spin-density wave (SDW) that leads to gapping of the Fermi surface, or (3) a Jahn-Teller effect in addition to the magnetic phase transition, that leads to a distortion of the crystal lattice to tetragonal or lower symmetry. As already mentioned, CEF effects play a key role in the ground state properties of YbBiPt. The eightfold degenerate $J = 7/2$ multiplet of Yb^{3+} is split into two doublets ($\Gamma_{6,7}$) and a Γ_8 quartet by the cubic crystal field. There has been some controversy about the exact positions of those levels[232, 228]. From specific heat data it can be concluded that there must be one doublet (Γ_6 or Γ_7) and the quartet Γ_8 below 20 K, and one doublet well above 20 K[228]. The best fit of the specific heat data is obtained for a Γ_8 ground state and a doublet at 12 K. Neutron inelastic scattering data, on the other hand, suggest a Γ_7 ground state that is nearly degenerate with Γ_8, i.e. $T_{CEF} \approx 1$ K[232]. An excitation to the Γ_6 doublet is seen at 5.8 meV (67 K). Agreement between specific heat and neutron scattering data is fair. However, neither of the

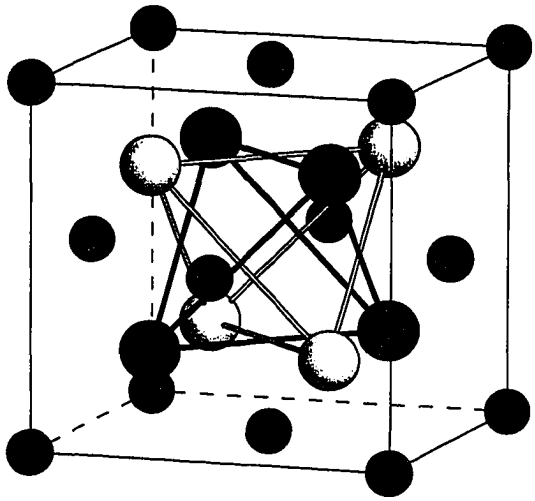

Figure 8.13 Conventional face-centered cubic (fcc) unit cell of YbBiPt. Large black spheres are Yb, large white spheres are Bi, and small gray spheres are Pt, respectively. Each atom forms a fcc lattice. Bonds indicate the tetrahedral coordination of Yb and Bi. The $(\frac{1}{2}\frac{1}{2}\frac{1}{2})$ site is empty.

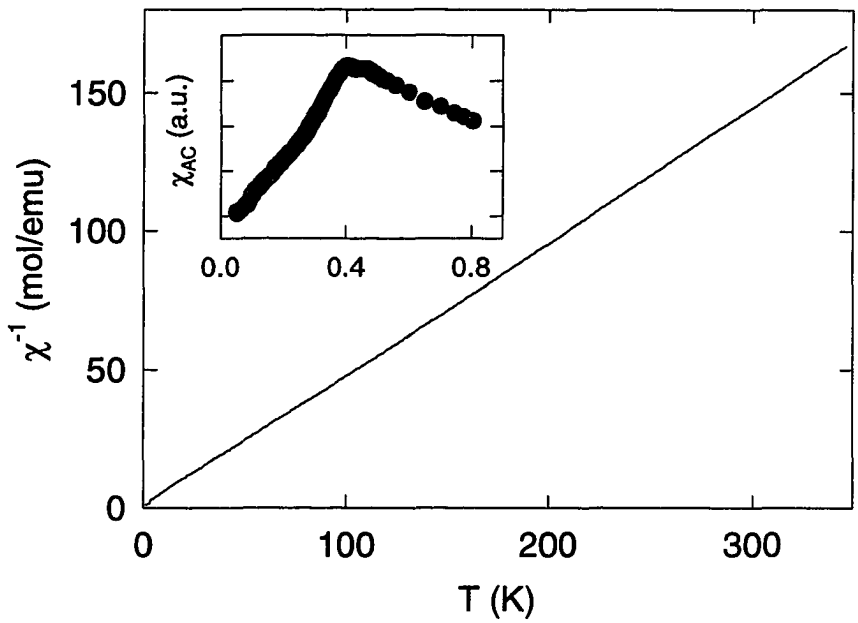

Figure 8.14 Inverse susceptibility of YbBiPt single crystal. A Curie-Weiss fit yields $\mu_{eff} = 4.2\mu_B$ and $\Theta = -2$ K. Inset: Low-temperature AC susceptibility, indicating a phase transition at 0.4 K. Data were taken from Ref. [191].

proposed splitting schemes can explain the reduced high-temperature moment. In Fig. 8.15 we show magnetization versus field for YbBiPt below (0.35 K) and above (1.0 K $\approx$ 2 T_N) the phase transition. M(H) is curved at low temperature, but the shape is not well fit with a Brillouin function. Furthermore, the moments found from μ^+ spin relaxation (μSR, $\approx 0.1\mu_B$)[233, 234, 235] are much smaller than those expected for either the Γ_7 or Γ_8 CF state. Based on entropy considerations and the reduced moment, it was suggested that Kondo-type interactions should be considered at low temperature[228]. The Kondo temperature must then be of the same order as the CEF energy. From the neutron quasi-elastic line width a Kondo temperature of 2 and 10 K was estimated for the ground state doublet and the quartet, respectively[232]. It should be considered that the CEF splitting model might not be an appropriate description of the ground state in the spin fluctuation regime.

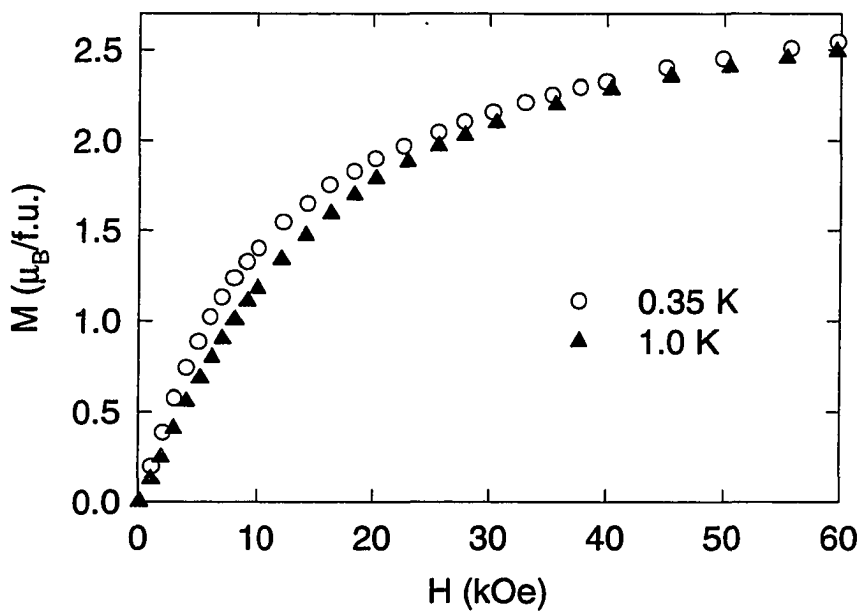

Figure 8.15 Magnetization versus field for a single crystal of YbBiPt. A maximum moment of 2.54μ_B is reached at 0.35 K and 60 kOe. Data were taken from Ref. [229].

From the magnetization data presented here, in conjunction with transport and scattering data, it becomes apparent that YbBiPt could be the *counterpart* to $YbNi_2B_2C$ (see Chapter 7), in the sense that, in the borocarbide the energy scales are largely separated (T_C, $T_N \ll T_K \ll T_{CEF}$), whereas in YbBiPt all these energies are of the same order, i.e. T_N = 0.45 K, 1 K < T_{CEF} < 12 K, and 2 K < T_K < 10 K.

8.3.2 Electronic structure

Inspired by the intriguing low-temperature properties, in particular the extremely large value for γ, Eriksson *et al.*[236] and McMullan and Ray[237] investigated the electronic structure of YbBiPt using fully relativistic LMTO calculations based on the LDA. Both calculations assumed that Bi was in the unique (000) position[191], which turned out not to be the case[227].

Eriksson's work[236] focused on the transition from semiconducting to metallic behavior as one moves across the rare-earths from Y to Lu. Although all three atoms in the RBiPt series are good metals, the compounds are semiconductors or semimetals, with the exception of YbBiPt and LuBiPt, which are metals. It was found that the reduced lattice constants, i.e. the well known lanthanide contraction, leads to a slight broadening of the Pt-*d* and Yb-*d* bands. The broader bands overlap and the gap disappears for the Yb and Lu compound. Scalar relativistic calculations, which neglect spin-orbit coupling, do not reproduce a metallic ground state for YbBiPt.

McMullan and Ray[237] compared the γ observed in specific heat measurements[191] with their calculation. Due to a fairly low DOS at E_F (4.5 states/eV cell) they proposed an enhancement factor of 750 to account for electron correlations. Assuming the same enhancement factor for the electron mass, they proposed quasiparticles of up to $4000m_e$. The predicted Fermi surface is fairly simple. It is pointed out that, provided their estimate of the quasiparticle mass is correct, an experimental observation, using the dHvA effect, would be extremely difficult.

BS calculations were performed using the TB-LMTO method in the ASA. The atomic positions and lattice parameters are given in Table 8.3. We also give the the basis functions used for the calculation and the radius of the WS spheres. An empty sphere was inserted on the vacant $(\frac{1}{2},\frac{1}{2},\frac{1}{2})$ site. Since YbBiPt was found to order magnetically at 400 mK, we performed a spin-polarized calculation. For simplicity we assumed a ferromagnetic structure. The self-consistent charges and moments inside the WS spheres are shown in Table 8.4. It was found that only Yb contributes to the magnetism in this compound. Moments on the other sites are negligible. We notice a promotion of the Yb-4*f* state, which is occupied by 13.77 electrons. Strong contributions to the DOS can also be expected from Bi-(6*s*6*p*) and Pt-5*d* states, which are completely filled, i.e. they are occupied by about 10 electrons. The total spin moment of $0.33\mu_B$ is entirely due to Yb-4*f* polarization. This is rather surprising, since we also expected a contribution from Yb-5*d* states, which, in general, become polarized through intra-atomic coupling to the 4*f* states. The spin moment obtained from our calculation is in agreement with the experimentally observed moment. It should be kept in mind that the strongly reduced moment was attributed to Kondo-type fluctuations, which are not considered in our BS calculation. The reduced

Table 8.3 Atomic positions for YbBiPt in units of the lattice constant a = 6.5953 Å. We also show the radius of the Wigner Seitz spheres, R, in atomic units and the basis functions included for the TB-LMTO calculation. E designates the empty sphere that was inserted in order to achieve space filling.

Atom	x (a)	y (a)	z (a)	R (a.u.)	Basis set
Yb	-1/4	-1/4	-1/4	3.188	$(6s6p5d4f)$
Bi	1/4	1/4	1/4	3.188	$(6s6p6d5f)$
Pt	0	0	0	2.943	$(6s6p5d5f)$
E	1/2	1/2	1/2	2.943	$(1s2p3d4f)$

moment predicted by LDA is most likely the result of strong mixing of Yb-f states with valence states from the ligand atoms. As already pointed out in Chapters 5 and 8.2, the orbital moment for localized states is overestimated by LDA calculations.

In Fig. 8.16 we show the DOS of YbBiPt and the BS along major symmetry lines. Our result is surprisingly similar to the BS shown in Ref. [237], although the arrangement of the atoms in the unit cell is different. The most striking feature of the BS are the two narrow $4f$ bands, i.e. the spin-orbit split $J = 5/2$ and $J = 7/2$ states. The lower band, originating from the $J = 5/2$ Yb^{3+} state, is 1.55 eV below the Fermi level, the nearly filled $J = 7/2$ band is 0.15 eV below E_F. The partial DOS is plotted in Figs. 8.17 and 8.18. The electronic structure in the vicinity of E_F is dominated by the minority spin contribution from Yb. Exchange interaction shifts the minority spin $4f$ band to higher energy, thereby increasing the DOS at E_F. The total DOS at E_F amounts to about 11.3 states/eV cell (more than twice the value reported in Ref. [237]), of which 89% are Yb-$4f$ states. This leads to a Sommerfeld coefficient of $\gamma = 26.7$ mJ/K^2 mol. To account for the large linear specific heat coefficient, derived from heat capacity measurements[191], an enhancement factor of 300 is required. This is much larger than anything we have observed so far. For the magnetic Ce HF compounds, discussed earlier, we estimated

Table 8.4 Results of charge and moments inside the Wigner-Seitz spheres in YbBiPt from self-consistent spin-polarized BS calculations including spin-orbit coupling. Charges are given in electrons; Moments in μ_B; DOS in states/eV cell.

	Charge					Moment		DOS
	s	p	d	f	Total	μ_S	μ_L	N(E_F)
Yb	0.44	0.44	0.96	13.77	15.61	0.337	0.947	10.08
Bi	1.68	1.54	0.26	0.12	3.60	0.002	-0.009	0.45
Pt	0.90	0.72	8.49	0.04	10.15	-0.004	-0.048	0.70
E	0.34	0.36	0.16		0.86	0.000	0.009	0.09

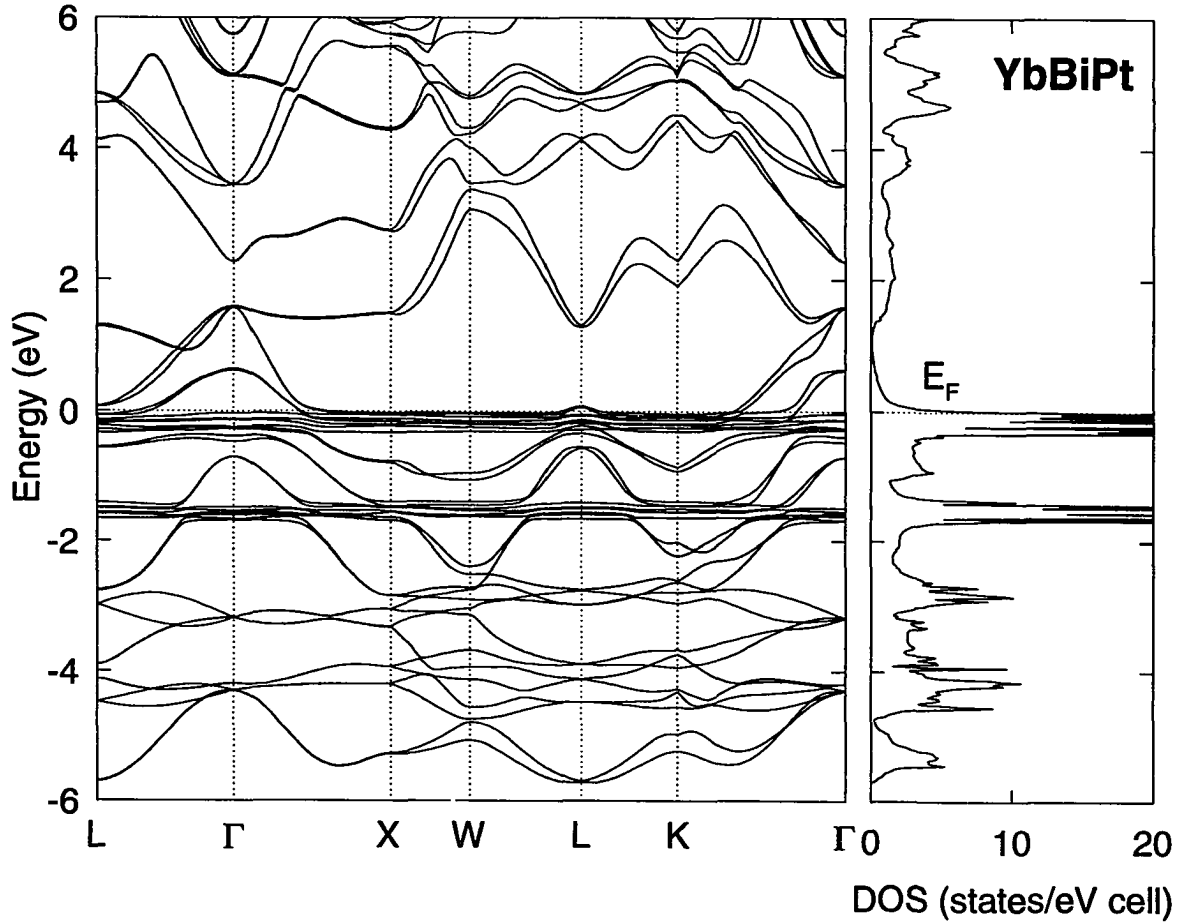

Figure 8.16 Spin-polarized band structure, including spin-orbit interaction, for hypothetical ferromagnetic YbBiPt.

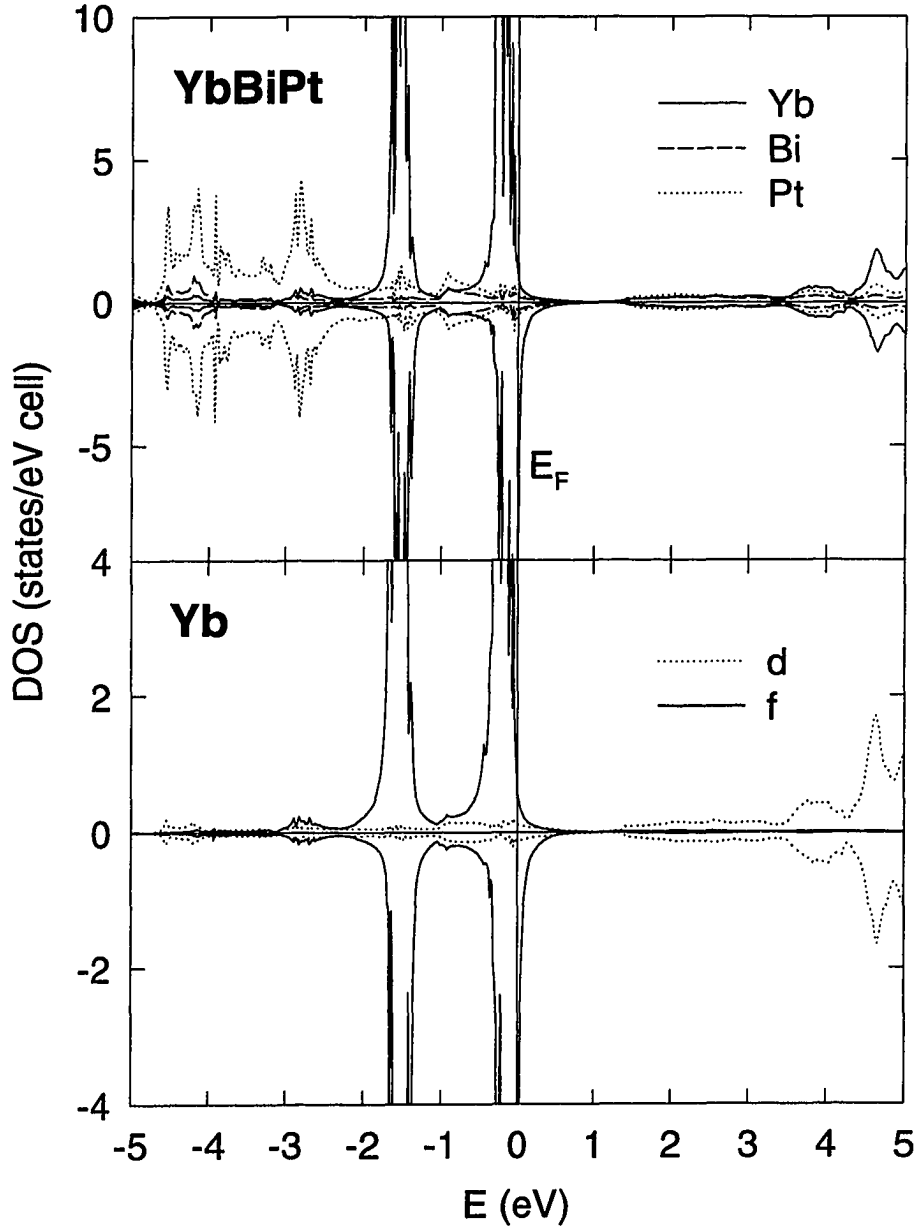

Figure 8.17 Partial DOS for YbBiPt (upper panel) and orbital decomposition for Yb (lower panel).

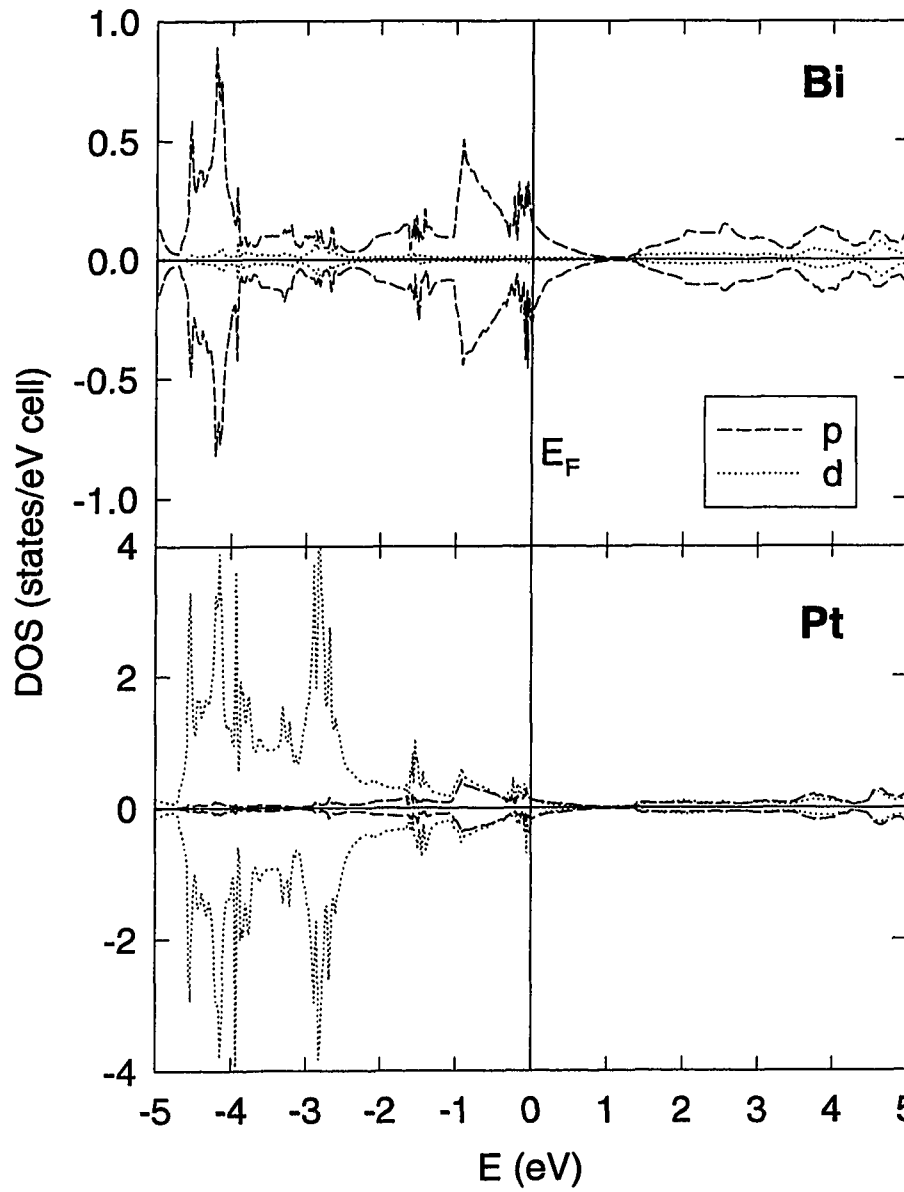

Figure 8.18 Orbital decomposition of the DOS of YbBiPt for Bi and Pt.

an enhancement factor of 8 ($CeAl_2$) to 10 (CeB_6). Above the Fermi level the DOS is rather small. All three atoms contribute equally to the DOS above 1.5 eV. Between 3.7 and 5 eV Yb-d states are dominant with little Bi and Pt character. Below E_F the situation is more complex. The Yb-4f states are strongly mixed with Bi-p and Pt-(pd) character, which form the top of the valence bands. A broad Pt-d band is seen between -2.5 and -4.5 eV. Substantial hybridization with Yb-d states is evident in this energy range. Below about -4 eV bands are Bi-p character. The lowest bands originate from Bi-s states and are not shown here.

8.3.3 Optical properties

We are not aware of any report on the optical properties of YbBiPt. In the following we will present the electrodynamic response and create the connection to the BS presented in the previous section. The diagonal optical conductivity was measured at room temperature between 1.4 and 5.1 eV using ellipsometry. No magnetic field was applied. The upper panel of Fig. 8.19 shows the real and imaginary part of σ_{xx}. The shape of σ_{xx}, as in the case of CeB_6 (Section 8.2), does not show metallic behavior, indicating a low carrier concentration. The optical absorption shows a maximum at 3.4 eV and drops off as the energy increases. A local minimum is reached at 3.6 eV. Above 3.6 eV σ_{1xx} increases slightly. The sample was of high quality and ellipsometric spectra showed very little noise. This enables us to identify at least four interband transitions in the spectral range covered in this experiment. Arrows indicate the energy of the transitions, which we estimate at 1.9, 2.4, 3.9, and 4.7 eV. Corresponding features are also found in σ_{2xx}. Fig. 8.20 shows the Kerr effect at 2.2 K in an applied field of 40 kOe. Θ_K decreases with increasing energy and shows structures over the entire spectral range. The ellipticity was calculated from the measured rotation using the appropriate Kramers-Kronig relations. A plot of Kerr rotation versus field, taken at 2 eV and 2.5 K (Fig. 8.21), indicates that the Kerr angle is increasing nearly linearly up to 20 kOe. At higher field Θ_K still increases and saturation is reached above 60 kOe. This behavior is quite similar to the magnetization, which is also reproduced in Fig. 8.21. This is not surprising, considering that Yb is the only ion carrying a magnetic moment in this compound. It also means that, at 2 eV, Yb contributes, either directly or through hybridization, to the off-diagonal optical conductivity. From σ_{xx} and (Θ_K, ϵ_K) we calculated σ_{xy}. The spectra are shown in the lower panel of Fig. 8.19. Arrows indicate the positions where we found transitions in σ_{xx}. It appears that the transitions at 1.9 and 2.4 eV give large contributions to the off-diagonal absorption. The transitions at 3.9 and 4.7 eV are less pronounced in σ_{2xy}, leading to only small structures on top of a large and increasing background.

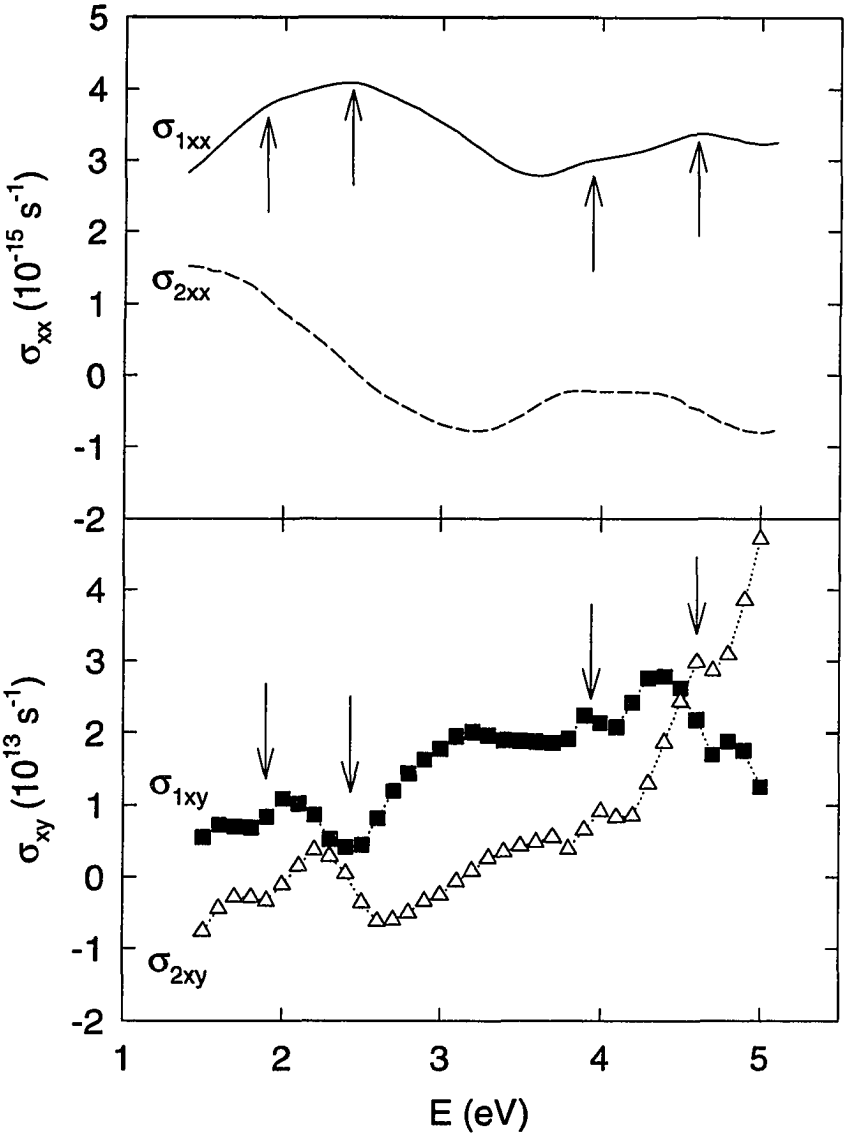

Figure 8.19 Optical conductivity of YbBiPt. Upper panel: Diagonal component at room temperature in zero field. Lower panel: Off-diagonal component determined from σ_{xx} and the Kerr parameters shown in Fig. 8.20. Arrows indicate interband transitions.

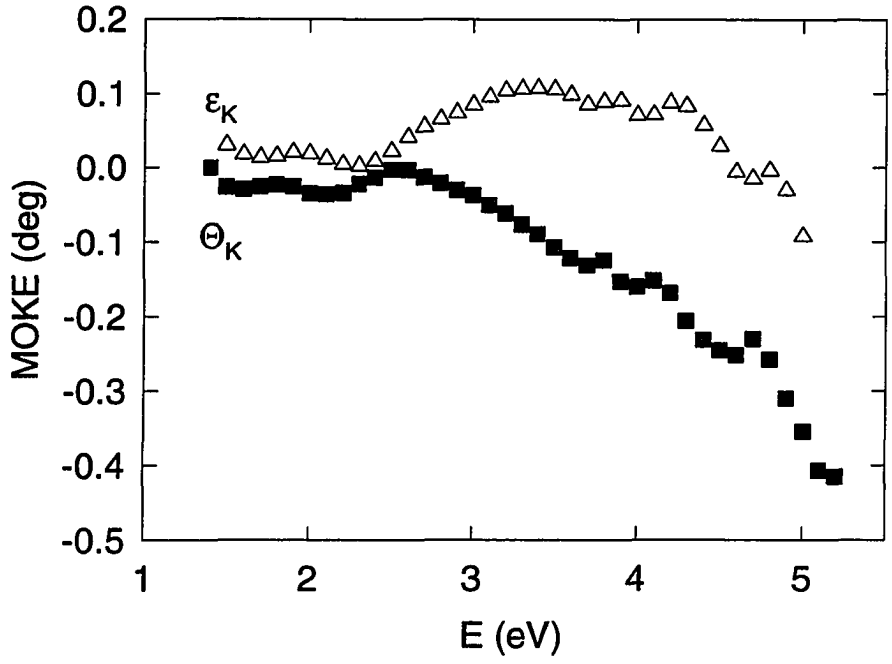

Figure 8.20 Magneto-optic Kerr effect of YbBiPt at 2.2 K in a 40 kOe field. ϵ_K was calculated from Θ_K using Kramers-Kronig relations.

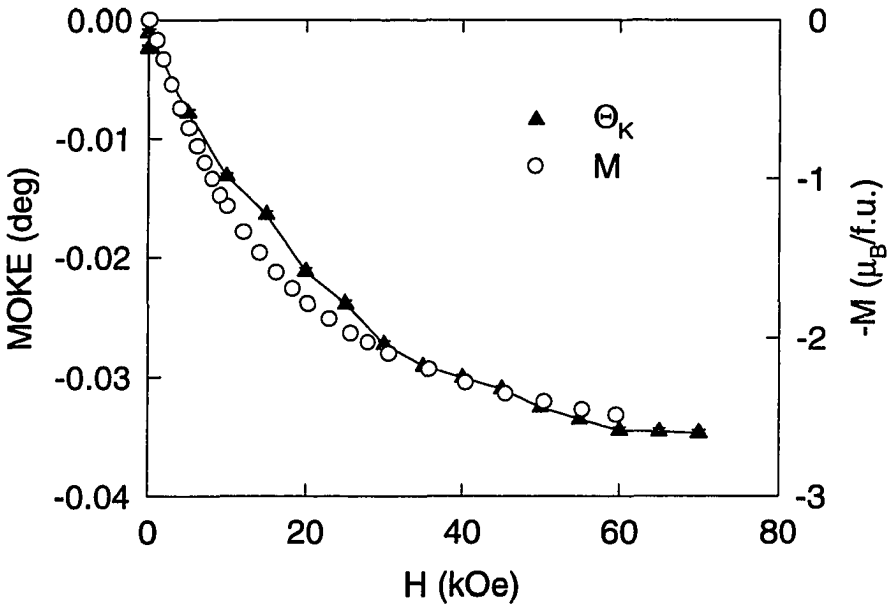

Figure 8.21 Kerr rotation versus field for YbBiPt. Data were taken at 2 eV and 2.5 K. Open circles show the (negative) magnetization at 1.0 K (reproduced from Fig. 8.15).

We can assign the transitions observed in our spectra using the calculated BS. It should be kept in mind that all atoms in this compound are very heavy, i.e. they show large spin-orbit splitting, which leads to substantial changes in the electronic structure. An investigation of interband absorptions based on a BS including spin-orbit coupling is not feasible in the case of YbBiPt, due to the enormous number of bands between -5 and 5 eV (see Fig. 8.16). Despite the importance of spin-orbit coupling we will try to identify transitions using a BS where spin-orbit coupling was neglected. The basic character of the bands remains unchanged, but their number is greatly reduced. In Fig. 8.22 we indicate the four transitions found in σ_{xx} by arrows. Transitions at 1.9 eV most likely originate from the Γ, X, and L point. At X we find bands that contribute to the 2.4 eV structure. We tentatively assign the 3.9 eV transition to regions around the Γ and W point. Absorption at 4.7 eV can be expected from bands around the X, L, and Γ point. From a plot of the BS including the orbital character of the bands, shown in Fig. 8.23, we can determine the character of the initial and final states. The result is shown in Table 8.5. It can be seen that all three atoms contribute equally to the observed transitions.

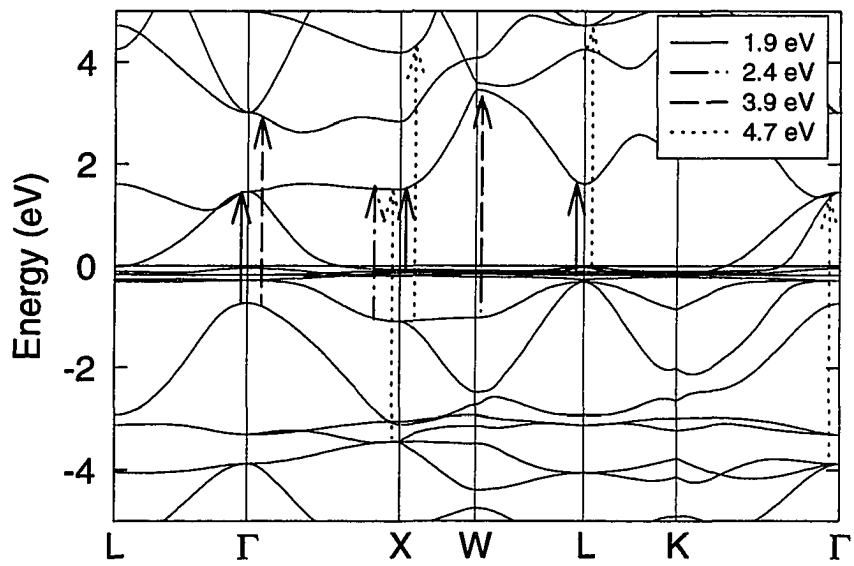

Figure 8.22 Non-magnetic BS of YbBiPt. Spin-orbit splitting was neglected. Arrows indicate interband transitions.

In this section we presented another HF compound with a low carrier concentration. Magnetic and transport measurements indicate strong hybridization of the Yb derived $4f$ bands with conduction electrons. This was supported by our BS calculation, which shows strong mixing of Yb-$4f$ states with the top of the valence band (Bi-$6p$ and Pt-$5d$ states) and the bottom of the conduction band (Bi-$6p$

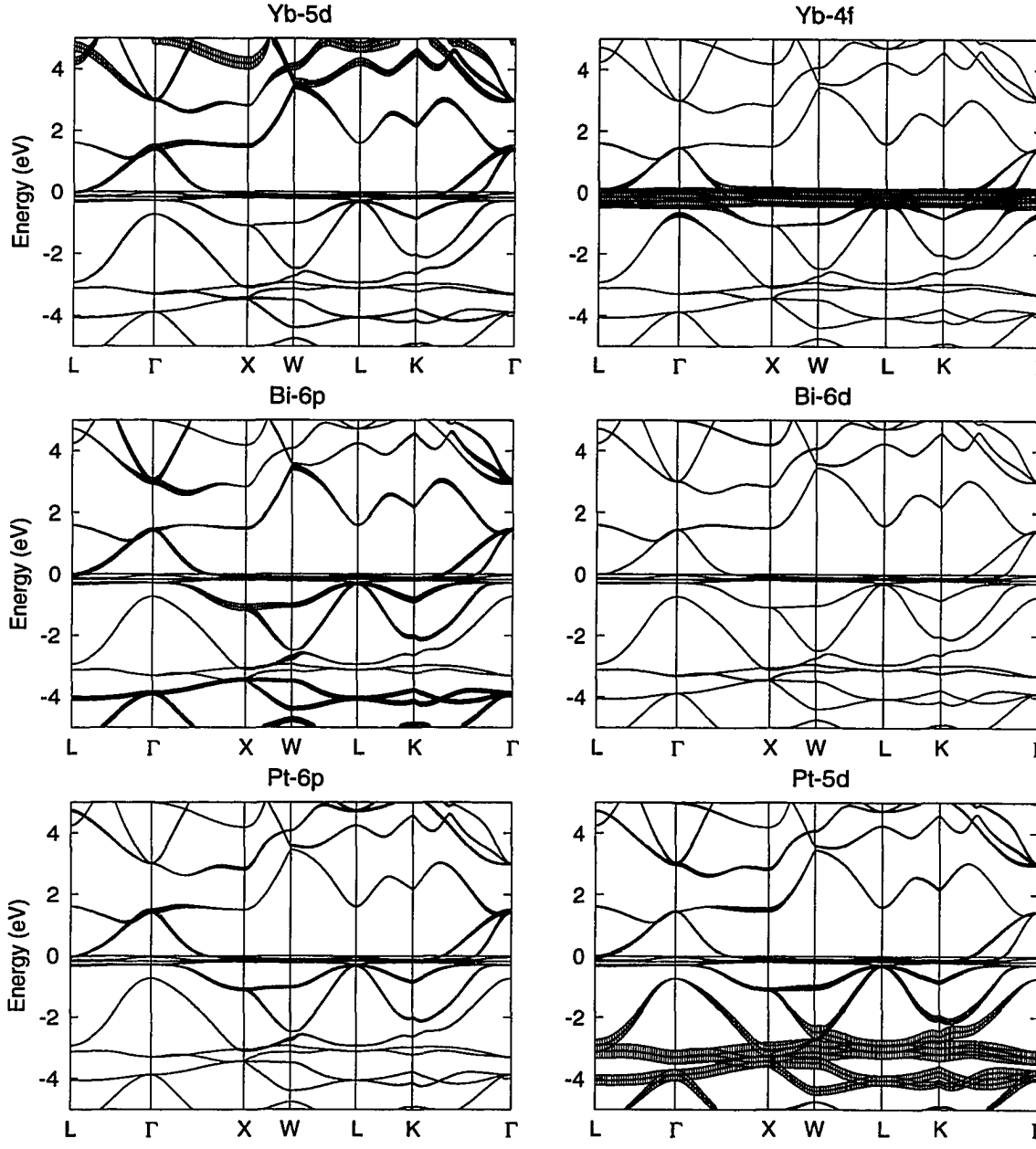

Figure 8.23 Relativistic non-magnetic band structure of YbBiPt projected on the atomic and orbital character. Spin-orbit coupling was neglected. The width of the hatched bands is proportional to the amount of a particular character in a band.

Table 8.5 Interband transition energies, their origin within the fcc Brillouin zone, and the character of the initial and final states. Contributions to the initial and final states (limited to the two major components) are given in decreasing order.

Energy (eV)	Symmetry point	Initial state	$\longrightarrow$	Final state
1.9	Γ	Yb($4f$)Pt($5d$)	$\longrightarrow$	Yb($5d$)Pt($6p$)
	X	Yb($4f$)Bi($6p$)	$\longrightarrow$	Yb($5d$)Pt($5d$)
	L	Yb($4f$)Pt($5d$)	$\longrightarrow$	Bi($6p$)Pt($5d$)
2.4	X	Bi($6p$)Pt($5d$)	$\longrightarrow$	Yb($5d$)Pt($5d$)
3.9	Γ	Yb($4f$)Pt($5d$)	$\longrightarrow$	Bi($6p$)Yb($5d$)
	W	Pt($5d$)Bi($6p$)	$\longrightarrow$	Yb($5d$)Bi($6p$)
4.7	X	Pt($5d$)Bi($6p$)	$\longrightarrow$	Yb($5d$)Pt($5d$)
	X	Bi($6p$)Pt($5d$)	$\longrightarrow$	Yb($5d$)Bi($6d$)
	L	Yb($4f$)Pt($5d$)	$\longrightarrow$	Yb($5d$)Bi($6p$)
	Γ	Pt($5d$)Bi($6p$)	$\longrightarrow$	Yb($5d$)Pt($6p$)

and Yb-$5d$ states). The spin magnetic moment is strongly reduced, which is in agreement with μSR experiments. We find four interband transitions in the optical and magneto-optical spectra. These absorptions have been tentatively assigned to transitions occurring at points of high symmetry in the BZ. It was found that all three atoms contribute to the absorption spectra. The magneto-optic Kerr rotation at 2 eV and 2.5 K was proportional to the net spin polarization. This is in accord with our assignment of the 1.9 eV transition, which, we believe, occurs from Yb-$4f$ states at the Γ, X, and L point to empty states of mostly Yb-$5d$ and Pt-$5d$ character. Compared to CeB_6 we did not notice an enhancement of the Kerr effect due to plasma oscillations.

9 CONCLUSION

We investigated the optical and magneto-optical properties of strongly correlated electron systems showing a variety of phenomena due to strong electron-electron and electron-phonon interaction. The energy scales of correlated electron effects are rather low (the Kondo temperature is typically on the order of 10 K) and it became clear that we needed to measure at low temperature and high magnetic field. The Kerr spectrometer was modified and the compensation method was introduced, which resulted in a broader spectral range and a reduced error, especially in the high energy region of our instrument. It also allows us to measure Kerr spectra under high magnetic field, where the intensity method was inappropriate.

Summaries of our experimental and theoretical findings are given at the end of each section. However, we would like to state some general results of this work here. We investigated four different groups of materials, which were related only by their low-temperature correlated electron behavior. Due to their largely different properties (crystal structure, magnetic properties, transport properties, etc.) a direct comparison is not possible. $CeAl_2$ is a Kondo magnet, i.e. local moment ordering is observed but the Ce moment is strongly reduced, compared to the free ion value. Hybridization is stronger in $CeFe_2$, leading to partial loss of the $4f$ electron and almost complete quenching of the magnetic moment. Motivated by its unusual magnetic properties[123] we doped $CeFe_2$ with Co and investigated the metamagnetic phase transition using the Kerr effect. Kerr spectroscopy was performed on the magnetic superconductor $TmNi_2B_2C$. The isostructural compound $YbNi_2B_2C$ should, according to de Gennes scaling, superconduct. However, this transition is not observed and increased linear specific heat coefficient identifies $YbNi_2B_2C$ as a heavy-Fermion compound. We investigated its optical and magneto-optical properties and compared them to data obtained for $TmNi_2B_2C$. We then investigated two heavy-Fermion compounds with a low carrier concentration, namely CeB_6 and YbBiPt.

LDA calculations were carried out for all compounds. In general, the spin magnetic moment was in good agreement with experiment. The orbital contribution to the magnetic moment was found to agree well with experiment for delocalized $4f$ electrons, as seen for $CeFe_2$. For localized $4f$ states, as

for example found in $PrAl_2$ and CeB_6, the orbital contribution was overestimated. In the case of $PrAl_2$ this led to complete quenching of the Pr moment. Hybridization of the $4f$ states in the vicinity of the Fermi level, which can be identified from BS and DOS plots or from a plot of the BS including the orbital character of the bands, was found to be important in all compounds.

The optical conductivity of RAl_2, RFe_2, and RNi_2B_2C shows metallic behavior. For CeB_6 and YbBiPt the shape of the spectra is dominated by interband transitions and infrared optical data are required to identify them as low carrier concentration metals. The optical conductivity was calculated using the LDA. Results for $LaAl_2$ and YFe_2 agree well with experimental spectra. For the other compounds agreement was worse. We attribute this to the narrow $4f$ states, which cannot be treated properly in LDA. For some of the compounds the number of bands between -5 and 5 eV is small, and we were able to assign interband transitions observed in the optical conductivity using plots of the BS which included the optical character of the bands.

The optical response of RAl_2 was found to be dominated by $p \rightarrow d$ and $d \rightarrow p$ transitions. The Kerr effect is proportional to the magnetization. This can be understood in terms of a $5d$ polarization induced through intra-atomic coupling with the magnetic $4f$ state. The low energy structure (around 2 eV) in the Kerr spectra is also observed in RFe_2. The off-diagonal optical absorption, σ_{2xy}, is very similar for $CeFe_2$ and YFe_2, supporting our interpretation of rare-earth derived transitions around 2 eV. The rare-earth $6p$ and $5d$ states do not change much as Ce is replaced by heavier lanthanides. Thus, the same structure is found in the Kerr spectra of heavy RFe_2 compounds. The absorption peak around 4 to 4.6 eV is found in RFe_2 compounds but not in RAl_2. We therefore believe that this structure is due to absorption by Fe derived states.

Alloying $CeFe_2$ with 10% Co leads to a magnetic instability. We measured the Kerr effect in the low-temperature antiferromagnetic phase as well as in the ferromagnetic regime. The Kerr effect for the ferromagnetic spin structure resembles that of $CeFe_2$. In the antiferromagnetic state we observe a fairly large rotation at high photon energy. The magneto-optic absorption at 2 eV nearly vanishes in the antiferromagnetic state. We investigated the phase transition at 1.8 and 4 eV. The Kerr angle increases with magnetic field and saturates at 15 kOe. At 50 K we observe a metamagnetic transition between 35 and 40 kOe, where the magnetization shows a steep increase. The magnitude of Θ_K increases at 1.8 eV but decreases at 4 eV. A larger rotation could be interpreted in terms of a larger magnetization. However, this inevitably leads to the question why the Kerr rotation is not proportional to the magnetization below 30 kOe. It appears that the Kerr effect probes an electronic state that does not contribute to the magnetization of the compound, but gives rise to a large magneto-optic

absorption. This state is presumably the Ce-5d level. However, an unambiguous assignment cannot be made.

Kerr spectra of $TmNi_2B_2C$ and $YbNi_2B_2C$ are very similar. The magnitude is smaller for $YbNi_2B_2C$. Optical absorption in RNi_2B_2C between 1.4 and 6 eV occurs between p and d states. All four atoms contribute to the optical absorption, which confirms earlier findings that the borocarbide superconductors behave three dimensionally despite their two-dimensional layered structure. From Θ_K versus field data we were able to identify the superconducting-to-normal state transition at 10 kOe, which is in good agreement with the critical field derived from magnetization data.

The Kerr spectrum of CeB_6 shows a narrow peak at 2 eV. We associate this with $(pd) \rightarrow f$ and $f \rightarrow (pd)$ transitions, involving B-derived p states. Magneto-optic absorption is small and the rather large Kerr rotation is due to enhancement by the plasma minimum, as observed in σ_{1xx}. The magnitude of the Kerr effect in YbBiPt is smaller and no plasma enhanced peaks were observed. The spectrum is very rich in structure. We were able to identify four interband transitions, and we gave a tentative assignment based on BS plots that also showed the orbital character of the bands.

We presented the optical and magneto-optical response of strongly correlated electron systems. Limited success was achieved using LDA calculations. The magnetic properties are well reproduced in many cases, especially for delocalized states where this theory is more appropriate. Since the $4f$ state of Ce is pinned at the Fermi level, we expect the infrared magneto-optic response to provide more information about this state. The magneto-optic setup can easily be modified to measure reflectivity spectra. It is then possible to determine the optical constants of a sample under the same experimental conditions that the Kerr spectra are taken at. Infrared optical spectroscopy has turned out to be a powerful tool to investigate low energy excitations in heavy-Fermion or superconducting compounds.

APPENDIX A ALIGNMENT OF THE KERR SPECTROMETER

Including the compensator in the setup and a change to the PS(C)MA configuration (Fig. 4.4) requires alignment procedures different from those described by Lee[44]. We will give the necessary steps to align the optical components. For more detailed information we refer to the manuals and the source code of the data acquisition program. All routines have been included in the program and need to be tested before Kerr ellipticity data can be taken with the compensation method.

Figure A.1 shows the desired alignment. We indicate the optical axes of the polarizer, compensator, modulator, and analyzer. Calibration is performed using an Al reference mirror in zero field. As calibration point we may choose any arbitrary wavelength that gives a signal of sufficient intensity. Since all optical elements can be rotated, except for the modulator, the reference is set by the modulator optical axes. Complete alignment is performed by the procedure outlined below.

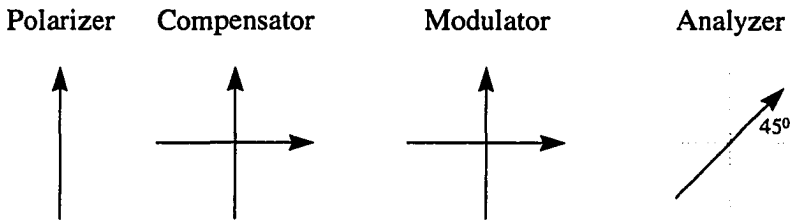

Figure A.1 Alignment of the optical elements of the Kerr spectrometer.

- **Polarizer angle:** The compensator is removed from the optical path. The analyzer is set to approximately 45°. A misalignment of several degrees does not matter at this point. Modulation is set to $\delta_0 = 2.41$. We measure $I_{2\omega}$ as a function of polarizer angle. Light polarization parallel to either optical axis of the modulator will result in $I_{2\omega} = 0$. The zero position of the polarizer is thus determined by the zero crossing of $I_{2\omega}(\psi)$.

- **Analyzer angle:** We set the polarizer transmission axis to $\psi = -45°$. The analyzer is then adjusted manually to give minimum light intensity, which can either be done visually or by

measuring the dc component at the calibration wavelength. Since the dc component is constant for $\delta_0 = 2.41$, the modulator can be on or off during this alignment. Minimum light intensity is obtained for crossed polarizer and analyzer, i.e. at $\phi = 45°$.

- **Compensator retardation:** This is a separate measurement to calibrate the compensator. The compensator is put back into the beam path. The zero position of the compensator is defined by a minimum in the transmitted light intensity for white light. Using the computer we measure the dc voltage as a function of retardation at the calibration wavelength. Intensity minima will be found for positive and negative retardation. The position of the n-th minimum corresponds to the n-th order retardation, which is a retardation by n wavelengths. Calibration at a single wavelength is sufficient.

- **Compensator angle:** The retardation is set to $\lambda/4$ at the calibration wavelength. The optical axis parallel to the long edge of the quartz bar of the compensator is set to 0°. A misalignment of several degrees is not important here. We then measure $I_{1\omega}$ as a function of the polarizer angle. If the polarizer transmission axis is parallel to either optical axis of the compensator, the transmitted light will be linearly polarized, thus giving $I_{1\omega} = 0$.

- **Polarizer/Compensator angle:** In principle, the last step aligned the compensator with respect to the polarizer, which was already aligned in the first step. Alternatively, one can use the setting found in the previous step, i.e. $I_{1\omega} = 0$, and rotate the polarizer and compensator simultaneously until $I_{2\omega} = 0$. In this position the optical axes of the polarizer and compensator are parallel to that of the modulator.

Alignment without the compensator can be performed within 10 min and should be repeated before taking data, but not in between scans. Alignment of the compensator appears to be more difficult. In particular, calibration of the retardation needs to be performed only once.

APPENDIX B RECIPROCAL LATTICES AND BRILLOUIN ZONES

The eigen-energies of electrons moving in a three-dimensional periodic crystal lattice depend on the crystal momentum **k**. They are plotted as energy versus **k** (band structure) along particular symmetry lines in k-space (or reciprocal space). Analogous to the WS cell of real space one can define the *WS cell in reciprocal space*, which is called the Brillouin zone (BZ). Symmetry points and lines in the BZ can be identified from Figs. B.1–B.3, which show the BZ for the simple cubic, the face-centered cubic, and the body-centered tetragonal lattice. The $\mathbf{g}_i$ (i=1,2,3) are the basis vectors in reciprocal space. In the following table we give a summary of the samples presented and their Bravais lattice. For more information consult Refs. [177, 238].

Table B.1 Compounds discussed in this work and their Bravais lattices.

Bravais lattice	Figure	Samples
Simple cubic (sc)	B.1	CeB_6
Face-centered cubic (fcc)	B.2	RAl_2 (R=La, Ce, Pr), RFe_2 (R=Y, Ce), YbBiPt
Body-centered tetragonal (bct)	B.3	RNi_2B_2C (R=Tm, Yb, Lu), $Yb_{14}MnSb_{11}$

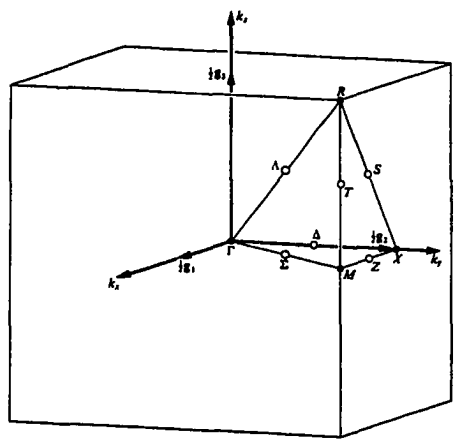

Figure B.1 BZ for the sc lattice. $\Gamma = (000)$; $X = (0\frac{1}{2}0)$; $M = (\frac{1}{2}\frac{1}{2}0)$; $R = (\frac{1}{2}\frac{1}{2}\frac{1}{2})$.

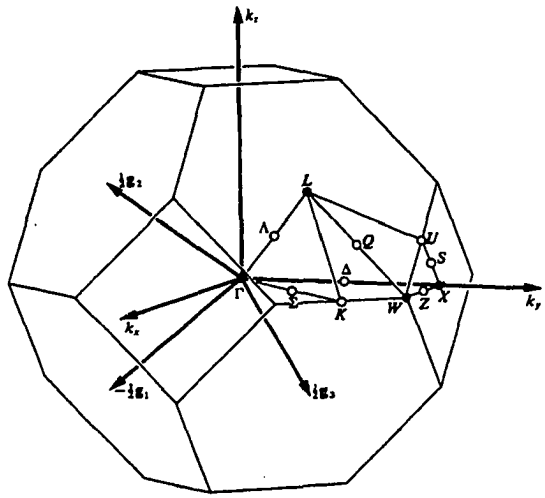

Figure B.2 BZ for the fcc lattice. $\Gamma = (000)$; $X = (\frac{1}{2}0\frac{1}{2})$; $L = (\frac{1}{2}\frac{1}{2}\frac{1}{2})$; $W = (\frac{1}{2}\frac{1}{4}\frac{3}{4})$.

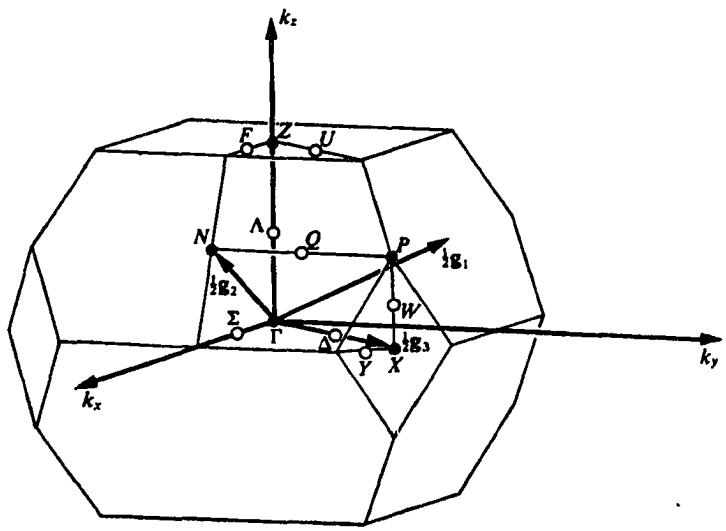

Figure B.3 BZ for the bct lattice with $c > a$. $\Gamma = (000)$; $N = (0\frac{1}{2}0)$; $X = (00\frac{1}{2})$; $Z = (\frac{1}{2}\frac{1}{2}\frac{\bar{1}}{2})$; $P = (\frac{1}{4}\frac{1}{4}\frac{1}{4})$.

APPENDIX C FARADAY AND STRAIN CONTRIBUTIONS TO THE MAGNETO-OPTICAL SIGNAL

For magneto-optical measurements the specimen is kept in the sample space of a cryostat. Fig. C.1 shows a horizontal cut through the cryostat. The light, which is focused onto the sample, passes the outer and inner window twice. This leads to a Faraday rotation, which needs to be subtracted from the magneto-optical signal of the sample. In principle, we could take the difference of two spectra obtained with an Al reference mirror, M (whose Kerr rotation is negligible), to obtain the Faraday contribution. Since strain in the windows, which depends sensitively on alignment, also contributes to the signal, this is not sufficient. The Faraday rotation, like the polar Kerr angle, is proportional to the applied field. Reversing the magnetic field will reverse the sense of rotation. The strain contribution does not depend on the applied field. Therefore, we can obtain the Faraday rotation of the windows from two scans with opposite magnetic field,

$$\Theta_F = \frac{1}{2}(\Theta_M^+ - \Theta_M^-), \tag{C.1}$$

where + and − indicate the two different field directions. The sign of the field is chosen such that a positive field yields a positive Faraday rotation. This corresponds to a negative Kerr rotation for Ni[10], which we use as a standard. The combined Kerr and Faraday rotation signal, Θ_S, of a sample, corrected for strain contributions is determined by

$$\Theta_S = \frac{1}{2}(\Theta_S^+ - \Theta_S^-). \tag{C.2}$$

The Kerr rotation of the sample is given by the difference of Θ_S and Θ_M,

$$\Theta_K = \Theta_S - \Theta_F = \frac{1}{2}\left[(\Theta_S^+ - \Theta_M^+) - (\Theta_S^- - \Theta_M^-).\right] \tag{C.3}$$

Thus, the Kerr rotation is determined from four separate scans. Depending on the number of data points a single spectrum takes between 40 and 80 minutes. The system has to be kept stable (constant temperature, no mechanical shocks, etc.) for the entire period of four scans, which turned out to be very difficult.

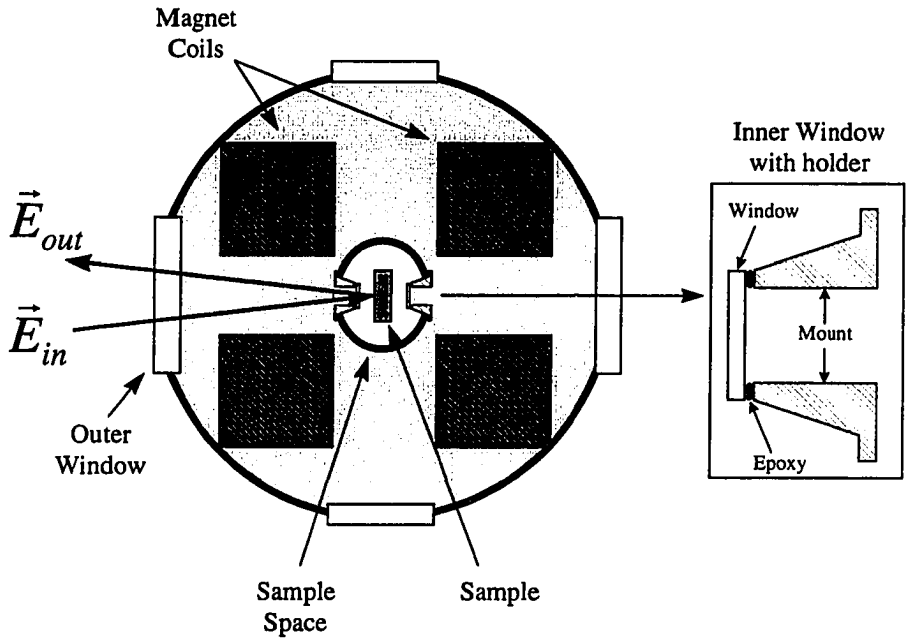

Figure C.1 Cross sectional cut of the optical cryostat. A detailed view of the window mount is shown on the right-hand side.

In Section 4.2.2 we mentioned that, for large rotation angles, the compensation method gives more accurate results than the intensity method. This is important for high magnetic fields. The Faraday rotation is proportional to the magnetic field and shows a quadratic energy dependence. In Fig. C.2 we show a typical scan for an Al mirror. Data were taken at 3 K in a 70 kOe applied field. The Faraday rotation (including a small contribution due to strain) reaches 50° at 5.2 eV. The data shown in Fig. C.2 could not have been taken with the intensity method.

As shown in Fig. C.1, two windows give horizontal optical access to the sample. The inner window, which is about 2 to 5 mm from the sample surface, tends to strain upon cooling. The strain, which is likely due to different thermal expansion coefficients of the holder, the glass, and the epoxy, is evidenced by very large values for the ellipticity (on the order of several degrees). Strained windows cannot be used for our experiment. It was found that the strain in commercially available polished windows is usually small. Currently we are using fused silica windows (200 ppm H_2O) from Dynasil. The windows have a diameter of 1/2" and a thickness of 62/1000". We tested several different designs for the window holder, as well as different epoxies. The mounts were machined at Ames Laboratory from oxygen free copper (CAD101). The depth of the mount is limited by the size of the sample space. The wall thickness of the holder should be made as thin as possible. The thin copper cylinder can easily accommodate

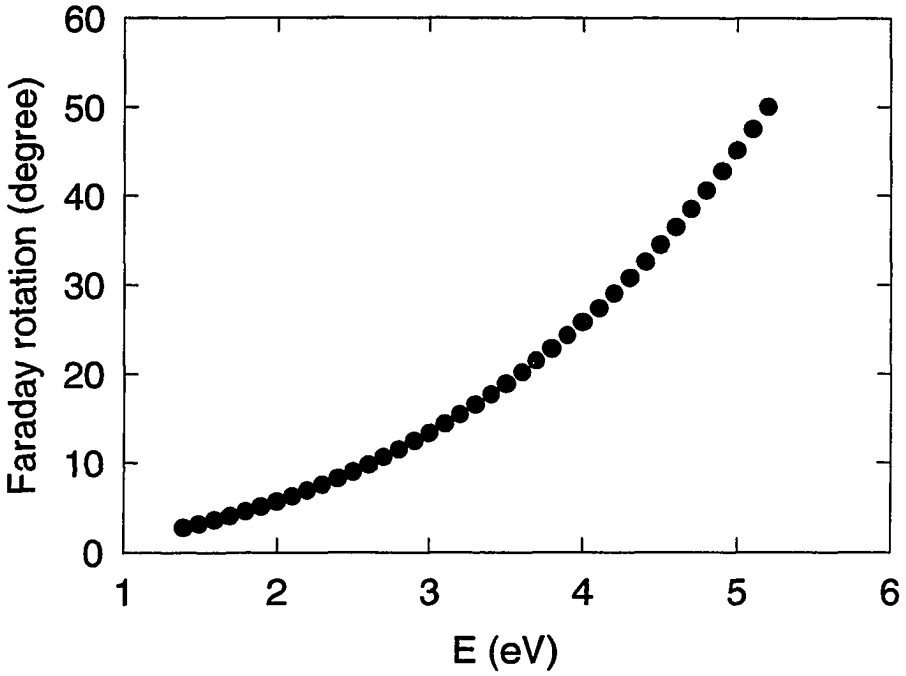

Figure C.2 Faraday rotation of the optical windows due to a 70 kOe applied field.

different thermal expansion of the glass and the mount. In order to soften the material, the window mounts are annealed for 2 days at 600° C. The pressure in the sample space is close to 1 atm, whereas there is vacuum around the sample tube (light gray area in Fig. C.1). The pressure pushes the window onto the holder and the epoxy works as a vacuum seal only. Several epoxies were tested and best results were obtained using a two component epoxy from Oxford (Versamid 140 and D.E.R. 331). The window mount is epoxied into the stainless steel sample tube using Ecobond 286 from Grace Specialty Polymers, which is also available though Oxford.

APPENDIX D CRYSTAL FIELD SPLITTING OF THE J = 5/2 AND J = 7/2 STATES

Bethe's paper on *splittings of terms in crystals*[239] marks the beginning of the application of symmetry principles to crystal electric field (CEF) effects. Degenerate energy levels of an atom may be split when the atom is placed in a crystal (see Fig. D.1). The reduction in symmetry from the full rotational group to the point symmetry of the lattice site of the atom can partially lift the degeneracy. An additional splitting is due to spin-orbit coupling, which is important in lanthanides, and about an order of magnitude larger than typical CEF splittings.

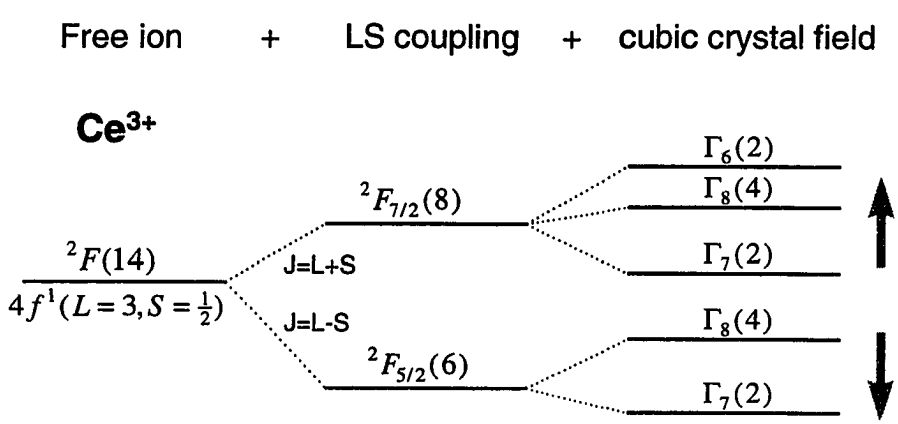

Figure D.1 CEF level scheme for the Ce^{3+} ion.

In this work we deal with compounds with either Ce or Yb. In Fig. D we show how the CEF level scheme for the Ce^{3+} ion evolves from the fourteenfold degenerate ^2F state. As a result of Hund's third rule, the ground state of trivalent Ce is the sixfold degenerate $^2F_{5/2}$ state, spin-orbit split from the eightfold degenerate $^2F_{7/2}$ state. When the Ce ion is placed in a cubic crystal field, the $J = 5/2$ ground state splits into a Γ_7 doublet and a Γ_8 quartet. If the symmetry is further reduced to tetragonal, the ground state will split into three doublets. The splittings shown in Fig. D were derived from group theory, which provides information on how, otherwise degenerate, levels will split under a certain

symmetry. However, group theory determines neither the size of the splitting nor the energies of the states. We know that in a cubic field, the $J = 5/2$ state of Ce will split into a doublet and a quartet, but either one could be the CEF ground state.

Since the ground state of trivalent Yb is the eightfold degenerate $^2F_{7/2}$ level, which has the same symmetry as the $J = 7/2$ state for Ce^{3+}, we see from Fig. D that the Yb ground state will be split into two doublets and one quartet under the influence of a cubic crystal field.

APPENDIX E TRANSMISSION OF THE UV INTERFERENCE FILTER

The Kerr spectrometer uses an interference filter to block higher order diffraction. Transmission curves were measured and confirmed a fairly narrow transmission band in the UV region.

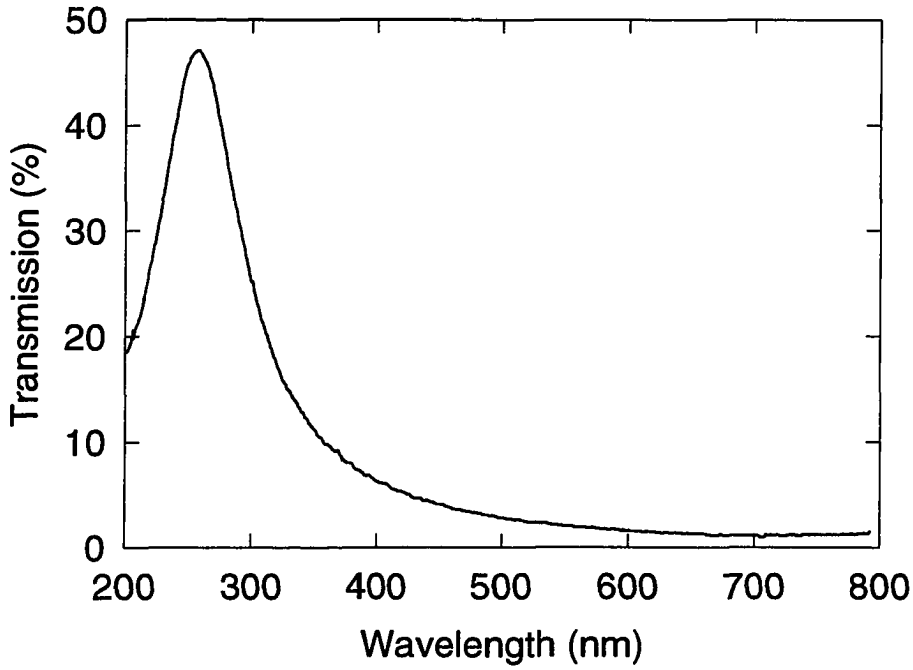

Figure E.1 Transmission of the UV interference filter used in the MOKE experiment.

REFERENCES

[1] M. Faraday, Philos. Trans. R. Soc. London **136**, 1 (1846).

[2] J. Kerr, Philos. Mag. **3**, 321 (1877).

[3] P.G. van Engen, K.H.J. Buschow, R. Jongebreur, and M. Erman, Appl. Phys. Lett. **42**, 202 (1983).

[4] H. Feil and C. Haas, Phys. Rev. Lett. **58**, 65 (1987).

[5] J. Schoenes, J. Mag. Soc. Jpn. Suppl. S1 **11**, 99 (1988).

[6] R. Pittini, J. Schoenes, O. Vogt, and P. Wachter, Phys. Rev. Lett. **77**, 944 (1996).

[7] W. Reim and J. Schoenes, in *Ferromagnetic Materials*, edited by E.P. Wohlfarth and K.H.J. Buschow (North-Holland, Amsterdam, 1990) Vol. 5, page 133.

[8] J. Schoenes, in *Materials Science and Technology*, edited by R.W. Cahn, P. Haasen, and E.J. Kramer (VCH, Weinheim, 1991) Vol. 3A, page 147.

[9] J. Schoenes, in *Handbook on the Physics and Chemistry of the Actinides*, edited by A.J. Freeman and G.H. Lander (Norht-Holland, Amsterdam, 1984) Vol. 1, page 341.

[10] K.H.J. Buschow, in *Ferromagnetic Materials*, edited by E.P. Wohlfarth and K.H.J. Buschow (North-Holland, Amsterdam, 1988) Vol. 4, page 493.

[11] D.K. Misemer, J. Mag. Mag. Mater. **72**, 267 (1988).

[12] F. Herman and S. Skillman, *Atomic Structure Calculations* (Prentice-Hall, Englewood Cliffs, NJ, 1963).

[13] R. Pittini, J. Schoenes, and P. Wachter, J. Mag. Mag. Mater. **177-181**, 472 (1998).

[14] P.S. Pershan, J. Appl. Phys. **38**, 1482 (1967).

[15] P.N. Argyres, Phys. Rev. **97**, 334 (1955).

[16] Y.R. Shen, Phys. Rev. **133**, 511 (1964).

[17] H.S. Bennett and E.A. Stern, Phys. Rev. **137**, A448 (1965).

[18] T. Murano and A. Ebina, J. Phys. Soc. Japan **20**, 997 (1965).

[19] L.D. Landau and E.M. Lifschitz, *Electrodynamics of Condensed Media* (Pergamon, New York, 1960).

[20] L.M. Roth, Phys. Rev. **133**, 542 (1964).

[21] Y.M. Agranovich and V.L. Ginzburg, *Spatial Dispersion in Crystal Optics and the Theory of Excitons* (Interscience Publishers, New York, 1966).

[22] P.Y. Yu and M. Cardona, *Fundamentals of Semiconductors* (Springer, Berlin, 1996).

[23] D.Y. Smith, J. Opt. Soc. Am. **66**, 547 (1976).

[24] P. Kielar, J. Opt. Soc. Am. **11**, 854 (1994).

[25] S.E. Schnatterly, Phys. Rev. **183**, 664 (1969).

[26] H.R. Hulme, Proc. R. Soc. London, Ser. A **135**, 237 (1932).

[27] J.L. Erskine and E.A. Stern, Phys. Rev. B **8**, 1239 (1973).

[28] W. Reim, O.E. Hüsser, J. Schoenes, E. Kaldis, P. Wachter, and K. Seiler, J. Appl. Phys. **55**, 2155 (1984).

[29] R.C. Fivaz, Phys. Rev. **183**, 586 (1969).

[30] J.L. Erskine and E.A. Stern, Phys. Rev. Lett. **30**, 1329 (1973).

[31] W. Reim, J. Schoenes, and O. Vogt, Solid State Commun. **47**, 579 (1983).

[32] O.K. Andersen, Phys. Rev. B **12**, 3060 (1975).

[33] O.K. Andersen and O. Jepsen, Phys. Rev. Lett. **53**, 2571 (1984).

[34] O.K. Andersen, Z.Pawlowska, and O. Jepsen, Phys. Rev. B **34**, 5253 (1986).

[35] W.R.L Lambrecht and O.K. Anderson, Phys. Rev. B **34**, 2439 (1986).

[36] O. Jepsen and O.K. Andersen, Solid State Commun. **9**, 1763 (1971).

[37] U. von Barth and L.Hedin, J. Phys. C **5**, 1629 (1972).

[38] C.S. Wang and J. Callaway, Phys. Rev. B **9**, 4897 (1974).

[39] D.G. Laurent, J. Callaway, and C.S. Wang, Phys. Rev. B **20**, 1134 (1979).

[40] K.J. Kim, T.C. Leung, B.N. Harmon, and D.W. Lynch, J. Phys.: Condens. Matter **6**, 5069 (1994).

[41] A.G. Nargizyan and Yu.A. Uspenskiĭ, Sov. Phys. JETP **76**, 530 (1993).

[42] B.N. Harmon, V.P. Antropov, A.I. Liechtenstein, I.V. Solovyev, and V.I. Anisimov, J. Phys. Chem. Solids **56**, 1521 (1995).

[43] R.J. Lange, S.J. Lee, D.W. Lynch, P.C. Canfield, B.N. Harmon, and S. Zollner, Phys. Rev. B **58**, 351 (1998).

[44] S.J. Lee, *Optical and magneto-optical properties of single crystal of* RFe_2 *(R=Gd, Tb, Ho, and Lu) and* $GdCo_2$ *intermetallic compounds*, PhD thesis, Iowa State University (1998).

[45] S.J. Lee, R.J. Lange, S. Hong, S. Zollner, P.C. Canfield, A.F. Panchula, B.N. Harmon, and D.W. Lynch, Thin Solid Films **313-314**, 223 (1998).

[46] A.I. Liechtenstein, V.P. Antropov, and B.N. Harmon, Phys. Rev. B **49**, 10770 (1994).

[47] V.P. Antropov, B.N. Harmon, and A.I. Liechtenstein, J. Appl. Phys. **76**, 6705 (1994).

[48] L.J. Sham and W. Kohn, Phys. Rev. **140**, A1133 (1965).

[49] J.F. Janak, A.R. Williams, and V.L. Moruzzi, Phys. Rev. B **11**, 1522 (1975).

[50] C.S. Wang and B.M. Klein, Phys. Rev. B **24**, 3417 (1981).

[51] N.I. Kulikov, D. Alouani, M.A. Khan, and M.V. Magnitskaya, Phys. Rev. B **36**, 929 (1987).

[52] J.E. Müller, O. Jepsen, and J.W. Wilkins, Solid State Commun. **42**, 365 (1982).

[53] C. Calandra and F. Manghi, Phys. Rev. B **45**, 5819 (1992).

[54] F. Aryasetiawan, Phys. Rev. B **46**, 13051 (1992).

[55] R.M.A. Azzam and N.M. Bashara, *Ellipsometry and Polarized Light* (North-Holland, Amsterdam, 1977).

[56] D.E. Aspnes and A.A. Studna, Appl. Opt. **14**, 220 (1975).

[57] Y.J. van der Meulen and N.C. Hien, J. Opt. Soc. Am. **64**, 804 (1974).

[58] D.E. Aspnes, J. Opt. Soc. Am. **64**, 812 (1974).

[59] R.W. Collins, Rev. Sci. Instrum. **61**, 2029 (1990).

[60] B. Johs, Thin Solid Films **234**, 395 (1993).

[61] K.E. Junge, *Spectroscopic ellipsometry of SiGeC alloys*, Master's thesis, Iowa State University (1998).

[62] W. Reim, J. Schoenes, F. Hulliger, and O. Vogt, J. Mag. Mag. Mater. **54-57**, 1401 (1986).

[63] S.N. Jasperson and S.E. Schnatterly, Rev. Sci. Instrum. **40**, 761 (1969).

[64] L.F. Mollenauer, D. Downie, H. Engstrom, and W.B. Grant, Appl. Opt. **8**, 661 (1969).

[65] J.C. Kemp, J. Opt. Soc. Am. **59**, 950 (1969).

[66] G.A. Osborne, J.C. Cheng, and P.J. Stephens, Rev. Sci. Instrum. **44**, 10 (1973).

[67] K.W. Hipps and G.A. Crosby, J. Phys. Chem. **83**, 555 (1979).

[68] K. Sato, Jap. J. Appl. Phys. **20**, 2403 (1981).

[69] K. Sato, H. Hongu, H. Ikekame, Y. Tosaka, M. Watanabe, K. Takanashi, and H. Fujimori, Jap. J. Appl. Phys. **32**, 989 (1993).

[70] W.S. Kim, M. Aderholz, and W. Kleemann, Meas. Sci. Technol. **4**, 1275 (1993).

[71] G. Stewart, Rev. Mod. Phys. **56**, 755 (1984).

[72] R.W. Hill and J.M. Machado da Silva, Phys. Lett. A **30**, 13 (1969).

[73] K.H.J. Buschow and H.J. van Daal, Phys. Rev. Lett. **23**, 408 (1969).

[74] W.M. Swift and W.E. Wallace, J. Phys. Chem. Solids **29**, 2053 (1969).

[75] E. Walker, H.G. Purwins, M. Landolt, and F. Hulliger, J. Less Comm. Metals **33**, 203 (1973).

[76] N. Grewe and F. Steglich, in *Handbook on the Physics and Chemistry of Rare Earths*, edited by K.A. Gschneidner Jr. and L. Eyring (Elsevier Science Publishers, London, 1989) Vol. 14, page 414.

[77] F. Steglich, C.D. Bredl, M. Loewenhaupt, and K.D. Schotte, J. Phys. Colloq. (Paris) **40**, C5-301 (1979).

[78] C.D. Bredl, F. Steglich, and K.D. Schotte, Z. Physik B **29**, 327 (1978).

[79] F. Patthey, W.D. Schneider, Y. Baer, and B. Delley, Phys. Rev. B **35**, 5903 (1987).

[80] M.A. Ruderman and C. Kittel, Phys. Rev. **96**, 99 (1954).

[81] T. Kasuya, Prog. Theor. Phys. **16**, 58 (1956).

[82] K. Yoshida, Phys. Rev. **106**, 893 (1957).

[83] Z. Fisk and J.P. Remeika, in *Handbook on the Physics and Chemistry of Rare Earths*, edited by K.A. Gschneidner Jr. and L. Eyring (Elsevier Science Publishers, London, 1989) Vol. 12, page 53.

[84] P.C. Canfield and Z. Fisk, Philos. Mag. **65**, 1117 (1992).

[85] I.R. Fisher, A. Thebe, and P.C. Canfield, Ames Tribune **August 3**, C8 (1998).

[86] B. Barbara, J.X. Boucherle, J.L. Buevoz, M.F. Rossignol, and J. Schweizer, Solid State Commun. **24**, 481 (1977).

[87] A. Hasegawa and A. Yanase, J. Phys. F: Metal Phys. **10**, 847 (1980).

[88] P. Villars and L.D. Calvert, *Pearson's Handbook of Crystallographic Data for Intermetallic Phases* (The Materials Information Society, Materials Park, OH, USA, Vols. 1-4, 2nd edition, 1991).

[89] R.E. Hungsberg and K.A. Gschneidner Jr., J. Phys. Chem. Solids **33**, 401 (1972).

[90] W.E. Pickett and B.M. Klein, J. Less Comm. Metals **93**, 219 (1983).

[91] B. Barbara, H. Bartholin, D. Florence, M.F. Rossignol, and E. Walker, Physica **86-88B**, 177 (1977).

[92] A. Delin, P.M. Oppeneer, M.S.S. Brooks, T. Kraft, J.M. Wills, B. Johansson, and O. Eriksson, Phys. Rev. B **55**, R10173 (1997).

[93] R.J. Lange, I.R. Fisher, K.D. Myers, P.C. Canfield, and D.W. Lynch, unpublished.

[94] A. Chelkowski, P. Morin, H. Oesterreicher, and K. Oesterreicher, in *Landoldt-Börnstein - Numerical Data and Functional Relationships in Science and Technology*, edited by H.P.J. Wijn (Springer Verlag, Berlin, 1989) Vol. III/19e2.

[95] M.E. Fisher, Philos. Mag. **7**, 1731 (1962).

[96] A.A. Vasil'kevich, Phys. Metals **14**, 669 (1995).

[97] B. Barbara, B. Bècle, R. Lemaire, and R. Pauthenet, J. Appl. Phys. **39**, 1084 (1968).

[98] K.H. Mader and W.M. Swift, J. Phys. Chem. Solids **29**, 1759 (1968).

[99] T.B. Massalski, *Binary Alloy Phase Diagrams* (ASM International, Materials park, OH, USA, 1996).

[100] Y. Ōnuki, Y. Nakai, T. Omi, T. Yamazaki, and T. Komatsubara, J. Mag. Mag. Mater. **76&77**, 119 (1988).

[101] N. Nereson, C. Olson, and G. Arnold, J. Appl. Phys. **39**, 4605 (1968).

[102] H.G. Purwins, E. Walker, B. Barbara, M.F. Rossignol, and P. Bak, J. Phys. C **7**, 3573 (1974).

[103] A.C. Switendick, in *Proc. 10th Rare Earth Res. Conf. (Carefree, Arizona)*, edited by C.J. Kevane and T. Moeller (National Technical Information Service, U.S. Department of Commerce, Springfield, VA 22151, 1973), page 235.

[104] T. Jarlborg, A.J. Freeman, and D.D Koelling, J. Phys. Colloq. (Paris) **12**, C7–317 (1982).

[105] T. Jarlborg, A.J. Freeman, and D.D Koelling, J. Mag. Mag. Mater. **60**, 291 (1986).

[106] J. Reichelt and K. Winzer, Phys. Stat. Solidi B **89**, 489 (1978).

[107] M. Croft, J.H Weaver, D.J. Peterman, and A. Franciosi, Phys. Rev. Lett. **46**, 1104 (1981).

[108] S.I Epstein, R.J. Higgins, D.H. Lowndes, F. Steglich, and J.F. Smith, Phys. Rev. B **32**, 5683 (1985).

[109] M. Springford and P.H.P Reinders, J. Mag. Mag. Mater. **76&77**, 11 (1988).

[110] P.H.P Reinders and M. Springford, J. Mag. Mag. Mater. **79**, 295 (1989).

[111] Y. Ōnuki, T. Goto, and T. Kasuya, in *Materials Science and Technology*, edited by R.W. Cahn, P. Haasen, and E.J. Kramer (VCH, Weinheim, 1991) Vol. 3A, page 543.

[112] R.D. Parks, S. Raaen, M.L. den Boer, and Y.S. Chaug, J. Mag. Mag. Mater. **47&48**, 163 (1985).

[113] G.Y. Guo, Physica B **165&166**, 335 (1990).

[114] J.Y. Rhee, X. Wang, and B.N. Harmon, Phys. Rev. B **51**, 15585 (1995).

[115] K.J. Kim and D.W. Lynch, J. Phys.: Condens. Matter **5**, 5971 (1993).

[116] T.A. Tibbetts and B.N. Harmon, Solid State Commun. **44**, 1409 (1982).

[117] D.E. Aspnes and A.A. Studna, Phys. Rev. B **27**, 985 (1983).

[118] D.A.G. Bruggemann, Ann. Phys. (Leipzig) **24**, 636 (1935).

[119] S.B. Roy and B.R. Coles, J. Phys.: Condens. Matter **1**, 419 (1989).

[120] S.B. Roy and B.R. Coles, Phys. Rev. B **39**, 9360 (1990).

[121] S.J. Kennedy and B.R. Coles, J. Phys.: Condens. Matter **2**, 1213 (1990).

[122] C.S. Garde, J. Ray, and G. Chandra, Phys. Rev. B **42**, 8643 (1990).

[123] L. Paolasini, P. Dervenagas, P. Vulliet, J.-P. Sanchez, G.H. Lander, A. Hiess, A. Panchula, and P. Canfield, Phys. Rev. B **58**, 12117 (1998).

[124] B. Johansson, O. Eriksson, L. Nordström, L. Severin, and M.S.S. Brooks, Physica B **172**, 101 (1991).

[125] M.S.S. Brooks and B. Johansson, in *Handbook of Magnetic Materials*, edited by K.H.J. Buschow (North-Holland, Amsterdam, 1993) Vol. 7, page 139.

[126] K.H.J. Buschow and R.P. van Stapele, J. Appl. Phys. **41**, 4066 (1970).

[127] D. Gignoux, in *Materials Science and Technology*, edited by R.W. Cahn, P. Haasen, and E.J. Kramer (VCH, Weinheim, 1991) Vol. 3A, page 367.

[128] G.L. Olcese, Boll. Sci. Fac. Chim. Ind. Bologna **24**, 165 (1966).

[129] M. Croft, R. Neifield, B. Qi, G. Liang, I. Perez, S. Gunapala, F. Lu, S.A. Shaheen, E.G. Spencer, N. Stoffel, and M. den Boer, in *5th Int. Conf. Valence Fluctuations*, edited by S.K. Malik and L.C. Gupta (Plenum Press, New York, 1987) Vol. 1, page 217.

[130] R.A. Neifeld, M. Croft, T. Milhalisin, C.U. Segre, M. Madigan, M.S. Torikachvili, M.B. Maple, and L.E. DeLong, Phys. Rev. B **32**, 6928 (1985).

[131] K.H.J. Buschow, Rep. Prog. Phys. **40**, 1179 (1977).

[132] K. Ideka and K.A. Gschneidner Jr., Phys. Rev. Lett. **45**, 1341 (1980).

[133] C. Ritter, J. Phys.: Condens. Matter **1**, 2765 (1989).

[134] M. Forsthuber, F. Lehner, G. Wiesinger, G. Hilscher, T. Huber, E. Gratz, and G. Wortmann, J. Mag. Mag. Mater. **90&91**, 471 (1990).

[135] H.G. Farrell and W.E. Wallace, J. Chem. Phys. **40**, 1167 (1964).

[136] S.J. Kennedy, P.J. Brown, and B.R. Coles, J. Phys.: Condens. Matter **5**, 5169 (1993).

[137] C. Giorgetti, S. Pizzini, E. Dartyge, A. Fontaine, F. Baudelet, C. Brouder, Ph. Bauer, G. Krill, S. Miraglia, D. Fruchart, and J.P. Kappler, Phys. Rev. B **48**, 12732 (1993).

[138] J.Ph. Schillé, F. Bertran, M. Finazzi, Ch. Brouder, J.P. Kappler, and G. Krill, Phys. Rev. B **50**, 2985 (1994).

[139] A. Delobbe, A.M. Dias, M. Finazzi, L. Stichauer, J.P. Kappler, and G. Krill, Europhys. Lett. **43**, 320 (1998).

[140] M.J. Cooper, P.K. Lawson, M.A.G. Dixon, E. Zukowski, D.N. Timms, F. Itoh, H. Sakurai, H. Kawata, Y. Tanaka, and M. Ito, Phys. Rev. B **54**, 4068 (1996).

[141] V.S. Pokatilov, J. Mag. Mag. Mater. **189**, 189 (1998).

[142] S.J. Kennedy, A.P. Murani, J.K. Cockroft, and B.R. Coles, J. Phys.: Condens. Matter **1**, 629 (1989).

[143] S.J. Kennedy, A.P. Murani, B.R. Coles, and O. Moze, J. Phys. F: Metal Phys. **18**, 2499 (1988).

[144] H. Wada, M. Nishigori, and M. Shiga, J. Phys.: Condens. Matter **3**, 2083 (1991).

[145] H. Wada, M. Nishigori, and M. Shiga, J. Phys. Soc. Japan **62**, 1337 (1993).

[146] H. Wada, T. Harada, and M. Shiga, J. Phys.: Condens. Matter **9**, 9347 (1997).

[147] N. Ali and X. Zhang, Int. J. Mod. Phys. B **7**, 822 (1993).

[148] X. Zhang and N. Ali, J. Alloys Comp. **207/208**, 300 (1994).

[149] H. Yamada, J. Inoue, K. Terao, S. Kanda, and M. Shimizu, J. Phys. F: Metal Phys. **14**, 1943 (1984).

[150] P. Mohn and K. Schwarz, Physica **130B**, 26 (1985).

[151] O. Eriksson, L. Nordström, M.S.S. Brooks, and B. Johansson, Phys. Rev. Lett. **60**, 2523 (1988).

[152] O. Eriksson, B. Johansson, M.S.S. Brooks, and H.L. Skriver, Phys. Rev. B **40**, 9519 (1989).

[153] O. Eriksson, L. Nordström, A. Pohl, L. Severin, A.M. Boring, and B. Johansson, Phys. Rev. B **41**, 11807 (1990).

[154] J.Y. Rhee, J. Phys.: Condens. Matter **10**, 4307 (1998).

[155] L. Severin and B. Johansson, Phys. Rev. B **50**, 17886 (1994).

[156] J. Trygg, J.M. Wills, B. Johansson, and O. Eriksson, Phys. Rev. B **50**, 4200 (1994).

[157] P.K. Khowash, Phys. Rev. B **43**, 6170 (1991).

[158] Y. Muraoka, M. Shiga, and Y. Nakamura, J. Phys. Soc. Japan **42**, 2067 (1977).

[159] J.J.M. Franse, P.H. Frings, F.R. de Boer, and A.A. Menovski, in *Physics of Solids under High Pressure*, edited by J.S. Schilling and R.N. Shelton (North-Holland, Amsterdam, 1981) Vol. 1, page 181.

[160] J.R. Cullen and A.E. Clark, Phys. Rev. B **15**, 4510 (1977).

[161] T. Katayama and K. Hasegawa, in *Rapidly Quenched Metals*, edited by T. Masumoto and K. Suzuki (Japan Institute of Metals, Sendai, 1982) Vol. 4, page 915.

[162] Sh.M. Sharipov, K.M. Mukimov, L.A. Ernazarova, A.V. Andreyev, and N.V. Kudrevatykii, Phys. Met. Metall. **69**, 50 (1990).

[163] R.J. Cava, H. Takagi, B. Batlogg, H.W. Zandbergen, J.J. Krajewski, W.F. Peck Jr., R.B. van Dover, R.J. Felder, T. Siegrist, K. Mizuhashi, J.O. Lee, H. Eisaki, S.A. Carter, and S. Uchida, Nature (London) **367**, 146 (1994).

[164] R.J. Cava, H. Takagi, H.W. Zandbergen, J.J. Krajewski, W.F. Peck Jr., T. Siegrist, B. Batlogg, R.B. van Dover, R.J. Felder, K. Mizuhashi, J.O. Lee, H. Eisaki, and S. Uchida, Nature (London) **367**, 252 (1994).

[165] D.C. Johnston, F. Borsa, B.K. Cho, P.C. Canfield, P. Dervenagas, A.I. Goldman, B.N. Harmon, L.L. Miller, C. Stassis, B.J. Suh, D.R. Torgeson, M. Xu, J. Zarestky, M.F. Hundley,

R. Movshovich, J.D. Thompson, A.V. Chubukov, and B. Sternlieb, Chinese J. Phys. **34**, 397 (1996).

[166] P.C. Canfield, S.L. Bud'ko, B.K. Cho, W.P. Beyermann, and A. Yatskar, J. Alloys Comp. **250**, 596 (1997).

[167] M.R. Eskildsen, K. Harada, P.L. Gammel, A.B. Abrahamsen, N.H. Andersen, G. Ernst, A.P. Ramirez, D.J. Bishop, K. Mortensen, D.G. Naugle, K.D.D. Rathnayaka, and P.C. Canfield, Nature (London) **393**, 245 (1998).

[168] P. Fumagalli, J. Schoenes, M. Decroux, and Ø. Fischer, J. Appl. Phys. **67**, 5035 (1990).

[169] P. Fumagalli and J. Schoenes, Phys. Rev. B **44**, 2246 (1991).

[170] M. Xu, P.C. Canfield, J.E. Ostenson, D.K. Finnemore, B.K. Cho, Z.R. Wang, and D.C. Johnston, Physica C **227**, 321 (1994).

[171] B.K. Cho, P.C. Canfield, L.L. Miller, W.P. Beyermann, and A. Yatskar, Phys. Rev. B **52**, 3684 (1995).

[172] B.K. Cho, M. Xu, P.C. Canfield, L.L. Miller, and D.C. Johnston, Phys. Rev. B **52**, 3676 (1995).

[173] A. Yatskar, N.K. Budraa, W.P. Beyermann, P.C. Canfield, and S.L. Bud'ko, Phys. Rev. B **54**, R3772 (1996).

[174] T. Siegrist, H.W. Zandbergen, R.J. Cava, J.J. Krajewski, and W.F. Peck Jr., Nature (London) **367**, 254 (1994).

[175] H. Eisaki, H. Takagi, R.J. Cava, B. Batlogg, J.J. Krajewski, W.F. Peck Jr., K. Mizuhashi, J.O. Lee, and S. Uchida, Phys. Rev. B **50**, 647 (1994).

[176] R. Movshovich, M.F. Hundley, J.D. Thomson, P.C. Canfield, B.K. Cho, and A.V. Chubukov, Physica C **227**, 381 (1994).

[177] N.W. Ashcroft and N.D. Mermin, *Solid State Physics* (Saunders College Publishing, Fort Worth, 1976).

[178] B.K. Cho, P.C. Canfield, and D.C. Johnston, Phys. Rev. B **52**, 3844 (1995).

[179] P.C. Canfield, B.K. Cho, D.C. Johnston, D.K. Finnemore, and M.F. Hundley, Physica C **230**, 397 (1994).

[180] W.E. Pickett and D.J. Singh, Phys. Rev. Lett. **72**, 3702 (1994).

[181] L.F. Mattheiss, Phys. Rev. B **49**, 13279 (1994).

[182] H. Kim, C.-D. Hwang, and J. Ihm, Physica C **235-240**, 2107 (1994).

[183] H. Kim, C.-D. Hwang, and J. Ihm, Phys. Rev. B **52**, 4592 (1995).

[184] H. Kim, C.-D. Hwang, and J. Ihm, in *Proc. Top. Int. Cryog. Mag. Conf.*, edited by K. Tachikawa (World Scientific, Singapore, 1995) Vol. 1, page 130.

[185] D. Johrendt, C. Felser, O. Jepsen, O.K. Andersen, A. Mewis, and J. Rouxel, J. Solid State Chem. **130**, 254 (1997).

[186] L.F. Mattheiss, Phys. Rev. Lett. **58**, 1028 (1987).

[187] F. Bommeli, L. Degiorgi, P. Wachter, B.K. Cho, P.C. Canfield, R. Chau, and M.B. Maple, Phys. Rev. Lett. **78**, 547 (1997).

[188] F. Bommeli, L. Degiorgi, P. Wachter, B.K. Cho, P.C. Canfield, R. Chau, and M.B. Maple, Physica C **282-287**, 1475 (1997).

[189] F. Bommeli, L. Degiorgi, P. Wachter, B.K. Cho, P.C. Canfield, R. Chau, and M.B. Maple, Physica B **230-232**, 879 (1997).

[190] L. Van Hove, Phys. Rev. **89**, 1189 (1953).

[191] Z. Fisk, P.C. Canfield, W.P. Beyermann, J.D. Thompson, M.F. Hundley, H.R. Ott, E. Felder, M.B. Maple, M.A. Lopez de la Torre, P. Visani, and C.L. Seaman, Phys. Rev. Lett. **67**, 3310 (1991).

[192] P. Blum and F. Bertaut, Acta Cryst. **7**, 81 (1954).

[193] T. Komatsubara, N. Sato, S. Kunii, I. Oguro, Y. Furukawa, Y. Ōnuki, and T. Kasuya, J. Mag. Mag. Mater. **31-34**, 368 (1983).

[194] N. Sato, S. Kunii, I. Oguro, T. Komatsubara, and T. Kasuya, J. Phys. Soc. Japan **53**, 3967 (1984).

[195] H. Bergmann, I. Hinz, C. Koeppel, U. Vetter, and E. Warkentin, in *Gmelin Handbook of Inorganic and Organometallic Chemistry*, edited by H. Bergmann, G. Czach, H. Hein, C. Koeppel, and U. Vetter (Springer Verlag, Berlin, 1991) Vol. C 11b.

[196] S. Horn, F. Steglich, M. Loewenhaupt, H. Scheuer, W. Felsch, and K. Winzer, Z. Physik B **42**, 125 (1981).

[197] T. Fujita, M. Suzuki, T. Komatsubara, S. Kunii, T. Kasuya, and T. Oktsaka, Solid State Commun. **35**, 569 (1980).

[198] E. Zirngiebl, B. Hillebrands, S. Blumenröder, G. Güntherodt, M. Loewenhaupt, J.M. Carpenter, K. Winzer, and Z. Fisk, Phys. Rev. B **30**, 4052 (1984).

[199] B. Lüthi, S. Blumenröder, B. Hillebrand, E. Zirngiebl, G. Güntherodt, and K. Winzer, Z. Physik B **58**, 31 (1984).

[200] B. Lüthi, S. Blumenröder, B. Hillebrand, E. Zirngiebl, G. Güntherodt, and K. Winzer, J. Mag. Mag. Mater. **47&48**, 321 (1985).

[201] T. Goto, A. Tamaki, T. Suzuki, S. Kunii, N. Sato, and T. Suzuki, J. Mag. Mag. Mater. **52**, 253 (1985).

[202] T. Tanaka, R. Nishitani, C. Oshima, E. Bannai, and S. Kawai, J. Appl. Phys. **51**, 3877 (1980).

[203] C.D. Bredl, J. Mag. Mag. Mater. **63&64**, 355 (1987).

[204] M. Kawakami, S. Kunii, T. Komatsubara, and T. Kasuya, Solid State Commun. **36**, 435 (1980).

[205] A. Yanase, J. Mag. Mag. Mater. **31-34**, 453 (1983).

[206] P.A.M. van der Heide, H.W. ten Cate, L.M. ten Dam, R.A. de Groot, and A.R. de Vroomen, J. Phys. F: Metal Phys. **16**, 1617 (1986).

[207] H.D. Langford and W.M. Temmerman, J. Mag. Mag. Mater. **76&77**, 43 (1988).

[208] H.D. Langford, W.M. Temmerman, and G.A. Gehring, J. Phys.: Condens. Matter **2**, 559 (1990).

[209] M.B. Suvasini, G.Y. Guo, W.M. Temmerman, and G.A. Gehring, Physica B **206&207**, 37 (1995).

[210] M.B. Suvasini, G.Y. Guo, W.M. Temmerman, G.A. Gehring, and M. Biasini, J. Phys.: Condens. Matter **8**, 7105 (1996).

[211] H. Ripplinger, K. Schwarz, and P. Blaha, J. Solid State Chem. **133**, 51 (1997).

[212] S. Kimura, T. Nanba, S. Kunii, T. Suzuki, and T. Kasuya, Solid State Commun. **75**, 717 (1990).

[213] S. Kimura, H. Harima, T. Nanba, S. Kunii, and T. Kasuya, J. Phys. Soc. Japan **60**, 745 (1991).

[214] S. Kimura, T. Nanba, M. Tomikawa, S. Kunii, and T. Kasuya, Phys. Rev. B **46**, 12196 (1992).

[215] Y.S. Kwon, S. Kimura, T. Nanba, S. Kunii, M. Ikesawa, T. Suzuki, and T. Kasuya, J. Phys. Colloq. (Paris) **49**, C8–737 (1988).

[216] P. Wachter, in *Handbook on the Physics and Chemistry of Rare Earths*, edited by K.A. Gschneidner Jr., L. Eyring, G.H. Lander, and G.R. Choppin (Elsevier Science Publishers, London, 1994) Vol. 19, page 334.

[217] F. Marabelli, P. Wachter, and E. Walker, Phys. Rev. B **39**, 1407 (1989).

[218] F. Marabelli and P. Wachter, Phys. Rev. B **42**, 3307 (1990).

[219] M. Aono, T.C. Chiang, J.A. Knapp, T. Tanaka, and D.E. Eastman, Solid State Commun. **32**, 271 (1979).

[220] A. Hasegawa and A. Yanase, J. Phys. F: Metal Phys. **7**, 1245 (1977).

[221] N. Shino, S. Shigemasa, S. Imada, Y. Saitoh, H. Yamada, T. Nanba, S. Kimura, and S. Kunii, J. Phys. Soc. Japan **64**, 2980 (1995).

[222] R. Pittini, J. Schoenes, and P. Wachter, Phys. Rev. B **55**, 7524 (1997).

[223] R. Pittini, J. Schoenes, and P. Wachter, Physica B **230-232**, 538 (1997).

[224] R. Pittini, J. Schoenes, F. Hulliger, and P. Wachter, Phys. Rev. Lett. **78**, 725 (1997).

[225] R. Pittini and P. Wachter, J. Mag. Mag. Mater. **177-181**, 1025 (1998).

[226] J. Schoenes, J. Alloys Comp. **250**, 627 (1997).

[227] R.A. Robinson, A. Purwanto, M. Kohgi, P.C. Canfield, T. Kamiyama, T. Ishigaki, J.W. Lynn, R. Erwin, E. Peterson, and R. Movshovich, Phys. Rev. B **50**, 9595 (1994).

[228] P.C. Canfield, R. Movshovich, R.A. Robinson, J.D. Thompson, Z. Fisk, W.P. Beyermann, A. Lacerda, M.F. Hundley, R.H. Heffner, D.E. MacLaughlin, F. Trouw, and H.R. Ott, Physica B **197**, 101 (1994).

[229] J.D. Thompson, P.C. Canfield, A. Lacerda, M.F. Hundley, Z. Fisk, H.R. Ott, E. Felder, M. Chernikov, M.B. Maple, P. Visani, C.L. Seaman, M.A. Lopez de la Torre, and G. Aeppli, Physica B **186-188**, 355 (1993).

[230] R. Movshovich, A. Lacerda, P.C. Canfield, D. Arms, J.D. Thompson, and Z. Fisk, Physica B **199&200**, 67 (1994).

[231] R. Movshovich, A. Lacerda, P.C. Canfield, J.D. Thompson, and Z. Fisk, Phys. Rev. Lett. **73**, 492 (1994).

[232] R.A. Robinson, M. Kohgi, T. Osakabe, P.C. Canfield, T. Kamiyama, T. Nakane, Z. Fisk, and J.D. Thompson, Physica B **186-188**, 550 (1993).

[233] A. Amato, P.C. Canfield, R. Feyerherm, Z. Fisk, F.N. Gygax, R.H. Heffner, D.E. MacLaughlin, H.R. Ott, A. Schenck, and J.D. Thompson, Phys. Rev. B **46**, 3151 (1992).

[234] A. Amato, P.C. Canfield, R. Feyerherm, Z. Fisk, F.N. Gygax, R.H. Heffner, E.A. Knetsch, D.E. MacLaughlin, H.R. Ott, A. Schenck, J.D. Thompson, and U. Zimmermann, Physica B **186-188**, 615 (1993).

[235] R.H. Heffner, A. Amato, P.C. Canfield, R. Feyerherm, Z. Fisk, F.N. Gygax, D.E. Maclaughlin, A. Schenck, J.D. Thompson, and H.R. Ott, Physica B **199&200**, 113 (1994).

[236] O. Eriksson, J.M. Wills, and A.M. Boring, J. Alloys Comp. **185**, 145 (1992).

[237] G.J. McMullan and M.P. Ray, J. Phys.: Condens. Matter **4**, 7095 (1992).

[238] C.J. Bradley and A.P. Cracknell, *The Mathematical Theory of Symmetry in Solids* (Clarendon Press, Oxford, 1972).

[239] H.A. Bethe, Ann. Phys. (Leipzig) **3**, 133 (1929).

ACKNOWLEDGEMENTS

I would like to thank:

- Prof. David Lynch for advising me throughout the course of my graduate work. The trust he had in me was frightening at first. I deeply appreciate the way he guides graduate students which gave me the opportunity to chose my own thesis projects and to work independently. I could always count on his support, no matter what I was trying to do. I also enjoyed our discussions about physics as well as new travel destinations. I hope that I will find this again in my future career.

- Profs. Paul Canfield, Bruce Harmon, William McCallum, and Russell Lavery for serving on my committee and their suggestions on my thesis.

- Dr. Stefan Zollner who gave me the opportunity to come to Iowa (in January!!!). After working in his lab for six months I decided to continue my graduate work at Iowa State University. Stefan introduced me to solid state physics and ellipsometry, which set the way for my work at ISU and possibly for my future career.

- The followers of PCC, Dr. Ian Ronda Fisher, fresh-Dr. Ken Duane Myers, and Tim Wiener for the small samples and the magnetization measurements. Although they sometimes failed the samples they provided were excellent. Special thanks to Ian for many discussions about the interpretation of magnetization data and how to determine T_C and T_N, a point that still has not been settled, as is our dispute over how to measure wind chill and heat index, provided they are physical quantities. I would like to thank Paul for many answers to my favorite question, "what's next?".

- Prof. Bruce Harmon for many interesting ideas on how to interpret *the stuff* we see in our spectra as well as for the help he provided modelling the magnetization of some *unusual* samples.

- Dr. Vladimir Antropov for providing the software support and valuable tips on how to run the band structure programs. He gave me valuable insight into the secret art of electronic structure calculations.

- Paul and Mike, the support personnel from the low-temperature lab, for keeping me cool.
- The Ames Lab machine shop for excellent production of whatever unusual prototypes I needed.
- Jerry Ostenson for a good vacuum and excellent company as a member of the international dining society. He also pointed out the best retail store in the entire Midwest (located near Owatonna, MN).
- The entire Lynch-group: Derek Brammeier, Joong Mok Park, Ye Feng, and Dr. S.J. Lee for many interesting cultural exchanges. My advice to Joong Mok, handle with extreme care and good luck with that beast.
- Kelly Junge for half-way decent company at the lab and as a permanent member of our seminars at 2430 Lincoln Way, which many people knew about but only few appreciated. He taught me the part of the English language I missed at school. "It don't matter no more" became part of my vocabulary.
- My dear friend Abby who refrained from kicking out the grouchy German who was so much absorbed by his work. I will always appreciate her unconditional love and support. She is an awesome person!
- Pris and Chuck for many many extremely funny evenings and the experience of New Mexico chilies. During our weekend discussion groups and pancake dinners I learned valuable lessons about American politics. They had to put up with a lot of German-style cooking while I was around (including highly nutritious foods like cream and lard). I have to admit that my primary interest is the old green frige in the basement which Chuck keeps stocked with the best homebrew available.
- All the Princes of Kabekona for introducing me to their ideologies. Boys, you are good!
- Everybody who made my life in Ames easier and more fun.
- Many people in the department who I enjoyed working with.
- and last but not least vielen Dank an meine Familie daheim für die ständige Unterstützung. Der Rat meiner Eltern - "Lern soviel wie Du kannst" - hat mich bis hierher getragen. Die herzlichen feuchtfröhlichen Empfänge während meiner Heimaturlaube sind unvergeßlich.

IMAGE EVALUATION
TEST TARGET (QA-3)

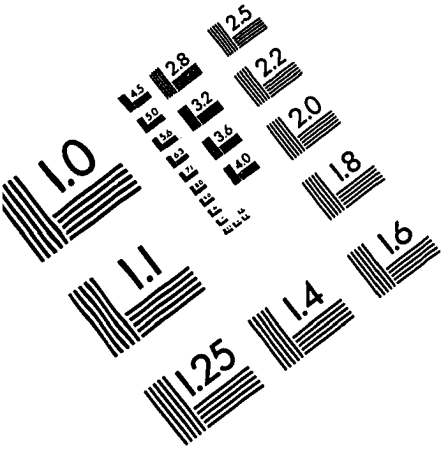

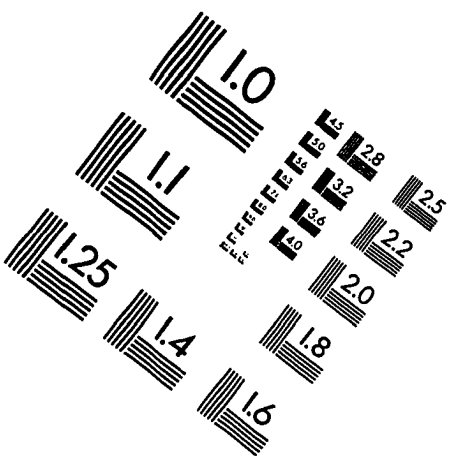

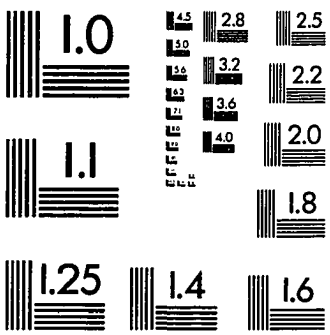

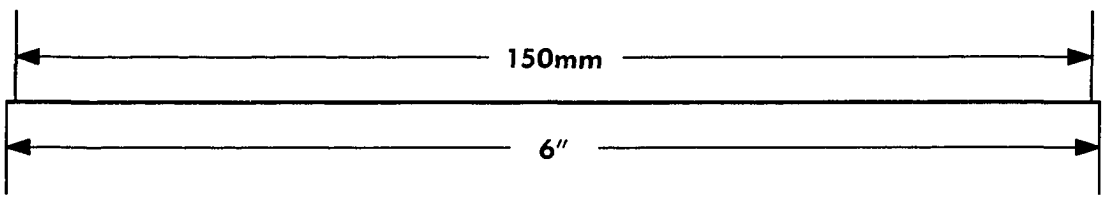

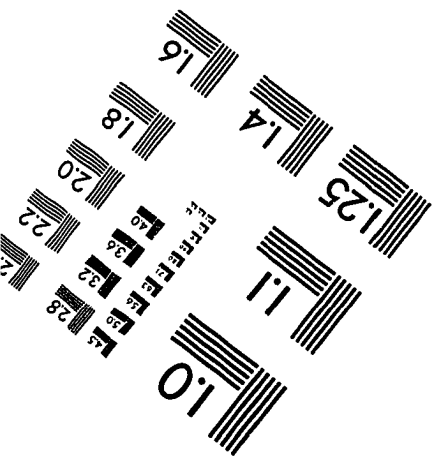

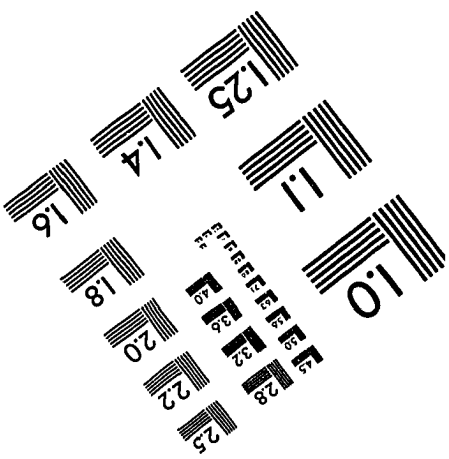

APPLIED IMAGE, Inc
1653 East Main Street
Rochester, NY 14609 USA
Phone: 716/482-0300
Fax: 716/288-5989